

**TECHNISCHE  
UNIVERSITÄT  
DRESDEN**

---

---

**Two-Pion Intensity-Interferometry  
in Collisions of  
Au+Au at  $\sqrt{s_{\text{NN}}} = 2.41 \text{ GeV}$   
measured with HADES**

Dissertation  
zur Erlangung des akademischen Grades  
Doktor der Naturwissenschaften  
(Dr. rer. nat.)

Erstellt von

Robert André Heinrich Greifenhagen  
geboren am 28. August 1990  
in Annaberg-Buchholz

Institut für Kern- und Teilchenphysik  
Fakultät Physik  
Fachbereich Mathematik und Naturwissenschaften  
Technische Universität Dresden  
Dresden 2020

Eingereicht am 26.06.2020

Verteidigt am 11.12.2020

Erstgutachter: Prof. Dr. B. Kämpfer

Zweitgutachter: Prof. Dr. C. Blume

Drittgutachter: Prof. Dr. T. E. Cowan

# Abstract

In this thesis high-statistics  $\pi^-\pi^-$  and  $\pi^+\pi^+$  femtoscopy data are presented for Au + Au collisions at  $\sqrt{s_{\text{NN}}} = 2.4 \text{ GeV}$ , measured with the High Acceptance Di-Electron Spectrometer HADES located at the heavy-ion synchrotron SIS18 at GSI.

Due to space-momentum correlations the technique of intensity interferometry allows only to measure regions of homogeneity where pairs of particles with certain momentum origin. The determination of the space-time extent of the corresponding emission sources is then only possible via a comparison to models. The purpose of this thesis is to provide a multi-differential data set as input for such models and calculations, to draw conclusions from the total spatial and temporal extension of the pion emitting source.

More than two billion events of the 45 % most central collisions are analysed. A complex data-driven pair cut is established to account for the close-track deficits in the non-trivial hexagonal geometry of the HADES setup. The correlation function is studied in the longitudinally co-moving system using the Bertsch-Pratt parametrisation. The region of homogeneity, parametrised as three-dimensional Gaussian distribution, is studied in dependence on pair transverse momentum, rapidity, azimuthal emission angle with respect to the event plane, collision centrality, and beam energy. For all centralities and transverse momenta, a geometrical distribution of ellipsoidal shape is found in the plane perpendicular to the beam direction with the larger extension perpendicular to the reaction plane. For large transverse momenta, the corresponding eccentricity approaches the initial eccentricity. The eccentricity is smallest for most central collisions, where the shape is almost circular. Furthermore, a tilt of the source w.r.t. the beam axis is found. The magnitude of the tilt angle of the emission ellipsoid in the reaction plane decreases with increasing centrality and increasing transverse momentum. All source radii increase with centrality, largely exhibiting a linear rise with the cubic root of the number of participants. A substantial charge-sign difference of the source radii is found, appearing most pronounced at low transverse momentum, which is addressed to the central Coulomb potential generated by the electrical charge of the participating nucleons in the collision. The extracted source parameters agree well with a smooth extrapolation of the

center-of-mass energy dependence established at higher energies, extending the corresponding excitation functions down towards a very low energy.

# Kurzdarstellung

In dieser Arbeit werden femtoskopische  $\pi^-\pi^-$ - und  $\pi^+\pi^+$ -Daten mit hoher Statistik präsentiert, welche in Kollisionen von Au + Au bei einer Schwerpunktsenergie von  $\sqrt{s_{\text{NN}}} = 2.4 \text{ GeV}$  pro Nukleonpaar mithilfe von HADES (Zwei-Elektronen Spektrometer mit hoher Akzeptanz) am Schwerionen-Synchrotron an der GSI gemessen wurden.

Aufgrund von Orts-Impuls-Korrelationen können mittels der Methode der Intensitäts-Interferometry nur Homogenitätsbereiche gemessen werden, aus welchen Teilchenpaare mit bestimmten Impuls entspringen. Die Bestimmung der raum-zeitlichen Ausdehnung der entsprechenden Emissionsquelle ist dann nur über die Hinzunahme von Modellvergleichen möglich. Die Absicht dieser Arbeit ist es, einen multi-differenziellen Daten-Satz zur Verfügung zustellen, welcher als Eingabe für solche Modelle und Rechnungen genutzt werden kann, um dann Rückschlüsse auf die absolute räumliche und zeitliche Ausdehnung der Pionen-emittierenden Quelle ziehen zu können.

Mehr als zwei Milliarden Ereignisse der 45 % zentralsten Kollisionen werden analysiert. Eine komplexe Daten-basierende Paarselektion wird eingeführt, um die Verluste nah beieinander verlaufender Teilchenspuren innerhalb des nicht-trivialen hexa-geometrischen HADES-Aufbaus zu berücksichtigen. Die Korrelationsfunktion wird im longitudinal mitbewegten Inertialsystem in Bertsch-Pratt-Parametrisierung untersucht. Der als dreidimensionales Ellipsoid parametrisierte Homogenitätsbereich wird in Abhängigkeit von Transversalimpuls, azimuthalem Emissionswinkel relativ zur Reaktionsebene und Rapidität des Paars sowie Zentralität der Kollision und der Strahlenergie untersucht. In allen Zentralitäts- und Transversalimpulsbereichen wird eine geometrische Verteilung mit elliptischer Form innerhalb der auf die Strahlachse bezogenen transversalen Ebene beobachtet, wobei die größte Ausdehnung senkrecht zur Reaktionsebene zeigt. Für große Transversalimpulse stimmt die zugehörige Exzentrizität mit derjenigen der initialen Nukleonenverteilung überein. Die Exzentrizität ist am kleinsten für die zentralsten Kollisionen, bei denen eine fast kreisrunde Form beobachtet wird. Des Weiteren ist eine Neigung der Emissionsquelle relativ zur Strahlachse feststellbar. Der Wert des Neigungswinkels des Ellipsoids innerhalb der Reaktionsebene verringert sich mit zunehmend zentraleren Kollisionen und

steigendem Transversalimpuls. Alle Quellradien werden größer mit zunehmender Zentralität und zeigen einen nahezu linearen Anstieg mit der Kubikwurzel der Anzahl der Partizipanten. Ein beträchtlicher Unterschied der Quellradien bezogen auf das Ladungsvorzeichen der Pionen wird beobachtet, welcher am prägnantesten bei kleinen Transversalimpulsen auftritt. Dieser wird dem zentralem Coulomb-Potential zugeschrieben, welches durch die elektrische Ladung der an der Kollision teilnehmenden Nukleonen generiert wird. Die extrahierten Quellparameter stimmen gut mit glatten Extrapolationen der Schwerpunktsenergie-Abhängigkeit überein, welche bei höheren Strahlenergien fixiert wurden, und erweitern diese hinab bis zu sehr kleinen Energien.

# Contents

<b>1</b>	<b>Introduction</b>	<b>1</b>
1.1	Heavy-Ion Collisions . . . . .	2
1.2	Intensity Interferometry . . . . .	5
1.2.1	History . . . . .	5
1.2.2	Length of homogeneity . . . . .	6
1.2.3	Overview . . . . .	7
1.3	Motivation of this work . . . . .	8
<b>2</b>	<b>Two-particle interferometry</b>	<b>11</b>
2.1	Quantum-statistic effects . . . . .	11
2.2	Two-particle correlation-function . . . . .	13
2.2.1	Finite source: Wigner density distributions . . . . .	13
2.2.2	Correlation with relative coordinates . . . . .	13
2.2.3	Static and dynamic sources . . . . .	14
2.2.4	Partial coherence: the $\lambda$ parameter . . . . .	15
2.3	Final state interactions . . . . .	17
2.3.1	Two-particle Coulomb interaction for extended sources	18
2.3.2	$N$ -particle Coulomb interaction . . . . .	18
2.4	Gaussian approximation . . . . .	19
2.4.1	Bertsch-Pratt parametrisation . . . . .	20
2.4.2	Azimuthally symmetric collisions . . . . .	22
2.4.3	Finite impact parameter . . . . .	24
2.5	Models for the source distribution . . . . .	25
<b>3</b>	<b>The HADES experiment</b>	<b>27</b>
3.1	Target . . . . .	28
3.2	RICH . . . . .	29
3.3	Magnetic spectrometer . . . . .	30
3.3.1	Magnet . . . . .	30
3.3.2	Mini Drift Chambers . . . . .	31
3.4	Time-of-flight system . . . . .	33
3.4.1	META detectors . . . . .	33
3.4.2	START and VETO detector . . . . .	35

3.5	Forward hodoscope . . . . .	36
3.6	Data acquisition and trigger . . . . .	37
3.7	UrQMD simulations . . . . .	38
<b>4</b>	<b>Analysis</b>	<b>39</b>
4.1	Event characterization . . . . .	39
4.1.1	Event Vertex . . . . .	40
4.1.2	Event cleaning . . . . .	40
4.1.3	Centrality . . . . .	43
4.1.4	Event plane . . . . .	46
4.1.5	Event selection . . . . .	49
4.2	Particle identification . . . . .	50
4.2.1	Tracking . . . . .	50
4.2.2	Momentum reconstruction . . . . .	54
4.2.3	TOF/RPC-META matching . . . . .	56
4.2.4	Identification using time-of-flight . . . . .	56
4.2.5	Single particle selection . . . . .	58
4.3	Experimental correlation function . . . . .	61
4.3.1	Construction . . . . .	61
4.3.2	Pair selection . . . . .	64
4.3.3	Mixing . . . . .	65
4.3.4	Accounting for non-physical correlations . . . . .	66
4.4	Extracting the local space informations . . . . .	81
4.4.1	Two-particle correlation function including FSI . . . . .	81
4.4.2	Finite relative momentum resolution . . . . .	84
4.4.3	Fit range . . . . .	89
4.4.4	Direct imaging: deviations from Gaussian sources . . . . .	89
4.5	Including the azimuthal dependence . . . . .	91
4.5.1	Accounting for the explicite $\Phi$ dependence . . . . .	91
4.5.2	Finite event plane resolution . . . . .	92
4.5.3	Final observables in the RP-fixed coordinate system .	94
<b>5</b>	<b>Results</b>	<b>97</b>
5.1	Correlation functions . . . . .	97
5.1.1	One-dimensional correlation function . . . . .	97
5.1.2	Three-dimensional correlation function . . . . .	100
5.2	Azimuthally integrated correlations . . . . .	109
5.2.1	Dependence on $\mathbf{p}_{t,12}$ and centrality . . . . .	109
5.2.2	The cross-term $R_{\text{out long}}^2$ under variation of $\mathbf{y}_{12}$ . . . . .	113
5.2.3	Other systematic influences . . . . .	115
5.2.4	Dependence on polarity for central collisions . . . . .	119
5.2.5	Interpretation of the $k_t$ dependence . . . . .	123
5.2.6	Excitation functions . . . . .	128
5.3	Azimuthally dependent correlations . . . . .	130

5.3.1	Oscillations of the femtoscopic variances . . . . .	130
5.3.2	Excitation functions . . . . .	137
5.3.3	Dependence on centrality . . . . .	146
<b>6</b>	<b>Conclusion and Outlook</b>	<b>157</b>
<b>Appendix</b>		<b>161</b>
<b>A</b>	<b>Details on analysis</b>	<b>163</b>
A.1	Minimisation procedures . . . . .	163
A.1.1	Least $\chi^2$ method . . . . .	163
A.1.2	Maximum-likelihood method . . . . .	163
A.2	Gaussian convolution . . . . .	165
<b>B</b>	<b>Further systematics</b>	<b>169</b>
B.1	$R_{\text{out long}}^2$ in $\Phi$ -integrated analyses . . . . .	169
B.2	Results for reversed magnetic field . . . . .	170
B.3	Effective potentials . . . . .	171
B.4	Tilt angle systematics . . . . .	175
B.5	Charge-sign corrected extensions of the emission ellipsoid . .	180
B.6	Eccentricity - different calculations . . . . .	181
B.7	Volume calculation . . . . .	183
<b>C</b>	<b>Explicit models for the source distribution</b>	<b>185</b>
C.1	Three-dimensional Gaussian source with flow . . . . .	185
C.2	Boost-invariant blast-wave . . . . .	187
<b>D</b>	<b>Data summary tables</b>	<b>189</b>
D.1	Azimuthally integrated . . . . .	189
D.2	Azimuthally dependent . . . . .	192
<b>List of Figures and Tables</b>		<b>211</b>



# 1 | Introduction

The known world can be described by the four fundamental interactions: electro-magnetism, weak interaction, strong interaction and gravitation. Beside the last one these fundamental forces of nature are described by quantum-field theories, quantum electrodynamics (QED), quantum-flavour dynamics (QFD) and quantum chromodynamics (QCD). They are unified in the Standard Model of particle physics, which is the most proven and imperishable theory up to today. It contains 17 named elementary particles, 12 fermions and 5 bosons, where the Higgs boson discovered in 2012 is the most recent. Quantum chromodynamics is the quantum field theory for describing strong interaction phenomena. It can be seen as an analogon to QED containing instead of leptons and photons quarks and gluons and describing the interaction among them. Furthermore QED is an Abelian gauge theory with symmetry group  $U(1)$ , while QCD is a non-Abelian gauge theory with symmetry group  $SU(3)$ , which results in eight gauge bosons, called gluons, and leads to the self interaction of them. A consequence of the latter is the different behaviour of the running coupling compared to QED. Running coupling means, that the interaction strength depends on the energy scale of the examined processes. In QED the interaction is weak at low energies. In QCD the interaction is weak at large energies, which is known as asymptotic freedom. In that regime processes can be evaluated by perturbation theory (pQCD) very well. For low energies the interaction strength of QCD becomes very large, which results in confinement. It can be visualised in such a manner that the force between quarks rises if one tries to separate them and the energy of the gluon field increases until it is high enough to create a new quark-antiquark pair, so the quarks will never appear free but are always bound into bound states. The bound states of the strong interaction are called hadrons. They are composite objects containing two or more quarks and anti-quarks, respectively. They can contain three quarks (baryons), three anti-quarks (anti-baryons), one quark and one anti-quark (mesons) or higher numbered combinations of quarks and anti-quarks (exotica, like tetra-quarks or penta-quarks). The lightest charged meson is the pion with a mass of 139.57 MeV. Analogously to atomic physics these bound states exist not only as ground states, but can appear as excited states or resonances

## 1. Introduction

---

with certain decay width and lifetime. To account for the phenomena at low energies several approaches exist. Lattice QCD (lQCD) evaluates the strong interaction numerically on a finitely sized grid and by-passes the leak of perturbation calculations. In contrast the use of Dyson-Schwinger equations delivers a self-contained system of integral equations describing exactly the propagators of quarks and gluons with self interaction. However, the first approach depends on the size of the underlying grid, and evaluations require immediately more resources of numerical calculation power when increasing the grid number. The second approach depends strongly on the truncations of the integral equations, since otherwise a practical evaluation is not possible. The description of strongly interacting particles becomes even more complicated when the couple of considered quarks and gluons is not located in vacuum, but surrounded by a medium of strongly interacting matter, especially if this surrounding medium is not in the ground state, like in nuclei of heavy particles, but very hot and/or dense. In a thermodynamical approach this medium can be characterised by a temperature  $T$ , describing the average energy of the particles, and a baryonic chemical potential  $\mu_B$ , being a measure for the baryon density. Masses and propagators of the particles change as well as lifetimes, cross-sections and production thresholds of resonances, since the medium offers additional energy for the particular interaction processes. In nature such a medium is supposed to exist in the early stage of the universe a few microseconds after the big bang as well as in compact stellar objects like neutron stars. For a deeper understanding of the early stage of the universe and the physics within the high mass collapse products of giant stars one is interested in the equation of state (EoS) of the nucleonic matter. For developing meaningful models and effective theories and for testing of them it is inevitable to generate data of experimental observables, which can be used for adjusting the theoretical approaches. The most useful tool up to date to generate such a hot and/or dense medium in the laboratory is a heavy-ion collision (HIC).

In Section 1.1 the physics of heavy-ion collisions will be explained. In Section 1.2 a tool for measuring the extension of the collision area will be presented. Finally in Section 1.3 the aim of this thesis will be exemplified.

### 1.1 Heavy-Ion Collisions

Nuclei of heavy elements like gold, lead or uranium are accessible objects with the highest aggregation of baryons in one place with densities around  $\rho_0 \approx 0.16$  nucleons/fm<sup>3</sup>. To create matter with even higher baryonic density and high energy one aims at collisions of two of these nuclei. For that purpose ion accelerators are used, boosting the ions to relativistic energies, i.e. kinetic energies as high as their rest energy or even higher. The achievable energy of actually operating facilities for heavy-ions ranges from about

1A GeV at the heavy-ion synchrotron SIS18 over the Alternating Gradient Synchrotron (AGS), Super Proton Synchrotron (SPS), Relativistic Heavy Ion Collider (RHIC) up to 5A TeV at the Large Hadron Collider (LHC). There exist two general types of relativistic heavy-ion collision experiments. First the so-called fixed target experiments, where the ion beam is focused on a target at rest in form of e.g. a thin foil. The produced particles are emitted in forward direction and measured by a particle spectrometer around the beam axis. Secondly the collider experiments, where bunches of ions are moving in opposite directions inside a storage ring. At dedicated interaction points the bunches are directed to cross each other allowing the ions to collide with each other. The characteristic cylindrically symmetric spectrometers are constructed around these interaction areas. While in collider experiments much higher nucleon-nucleon energies are achievable within the same accelerator rigidity, fixed target experiments are characterised by much higher interaction rates.

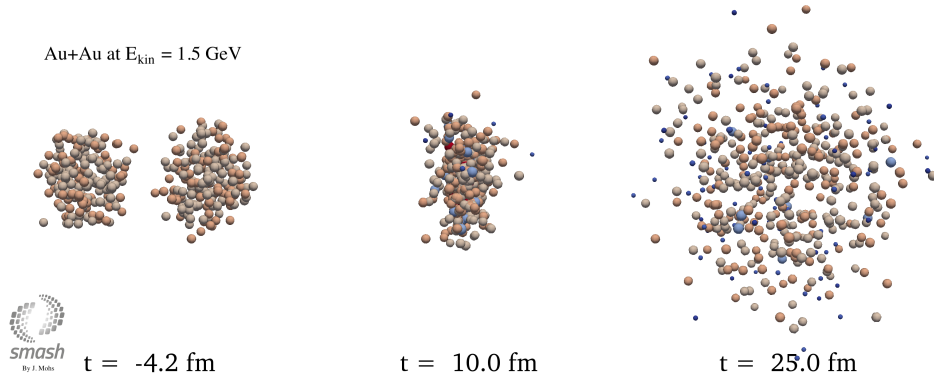


**Figure 1.1:** Scheme of the evolution of a relativistic heavy-ion collision at SIS energies generated with the transport model SMASH [1] (<https://smash-transport.github.io/>).

The evolution of a heavy-ion collision is illustrated in Figure 1.1. The two nuclei are moving towards each other with Lorentz-contracted extension in beam direction. The moment they meet each other is characterised by first-chance nucleon-nucleon collisions. It follows the stage of high density, where at SIS18 energies the matter is assumed to be compressed up to  $\rho \approx 3\rho_0$  with temperatures around  $T = 80 - 100$  MeV. Depending on the initial energy of the ions a quark-gluon plasma (QGP) can be created, i.e. a state of deconfined quarks and gluons. It was predicted as a consequence of the asymptotic freedom for sufficiently high temperatures and densities and is of special interest in heavy-ion collisions at ultra-relativistic energies, i.e. larger than 10 – 20A GeV. With or without a QGP a hydro-dynamical expansion follows, where the so-called 'fireball' cools down until no inelastic processes

## 1. Introduction

---

take place and produced stable particles do not transform anymore. This point of the evolution is called the chemical freeze-out. The fireball continues to expand and the particles can still interact elastically with each other until the kinetic freeze-out. At that point the last interaction takes place, and the particles move away with constant momenta, eventually affected by the Coulomb potential created by the sum of all charged particles.

Besides the chosen size and the adjustable kinetic energy of the nuclei, the collision geometry is important for the product of the heavy-ion collision. The closest distance between the centers of the nuclei is defined as the impact parameter  $b$ . It characterises the centrality of a collision, i.e. a small value of the impact parameter is related to central collisions. If the value of  $b$  is large the collision is called a peripheral collision. Nucleons inside the overlap region which take place in the collision are called participants. The other nucleons, passing by without interaction, are called spectators. The impact parameter can not be determined directly, but is, e.g., related to the sum of emitted particles, called multiplicity, or to the total energy released in direction transverse to the beam. The vector of the direction of  $b$  and the beam axis span the reaction plane of the collision.

The temperature and the baryonic density of heavy-ion collisions in the 1A GeV energy region are comparable to those of neutron star mergers or the formation of a supernova. Thus they can be used to study the equation of state in this hot and dense hadronic medium, assuming to have for a short time a system at equilibrium. The EoS is implemented in hydrodynamical models (e.g. UrQMD), which are used to simulate a heavy-ion collision. The outcome of these simulations is compared to experimental data allowing for adjusting the parameters and the EoS. Typical observables are particle yields, which can be studied multi-differentially, e.g. in transverse momentum, rapidity and azimuthally direction. Of special interest is also the volume of the fireball, since it is another extensive state variable in the EoS. If it is possible to determine it independently from the particle yields, one has direct experimental access to one intensive state variable via the ratio of those two.

Furthermore, a hydrodynamical expansion of the fireball, driven by high pressure gradients, implicates a collective motion of the particles, known as collective flow. It is mainly directed in outward direction, called radial flow, but can have higher moments with preferred angular direction due to the initial collision geometry of the nuclei. At SIS energies especially the so-called 'elliptic flow' is of interest, pointing out of the reaction plane and forming a squeeze-out at the early stage of the collision, illustrated in Figure 1.2. In contrast, the opposite is observed at SPS and higher energies, where the expansion is more directed inside the reaction plane. Indications of the collective motion will be visible in the angular distributions of the momentum dependent particle yields and higher order observables. It can

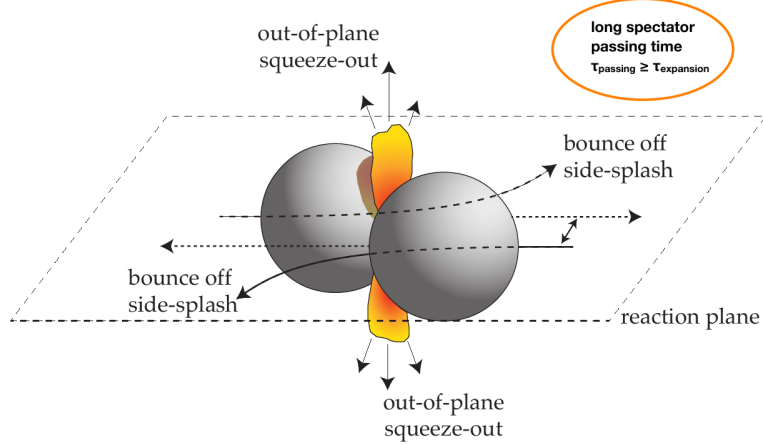


**Figure 1.2:** Illustration of a heavy-ion collision at SIS energies with long spectator passing times and the typical squeeze-out. Figure taken from [2].

also be expected that this collective flow influences the configuration of the spatial extension of the source at freeze-out.

Thus, it is inevitable to have knowledge about the spatio-temporal size of the fireball region for discussing dynamical processes. The length scales of heavy-collisions are in the order of  $1 \times 10^{-14}$  m and the time scales in the order of  $1 \times 10^{-22}$  s, which is highly non-trivial to measure. Here, the technique of intensity interferometry emerges.

## 1.2 Intensity Interferometry

Two-particle intensity interferometry of hadrons is widely used to study the spatio-temporal size, shape and evolution of their source in heavy-ion collisions or other similar reactions. A detailed review is given in [3].

### 1.2.1 History

The technique of intensity interferometry was pioneered by Hanbury Brown and Twiss [4], based on the quantum-statistical interference of identical particles. In 1956 they measured correlations of photons emitted from star Sirius in their intensities without collecting the phase information. After publishing the measured angular radii of stars claiming excellent resolution, the technique later on was named HBT interferometry. Independently and nearly the same time Goldhaber et al. [5, 6] first applied intensity interferometry to hadrons. In 1959, when discovering the  $\rho^0$  resonance in proton-antiproton collisions, they found an unexpected angular correlation

## 1. Introduction

---

between identical pions. In the 1970s many effort was invested by Russian scientists, e.g. Kopylov and Podgoretsky [7–9], to refine the known methods for source-size measurements of excited nucleonic systems. Next to the quantum-statistical effect also other correlations, like Coulomb or strong interactions, were shown to be useful for measuring source sizes [10]. Although stars and excited heavy ions can be hardly more different in sense of lifetime, size and distance to the detector, the notion HBT is well established in the community of heavy-ion physics as term for identical-particle interferometry. The term *femtoscopy* was embossed by Lednický [11] including all kinds of measurements providing access to the spatio-temporal information of nucleonic systems.

### 1.2.2 Length of homogeneity

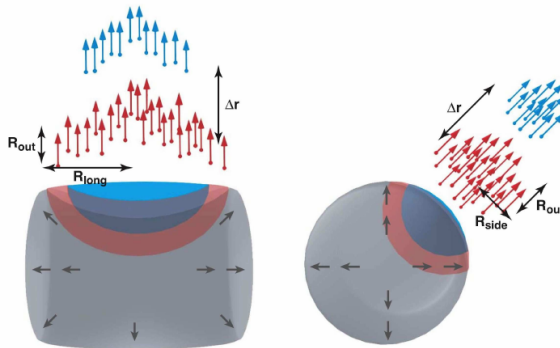


**Figure 1.3:** The source sizes measured by intensity interferometry are influenced by momentum-space correlations leading to reduced lengths of homogeneity. Figure taken from [3].

In heavy-ion collisions, the intensity interferometry does not allow to measure directly the reaction volume, as the emission zone, changing shape and size in the course of the collision, is affected by dynamically generated space-momentum correlations, e.g. radial expansion after the compression phase or resonance decays. Thus, intensity interferometry generally does not yield the proper source size, but rather an effective 'length of homogeneity' [3], illustrated in Figure 1.3. It measures source regions in which particle pairs are close in momentum, so that they are correlated as a consequence of their quantum statistics or due to their two-body interaction. At energies in the GeV region, the measured particles can originate from many different processes. Therefore, the intensity interferometry may provide additional information to the understanding of reaction mechanisms which finally determine the particle emission sources.

### 1.2.3 Overview

In general, the sign and strength of the correlation are affected by (i) the strong interaction, (ii) the Coulomb interaction if charged particles are involved, and (iii) the quantum statistics in the case of identical particles (Fermi-Dirac suppression for fermions, Bose-Einstein enhancement for bosons). In the case of  $\pi\pi$  correlations, when probed by small momentum differences, the mutual strong interaction appears to be negligible [11, 12] compared to the effects (ii) and (iii).

Source size measurements with pairs of the lightest mesons for heavy systems like Au + Au, Au + Pb and Pb + Pb have been performed over three orders of magnitude in center of mass energy at AGS [13, 14], SPS [15, 16], RHIC [17] and LHC [18]. They combine to an excitation function of the source extensions both in longitudinal and transverse directions relative to the beam axis. A slightly increasing trend in longitudinal, but nearly no dependence of correlation measures in transverse direction as a function of center of mass energy have been observed. Additionally, a strongly increasing source size at small energies in both directions is postdicted, as derived by the data of E895. Of special interest are the azimuthally dependent HBT measurements provided by E895 [19], CERES [20], STAR [17] and ALICE [21]. Especially at the lowest beam energies between 2 and 6A GeV a tilt of the ellipsoidal source within the reaction plane was extracted. For the somewhat smaller system La + La, studied at 1.2A GeV with the HISS spectrometer at the Lawrence Berkeley Laboratory (LBL) Bevalac, pion correlation data were reported by Christie et al. [22, 23]. An oblate shape of the pion source and a correlation of the source size with the system size were found. Also, pion intensity interferometry for small systems (Ar + KCl, Ne + NaF) was studied at 1.8A GeV at the LBL Bevalac using the Janus spectrometer by Zajc et al. [24]. Both groups made first attempts to correct the influence of the pion-nuclear Coulomb interaction on the pion momenta. The effect on the source radii, however, was found negligible for their experiments.

Further investigations of the charge-sign dependence in heavier systems, but at larger beam energies, have been done by [14, 25]. The source extension for negatively charged pairs was found to be slightly larger than for positive pion pairs, but results are overlapping within their statistical uncertainties. An opposite effect is reported by [26], also having large statistical uncertainties giving the effect a significance of less than  $2\sigma$ .

Not only  $\pi\pi$  correlations are studied, but also two-kaon correlations [28], proton-proton correlations or higher mass particles interacting via the strong interaction are used to extract source sizes. A scaling of the source extension with the transverse mass of the testing particles,  $m_t = (m^2 + k_t^2)^{1/2}$  with transverse momentum  $k_t$ , has been found. This is illustrated in Figure 1.4 [27] and known as  $m_t$ -scaling of the HBT radius parameters. One can also invert the strategy of HBT interferometry, i.e. fixing the source size by model

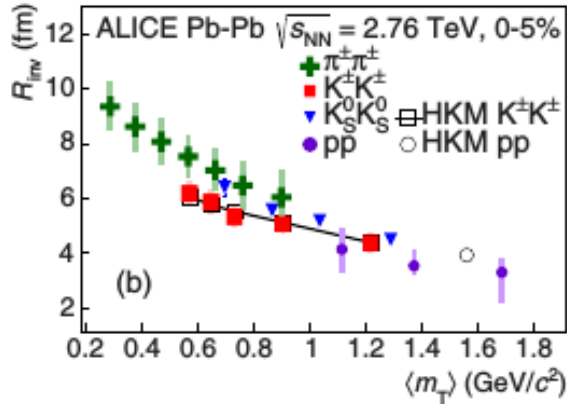


**Figure 1.4:** Illustration of the so-called  $m_t$ -scaling: The source radius  $R_{\text{inv}}$  inversely scales with the transverse mass of different testing particles. Figure taken from [27].

calculations or reference measurements and then to study the potential of the strong two-particle interaction [29–33]. Such investigations can be extended to unlike-sign pairs of particles [34] or even pairs of unequal mass particles [35–37].

### 1.3 Motivation of this work

The purpose of this work is to measure the extension of the fireball generated in fixed-target heavy-ion collisions at a beam energy of  $1.23A$  GeV using the technique of intensity interferometry applied to pairs of charged pions. Pions are ideal candidates for imaging the hot and dense fireball generated in heavy-ion collisions in the  $1A$  GeV regime, because

- produced-only particles, i.e. vanishing contributions from the initial state,
- $m_t$ -scaling, see Figure 1.4, i.e. space-momentum correlations are the smallest for the lightest particles,
- up to 20 measured pions per event in central collisions,
- the mutual strong interaction appears to be negligible [11, 12],
- the mutual Coulomb interaction is correctable [38],
- an eventual Coulomb effect from the interaction with the positively charged fireball can be taken into account by considering  $\pi^-$  and  $\pi^+$  separately,

- no jet contributions as seen at higher beam energies [39].

The measurement performed with the HADES setup at SIS18 provides a data set with excellent purity and very high statistics. This allows to perform a multi-differential HBT analysis, being sensitive within the three spatial directions and studying the dependence on the momentum of the pion pairs and on the impact parameter of the collision. Imaging the fireball as three-dimensional tilted ellipsoid allows a precise calculation of the volume of homogeneity, which has direct impact on the equation of state of hot and dense matter in an extensive description. Furthermore, the  $m_t$ -dependence of the source extension gives access to dynamical effects, like space-momentum correlations and resonance contributions. On the one hand this can be used for determining the dynamical parameters of certain models like temperatures or flow velocities [40]. On the other hand, the dependencies on  $m_t$  can be used to trace back the measured lengths of homogeneity to the geometrical size of the fireball. Studying the tilt angle and the out-of-plane eccentricities in an azimuthally sensitive analysis in dependence on transverse momentum will allow to make predictions for the temporal evolution of the collision. The results can be used for gauging existing simulation tools and help to fine-tune certain parameters of them.

It is worth emphasising that, prior the measurement presented in this thesis, only preliminary data [41] of identical-pion HBT data existed for large symmetric collision systems, like Au + Au or Pb + Pb, at beam kinetic energies of about 1A GeV. The results of this work are therefore of high interest for extending the existing excitation functions [17] of the HBT radius parameters and the connected volume of homogeneity, as well as the one of derived quantities like the freeze-out duration, eccentricities or the tilt angle relative to the beam axis. Also the question of an influence of the central Coulomb potential on the HBT results will be looked at. The system Au + Au carries a much higher Coulomb charge compared to the previously studied La + La system [22, 23]. With the much better statistics of both, negatively and positively charged pions, the Coulomb-related effects might be visible.

This thesis is structured as follows. In Chapter 2, a brief outline is presented, how the quantum-statistical effect between identical particles can be used for measuring source extensions in coordinate space. HADES, the fixed target experiment with high acceptance and excellent performance, which provided the data for this thesis, will be introduced with its components in Chapter 3. Afterwards all necessary steps for transforming the electronic signals of the sub-detectors into physical quantities will be explained. The properties of the collision like centrality, event plane and primary vertex as well as expressions for the one- and three-dimensional experimental correlation functions are obtained in Chapter 4. Combining theory and experiment in Chapter 5 the results are shown, starting with the correlation functions and continuing with the HBT radius parameters, divided into two sections,

## 1. Introduction

---

one for the azimuthally integrated and one for the azimuthally sensitive analysis. In both sections the impact of the HADES results on the excitation functions will be shown, while in the azimuthally sensitive investigation the focus is on the derived quantities like eccentricities and tilt angles. Finally in Chapter 6, the thesis ends with a summary, and an outlook will be given.

## 2 | Two-particle interferometry

### 2.1 Quantum-statistic effects

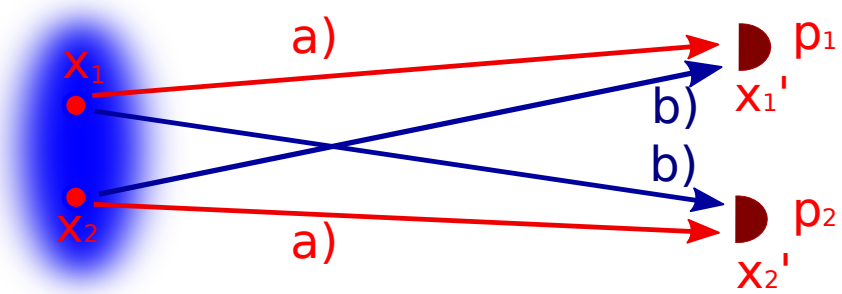


**Figure 2.1:** Illustration of measuring two identical particles emitted from locations in a source. When the particles arrive at the detectors  $x'_{1,2}$  it is not possible to decide whether they took the paths a) or the paths b), and a superposition of both possibilities must be considered.

The starting point of the description of two-particle interferometry of identical particles is quantum statistics. The elementary particles can be divided into two groups, on the one hand bosons, having a whole-number spin quantum number, and on the other hand, fermions with a half-integral spin quantum number. Following the spin-statistics theorem a bosonic two-particle state is symmetric, while a fermionic two-particle state is anti-symmetric. That means, considering the general two-particle wave function,

$$\Phi_{1,2}(x_1, x_2) = \Phi_1(x_1) \Phi_2(x_2), \quad (2.1)$$

and exchanging the particles one and two by swapping the indices 1 and 2, the sign in front of the wave function changes if fermions are described, but for bosons not. If the particles are identical it is not possible to assign the

## 2. Two-particle interferometry

---

indices to one or the other particle, but the squared wave function should not change under this exchange. Therefore one uses a linear combination of both cases for describing the two-particle state,

$$\Phi_{1,2}(x_1, x_2) = \frac{1}{\sqrt{2}}(\Phi_1(x_1)\Phi_2(x_2) + \Phi_1(x_2)\Phi_2(x_1)) \text{ for bosons,} \quad (2.2)$$

$$\Phi_{1,2}(x_1, x_2) = \frac{1}{\sqrt{2}}(\Phi_1(x_1)\Phi_2(x_2) - \Phi_1(x_2)\Phi_2(x_1)) \text{ for fermions.} \quad (2.3)$$

Equation (2.3) leads directly to the Pauli principle: two fermions can not have the same quantum mechanical state, if they conform in all their quantum numbers. If two bosons are emitted with a distance to each other of  $\Delta x = |x_1 - x_2|$  and measured at  $x'_1$  with momentum  $p_1$  and at  $x'_2$  with momentum  $p_2$ , respectively, their wave function is written according to Equation (2.2):

$$\Phi_{1,2}(x_1, x_2, x'_1, x'_2) = \frac{1}{\sqrt{2}}[e^{\frac{i}{\hbar}(x'_1 - x_1)p_1}e^{\frac{i}{\hbar}(x'_2 - x_2)p_2} + e^{\frac{i}{\hbar}(x'_1 - x_2)p_1}e^{\frac{i}{\hbar}(x'_2 - x_1)p_2}]. \quad (2.4)$$

It is worth to mention that the momentum difference  $\Delta p = |p_1 - p_2|$  and the displacement  $\Delta x$  should obey  $\Delta p \Delta x \simeq \hbar$  to keep the argument of indistinguishability (this condition is comparable with the coherence criteria of electromagnetic radiation for showing interference effects). The possible paths of the two identical bosons are depicted in Figure 2.1. Inserting  $\Delta x$  and  $\Delta p$  into Equation (2.4), the expectation value of the two-boson state  $\Phi_{1,2}$  reads

$$|\Phi_{1,2}|^2 = |\Phi_{2,1}|^2 = 1 + \cos\left(\frac{\Delta x \Delta p}{\hbar}\right). \quad (2.5)$$

For vanishing relative distance in phase space the argument of the cosine in Equation (2.5) vanishes and the expected value reaches a maximum at two. This means that the probability of measuring simultaneously two identical bosons with vanishing momentum difference from a given source is twice as large as measuring two uncorrelated particles. The maxima of the cosine term in Equation (2.5) at higher arguments are suppressed by the coherence condition  $\Delta p \Delta x \simeq \hbar$ .

The larger the source is the smaller the momentum difference has to be to measure the correlation. This implies that the measurement of relative momenta of two identical particles is equivalent to the measurement of the inverse size of the particle emitting source. For that reason, source sizes in the femtometer regime are accessible with particle interferometry by momentum differences in the order of magnitude of a few MeV/c.

## 2.2 Two-particle correlation-function

### 2.2.1 Finite source: Wigner density distributions

To construct the two-particle correlation function for heavy-ion collisions one has to know the source distribution of the emitted particles. In Equation (2.5) only certain values of  $x_{1,2}$  and  $p_{1,2}$  have been considered. The complete two-particle distribution  $P_{1,2}(p_1, p_2)$  from an extended source is obtained by summing over all possible emission places and emission probabilities,

$$P_2(p_1, p_2) = \int d^4x_1 d^4x_2 S(x_1, p_1) S(x_2, p_2) |\Phi_{1,2}|^2, \quad (2.6)$$

with the Wigner density distribution  $S(x, p)$  [42], which will be referred to as the source function. The latter one gives the emission probability of a particle dependent on its origin and its momentum. It is also used for calculating the single particle distribution  $P_1(p)$ ,

$$P_1(p) = \int d^4x S(x, p) |\Phi_i|^2, \quad (2.7)$$

since  $|\Phi_i|^2 = 1$  by convention. The two-particle distribution (2.6) contains in addition to the correlated pairs also the uncorrelated pairs. If the correlation vanishes, i.e. the term  $|\Phi_{1,2}|^2$  becomes one, the pair distribution factorises,  $P_2(p_1, p_2) = P_1(p_1) P_1(p_2)$ , and is expressed by the single particle distributions. To be sensitive to the correlations of Equation (2.6) one divides it by the product of  $P_1(p_1)$  and  $P_1(p_2)$  and defines the correlation function as

$$C(p_1, p_2) = \frac{P_2(p_1, p_2)}{P_1(p_1) P_1(p_2)}. \quad (2.8)$$

### 2.2.2 Correlation with relative coordinates

The expectation value (2.5) depends only on  $\Delta x$  and  $\Delta p$  and therefore implies the usage of pair momentum  $k = (p_1 + p_2)/2$  and relative momentum  $q = (p_1 - p_2)/2$ . The correlation function (2.8) reads then

$$C(q, k) = 1 + \frac{|\int d^4x S(x, k) e^{i2qx}|^2}{\int d^4x S(x_1, p_1) \int d^4y S(x_2, p_2)}. \quad (2.9)$$

Assuming the emission function to have a very smooth momentum dependence one can replace

$$S(x, k - q) S(y, k + q) \approx S(x, k) S(y, k). \quad (2.10)$$

This relation is called the smoothness approximation [40]. Inserting it into Equation (2.9) leads to

$$C(q, k) \approx 1 + \frac{|\int d^4x S(x, k) e^{i2qx}|^2}{|\int d^4x S(x, k)|^2}. \quad (2.11)$$

In principle, the emission function  $S(x, k)$  depends on the off-shell momentum  $k$  with  $k^0 = (E_1 + E_2)/2$ . In practise, one uses the on-shell approximation  $S(x, k^0, \vec{k}) \approx S(x, E_k, \vec{k})$ ,  $E_k = [m^2 + \vec{k}^2]^{1/2}$  with  $m$  being the particle rest mass. The corrections to this form were shown to be small [43].

The correlation function (2.11) can be reformulated with relative spatial coordinates  $X = (x_1 + x_2)$ ,  $r = (x_1 - x_2)/2$  and a normalised relative distance distribution [40],

$$d(r, k) = \int d^4X s(X/2 + r, k) s(X/2 - r, k), \quad (2.12)$$

$$s(r, k) = \frac{S(r, k)}{\int d^4r S(r, k)}, \quad (2.13)$$

with the normalised emission function  $s(r, k)$ . The relative distance function is an even function of  $r$ ,  $d(-r, k) = d(r, k)$ . Writing the mass shell constraint as  $q^0 = \vec{\beta} \cdot \vec{q}$  the correlation function can be written as:

$$\begin{aligned} C(q, \vec{k}) &= 1 + \int d^4r \cos(q \cdot r) d(r, k), \\ &= 1 + \int d^3r \cos(\vec{q} \cdot \vec{r}) \int dt d(\vec{r} + \vec{\beta}t, t, k). \end{aligned} \quad (2.14)$$

If the pair of particles is in the rest frame ( $\vec{\beta} = 0$ ), the time structure is completely integrated out,

$$C(\vec{q}, \vec{k}) = 1 + \int d^3r \cos(\vec{q} \cdot \vec{r}) S_{\vec{k}}(\vec{r}), \quad (2.15)$$

and the relative source function  $S_{\vec{k}}(\vec{r})$  is simply the integral over the time argument of  $d(r, k)$ .

### 2.2.3 Static and dynamic sources

If no collective motion is present and the momentum of the emitted particle does not depend on the emission time, the particle emitting source is called a static source, and the spatial part factorises with the momentum dependent part,

$$S(x, p) = \rho(x)g(p), \quad (2.16)$$

with the normalised spatial emission function  $\rho(x)$ . With Equation (2.7) the single particle distribution is then simply:

$$P_1(p) = g(p), \quad (2.17)$$

and the two-particle distribution becomes:

$$\begin{aligned} P_2(p_1, p_2) &= g(p_1)g(p_2) \int d^4x_1 d^4x_2 \rho(x_1)\rho(x_2) |\Phi_{1,2}|^2, \\ &= g(p_1)g(p_2)(1 + |\tilde{\rho}(q)|^2). \end{aligned} \quad (2.18)$$

Inserting the one- and two-particle distributions into Equation (2.8), one gets

$$C(q) = 1 + |\tilde{\rho}(q)|^2, \quad (2.19)$$

where  $|\tilde{\rho}(q)|^2$  can be identified with the Fourier transform of  $\rho(x)$ . Since in general the inversion of a Fourier transform is not unambiguous, the source function can not be read off directly from  $|\tilde{\rho}(q)|^2$ . Not least this follows from the mass-shell constraint,

$$k \cdot q = p_1^2 - p_2^2 = m_1^2 - m_2^2 = 0, \quad (2.20)$$

which means that only three of the four relative momentum components are kinematically independent [40]. This introduces an inevitable model dependence not resolvable with the information from identical two-particle interferometry. In practise a realistic assumption is made for the source function  $S(x, p)$ , which can then be compared to experimental data for proving it.

A more realistic expanding source model for relativistic heavy-ion collisions does not simply factorise into a spatial part and a momentum dependent part. The correlation between space and momentum can lead to much higher relative momenta and obviously smaller source sizes. The overall coherence condition  $\Delta x \Delta p \simeq \hbar$  is not fulfilled for all particle pairs and only in small regions, where the gradients of emission velocities are not too large, interference can be observed. The investigation of the correlation function has therefore to be done differentially in the pair particle momenta, and the obtained source sizes are called lengths of homogeneity. The emission velocity gradients depend for example on the collective velocity gradients, the temperature gradients and the transverse mass, which are included in the explicit model expressions of  $S(x, p)$ . A few examples will be introduced in Section 2.5.

#### 2.2.4 Partial coherence: the $\lambda$ parameter

From quantum optics it is known that the HBT effect according to Bose-Einstein statistics does not appear for pairs of particles emitted with phase

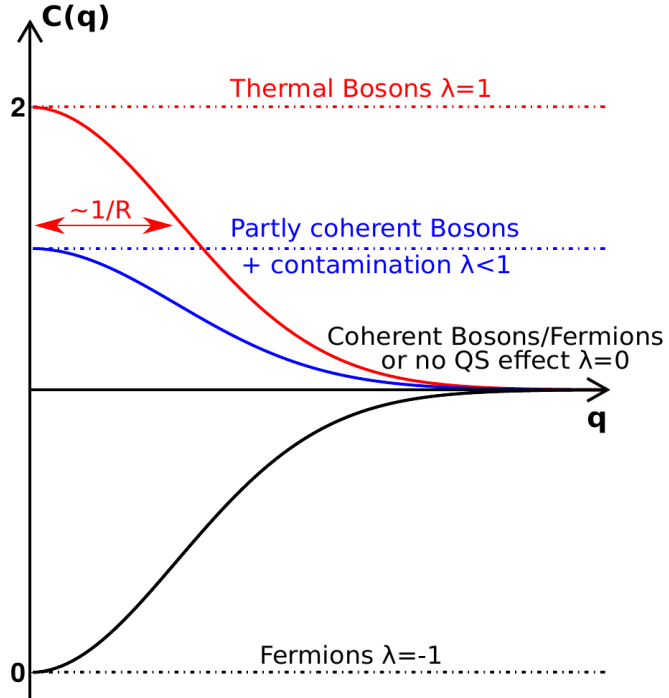


**Figure 2.2:** Illustration of the correlation signal at small relative momenta  $q$ . For an ideal chaotic bosonic source (red), the probability of registering the pair increases up to two at vanishing  $q$ . For a partially coherent source (blue), the correlation signal is reduced. For an ideal coherent source the correlations signal vanishes just as for distinguishable particles. An ideal fermionic source (lower black curve) can be described with coherence parameter  $\lambda = -1$  and vanishing probability at  $q = 0$ .

coherence [44]. Instead a chaotic source is required. A possible partial phase coherence would weaken the measured correlation signals. To illustrate this consequence one could split the source function into a coherent and a chaotic part,

$$S(\vec{q}, \vec{k}) = S_{\text{coh}}(\vec{q}, \vec{k}) + S_{\text{cha}}(\vec{q}, \vec{k}). \quad (2.21)$$

Inserting Equation (2.21) into Equation (2.11) and assuming only  $S_{\text{cha}}(\vec{q}, \vec{k})$  to contain the HBT effect introduces a weighting  $\lambda(\vec{k})$  for the correlated term [45],

$$\begin{aligned} \lambda(\vec{k}) &= 1 - D^2(\vec{k}), \\ D(\vec{k}) &= \frac{n_{\text{coh}}(\vec{k})}{n_{\text{coh}}(\vec{k}) + n_{\text{cha}}(\vec{k})}, \end{aligned} \quad (2.22)$$

where  $n_{\text{coh}(\text{cha})}$  denotes the number of coherently (chaotically) emitted particles. Equation (2.22) enters in Equation (2.19) in the form

$$C(q) = 1 + \lambda |\tilde{\rho}(q)|^2. \quad (2.23)$$

The experimentally determinable intercept parameter  $\lambda(\vec{k})$  is therefore often referred to as the incoherence parameter. It is always found to be between zero and unity. However, in practise other effects like misidentified particles, resonance decays or final state interactions contribute to the deviation of  $\lambda(\vec{k})$  from unity. In Figure 2.2 the impact of the incoherence parameter on the correlation function is shown. In the ideal case  $\lambda(\vec{k}) = 1$ , the correlation function depicted by the red curve reaches at  $q = 0$  twice the value of uncorrelated pairs; for  $\lambda(\vec{k}) < 1$  this value is reduced.

## 2.3 Final state interactions

Besides the quantum statistical effects, correlations between multiple particles can origin from the fundamental forces and conservation laws. The latter ones become less important the higher the multiplicities of produced particles are and the more degrees of freedom are involved in the considered process. Therefore, for high-multiplicity heavy-ion collisions the constraints by energy-momentum conservation or isospin and charge conservation are often supposed to be negligibly small concerning particle pairs. At least particles from resonance decays are strongly correlated, but they only rarely produce two identical charged particles at the same time. Therefore, this effect does not matter in practical investigations. Hence the final state interactions (FSI) caused by the strong force and the Coulomb force are left over. While the strong interaction dominates the region of small relative momenta for pairs of heavier particles (like protons), it is negligible in the consideration of like-sign pions [12]. <sup>1</sup> In contrast, the long-range Coulomb interaction significantly enters the two-pion correlation function and mixes with the quantum statistical effect at low relative momenta.

---

<sup>1</sup>In that reference a scattering length of 0.2 fm is predicted, where around 1% of the source is affected. Note that on a more precise level the effect of the strong FSI can change the correlation function, as shown in [46].

### 2.3.1 Two-particle Coulomb interaction for extended sources

For taking into account the Coulomb force between two emitted particles, a relative Coulomb wave function part modifies the wave functions  $\Phi_{1,2}$  in Equations (2.6) and (2.18):

$$\Phi^{\text{coul}}(\vec{r}) = \Gamma(1 + i\eta)e^{-\frac{1}{2}\pi\eta}e^{\frac{i}{2}\vec{q}\vec{r}}F(-i\eta; 1; z_-), \quad (2.24)$$

$$z_{\pm} = \frac{1}{2}(qr \pm \vec{q}\vec{r}) = \frac{1}{2}qr(1 \pm \cos\theta), \quad (2.25)$$

with  $r = |\vec{r}|$ ,  $q = |\vec{q}|$ , and  $\theta$  denotes the opening angle between the vectors  $\vec{r}$  and  $\vec{q}$ . The analytical expression (cf. [38] for the rationale) uses the confluent hyper-geometrical function  $F$  and the Gamma function  $\Gamma$ . The Sommerfeld parameter  $\eta$  is given by

$$\eta_{\pm} = \pm \frac{me^2}{8\pi q}, \quad (2.26)$$

containing the dependence on the particle mass  $m$  and the electromagnetic coupling strength  $e$ . The plus signs are for pairs with unlike-sign particles and the minus signs apply for like-sign pairs. For particle emission from a point-like source, the correlator simplifies to

$$|\Phi^{\text{coul}}(0)|^2 = |\Gamma(1 + i\eta)e^{-\frac{1}{2}\pi\eta}|^2 = \frac{2\pi\eta}{e^{2\pi\eta} - 1} =: G(\eta), \quad (2.27)$$

with  $G(\eta)$  being known as the Gamow factor. For an extended source, the Coulomb interaction will always be weaker, and the Gamow factor (2.27) can be considered as upper limit.

### 2.3.2 $N$ -particle Coulomb interaction

Besides the Coulomb interaction within the pair of charged particles the Coulomb interaction with the remaining cloud of charged particles is of interest. The Coulomb charge carried by the participating protons of a heavy-ion collision leads to an effective potential of the fireball, which pushes positively charged particles away in radial direction and pulls back negatively charged particles. The net effect will be therefore referred to as the central Coulomb potential. The effect scales with the total charge inside the interaction region of the colliding nuclei and with the spatio-temporal extension of the charge distribution. Therefore it becomes important for heavy-ion collisions of large systems, like Au+Au at lower beam energies producing fireballs with high baryonic density. In [47, 48], the effect was quantified by an effective potential  $V_{\text{eff}}$ , which changes the “initial energy”  $e_i(p_i)$  of a single particle by

$$e_f(p_f) = e_i(p_i) \pm V_{\text{eff}}, \quad (2.28)$$

where  $e_f$  is the “final energy” of the measured particle with momentum  $p_f$ , and the plus (minus) sign belongs to positively (negatively) charged particles. This leads to a distortion of the relative momentum spectra and hence to a change of the width of the correlation signal. Especially for relative momenta pointing perpendicular to the emission direction one finds

$$\frac{q_i}{q_f} = \frac{|\vec{p}_i|}{|\vec{p}_f|} = \sqrt{1 \mp 2 \frac{V_{\text{eff}}}{|\vec{p}_f|} \sqrt{1 + \frac{m_\pi^2}{|\vec{p}_f|^2} + \frac{V_{\text{eff}}^2}{|\vec{p}_f|^2}}}, \quad (2.29)$$

with  $q_i$  ( $q_f$ ) being the initial (final) relative momentum of the pair. A different ansatz is made in [49, 50], where the effective Coulomb potential is already included in the pion wave-function and propagated through the calculations ending up in significant changes of extracted source sizes. The evaluation of the central Coulomb potential in [49, 50] goes more in detail and seems more accurate, but does not deliver a simple expression for correcting the correlation signal. For non-central collisions, the problem becomes even more complicated, since next to the effective potential in the collision center the contributions of the spectators have to be included. Especially for small freeze-out times, when the spectators are still close to the participants, their impact can not be neglected. Reference [24] made an assumption including three charged fragments of the collision nuclei (one participant zone and two spectator areas) and to correct accordingly the final momenta  $\vec{p}$  of the charged pions.

Nevertheless, the treatment of the central Coulomb potential in two-particle correlation functions still is an important open question, which becomes relevant if new experimental data with well-distinguished  $\pi^+\pi^+$  and  $\pi^-\pi^-$  correlation data appears.

## 2.4 Gaussian approximation

As mentioned above in Section 2.2.3, the complete source function  $S(x, k)$  can not be reconstructed from the correlation signal without further constraints. Therefore, the assumption of a Gaussian distribution around the point of maximum emission probability  $\bar{x}^\mu(k)$  is made [51]:

$$S(x, k) = N(k) S(\bar{x}(k), k) \exp \left[ -\frac{1}{2} \tilde{x}^\mu(k) B_{\mu\nu}(\vec{k}) \tilde{x}^\nu(k) \right], \quad (2.30)$$

where  $N(k)$  is a normalisation constant and  $B_{\mu\nu}(k)$  is the symmetric curvature tensor

$$B_{\mu\nu}(\vec{k}) = -\partial_\mu \partial_\nu \ln S(x, k). \quad (2.31)$$

The relative coordinates  $\tilde{x}^\mu(k)$  are given by

$$\tilde{x}^\mu(k) = x^\mu - \bar{x}^\mu(k), \quad \bar{x}^\mu(k) = \langle x^\mu \rangle(k), \quad (2.32)$$

where the brackets  $\langle \cdots \rangle$  stand for the spatial average over the emission function  $S(x, k)$ ,

$$\langle g \rangle(k) = \frac{\int d^4x g(x) S(x, k)}{\int d^4x S(x, k)}. \quad (2.33)$$

The point of maximum emission  $\bar{x}^\mu(k)$  is a space-time saddle point and can be formally defined as

$$\frac{\partial}{\partial x_\mu} \ln S(x, k)|_{\bar{x}} = 0. \quad (2.34)$$

The introduced formalism is referred to as the *quadratic saddle-point approximation*, where  $B_{\mu\nu}(k)$  is defined via

$$(B^{-1})_{\mu\nu}(k) = \langle \tilde{x}^\mu \tilde{x}^\nu \rangle(k). \quad (2.35)$$

The choice of a Gaussian form of the source function is on the one hand reliable, since it describes the data quite good and conforms with a particle emitting thermal source. On the other hand, the Fourier transform of a Gaussian function has also a Gaussian shape, which makes the translation of the correlation signal into a source width quite easy, cp. Equation (2.19). Furthermore, the Gaussian widths in both, the source function and the correlation function, are convenient for a comparison with results delivered by other theoretical and experimental studies. Inserting Equation (2.30) into the relation (2.11) one obtains for the correlation function the expression

$$C(\vec{q}, \vec{k}) = 1 + \exp[-4q_\mu q_\nu \langle \tilde{x}^\mu \tilde{x}^\nu \rangle(\vec{k})]. \quad (2.36)$$

Since the smoothness and the on-shell approximations are already included here, the space-time variances  $\langle \tilde{x}^\mu \tilde{x}^\nu \rangle$  can be written as a function of  $\vec{k}$  only.

#### 2.4.1 Bertsch-Pratt parametrisation

To find a relation between Equation (2.36) and the experimental data, one of the four relative momentum components has to be eliminated via the mass-shell constraint (2.20). Then one has to choose a parametrisation for the other three components. A common choice is the *out-side-longitudinal* (osl) coordinate system, where the temporal component is eliminated by using

$$\begin{aligned} q^0 &= \vec{\beta} \cdot \vec{q}, & \vec{\beta} &= \vec{k}/k^0, \\ \vec{\beta} &= (\beta_t, 0, \beta_l), & \vec{q} &= (q_{\text{out}}, q_{\text{side}}, q_{\text{long}}). \end{aligned} \quad (2.37)$$

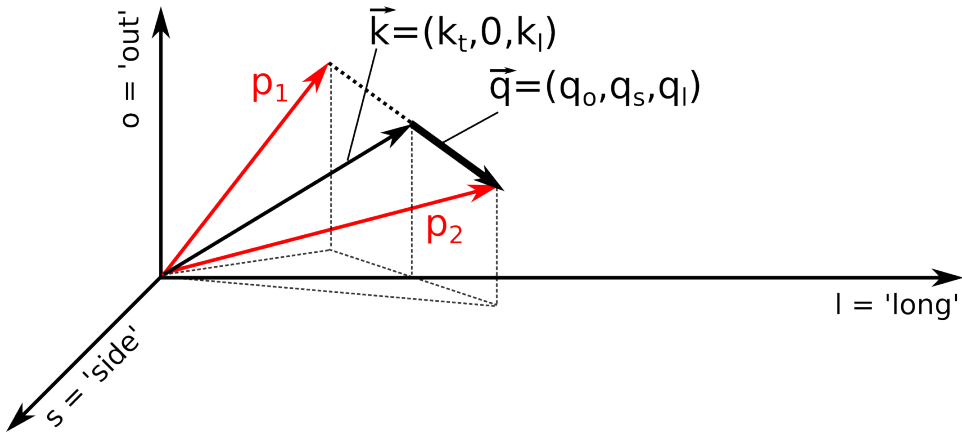


**Figure 2.3:** Illustration of the osl coordinate system: 'long' points along the beam axis, 'out' is parallel to the transverse pair momentum  $k_t$  of the two particles with momentum  $p_1$  and  $p_2$ , and 'side' points perpendicularly to the other two components, completing a right-handed orthonormal coordinate system.

The relative momentum component  $q_{\text{long}}$  points along the beam direction,  $q_{\text{out}}$  points into the same direction as the pair transverse momentum  $k_t$  and  $q_{\text{side}}$  is perpendicular to the other two components as illustrated in Figure 2.3. This choice is known as the Bertsch-Pratt parametrisation [52–54], sometimes it is also called the Cartesian parametrisation [40]. Inserting this parametrisation into Equation (2.36) delivers the relation

$$C(\vec{q}, \vec{k}) = 1 + \exp \left[ - \sum_{i,j} 4q_i q_j R_{ij}^2 \right], \quad (2.38)$$

where the sum runs over 'out', 'side' and 'long' and the quantities  $R_{ij}^2$  are the six HBT radius parameters. They can be seen as a symmetric  $3 \times 3$  matrix with six independent entries. With Equation (2.38) the correlation function has now a form, which can be compared to experimental data. In the following sections, the relation between the HBT radius parameters and the space-time extension of the source will be discussed.

For completeness it should be mentioned that, apart from the introduced Bertsch-Pratt parametrisation, other coordinate systems and restrictions made with the mass-shell constraint are possible. The most prominent is the Yano-Koonin-Podgoretsky parametrisation [55, 56], which includes directly the temporal component  $q^0$ . Details can be found in [40]. Within the analysis of this thesis, the Yano-Koonin-Podgoretsky parametrisation has not been used.

### 2.4.2 Azimuthally symmetric collisions

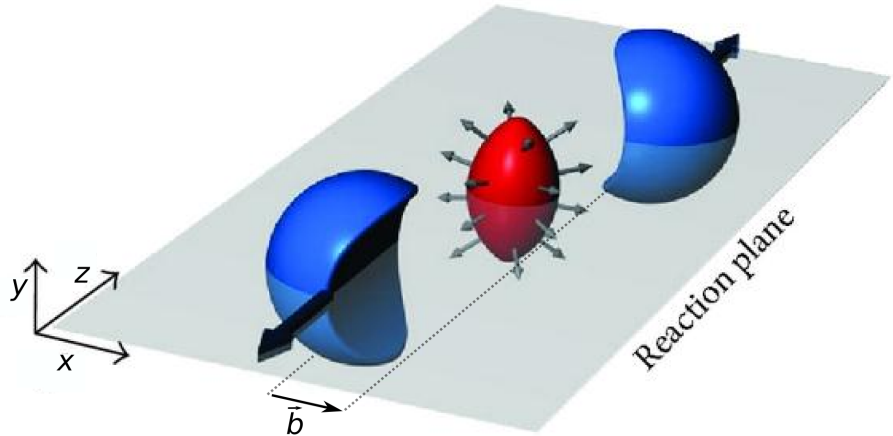


**Figure 2.4:** Illustration of a relativistic heavy-ion collision creating a particle emitting source (red, in the centre). The impact parameter  $b$  points perpendicular to the beam direction  $z$ . Both directions span the reaction plane of the collision. A finite value of  $b$  causes the source to be more extended in  $y$  than in  $x$  direction. Figure taken from [57].

The formal introduction of the osl system (2.37) includes explicit  $k_t$  and  $k_l$  dependences. However, in addition a dependence on the azimuthal orientation  $\phi_{12}$  of the pair momentum can appear, if azimuthal symmetry of the particle emitting source is not explicitly required. In the context of heavy-ion collisions, an asymmetry is caused by the finite impact parameter  $b$ , illustrated in Figure 2.4. With the assumption of spherically distributed nucleons in the colliding nuclei moving on parallel trajectories against each other one can at least require the source to be symmetric relative to the orientation  $\phi_{\vec{b}}$  of the impact parameter  $b$  in azimuthal direction:

$$S(x, k_t, (\phi_{\vec{b}} + \phi_{12}), k_l) = S(x, k_t, (\phi_{\vec{b}} - \phi_{12}), k_l). \quad (2.39)$$

Since in experiments the impact parameter  $b$  is randomly distributed in the laboratory system, one integrates over all azimuthal configurations when not considering  $\phi_{12} - \phi_{\vec{b}}$  explicitly. In this case, the  $\phi_{12}$  dependence vanishes automatically and an obvious cylindrical symmetric source remains. This consideration would be exact for  $|\vec{b}| = 0$  and is still reasonable for very

central collisions with small impact parameters. One obtains a reflection symmetry in 'side' direction,

$$\begin{aligned} S_{\text{lab}}(x, k_t, \phi_{12}, k_l) &= S_{\text{lab}}(x, k_t, \phi_{12} + \delta\phi_{12}, k_l), \\ \Leftrightarrow S_{\text{osl}}(x, y, z, t, k_t, k_l) &= S_{\text{osl}}(x, -y, z, t, k_t, k_l), \end{aligned} \quad (2.40)$$

and due to this the following relations for the HBT radius parameters from Equation (2.38) arise [58]:

$$\begin{aligned} R_{\text{out}}^2(\vec{k}) &= \langle (\tilde{x} - \beta_t \tilde{t})^2 \rangle(\vec{k}), \\ R_{\text{side}}^2(\vec{k}) &= \langle \tilde{y}^2 \rangle(\vec{k}), \\ R_{\text{long}}^2(\vec{k}) &= \langle (\tilde{z} - \beta_l \tilde{t})^2 \rangle(\vec{k}), \\ R_{\text{out long}}^2(\vec{k}) &= \langle (\tilde{z} - \beta_l \tilde{t})(\tilde{x} - \beta_t \tilde{t}) \rangle(\vec{k}), \\ R_{\text{out side}}^2(\vec{k}) &= 0, \\ R_{\text{side long}}^2(\vec{k}) &= 0. \end{aligned} \quad (2.41)$$

The two non-diagonal parameters  $R_{\text{out side}}^2$  and  $R_{\text{side long}}^2$  vanish for azimuthally symmetric collisions. The more symmetries are applied to the source function the simpler are the expressions for the HBT parameters. Assuming at mid-rapidity the reflection symmetry in longitudinal direction  $\tilde{z} \rightarrow -\tilde{z}$  in the longitudinally co-moving system (LCMS) another simplifications can be made:

$$\begin{aligned} R_{\text{long}}^2 &= \langle \tilde{z}^2 \rangle(\vec{k}), \\ R_{\text{out long}}^2 &= 0. \end{aligned} \quad (2.42)$$

The LCMS is defined as the system of the pair, where its longitudinal velocity vanishes,  $\beta_l = 0$ . If momentum-space correlations, mentioned in Section 2.2.3, are sufficiently weak and the emission duration is sufficiently large, i.e. the explicit  $\vec{k}$ -dependence dominates [40], then the following relation between the 'out' and the 'side' direction holds:

$$R_{\text{out}}^2(\vec{k}) - R_{\text{side}}^2(\vec{k}) \approx \beta_t^2 \langle \tilde{t} \rangle. \quad (2.43)$$

With Equations (2.41) and (2.42) a simple interpretation of the HBT parameters appears:  $R_{\text{side}}$  measures the width of the source in direction of 'side',  $R_{\text{out}}$  is a measure of the width in 'out' direction plus an additional contribution from the emission duration, and  $R_{\text{long}}$  is the width in longitudinal direction. Since for an azimuthally symmetric source the widths in 'side' and 'out' directions should be equal, the emission duration can be directly extracted with Equation (2.43).

The interpretation of a finite value  $R_{\text{out long}}^2$  is not that trivial and of kinematically nature [59]. One can introduce the linear correlation coefficient

$$\rho_{\text{ol}} = -\frac{R_{\text{out long}}^2(\vec{k})}{R_{\text{out}}(\vec{k})R_{\text{long}}(\vec{k})}, \quad (2.44)$$

which is a normalised quantity bound to  $|\rho_{\text{ol}}| \leq 1$  and relates  $R_{\text{out long}}^2$  to the diagonal HBT radius parameters  $R_{\text{out}}$  and  $R_{\text{long}}$ .

### 2.4.3 Finite impact parameter

If the azimuthal symmetry is explicitly broken, the HBT radius parameters have to be considered in dependence on the direction of the emitted pairs. The coordinates  $x, y, z$  are now aligned with the impact parameter-fixed system, where  $x$  points into the direction of  $b$ , and  $\mathcal{D}_\Phi$  describes the rotation into the osl coordinate system [60],

$$\begin{aligned} R_{ij}^2(\vec{k}) &= \langle [(\mathcal{D}_\Phi \tilde{x})_i - (\mathcal{D}_\Phi \vec{\beta})_i \tilde{t}] [(\mathcal{D}_\Phi \tilde{x})_j - (\mathcal{D}_\Phi \vec{\beta})_j \tilde{t}] \rangle, \\ (\mathcal{D}_\Phi \vec{\beta}) &= (\beta_t, 0, \beta_l). \end{aligned} \quad (2.45)$$

The pair azimuthal angle  $\Phi$  is defined relative to the impact parameter,  $\Phi = \phi_{12} - \phi_b$ . Hence, the expressions for the HBT parameters follow:

$$\begin{aligned} R_{\text{side}}^2(\vec{k}) &= \langle \tilde{x}^2 \rangle \sin^2 \Phi + \langle \tilde{y}^2 \rangle \cos^2 \Phi - \langle \tilde{x} \tilde{y} \rangle \sin 2\Phi, \\ R_{\text{out}}^2(\vec{k}) &= \langle \tilde{x}^2 \rangle \cos^2 \Phi + \langle \tilde{y}^2 \rangle \sin^2 \Phi + \langle \tilde{x} \tilde{y} \rangle \sin 2\Phi \\ &\quad - 2\beta_t \langle \tilde{t} \tilde{x} \rangle \cos \Phi - 2\beta_t \langle \tilde{t} \tilde{y} \rangle \sin \Phi + \beta_t^2 \langle \tilde{t}^2 \rangle, \\ R_{\text{out side}}^2(\vec{k}) &= \langle \tilde{x} \tilde{y} \rangle \cos 2\phi + \frac{1}{2} (\langle \tilde{y}^2 \rangle - \langle \tilde{x}^2 \rangle) \sin 2\Phi \\ &\quad + \beta_t \langle \tilde{t} \tilde{x} \rangle \sin \Phi - \beta_t \langle \tilde{t} \tilde{y} \rangle \cos \Phi, \\ R_{\text{long}}^2(\vec{k}) &= \langle (\tilde{z} - \beta_l \tilde{t})^2 \rangle, \\ R_{\text{out long}}^2(\vec{k}) &= \langle (\tilde{z} - \beta_l \tilde{t}) (\tilde{x} \cos \Phi + \tilde{y} \sin \Phi - \beta_t \tilde{t}) \rangle, \\ R_{\text{side long}}^2(\vec{k}) &= \langle (\tilde{z} - \beta_l \tilde{t}) (\tilde{y} \cos \Phi - \tilde{x} \sin \Phi) \rangle. \end{aligned} \quad (2.46)$$

The explicit  $\Phi$  dependence is a purely geometrical consequence arising from the rotation of the reaction plane-fixed  $xyz$  system to the osl system via  $\mathcal{D}_\Phi$ , i.e. the rotation of the  $x$  axis from the direction of  $\vec{b}$  to the direction of  $\vec{k}_t$ , respectively. In addition, an implicit  $\Phi$  dependence exists, which describes the dynamical correlations (higher order flow) between the direction of emitted particles and the size of the region of homogeneity from where they originate.

## 2.5 Models for the source distribution

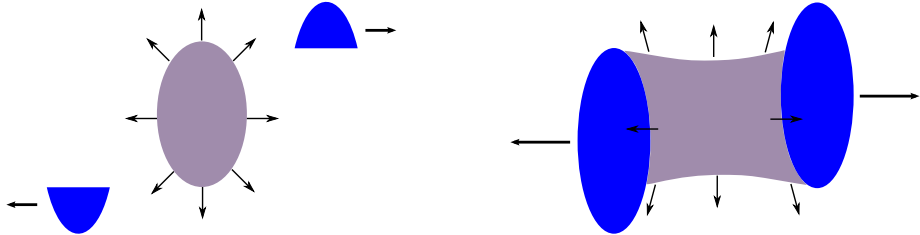


**Figure 2.5:** Scheme of two collision settings: Landau scenario (left) with total stopping of the participants and expanding fireball and Bjorken scenario (right) with partly transparent nuclei and longitudinally extended fireball region.

The choice of the explicit form of the source function  $S(x, k)$  depends on the assumptions one makes for the collision dynamics and is governed by the geometry, the beam energy, system size and others. A basic differentiation between two types of collision scenarios in relativistic heavy-ion collisions as a function of beam energy is customary. At high energies, e.g. larger than about 10-20 GeV in kinetic energy per nucleon, the nuclei are deformed in beam direction to oblate ellipsoids with decreased nucleonic cross section. When passing each other the nuclei are partly transparent, moving through each other and span a “firetube” region of high energy density in-between them with relatively large longitudinal expansion as compared to the transverse extension. This situation is referred to as the Bjorken scenario [61], illustrated at the right hand side of Figure 2.5. For lower energies the participating nucleons stop almost completely at mid-rapidity, which is also known as baryon stopping, and form an expanding fireball. The spectators continue their motion and leave a baryon-dense particle-emitting source behind. This picture is called the Landau scenario, depicted on the left side of Figure 2.5. Both scenarios are extreme cases, assuming a fast transition to thermal equilibrium and following (isotropic) expansion. However, they predict basic constraints for the modelling of  $S(x, k)$ . In the Bjorken scenario, one can assume a much faster expansion in longitudinal direction with relativistic longitudinal flow. In the Landau scenario, the expansion in longitudinal and transverse direction can be treated similarly due to the stopping, but still differentially according to different pressure gradients into the different directions.

For the  $m_t$ -scaling of the three HBT radius parameters  $R_{\text{out}}$ ,  $R_{\text{side}}$  and  $R_{\text{long}}$ , the following common dependencies are used [62]:

$$R_{\text{side}}^2 = \frac{R_G^2}{1 + v_t^2 m_t / T}, \quad (2.47)$$

$$R_{\text{out}}^2 = R_{\text{side}}^2 + \beta_t^2 (\Delta\tau)^2, \quad (2.48)$$

$$R_{\text{long}}^2 = \begin{cases} \tau_0^2 \frac{T}{m_t} & \text{w/o transverse flow, LO, } m_t \gg T, \\ \tau_0^2 \frac{T}{m_t} \frac{K_2(m_t/T)}{K_1(m_t/T)} & \text{w/o transverse flow, NLO,} \\ \tau_0^2 \frac{T}{m_t} \frac{1}{1 + \frac{T}{m_t} \left( \frac{1}{\Delta\eta^2} - 1 \right)} & \text{with transverse flow, LO,} \end{cases} \quad (2.49)$$

$$= \frac{L_G^2}{1 + v_t^2 m_t / T} + \beta_l^2 (\Delta\tau)^2 \quad \text{stopping szenario,} \quad (2.50)$$

where  $R_G$  is the Gaussian radius of the fireball in transverse direction, and  $L_G$  the Gaussian radius in longitudinal direction. The lifetime of the fireball is given by  $\tau_0$ , which can be transferred into the longitudinal extension by multiplying with the squared width  $\Delta\eta^2$  of the longitudinal rapidity distribution.  $v_{t(l)}$  stands for the transverse (longitudinal) flow velocity, which needs to be non-relativistic,  $v \ll c$ .  $T$  is the temperature at freeze-out and  $K_{1,2}$  are the modified Bessel functions of second kind. A 'leading order' expression is denoted by LO and a 'next-to leading order' expression by NLO. As discussed above, the longitudinal expansion depends highly on the underlying model and therefore a couple of fit functions arises. For the transverse directions very elementary expressions are obtained. In Appendix C the commonly used basic Gaussian assumptions for  $S(x, k)$  are further specified.

### 3 | The HADES experiment

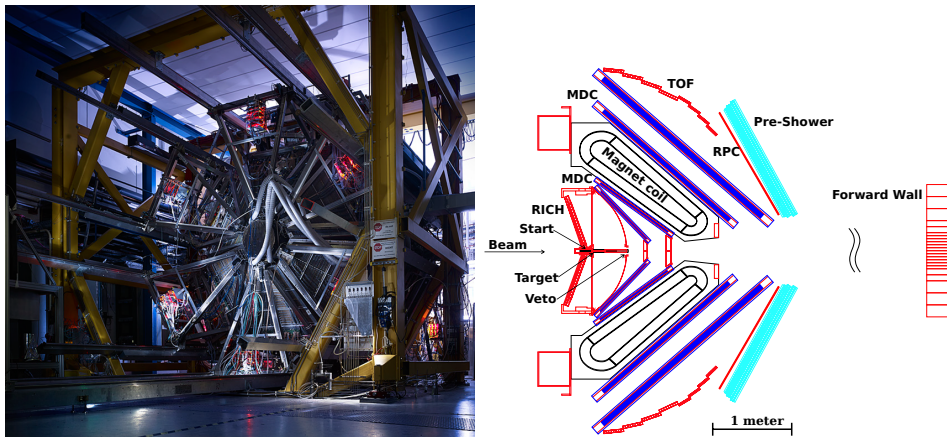


**Figure 3.1:** Left: Photograph of the HADES setup in operation mode from downstream (*Jan Michael Hosan/HA Hessen Agentur GmbH*). Right: Transverse cross section of the spectrometer with all sub-detectors. Following the beam the components are (i) the target surrounded by the Start and Veto detector, (ii) the Ring Imaging Cherenkov (RICH) detector, (iii) the Mini Drift Chambers (MDC) with the super-conducting magnet in between, (iv) the Time-Of-Flight (TOF) wall, RPC and Pre-shower detectors, combined in the Multiplicity Electron Triggering Area (META), and (v) the forward wall.

The **High Acceptance Di-Electron Spectrometer** (HADES) is a fixed target experiment located at the heavy-ion synchrotron SIS18 at the GSI Helmholtzzentrum für Schwerionenforschung in Darmstadt, Germany. Since starting of operation in 2002 HADES was used for investigating elementary, elementary + nucleus, nucleus + nucleus, and pion + nucleus collisions. The Au+Au experiment took place in April 2012 with a beam kinetic energy of  $1.23A$  GeV. One of the main purposes was to measure the in-medium modifications of the light vector mesons  $\omega, \rho, \phi$  with  $e^+e^-$  pairs. The HADES setup was designed and optimised for detecting pairs of the lightest leptons. Compared to other test particles the information carried by the leptons is not affected

### 3. The HADES experiment

---

by the strong interaction. Unfortunately, the leptonic decay channels of the vector mesons are strongly suppressed w.r.t. hadronic decays by typical factors of  $10^{-4} - 10^{-5}$ . Therefore, a lot of statistics is required, realised by fast sub-detectors for high event rates and high angular acceptance. Furthermore, a low material budget is essential to reduce background electrons, e.g. from conversion electrons, as much as possible. An important issue is also the discrimination of the electrons and positrons against the lightest hadrons, since their distributions are close to each other in most common particle identification processes. Under these boundary conditions a setup has been build up using the following sub-detectors (in beam direction):

- Target + START/VETO-detector,
- **R**ing **I**maging **C**Herenkov detector (RICH), the central element of HADES for discriminating lightest leptons against hadrons,
- Magnetic spectrometer,
- Multiplicity **E**lectron **T**rigger **A**rray (META) detectors, forming together with the START detector the time-of-flight system of the spectrometer,
- Forward-wall measuring the projectile spectators.

A photograph of the spectrometer in compact form without the forward wall is shown on the left side of Figure 3.1; on the right side, a transverse profile view is drawn. An unique characteristics of HADES compared to other high energy experiments is its hexagonal symmetry around the beam direction. Most of the above mentioned components are arranged in six identical sectors, symmetric around the beam axis. With its high momentum resolution and large geometrical acceptance HADES provides also an excellent tool for identifying hadrons, as used for the investigations in this thesis. A detailed description of the experimental setup can be found in [63]; other very illustrative descriptions of the Au+Au experiment are given by [64, 65].

#### 3.1 Target

For the experiment related to the investigated data a segmented Au-target [66] has been used, see Figure 3.2. It contains 15 gold foils with a diameter of 3 mm and a thickness of  $25 \mu\text{m}$  glued on  $7 \mu\text{m}$  thick Kapton foils with a distance of 4 mm to the next one. The holder is made of carbon. The segmentation is needed for reducing small-angle scattering and keeping simultaneously the total interaction probability at an optimum value of 2.0 %.

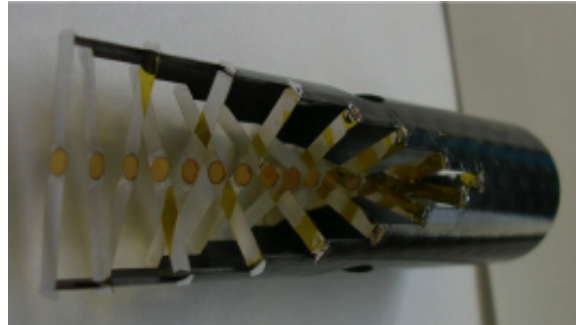


**Figure 3.2:** Photograph of the segmented Au-target. It consists of 15 gold foils glued on Kapton bands for reducing the effect of small-angle scattering.

## 3.2 RICH

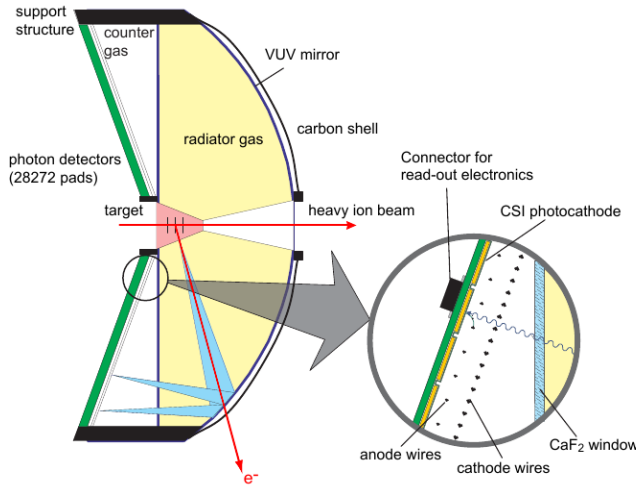


**Figure 3.3:** Scheme of the RICH detector. The passing electron (red down-pointing arrow) generates a light cone (blue) inside the radiator gas, which is mirrored onto a panel of photon detectors and appears as a ring. Figure taken from [67].

The RICH detector is a gas detector for identifying electrons and positrons. The passing leptons emit a cone of photons if their velocity  $v$  is faster than the speed of light  $c' = c/n$  inside the gaseous medium with the refractivity  $n$ , which is known as the Cherenkov effect. The emission angle of the cone is given by

$$\theta = \arccos \left( \frac{c}{v n} \right). \quad (3.1)$$

### 3. The HADES experiment

The radiator gas  $C_4F_{10}$  with  $n = 1.00151$  is optimized for leptons in the momentum range of 0.1 to 1.5 MeV, where only electrons and positrons exceed the threshold velocity to generate Cherenkov light. The light cones are mirrored backwards onto a panel of photon detectors with 28272 pads in total, see Figure 3.3. The registered ring-shaped signals are finally used for discriminating the lightest leptons from other particles.

### 3.3 Magnetic spectrometer

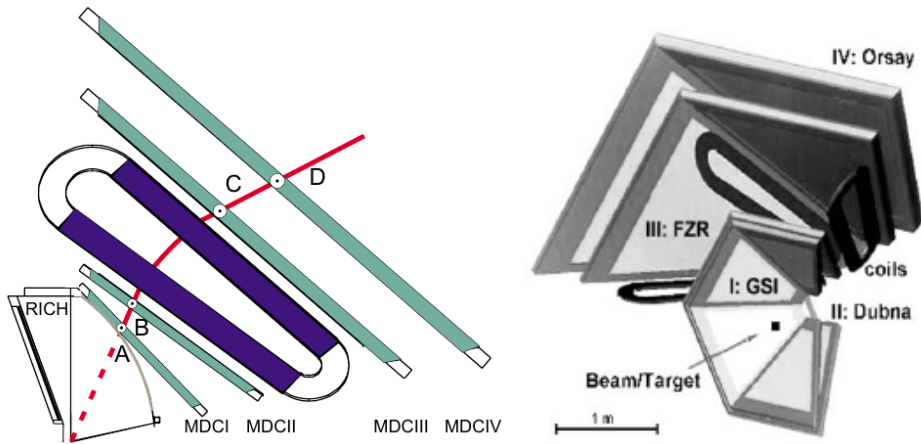


**Figure 3.4:** Left: Layout of the magnet spectrometer part of HADES consisting of a superconducting magnet with six coils generating a toroidal magnetic field, two mini drift chambers before (MDC I, MDC II) and two behind (MDC III, MDC IV) the magnet. Right: Section of the hexagonal arrangement of the magnetic coils and the mini drift chambers, including the origin where they were produced. The MDC I chambers were first build at GSI, but later exchanged by chambers built at Forschungszentrum Rossendorf (FZR) due to their high radiation exposure. MDC III chambers, also built in FZR, are in operation from the very beginning. Figures taken from [63, 67].

The magnetic spectrometer consists of 24 Mini Drift Chambers arranged symmetrically in two planes before and two behind a superconducting magnet, see Figure 3.4. Its main purpose is the determination of the momentum vector of the passing particles before the field by using the bending direction and the curvature of the tracks in the toroidal magnetic field.

#### 3.3.1 Magnet

The superconducting magnet ILSE (Iron Less Superconducting Electromagnet), which is exhibited in Figure 3.5, consists of six NbTi-coils arranged

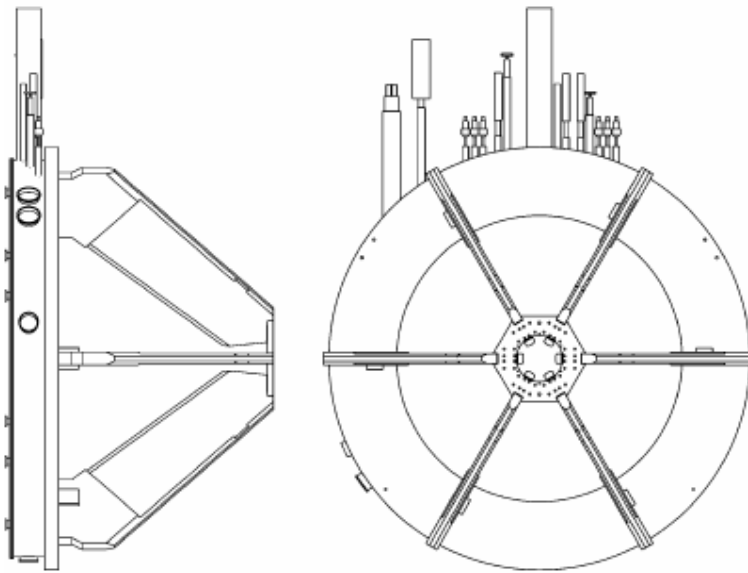


**Figure 3.5:** Technical illustration of the magnet ILSE (iron less superconducting electromagnet) in direction of the beam (right) and perpendicular from the side (left). Visible are the six coils and on top the supply slots for power supply and liquid helium cooling. Figure taken from [63].

symmetrically at the edges of the sectors between the inner and the outer MDC planes, see right panel of Figure 3.4. It generates a toroidal magnetic field, which deflects charged particles mainly in polar direction. This leads to a curvature of the particle track, from which the momentum can be determined. The geometry of the coils and the maximum current up to 3464 A was chosen such that the impact on the electronic components of the sub-detectors is as small as possible. The field strength of the magnetic field covers the range from 3.7 T at the surface of the coils down to 0.8 T in the center of the MDC sectors. To reach superconductivity the coils are cooled with liquid helium down to 4.6 K.

### 3.3.2 Mini Drift Chambers

The 24 trapezoidally shaped mini drift chambers are arranged downstream in four planes and azimuthally oriented in six sectors. Each sector covers an azimuthal angle of 60° with a few degrees gap of about 10° to the next sector. In polar direction the range from 18° to 85° is covered.

The smallest unit in a drift chamber is the drift cell, consisting of an anode wire (also called sense wire), two field wires and a couple of cathode wires. A transverse section of a drift cell with a traversing particle is depicted in the left panel of Figure 3.6. A passing charged particle ionises the atoms

### 3. The HADES experiment

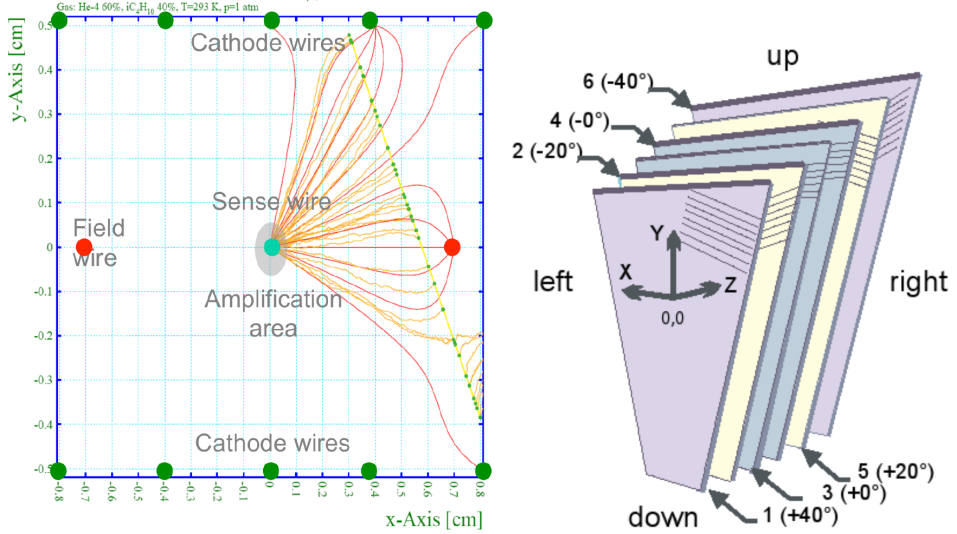


**Figure 3.6:** Left: Depiction of the transverse section of a smallest drift cell, containing one sense wire in the center (cyan dot), two field wires (red dots) and several cathode wires (dark-green dots). Red curves illustrate the electric field inside the cell. A traversing ionising particle (yellow curve) induces free charges in form of electrons (small green points), which drift in direction of the sense wire (yellow struggled curves) and were amplified in the grey area leading to a measurable signal. Right: Scheme of the six-stacked layers of mini drift chambers within one trapezoidal module with stereo angles of  $0^\circ$ ,  $\pm 20^\circ$  and  $\pm 40^\circ$  between the detector-system fixed  $x$  axis and the parallel arranged sense wires. Figures taken from [63, 65].

or molecules of the gas-filled chambers and a bias voltage accelerates the produced electrons in direction of the sense wire. They follow the field lines and drift with nearly constant velocity until they reach the amplification area close to the anode, where the field strength becomes high enough to ionise more atoms and create an avalanche of secondary electrons. This amplification is essential to measure very short electric pulses. In addition the drift time of the electrons between the entering of the charged particle and the arrival of the electron cloud at the anode can be measured. With the calculated drift velocity the minimal distance between particle trajectory and anode is determined. This delivers a very high spatial resolution of around  $100 - 200 \mu\text{m}$ . The equidistant parallel sense wires are aligned in six layers per MDC with different stereo angles, where the wires are inclined by  $\pm 40^\circ$  for the outermost over  $\pm 20^\circ$  to  $0^\circ$  as depicted in the right panel of Figure 3.6. The wires of the  $0^\circ$  layers are shifted by half a drift cell relative to each other. This setup allows to detect the traversing points of charged particles by projections of the fired wires on a convenient plane for

deducing their intersection points. The gas mixture for the Au+Au run was 70% argon and 30% carbon dioxide for MDC I, which are the mini drift chambers of the first plane in beam direction. The other planes MDC II - IV were operated with a mixture of 84% argon and 16% isobutane. Argon is the counting gas, while the CO<sub>2</sub> and the isobutane are used as quenching gases for absorbing the UV radiation of the excited gas ions after relaxation. Furthermore, it is also possible to use the time-over-threshold in the MDC front-end (preamplifier + time-to-digital converter) to deduce the energy loss  $dE/dx$  of ionising particles in the gaseous chambers [67]. It is strongly related to the momentum of the passing particles, described by the Bethe-Bloch equation ([68], Eq. (32.5)). As a consequence one has an additional information for the particle identification besides the time-of-flight measurement, see Section 3.4. However, for the pion identification in the present analysis it has not been used.

## 3.4 Time-of-flight system

Besides the magnetic spectrometer the **time-of-flight** system is the second essential part of the particle identification. The time-of-flight signal is deduced from the time difference between the start and the end time of tracks. The first is measured by a high-precise diamond START detector, the second by the META detectors, consisting of TOF scintillator stripes at large polar angles  $\theta$  and layers of **R**esistive **P**late **C**hamber (RPC) cells at lower polar angles.

### 3.4.1 META detectors

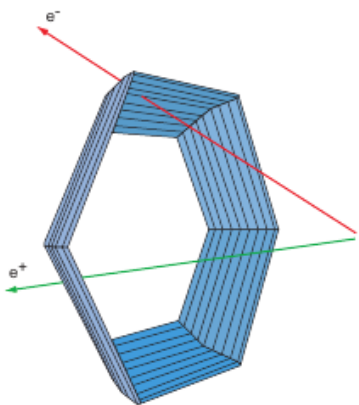


**Figure 3.7:** Scheme of the time-of-flight wall TOF with hexagonal symmetry and eight modules per sector, covering the polar angle range from 44° to 88°. Figure taken from [67].

The META detectors are located downstream behind the outer mini drift chambers and are divided into two groups of sub-detectors. The first one is the TOF wall, covering polar angles  $\theta$  between 44° and 88°. It is arranged

### 3. The HADES experiment

---

in six sectors symmetrically around the beam axis, and each sector consists of eight overlapping modules in polar direction, as depicted in Figure 3.7. Each module again is divided into eight plastic scintillator stripes, arranged in azimuthal direction at the center of the rods, possessing a connection to a photo multiplier tube (PMT) on each end. Passing charged particles excite the scintillator atoms, which emit photons at relaxation. The photon signals are amplified by the PMTs to measure an electric signal. The achievable time resolution is up to 150 ps. With the time difference of both PMTs the interaction point of the particle with the TOF strip can be deduced with a spatial resolution of 2-3 cm in azimuthal direction. In polar direction the resolution is limited by the granularity of the modules at about 2.5 cm. Same as for the MDCs the read-out signal can be used for determining the energy loss  $dE/dx$  of the ionising particles.

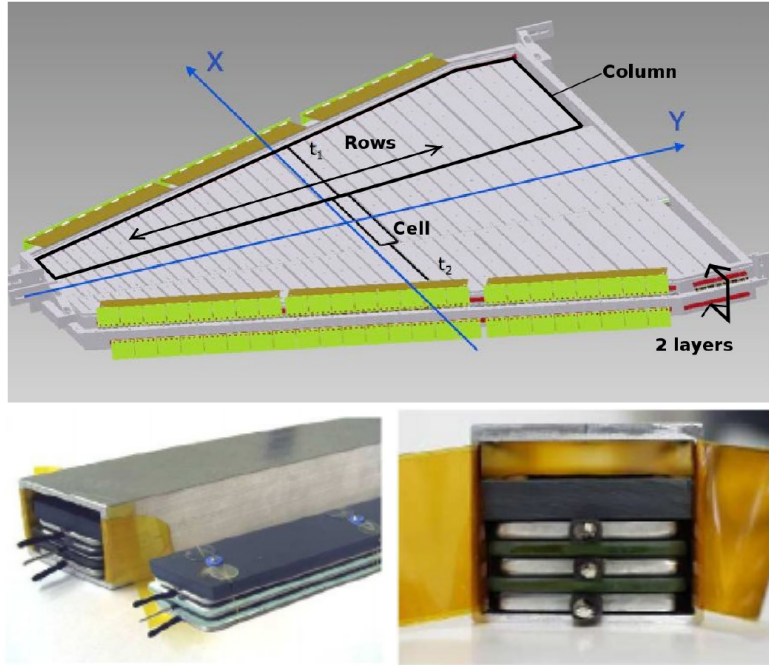


**Figure 3.8:** Top: Picture of the layer alignment of the RPCs of one sector. Bottom: Photographs of one RPC cell consisting of three stacked aluminum plates separated by two glass plates. On top the read-out electronics is installed. Figures taken from [64, 69].

The second group of META detectors are the resistive plate chambers (RPCs). They are again arranged in six sectors following the hexagonal symmetry of the other sub-detectors. Each sector contains 187 cells, arranged in rows in transverse direction and divided into three columns and two layers in downstream direction of the particle tracks, depicted in the top panel of

Figure 3.8. One cell is build up of three vertically stacked aluminum electrodes separated with two glass plates as shown by the photographs in the bottom panels of Figure 3.8. The gaps in between are filled with a gas mixture of 90% Freon and 10% Sulfur Hexafluoride [70]. A passing charged particle ionises the gas atoms and creates an avalanche of electrons, leading to a measurable discharge with a time resolution of about 70 ps. The spatial resolution in transverse direction is between 22 and 42 mm depending on the cell width at different location. In azimuthal direction the position resolution is 8 mm and the efficiency for detecting minimal ionising particles is around 95%. The RPCs cover the polar angles  $\theta$  between  $18^\circ$  and  $45^\circ$ , which is the inner region of the spectrometer closer to the beam axis. There the track densities in Au+Au collisions are comparatively high and the choice of the RPC system with higher granularity as compared to the TOF wall was inevitable. For more technical details see also [70, 71].

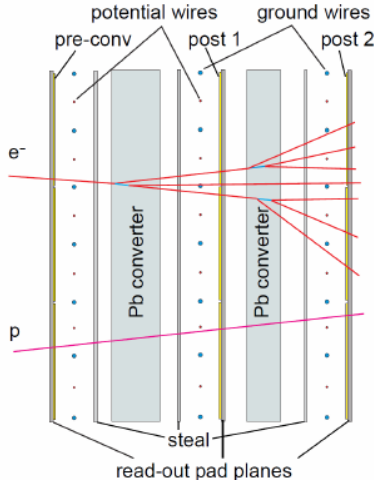


**Figure 3.9:** Cross section of one of the 1024 pads of one module of the hadron-blind Pre-Shower detector. Electrons and positrons generate an electromagnetic shower when passing the lead converters, measured with three drift chambers. Figure taken from [64].

Directly behind the RPC detectors six modules of shower detectors are installed with the same polar angle coverage. Each module covers one sector and consists of 1042 pads. One pad consists of three stacked drift chambers with two lead converters in between, having a width larger than twice the radiation length of the electrons in this material. A depiction is shown in Figure 3.9. In contrast to hadrons the lightest leptons create an electromagnetic shower when passing the lead converters, which is used for discriminating them from each other at momenta larger than  $300 \text{ MeV}/c$ .

### 3.4.2 START and VETO detector

About 2 cm in front of the target, a 4.7 mm broad and  $70 \mu\text{m}$  thick monocrystalline CVD diamond semiconductor [72] is installed, called START detector. It is divided into 16 stripes in both  $x$  and  $y$  directions and measures the passing time of the gold ions with a resolution of around 50 ps. For

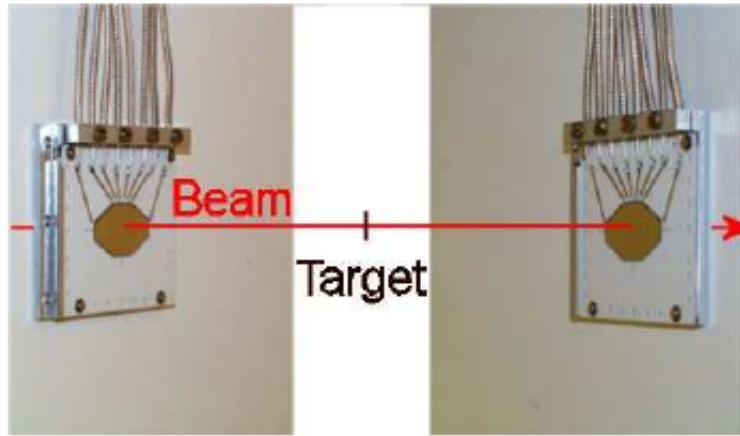


**Figure 3.10:** Photograph of the Start (left) and the Veto (right) detectors within their supports and a depiction of their orientation in front and behind the gold target. Figure taken from [63].

avoiding efficiency losses it was switched between nine disjunct beam spots and the efficiency was above 95%. A  $100\text{ }\mu\text{m}$  thick polycrystalline CVD diamond VETO-detector is installed 70 cm behind the target. If a signal from the VETO detector follows a signal from the START detector within a reasonable time difference ( $\sim 10\text{ ns}$ ) one can be sure that no reaction between projectile and target nucleons took place. This information allowed to reduce the dead time of the HADES setup. If no VETO hit is detected, the times from the START detector are taken as the start times of the Au+Au reactions. A scheme of the alignment of START and VETO detector is shown in Figure 3.10.

### 3.5 Forward hodoscope

Seven meters behind the target the forward wall is installed. Its main purpose is to measure the charged spectators of the projectiles for reconstructing the event plane of a collision. The hodoscope covers in total an area of  $1.8 \times 1.8\text{ m}^2$  and consists of 288 scintillator cells. Each cell has a thickness of  $2.58\text{ cm}$  and an area between  $4 \times 4\text{ cm}^2$  (closest to the beam) and  $16 \times 16\text{ cm}^2$  (outermost region) to account for different track densities, as depicted in Figure 3.11. Each cell is connected to one PMT. The measured energy deposit together with the time-of-flight information allow to identify the charge and the velocity of the incoming particles.

### 3.6 Data acquisition and trigger

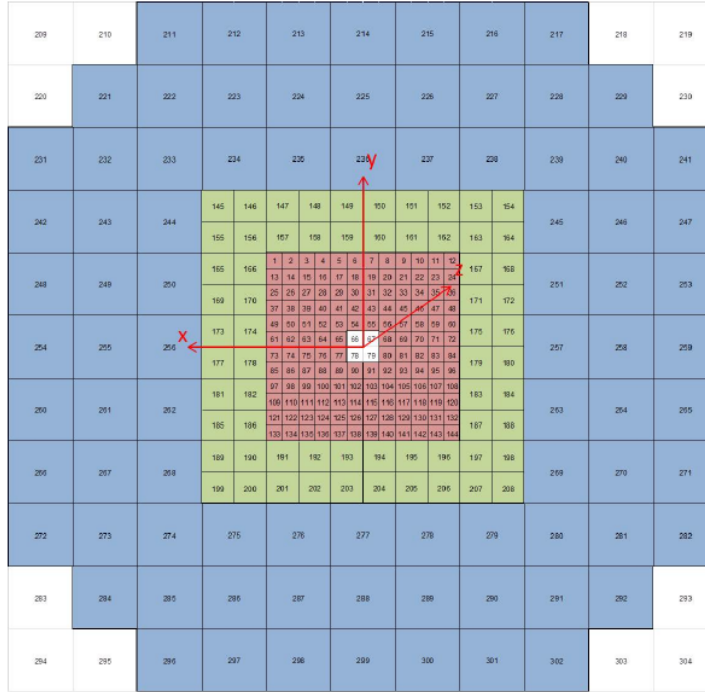


**Figure 3.11:** The forward hodoscope with the arrangement of scintillator cells surrounding the beam axis. Dimensions of the blocks are  $4 \times 4 \text{ cm}^2$  (red),  $8 \times 8 \text{ cm}^2$  (green) and  $16 \times 16 \text{ cm}^2$  (blue). Figure taken from [64].

### 3.6 Data acquisition and trigger

The data acquisition (DAQ) is performed by 500 modules of Field Programmable Gate Array (FPGA) based platforms. It satisfies the requirement of handling high data and event rates up to 8 kHz at 50% duty cycle. During measurement around 400 MByte/s are written to storage. Furthermore, the used DAQ system provides very low electromagnetic noise. The HADES DAQ system makes use of Trigger and Read-out Boards (TRB) developed at GSI. All sub-detector systems and the steps from read-out are combined in the dedicated network TrbNet, developed specifically for HADES [69]. All data is streamed via Gigabit Ethernet to the event builders, where the preparation for long time storage and the following analysis is performed. A scheme of the data processing is depicted in Figure 3.12.

Several triggers are installed to reduce the dead time of the data acquisition and to preserve the storage capacity for events with potential good quality. They are combined in the Central Trigger System (CTS) of HADES. The first level trigger (LVL1) selects only events with at least a certain track multiplicity. The track multiplicity is correlated to the centrality of the

### 3. The HADES experiment

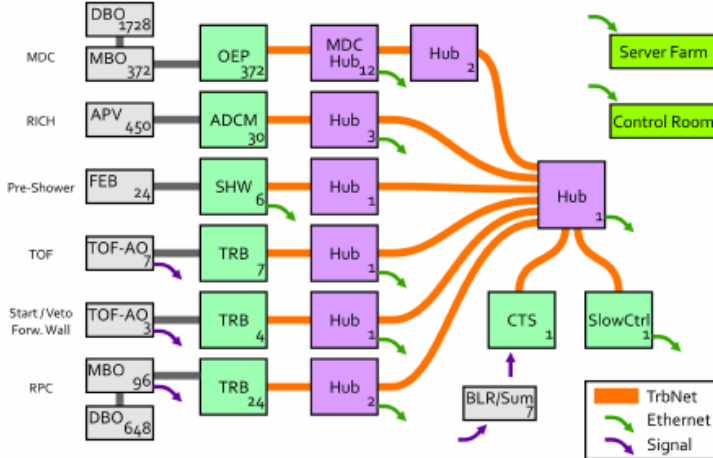


**Figure 3.12:** Scheme of the complete HADES DAQ network consisting of several network nodes (violet), read-out modules (green) and additional front-end modules (grey). All modules are connected via a dedicated network protocol (TrbNet). Data transfer to several servers is streamed via the Gigabit Ethernet. Figure taken from [69].

collisions, therefore most of the peripheral collisions and collisions with detector material outside the target are excluded. The decision time of this trigger of about 100 ns is much faster than the average time in between two collisions. In the Au+Au experiment, a minimal track multiplicity of 20 in the TOF wall was required by the so-called PT3 trigger. In addition, a minimum bias trigger, called PT2, selected collisions with at least five hits in the TOF wall, but reduced by a scaling factor of ten. All selected events were then written from the buffer memory into Hades List Data (HLD) files.

### 3.7 UrQMD simulations

In addition to the collected experimental data of Au+Au collisions a sample of 100 million events of UrQMD simulations has been produced. The ultra-relativistic quantum-molecular dynamics model is a transport implementation, introduced in [73]. The event tracks are propagated virtually through the HADES setup using the package HGEANT, which is an extension of the CERN software GEANT 3.21 [74] including the specific HADES geometry. It contains the magnetic field and all volumes and materials of the sub-detectors. Detector hits are generated along the particle tracks according to known physical processes. Then all detector hits are digitised analogously to experimental events and can be used for the analysis similar as the HLD files.

# 4 | Analysis

The data analysed in this thesis was taken in April 2012 at GSI in Darmstadt with the experimental setup described in the previous chapter. The heavy-ion synchrotron SIS18 provides the beam with bunches of gold nuclei with kinetic energy of  $1.23 \text{ A GeV}$  and intensities between  $1.2$  and  $1.5 \times 10^6$  ions per second. The nucleon-nucleon center-of-mass energy  $\sqrt{s_{\text{NN}}}$ <sup>1</sup> is  $2.4 \text{ GeV}$  and the corresponding mid-rapidity  $y_{\text{cm}}$  is  $0.74$ . Within 557 beam hours and with a trigger rate of up to  $8 \text{ kHz}$ ,  $7.3 \times 10^9$  events are collected in total. This corresponds to a data volume of  $140 \text{ TByte}$  written with a maximum data rate of  $400 \text{ MByte/s}$  and  $50 \%$  duty cycle. During the last 48 hours of data taking the magnetic field of ILSE was inverted (same amplitude, opposite direction). The generated reversed-field data can be used for cross-checks.

## 4.1 Event characterization

The analysis of the HADES data is done event-by-event. Within these events the fundamental parameters of the collision differ. Since the system size of the single nuclei is fixed by the choice of Au+Au, the remaining variables of interest are:

- the place of collision: primary event vertex,
- number of participating nucleons  $A_{\text{part}}$ ,
- the closest distance of the nuclei: impact parameter  $b$ ,
- orientation of the impact parameter: event plane / reaction plane.

In this section, the relevant steps for determining these physical properties are introduced. Furthermore, a general selection on the quality of the event data is performed. Detailed summaries with comparable content can be found in [64, 65].

---

<sup>1</sup>The invariant center-of-mass energy is defined as the square root of the sum of squared components of the four vector of all participating particles. For fixed-target experiments it can be calculated by  $\sqrt{s_{\text{NN}}} = (2E_{\text{kin, beam}}m_{\text{target}} + m_{\text{target}}^2 + m_{\text{beam}}^2)^{1/2}$  with the kinetic energy of the projectile  $E_{\text{kin, beam}}$ .

## 4. Analysis

---

### 4.1.1 Event Vertex

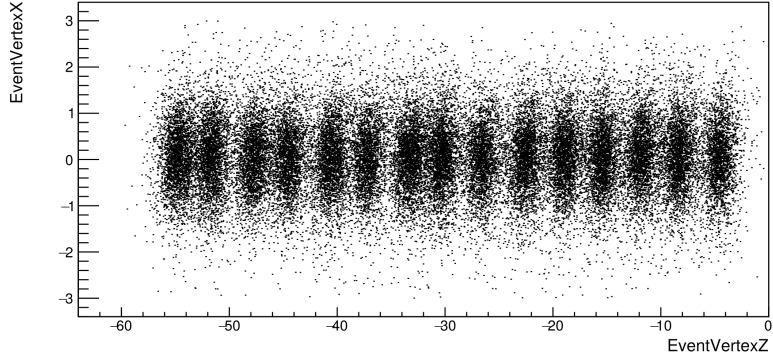


**Figure 4.1:** Reconstructed event vertices in  $x$  and  $z$  direction in units of mm. The 15 separated gold segments of the target are clearly visible.

The event vertex is determined in three steps. A first approximation uses the center of each target segment as projection point for the hits in the inner mini drift chambers MDC I and MDC II. Assuming straight lines the segment with the best projection resolution is considered as primary target slice. Although this approximation delivers with high efficiency the correct segment it is only sensitive to the position along the beam direction. In a second step, the inner segments found from the track reconstruction are extrapolated to the target region, and then, the geometrical center-of-gravity of acceptable points provides the vertex point. The last method uses the fully reconstructed tracks and delivers the most precise primary target vertices. Since the vertex reconstruction is an iterative procedure it is inevitable to anticipate the description of the track reconstruction already in this section. All of these methods are highly correlated to the total charged particle multiplicity per event and, therefore, they are more precise for higher track densities. In Figure 4.1 the primary vertex distribution in  $x$  and  $z$  direction is shown for an exemplary data set. The 15 target slices can be well distinguished.

### 4.1.2 Event cleaning

To make sure that only Au+Au events with good quality and meaningful physical content are used for the analysis, all recorded events have to pass a sequence of event conditions. Relevant criteria are:

- certain stability of the mini drift chamber operation,
- PT3 trigger,

- event vertex in the target region,
- no event pile-up, i.e. no temporal superpositions of two or more nucleus-nucleus reactions,
- well separable events in time.

### Stable MDCs

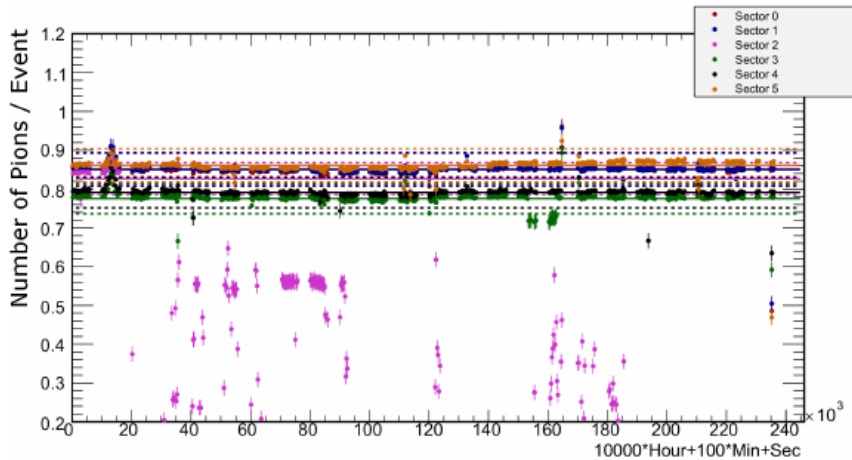


**Figure 4.2:** Mean number of charged pions per event (symbols, averaged per file) compared to the mean value (solid lines) for one day, individually for each sector (different colors in the legend). Dashed lines delineate a  $\pm 5\%$  range around the corresponding means, symbols with error bars are outside this range. Figure taken from [75].

During the measurement it turned out that the counting rates of the mini drift chambers were not completely stable all the time. Reasons for that are too high currents and corresponding high voltage changes during the beam-on time, which automatically ends up in different efficiencies of the sub-detectors over measuring time. Especially sector 2 was working properly only a few days and most of the time had to be turned off, which leads to a general exclusion of the region of azimuthal angles of  $\phi$  between  $240^\circ$  and  $300^\circ$ . For that reasons a careful and individual inspection of the files over the whole beam time was inevitable. To account for the inefficiencies of the sub-detectors, a time dependent day-by-day analysis of the counting rates of electrons, protons and pions per sector has been done. The values are compared to the average values, illustrated in Figure 4.2 exemplary for day 109. The dashed lines represent a  $\pm 5\%$  window around the mean values. If the counting rate in a certain HLD file is outside this window (depicted by symbols with error bars), the sector is declared as non-stable. Since sector

2 is already excluded for the whole measurement no other sector is allowed to work inappropriate and files with another non-stable sector are excluded completely from the analysis.

### Temporal and spatial location

For the further analysis only PT3 triggered events are used. Step-by-step selections are applied mostly related to the Start and Veto system and to the event vertex, hence imperfect events are removed if the following conditions are not fulfilled:

- *selectStart*: Only events with at least one hit in the Start detector segments and with no hit in the Veto detectors are used.
- *StartPileUp*: In a time interval of  $-5\text{ ns}$  to  $15\text{ ns}$  around the hit cluster in the Start detector no other hit took place. Otherwise the event cannot be clearly assigned to the exact start time, which leads to uncertainties in the time-of-flight determination of the particle tracks.
- *GoodClusterVertex*: The reconstructed event vertex is required to be located within  $-65 < z < 0\text{ mm}$ , i.e. the position of the gold target. In addition at least one reconstructed track and two identified particles (*GoodCandVertex*) have to be found.
- *NoVeto*: Events with a measured Veto hit in the time interval  $\pm 15\text{ ns}$  around the Start time are excluded. This second cut on the Veto information reduces the probability of having a second projectile nucleus in a time window of  $30\text{ ns}$ . Due to the finite efficiency of the Start detector the starting signal of one particle could get lost, but may be given by another beam particle, which would disturb the time-of-flight evaluation.
- *VetoStart*: To account for the limited Veto efficiency, events are discarded with a subsequent Start hit in the time interval from  $15$  to  $350\text{ ns}$  without a corresponding Veto hit.
- *StartMeta*: Events with a delayed Start hit and correlated signals in the META detectors in the time window of  $80$  to  $350\text{ ns}$  after the measured start time are removed to avoid pile-ups caused by other reactions. The lower time limit corresponds to the spectrometer passing time of the slowest particles. The upper time was chosen according to the data processing time through the electronic devices of the largest drift chambers.

Finally about  $2.1 \times 10^9$  events remain with high quality, which is around 50 % of the PT3 triggered data and about 42 % of the initial events after excluding inappropriate sectors.

### 4.1.3 Centrality

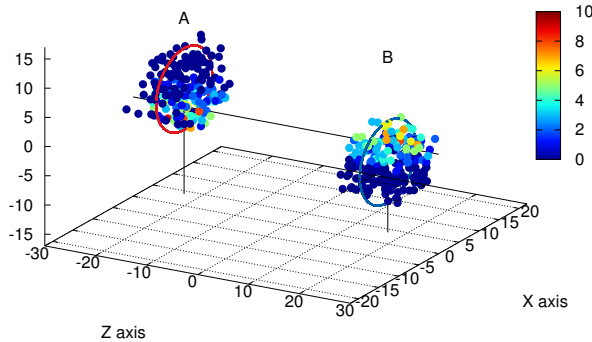


**Figure 4.3:** Distributions of the modelled nuclei A and B, with 197 nucleons each, in the Glauber approach with an impact parameter  $b = 6\text{ fm}$ . The color of the nucleons correspond to the number of inelastic collisions they will experience. Figure taken from [76].

The physical parameters of heavy-ion collisions like overlap volume, particle yield, etc., are not independent of the impact parameter  $b$  and scale with the number of participating nucleons  $A_{\text{part}}$ . Both, impact parameter and number of participants, are correlated to the number of produced particles (really produced particles, especially leptons, pions and kaons + scattered nucleons and fragments) and scale with the centrality of the collision. Only charged particles in the acceptance of the spectrometer can be measured by HADES. However, one can assume that the number of these particles scale with the total number of particles in accordance to the wounded nucleon model [77]. One can use either the number of reconstructed tracks from the MDCs,  $N_{\text{tracks}}$ , or the total number of hits in the META detectors,  $N_{\text{TOF+RPC}}$ . The first one has the advantage of being less contaminated by background hits. However, only fully reconstructed tracks from appropriately working sectors are taken into account, and tracks which are too close to each other are not resolvable. The total number of reconstructed tracks is clearly reduced w.r.t. the number of hits in the TOF wall and the RPCs. Without further good calibration,  $N_{\text{tracks}}$  is only hardly usable over the whole beam time. Therefore, for the rest of the present investigation only  $N_{\text{TOF+RPC}}$  is used as charged particle multiplicity, since it is measured very stably over the whole beam time. It must be taken into account that the complete distribution is truncated at low numbers of charged particles by the multiplicity triggers PT3 and PT2. Models have to be used for both,

#### 4. Analysis

---

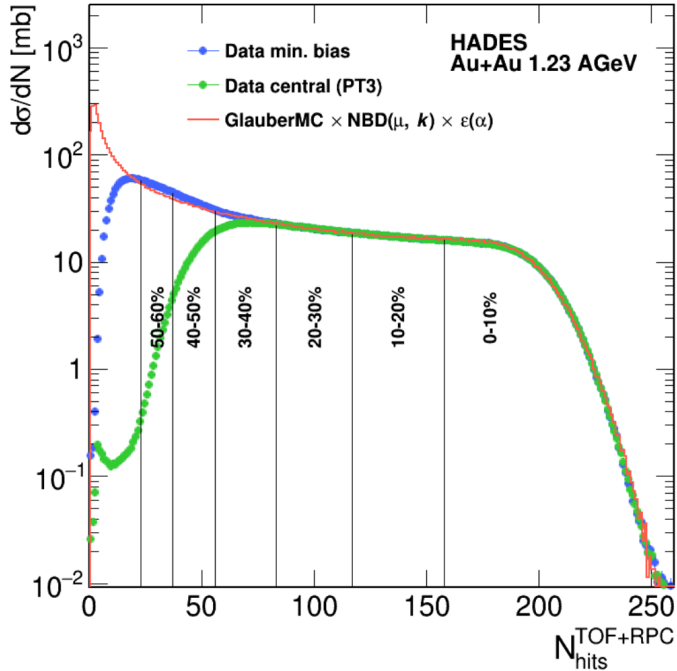


**Figure 4.4:** Cross section as a function of  $N_{\text{hits}}^{\text{TOF+RPC}}$ . Minimum bias (blue) and PT3 (green) data compared to the Glauber MC model (red histogram). Figure taken from [76].

estimating the shape of the whole distribution and the connection between the centrality classes and the average impact parameter and number of participating nucleons. Here a Glauber Monte-Carlo model [78] is used, implemented like in [79]. The model assumes two spherical nuclei with randomly distributed nucleons following a Fermi distribution of the density  $\rho$ ,

$$\rho(r) = \rho_0 \frac{1 + w(r/R)^2}{1 + \exp(\frac{r^2 - R^2}{a^2})} \quad (4.1)$$

and having a minimal separation distance  $d_{\min}$  of their centers. The radius parameter is set to  $R = 6.55$  fm and the skin depth  $a = 0.52$  fm. The parameter  $w$  is set to zero assuming a homogeneous radial density profile inside the nuclei. For more details see [76]. The centers of the nuclei are displaced in transverse direction by the impact parameter  $b$ , randomly distributed up to  $b_{\max} = 2R$ , following the distribution  $P(b) \sim b db$ . It is assumed that the nuclei and the nucleons as well follow straight lines parallel to the beam axis moving in direction of each other. The longitudinal position does not play a role within this approach. An illustration of the modelled nuclei is shown in Figure 4.3. If the distance of a nucleon from nucleus A to a nucleon of nucleus B is smaller than the interaction length  $D = \sqrt{\sigma_{\text{NN}}/\pi}$  in

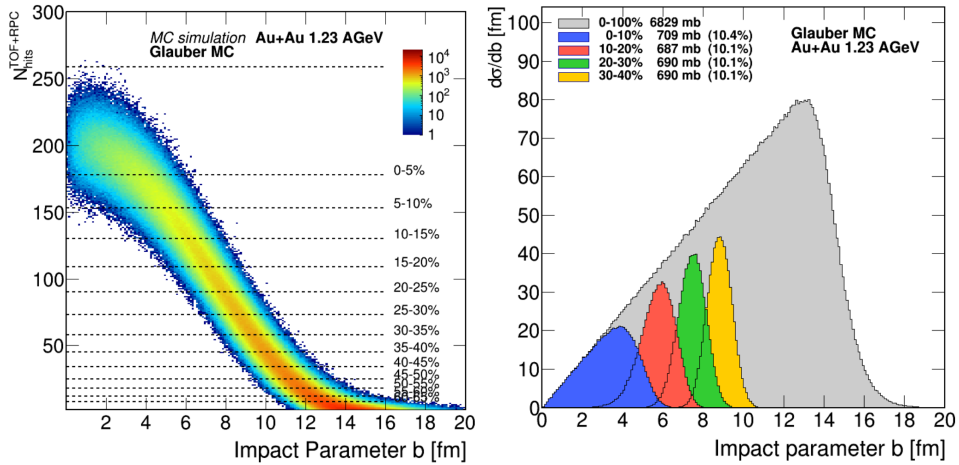


**Figure 4.5:** Left: Anti-correlation between charged particle multiplicity  $N_{\text{TOF+RPC}}$  and impact parameter  $b$  delivered by Glauber MC simulations. Right: Distributions of the impact parameter. Colored distributions belong to defined centrality classes (blue: 0 – 10 %, red: 10 – 20 %, green: 20 – 30 %, yellow: 30 – 40 %). Figures taken from [76].

the transverse plane, the two nucleons are assumed to collide and treated as participants. This criterion is checked for all possible combinations of nucleons. The isospin averaged inelastic cross section  $\sigma_{\text{NN}}$  is set to 23.8 mb [76].

The introduced Glauber model was applied in a simulation of a sample of at least one million events and then compared to the charged particle multiplicity given by  $N_{\text{TOF+RPC}}$ . As mentioned above, the number of charged particles should be proportional to the number of participants,  $\langle N_{\text{ch}} \rangle = \mu \langle A_{\text{part}} \rangle$ . To account for event-by-event fluctuations, the number of charged particles per participant is sampled with a negative binomial probability distribution (NBD),

$$P_{\mu,k}(n) = \frac{\Gamma(n+k)}{\Gamma(n+1)\Gamma(k)} \frac{(\mu/k)^n}{(\mu/k+1)^{n+k}}, \quad (4.2)$$

with the mean value  $\mu$ , the gamma function  $\Gamma$ , and  $k$  being related to the relative width of the distribution,  $\sigma/\mu = \sqrt{1/\mu + 1/k}$ . The parameters  $\mu$  and  $k$  take into account the acceptance, reconstruction efficiency and the resolution of  $N_{\text{ch}}$ . A further efficiency function  $\epsilon(\alpha)$  takes into account non-linear multiplicity-dependent inefficiencies. Finally, the distribution of  $N_{\text{TOF+RPC}}$  is fitted by

$$N_{\text{TOF+RPC}} = \text{GlauberMC} \times \text{NBD}(\mu, k) \times \epsilon(\alpha), \quad (4.3)$$

## 4. Analysis

---

which is illustrated in Figure 4.4. For more details and the used values of  $\mu$ ,  $k$  and  $\alpha$  see [76]. As also illustrated in Figure 4.4, the events can be divided into intervals of centrality as function of  $N_{\text{TOF+RPC}}$  for experimental data. Since the experimental data is reduced at low values of  $N_{\text{TOF+RPC}}$  due to the multiplicity triggers, the values at the edges of these centrality intervals are determined from the Glauber MC data and translated after the fit to the experimental data. Within a chosen centrality interval the mean impact parameter and the mean number of participants can be deduced from the Glauber model and easily adapted to the experimental data. On the left hand side of Figure 4.5, the correlation between impact parameter  $b$  and  $N_{\text{TOF+RPC}}$  from the Glauber MC data is exhibited. On the right hand side of the same figure, the distribution of the impact parameter for different centrality classes is shown. The grey shaded area illustrates the total distribution. One finds clearly the dependency  $\sigma \sim b db$  with Gaussian smearing.

### 4.1.4 Event plane

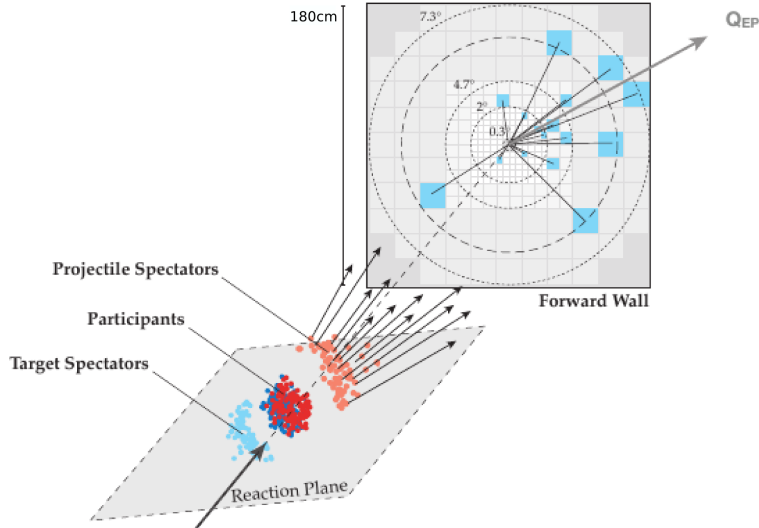


**Figure 4.6:** Illustration of the event plane reconstruction. The projectile spectators hit the forward wall and the sum of all hits relative to the beam center define the event plane vector  $\vec{Q}_{\text{EP}}$ . Figure taken from [2].

The reaction plane of a heavy-ion collision is defined as the plane spanned by the impact parameter vector  $\vec{b}$  and the beam axis. The strong directed flow in the SIS18 energy regime [80] allows to use the projectile spectators for determining the event plane with high resolution. The charged nuclei and fragments within the polar angle range of  $0.3^\circ$  to  $7.3^\circ$  hit the cells of

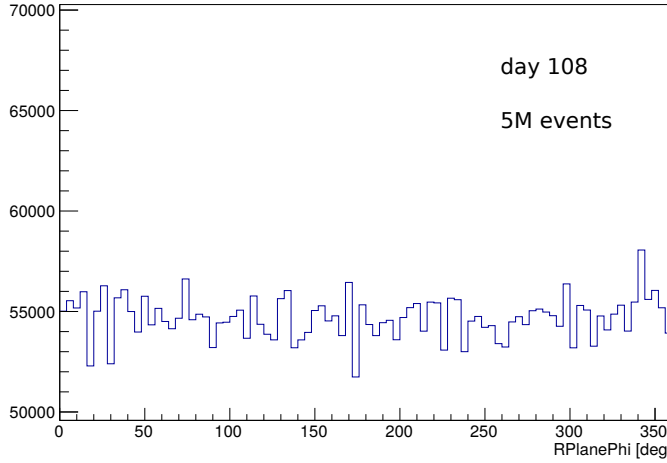


**Figure 4.7:** Distribution of the event plane angle for one day.

the forward wall. Adding all the vectors  $\vec{u}_i$  between the beam center and the centers of the hit scintillators one gets the  $Q$ -vector,

$$\vec{Q}_{EP} = \sum_{i=0}^N \vec{u}_i \omega_i, \quad (4.4)$$

see Figure 4.6. The event plane angle  $\phi_{EP}$  is defined by the direction of the  $Q$ -vector. The signals from the scintillator cells of the forward hodoscope are sensitive to the charge of the hits, incorporated by the weighting factor  $\omega_i$  taking into account charge states up to  $Z = 6$ . For this thesis,  $\vec{Q}_{EP}$  goes along with the  $x$  coordinate of the reaction-plane-fixed  $xyz$  coordinate system (while  $z$  goes along the beam axis and  $y$  is perpendicular to the reaction plane). The accuracy of the event-plane reconstruction is increased by a day-by-day re-arrangement of the beam center relative to the scintillator blocks with correct scaling, individually for all chosen centrality classes (for details see [2]). For the further analysis, only events with reconstructed event plane are considered, since the event plane angle will be used as one criterion for the combinatorial background determination in Section 4.3.3.

The estimated event plane angle differs from the underlying true physical reaction plane angle  $\phi_{RP}$  by  $\Delta\phi$ . On the one hand, the finite-number nucleon distribution inside the colliding nuclei is not homogeneous, but fluctuates from event to event around the ideal cylindric symmetry. On the other hand, the finite granularity of the forward wall has to be taken into account. Both, implicit and explicit aspects, lead to a finite resolution of the

#### 4. Analysis

---

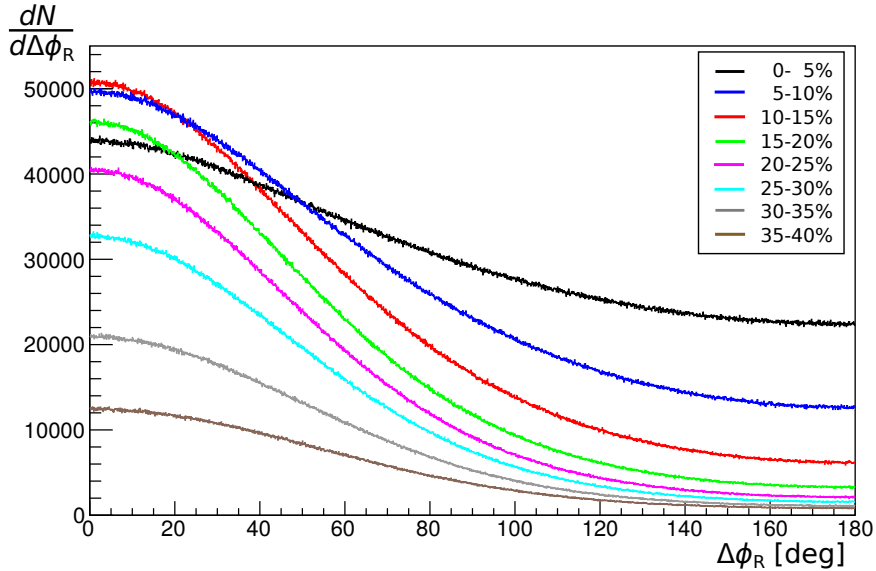


**Figure 4.8:** Distribution of the difference between the event plane angles of two sub-events A and B for different centrality classes.

event plane. One method for deducing the implicit resolution is introduced in [81] and described in the following.

For the general problem one starts with a normalised azimuthal distribution, expressed as Fourier series,

$$\frac{dN}{d\phi} = \frac{1}{2\pi} \left( 1 + 2 \sum_{n \geq 1} c_n \cos n\phi \right), \quad (4.5)$$

where it does not matter whether  $N$  describes a particle yield, a source radius or any other angular dependent measure. The Fourier coefficients  $c_n = \langle \cos n\phi \rangle$  of the measured distribution are related to the true coefficients by

$$\langle \cos n\phi_{\text{EP}} \rangle = \langle \cos n\phi_{\text{RP}} \rangle \langle \cos n\Delta\phi \rangle. \quad (4.6)$$

One can show, that the distribution of  $\Delta\phi$  is an universal function depending only on one real parameter  $\chi$ , which is a measure of the accuracy of the reaction plane determination [81]. It can be expressed as

$$\langle \cos n\Delta\phi \rangle = \frac{\sqrt{\pi}}{2} \chi e^{-\chi^2/2} \left[ I_{\frac{n-1}{2}} \left( \frac{\chi^2}{2} \right) + I_{\frac{n+1}{2}} \left( \frac{\chi^2}{2} \right) \right], \quad (4.7)$$

where  $I_j$  is the modified Bessel function of order  $j$ . The value of  $\chi$  can be extracted from experimental data. A widely used method is dividing

each event randomly into two sub-events A and B containing half of the particle number and calculating  $\vec{Q}_{\text{EP}}$  by Equation (4.4) for each of them. One constructs the distribution of the relative angle  $\Delta\phi_{\text{R}} = |\phi_{\text{EP}, \text{A}} - \phi_{\text{EP}, \text{B}}|$  and uses then the simple expression

$$\frac{N(90^\circ < \Delta\phi_{\text{R}} < 180^\circ)}{N(0^\circ < \Delta\phi_{\text{R}} < 180^\circ)} = \frac{\exp(-\chi^2/2)}{2} \quad (4.8)$$

to obtain the value of  $\chi$ . In Figure 4.8 the experimental distributions of  $\Delta\phi_{\text{R}}$  are exhibited for several centrality intervals, exemplary for an event sample of one day beam time. This procedure is called the sub-event method and has solely been used for deducing the event plane resolution in the present analysis.

#### 4.1.5 Event selection

**Table 4.1:** Centrality classes used in the azimuthally integrated analysis, corresponding boundary values of the charged particle multiplicity, correlated mean value of the impact parameter, and mean number of participating nucleons in Au+Au collisions at  $1.23A$  GeV.

centr. (%)	$N_{\text{hits, min}}^{\text{TOF+RPC}}$	$N_{\text{hits, max}}^{\text{TOF+RPC}}$	$\langle b \rangle [\text{fm}]$	$\langle A_{\text{part}} \rangle$
0-10	157	250	3.1	303
10-20	117	156	5.7	213
20-30	82	116	7.4	150
30-40	55	81	8.7	103

**Table 4.2:** Centrality classes used in the azimuthally dependent analysis, mean number of the impact parameter, the number of participants, and the event plane resolutions for the first and second order Fourier coefficients.

centr. (%)	$\langle b \rangle [\text{fm}]$	$\langle A_{\text{part}} \rangle$	$\langle \cos \Delta\phi \rangle$	$\langle \cos 2\Delta\phi \rangle$
0-10	3.1	303	0.648	0.298
10-20	5.7	213	0.847	0.572
20-30	7.4	150	0.887	0.653
25-35	8.1	125	0.886	0.651
30-45	9.0	93	0.871	0.620
10-30	6.5	181	0.866	0.609

The final analysis of the pion pairs is performed differentially w.r.t. collision centrality using intervals of the charged particle multiplicity  $N_{\text{hits}}^{\text{TOF+RPC}}$ .

The boundary values of these intervals and the corresponding values of the mean impact parameter  $b$  and number of participants  $A_{\text{part}}$  are summarised in Table 4.1. For more peripheral collisions, the intervals for the azimuthally dependent analysis are chosen slightly different. Overlapping intervals are chosen (25 – 35 %) to check, if the results of the analysis show a smooth behaviour in direction of centrality. The more peripheral the collisions is the less is the number of the produced pions per event and even less are the combinations of pion pairs. The choice of the interval 30 – 45 % improves the statistics a bit. However, due to the PT3 trigger it is implicitly shifted more to 30 – 43 %, visible in Figure 4.4. Furthermore, a larger semi-peripheral interval 10 – 30 % is considered with respect to existing results at larger beam energies, which will be discussed later.

## 4.2 Particle identification

Now the event-by-event particle identification is introduced leading finally to the single pion spectrum for the subsequent two-particle analysis. A detailed description of the content of this section can be found in [64, 65].

### 4.2.1 Tracking

Charged particles passing the active detector volume of the MDCs induce electronic signals in the sense wires of drift cells, and the corresponding wires are called 'fired'. Combining the signals of 'fired' wires of all six layers with different orientation of the stereo angles allows to deduce potential track hit points in the chamber. A pair of one hit in MDC I and one in MDC II form a linear inner track segment neglecting the almost vanishing magnetic field inside the MDC area. Analogously, one hit in MDC III and one in MDC IV form a linear outer track segment. The inner and outer segments are then matched to each other considering the magnetic field in between. The found tracks are finally extrapolated to the META layer and matched with the hits in TOF or RPC/SHOWER, respectively. Since the charged particle multiplicities in Au+Au collisions are relatively high, a lot of possible combinations between the hit points occur and a large number of so-called 'fake-tracks' or 'ghost-tracks' appear. To account for the high occupancy in the detector system a refined algorithm is needed, to search for the most probable selection of track candidates and reject efficiently the 'ghost-tracks'. The relevant steps of this algorithm are depicted schematically in Figure 4.9 and listed in the following with a few annotations:

- **Cluster Vertex Finder**

In a first approximation the target segment is determined. Each segment is taken as view point for a projection of the wire distribution of MDC I and II on a virtual projection plane, see Figure 4.10. The

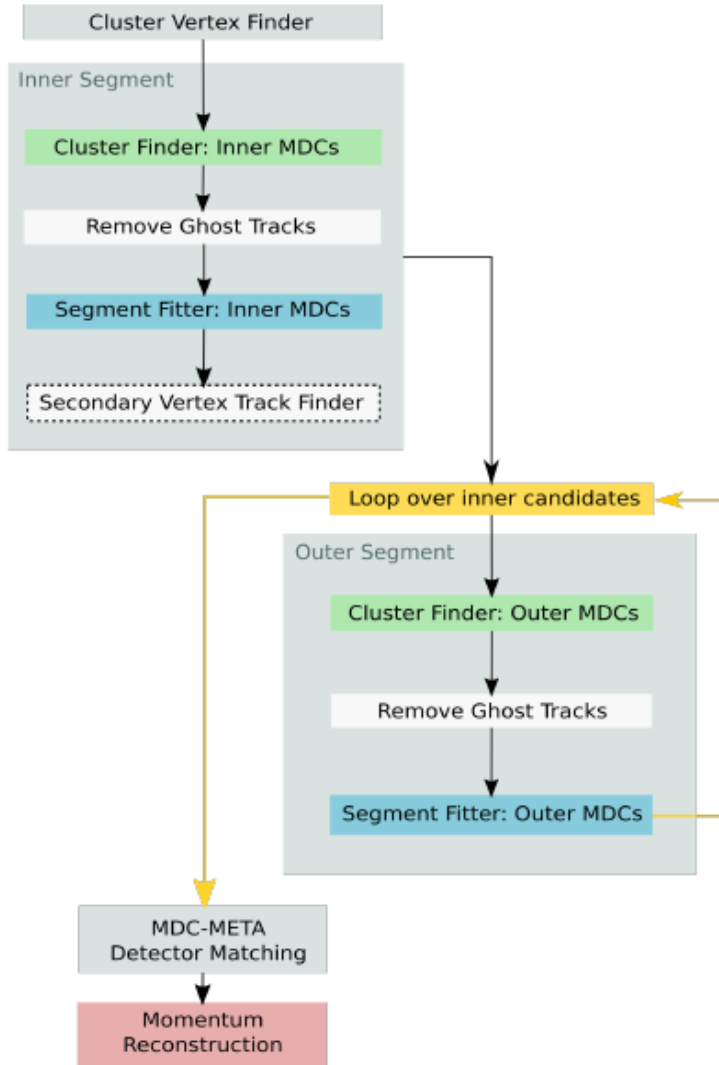


**Figure 4.9:** Flow chart of track reconstruction. Figure taken from [65].

segment with the best projection resolution (which is related to the cluster size) and the biggest amount of clusters is taken as the event vertex. Additionally, the information of the drift time is used to reduce the projected cell volume and to increase the spatial resolution (see right panel of Figure 4.10).

- **Cluster Finder Inner MDCs**

For the chosen target vertex, the fired wire clusters of MDC I and II are projected on the binned projection plane introduced in the first step. A fired wire increases the bins along its projection by one, and regions,

## 4. Analysis

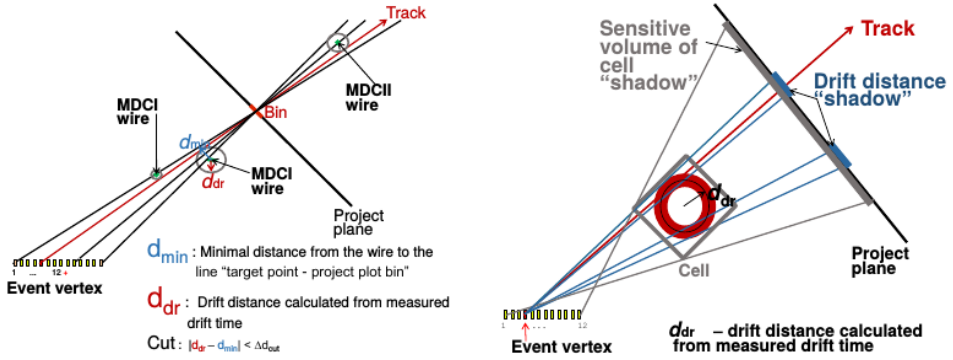


**Figure 4.10:** Left: Illustration of the vertex finder. Right: Illustration of the use of the drift time for reducing the projected volume and increasing the spatial resolution of the vertex finder procedure. Figure taken from [64].

where fired wires cross, form a local maximum. If the number in this maximum exceeds a dynamically set threshold (typically  $N_{\text{thr}} \geq 9$ ) it is accepted as a wire cluster. If the threshold is set too low, more ghost-tracks enter due to randomly crossing wires, while a too high threshold reduces the efficiency of the cluster-finding procedure. On the right side of Figure 4.11, an example for a clear local maximum formed by fired wires is exhibited.

### • Removal of ghost-tracks

There are several distinctive features of ghost-tracks compared to real tracks, which can be used to clean the track sample:

- smaller average amplitude of the local maxima of the projected wires,
- smaller average number of wires contributing uniquely to the clusters, i.e. wires which do not contribute to more than one cluster,
- smaller average cluster size w.r.t. the bins contributing to the maximum of the cluster.

In a first step those clusters are removed, which are practically formed by an identical set of wires as the real tracks. Secondly ghost-tracks formed by fired wires of different clusters are removed.

### • Pre-fit Procedure for Inner Segment and Inner Segment Fitter

The list of fired wires is now used for fitting all inner segments assuming a straight line from target vertex over the hit point in MDC I

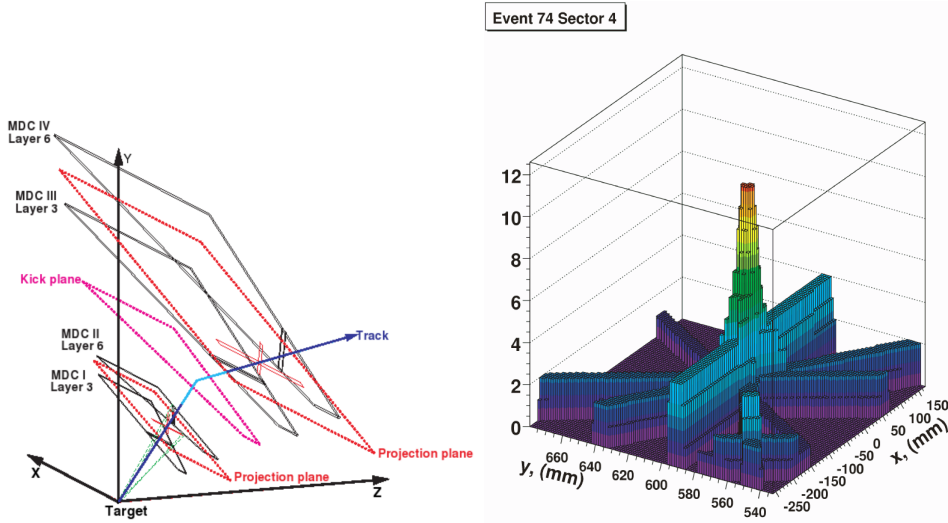


**Figure 4.11:** Left: Illustration of the segment finding process. Right: Projection of fired wires in the projection plane with a clear local maximum. Figure taken from [64].

to the hit point in MDC II. Using a Garfield<sup>2</sup> simulation the distance between the closest approach of the assumed line and the fired wires is translated into a drift time  $t_{\text{drift}}$ , which is used for minimising the functional  $F$  in the form

$$F = \sum_i \frac{(t_{\text{drift}}^i + t_{\text{off}} + t_{\text{TDC}}^i)^2}{(\Delta t_{\text{drift}}^i)^2} w_i, \quad (4.9)$$

where  $t_{\text{off}}$  is the time-of-flight of the particle from the target to the drift chamber,  $t_{\text{TDC}}$  is the drift time measured by the TDC minus the signal propagation time in the wire ( $t_{\text{measured}} - t_{\text{wire}}$ ),  $w_i$  is a weighting constant, and the error of the drift time measurement  $\Delta t_{\text{drift}}^i$  is determined from Garfield simulations. More details concerning drift time simulations can be found in [67]. The sum runs over all contributing fired wires, and minimisation is done using the  $\chi^2$ -method. The deviation between the fit and the hit points is given by  $\chi^2_{\text{inner}}$ , which acts as a quality parameter and can later be used to select the best track candidates.

Afterwards this procedure can be repeated with the previously lost wires and with giving up the restriction of a primary target vertex,

<sup>2</sup>Garfield is the name of a software from CERN for simulating two- and three-dimensional drift chambers

## 4. Analysis

---

which allows to collect also off-vertex tracks coming from different resonance decays.

- **Hit Point in Virtual Kick Plane**

Extending the inner segments towards the outer detector regions they cross an almost flat virtual kick plane, which is located in the region of maximal magnetic field. It approximates the continuous influence of the magnetic field on the charged particles by a deflection of their momenta in one single point. This procedure is illustrated in the left panel of Figure 4.11. The hit point inside the kick plane is the starting point for the tracking through the outer drift chambers, MDC III and IV.

- **Cluster Finder Outer MDCs**

The cluster finding for the outer MDCs is very similar compared to the inner MDCs. Instead of the target vertex the intercept between inner segment and kick plane is used as view point for the projection of fired wires in MDC III and IV. Furthermore, only the range of physical correlations of the momenta and the charge of the tracks are considered. Again, also the procedure for removing ghost-tracks is applied similarly to the inner segments. The outer cluster finding is repeated for each intersection point of the inner segments individually.

- **Outer Segment Fitter**

Analogue to the inner segment fitter, the outer segment fitter uses a  $\chi^2$ -minimisation procedure for fitting the outer segments w.r.t. the drift time from the TDCs and delivers a quality parameter  $\chi^2_{\text{outer}}$  for a later selection of the best track candidates.

- **META Matching**

Finally, the outer segments are roughly matched to a registered META hit within a  $5\sigma$  resolution range, while a more precise matching is done in line with the momentum reconstruction described in the following section.

### 4.2.2 Momentum reconstruction

The momentum of the charged particle tracks is determined by their curvature in the magnetic field. The Lorentz force  $\vec{F}_L$  is defined as

$$\vec{F}_L = q(\vec{v} \times \vec{B}), \quad (4.10)$$

with the particle having charge  $q$  and propagating through the magnetic field  $\vec{B}$  with velocity  $\vec{v}$ . The deflection  $\Delta\vec{p}_{\text{kick}}$  of the momentum follows then

$$\Delta\vec{p}_{\text{kick}} = \vec{p}_{\text{out}} - \vec{p}_{\text{in}} = \int d\vec{p} = \int \vec{F} dt = \int q(\vec{v} \times \vec{B}) dt = -q \int \vec{B} \times d\vec{s}, \quad (4.11)$$

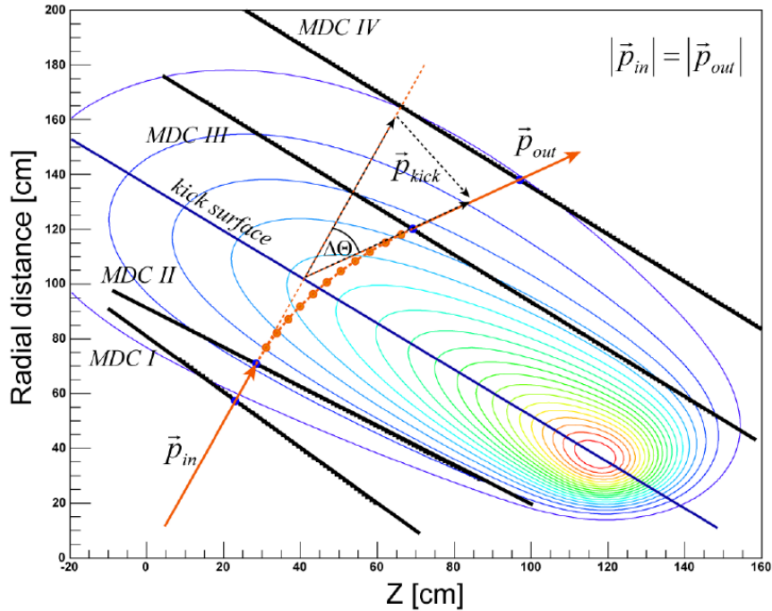


**Figure 4.12:** Illustration of the momentum reconstruction. The deflection of the particle in the magnetic field is first approximated by a single kick of the momentum calculated with Equation (4.11). A spline method is used afterwards for solving the equation of motion at some points between the inner and outer segment. This solution is used as input for an iterative Runge-Kutta procedure solving the equation of motion numerically. Figure taken from [64].

where  $\vec{p}_{in}$  is the incoming and  $\vec{p}_{out}$  the outgoing momentum vector of the particle. The deflection angle  $\Delta\theta$  can be approximately calculated using

$$\sin(\Delta\theta/2) = \frac{|\Delta\vec{p}_{\text{kick}}|}{2|\vec{p}|}, \quad (4.12)$$

with  $|\vec{p}_{in}| = |\vec{p}_{out}| = |\vec{p}|$ . In the following, three relevant procedures for the momentum reconstruction used in the HADES Au+Au analyses are explained:

- **Kick-plane method**

The deflection angle is deduced using the inner segment of the track and the straight connection of its interception point on the virtual kick plane with a hit in the META detector. With Equation (4.12) and the momentum kick calculated with Equation (4.11), one gets an absolute value of the momentum. For given  $\Delta\theta$  and  $\vec{p}_{\text{kick}}$ , the values of the particles momentum are stored in a look-up table in the HADES detector simulation software HGevent. For more details see [63].

## 4. Analysis

---

- **Spline method**

For increasing the momentum resolution the equation of motion is solved using a spline method on several points between MDC II and III using the well known (by Hall probe measurements) magnetic field in each point (denoted as orange dots in Figure 4.12). This method (as well as the kick plane method) neglects the influence of the magnetic field inside the inner and outer segments and still uses the approximation of straight track segments. This is not exact and leads especially for low momenta to significant uncertainties in the reconstructed momenta. Further details are discussed in [63].

- **Runge-Kutta method**

The solution of the spline method is used as input for an iterative numerical Runge-Kutta procedure. The equation of motion is solved taking into account the magnetic field over the whole track distance. The trajectory recursively determined in a first step is fitted in a second step to the measured hit points. This procedure is iterated up to eleven times and the finally provided quality parameter  $\chi_{\text{RK}}^2$  can be used for selecting tracks with best momentum reconstruction. The Runge-Kutta method provides a better treatment of effects like curly tracks, deflection of tracks close to the coils of the magnet, and energy-loss of the particles passing through. The momentum obtained from this method has a resolution of up to 1 %. For more details see again [63].

### 4.2.3 TOF/RPC-META matching

The particle trajectory deduced by the Runge-Kutta method is extrapolated to the META detector plane. The distance between the interception point and a nearby real META hit is parametrised in absolute  $xy$ -coordinates by  $dx$  and  $dy$  and the quality parameter is given by

$$\chi_{\text{MM}} = \sqrt{\frac{dx^2}{\sigma_x^2} + \frac{dy^2}{\sigma_y^2}}, \quad (4.13)$$

with the associated uncertainties  $\sigma_x$  and  $\sigma_y$ . A more detailed description can be found in [64].

### 4.2.4 Identification using time-of-flight

The momentum  $p$  of the charged particles has been determined by the curvature of their tracks in the magnetic field. The orientation of the magnetic field is such that positively charged particles are deviated in direction of the beam axis while negatively charged particles are deviated away from it.

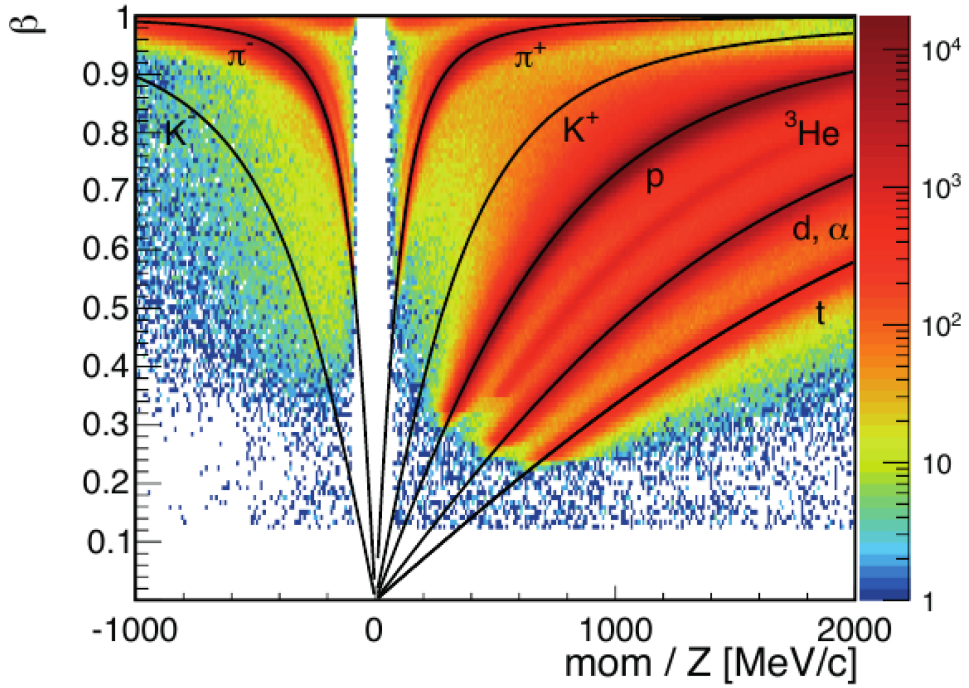


**Figure 4.13:** Scatter plot of particle velocities  $\beta$  in dependence of the rigidity  $mom / Z$  [MeV/c]. Black curves show the theoretical loci of several particle species calculated with Equation (4.17). Figure taken from [64].

Hence, the polarity  $q$  of the particles is also known. Combining this information with the time-of-flight measurement the species of the particle can be identified. The time-of-flight is given by

$$\Delta t = t_{\text{META}} - t_{\text{START}}, \quad (4.14)$$

where  $t_{\text{META}}$  is the time signal from the META detectors and  $t_{\text{START}}$  the time signal from the START detector. Together with the track distance  $s$ , which is the length of the reconstructed track derived from the Runge-Kutta procedure, the velocity of the particle can be calculated:

$$\beta = \frac{v}{c} = \frac{s}{c\Delta t}. \quad (4.15)$$

The mass of the particle can then be determined by using

$$m/q = \frac{p/q}{\beta\gamma c}, \quad (4.16)$$

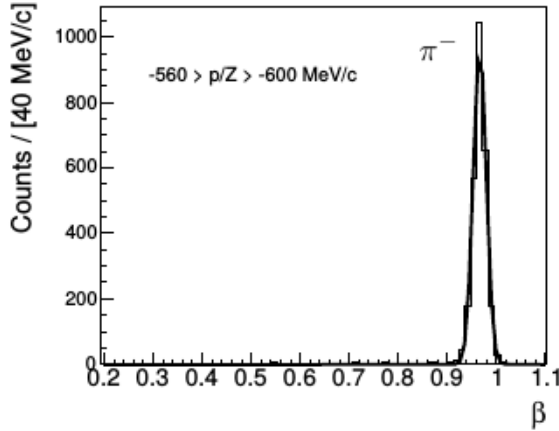


**Figure 4.14:** Slice in rigidity  $p/Z$  of Figure 4.13. The  $\pi^-$  distribution is fitted by a Gaussian distribution. Its mean value follows with high precision the calculated value from Equation (4.17). Figure taken from [64].

with the Lorentz-factor  $\gamma = 1/(1 - \beta^2)^{\frac{1}{2}}$ . In Figure 4.13 the correlation between velocity  $\beta$  and the rigidity  $p/Z$  of the particles is plotted. Transforming Equation (4.16) and setting  $c = 1$  yields

$$\beta^2 = \frac{1}{\left(\frac{m/q}{p/q}\right)^2 + 1}. \quad (4.17)$$

Using Equation (4.17) theoretical dependencies of several particles can be added in Figure 4.13, denoted by the labeled black curves. For the pions dependence the mass  $m_{\pi^\pm} = 139.57 \text{ MeV}$  [68] is taken as input in Equation (4.16). The distribution in Figure 4.13 is sliced into narrow bins in  $p/Z$  and the pion velocity-distributions are fitted with a Gaussian distribution, depicted exemplarily in Figure 4.14. The mean of this distributions matches with high accuracy with the calculated values from Equation (4.16). For each slice a  $3\sigma$  cut is applied according to this Gaussian distribution and the particles inside this selected area are the identified pions for the ongoing analysis.

#### 4.2.5 Single particle selection

As minimal conditions on the single particle tracks of the pions the following selections are applied:

- $0 < \chi_{\text{inner}}^2$ ,
- $0 < \chi_{\text{outer}}^2$ ,

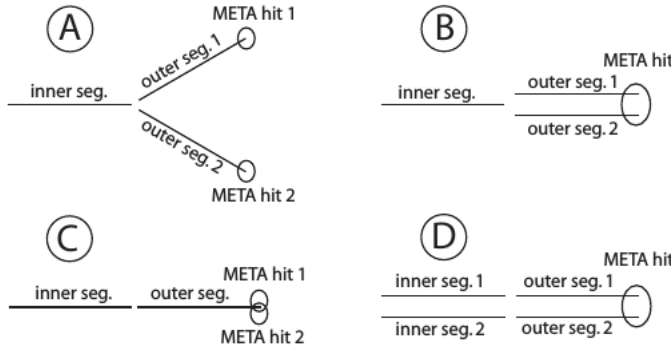


**Figure 4.15:** Possibilities for track candidates sharing same detector hits. One found inner segment can be matched to two different outer segments with two different META hits (A) or even the same META hit (B). The combination of one inner and one outer segment can have two different META hits (C) or, the other way around, two inner segments matched to separately two outer segments share the same META hit (D). Figure taken from [82].

- $0 < \chi_{RK}^2 < 1000$ ,
- $0 < \chi_{MM}^2 < 20$ .

Furthermore, only pions with unique detector hits are allowed, i.e. no combination of two pion tracks is allowed to share either the same inner or outer segment or the same META hit. The forbidden constellations are depicted in Figure 4.15 (in the next section, an even more strict condition will be defined). Unfortunately, the drift chambers in sector 2 did not work stably during the whole beam time. Mainly only on one day all MDCs worked stably and data with six active sectors is available. For all other days mostly five sectors delivered stable data output. Mixing together data from five sectors and six sectors with different acceptance and efficiency, respectively, would lead to biased distributions. Therefore, one has to decide either to take the data with all six active sectors only or the data with one sector less. Since for the aim of investigating correlation functions the total yield of the pions and the related efficiencies are not existential (the total yield cancels when considering the combinatorial background within the same acceptance and efficiency, compare Equation (2.9)), it was decided to take the data of all beam time days, but remove all tracks from sector 2. In Figure 4.16 the phase-space distribution in transverse mass  $m_t$  less rest mass  $m_0$  and rapidity  $y - y_{cm}$  of the selected negative pions (upper panel) and positive pions (lower panel) is shown. The dashed black curves give the corresponding polar angles in the laboratory system. Next to the HADES angular acceptance limits a clear shift between the reconstructed  $\pi^+$  and  $\pi^-$  spectrum is

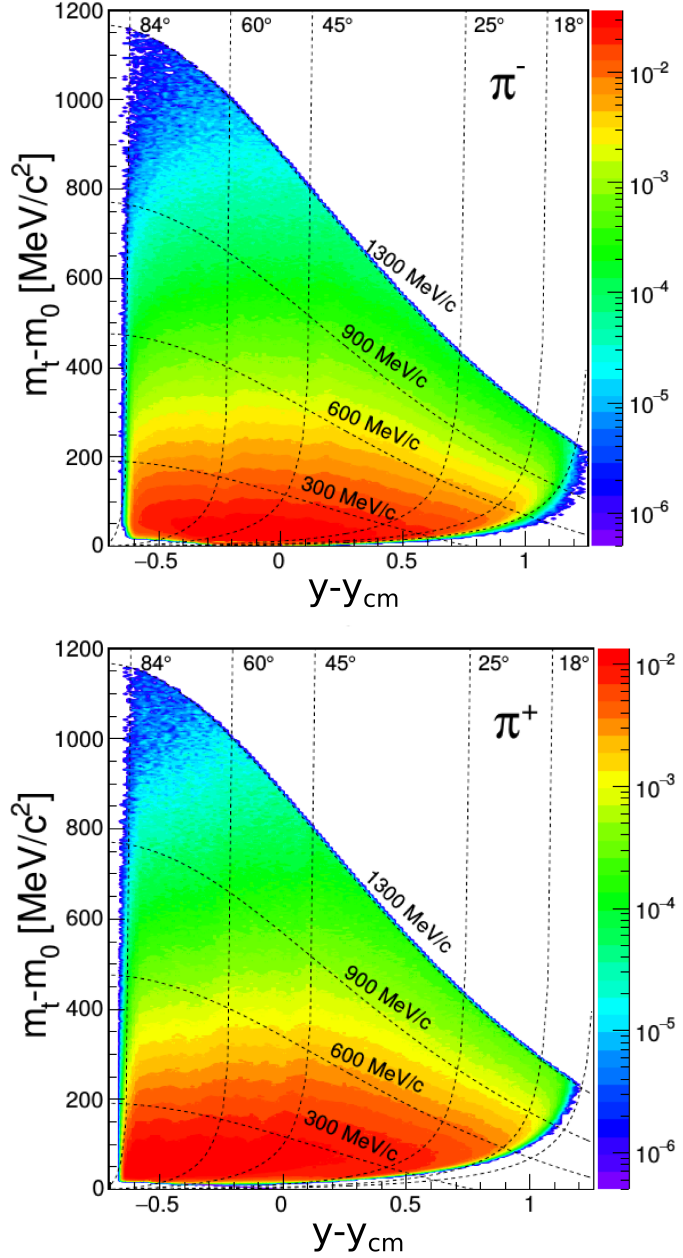


**Figure 4.16:** Phase-space distribution in reduced transverse mass  $m_t - m_0$  and rapidity  $y$  relative to mid-rapidity,  $y_{cm} = 0.74$ , of negative (upper panel) and positive (lower panel) pions measured with HADES and summed over all selected events. Dashed black curves are the corresponding polar angles in the laboratory system, gray dashed curves represent the total momentum of the pions. Figure taken from [83].

visible, due to the opposite curvature in the magnetic field. Contrary to the restriction on pion momentum  $p \leq 1300 \text{ MeV}/c$  applied in Figure 4.16, in the present investigation no upper momentum cut was set.

The total number of measured  $\pi^-$  mesons is by around a factor 1.86 larger than the number of measured  $\pi^+$ . The main reason is the initial  $\pi^+/\pi^-$  ratio governed by the isospin ratio, i.e. the ratio between protons and neutrons in the target and projectile nuclei, and the possible pion production processes. Since at beam energies around 1A GeV pions are mainly produced via  $\Delta$  resonances ( $\Delta^-, \Delta^0, \Delta^+, \Delta^{++}$ ), one has to consider all possible branching ratios with respect to the initial proton-to-neutron ratio of 79/118. In addition, the different cross sections of  $nn$ ,  $np$  and  $pp$  contribute. The expected value of the initial charge-sign pion ratio is calculated, e.g. in [84], with 1.85 by skipping the  $\Delta$  resonances, but taking directly the nucleon-nucleon cross sections for pion production from [85]. These values can deviate from the true ones due to higher order effects. An example is the so called neutron skin effect [86], a non-homogeneous proton-neutron distribution with a proton depletion near the surface caused by neutron balance and Pauli blocking. But also the contribution from other sub-threshold pion production processes can lead to deviations from the predicted number.

Another possible reason for the charge-sign difference of the yields of identified pions is the acceptance and efficiency of the spectrometer, which differs for each particle species. Since positive particles are deflected by the magnetic field into direction of the beam axis,  $\pi^+$  at low values of transverse momentum smaller than about  $100 \text{ MeV}/c$  are outside the region covered by the mini drift chambers. Contrary, negatively charged particles are deflected away from the beam axis and  $\pi^-$  with transverse momenta down to  $50 \text{ MeV}/c$  at mid-rapidity are still inside the acceptance of the spectrometer. This effect is clearly visible in Figure 4.16, when one compares the color map of the pion yields with the dashed black curves representing the polar angles in the laboratory frame. The opposite effect is visible at large polar angles, where positive pions beyond  $84^\circ$  are captured, but not negative pions, and equivalently near  $45^\circ$  visible at high pion momenta.

A full acceptance and efficiency corrected pion analysis of the present experiment was performed in [83], providing a normalised ratio of  $1.83 \pm 0.17$ .

## 4.3 Experimental correlation function

### 4.3.1 Construction

Generally, the two-particle correlation function is defined as the ratio of the probability  $P_2(\vec{p}_1, \vec{p}_2)$  to measure simultaneously two particles with momenta

## 4. Analysis

---

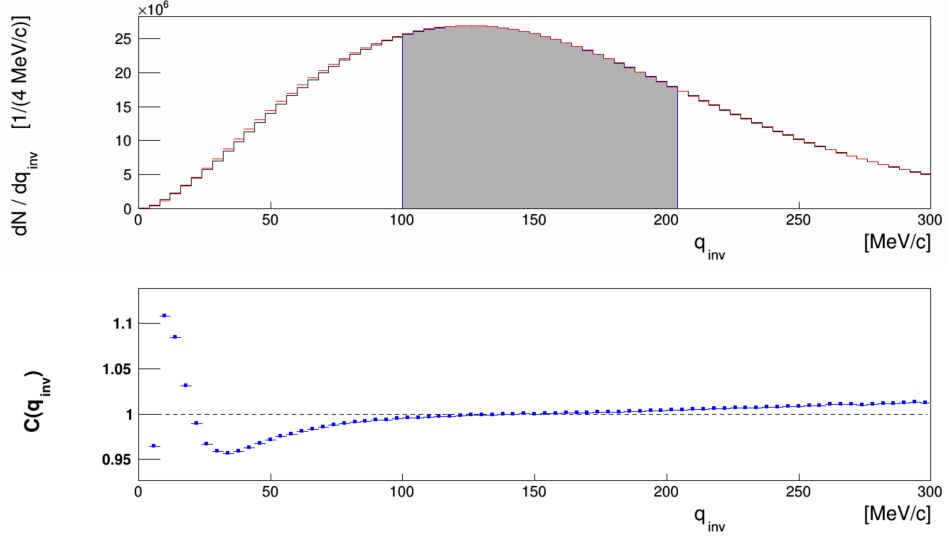


**Figure 4.17:** Upper panel: true distribution (black) and mixed distribution (red) of negatively charged pion pairs as function of the invariant relative momentum  $q_{\text{inv}}$  for centrality 0-5%. The gray shaded region indicates the range used for normalisation. Lower panel: Corresponding invariant correlation function, Equation (4.20), without further corrections.

$\vec{p}_1$  and  $\vec{p}_2$  and the product of the corresponding single-particle probabilities  $P_1(\vec{p}_1)$  and  $P_1(\vec{p}_2)$  [3],

$$C(\vec{p}_1, \vec{p}_2) = \frac{P_2(\vec{p}_1, \vec{p}_2)}{P_1(\vec{p}_1)P_1(\vec{p}_2)}, \quad (4.18)$$

already introduced above in Equation (2.8). Experimentally, the correlated numerator of Equation (4.18) is formed by the distribution of all pairs of particles coming from the same event,  $A(\vec{q})$ , as function of the relative momentum<sup>3</sup>,  $\vec{q} = (\vec{p}_1 - \vec{p}_2)/2$ . The denominator is formed constructing a combinatorial background using the method of event mixing, which was introduced first in [9]. Particles from different events are used to form the distribution  $B(\vec{q})$  of uncorrelated pairs having the same average phase-space distribution like the distribution of correlated pairs. Having high event statistics this mixed distribution can be filled with a much larger number of pairs than the true distribution to make its contribution to the statistical uncertainty negligible. For that reason a normalisation constant  $\mathcal{N}$  has to

---

<sup>3</sup>Note that this definition for the relative momentum is often used in elementary collisions, see e.g. [87], but investigating heavy-ion collisions usually  $\vec{q}' = \vec{p}_1 - \vec{p}_2 = 2\vec{q}$  is used, e.g. in [17]

### 4.3 Experimental correlation function

---

be introduced, and finally the experimental two-particle correlation function reads

$$C(q_{\text{out}}, q_{\text{side}}, q_{\text{long}}) = \mathcal{N} \frac{A(q_{\text{out}}, q_{\text{side}}, q_{\text{long}})}{B(q_{\text{out}}, q_{\text{side}}, q_{\text{long}})}. \quad (4.19)$$

The three-dimensional relative momentum is decomposed into components  $q_{\text{out}}$ ,  $q_{\text{side}}$  and  $q_{\text{long}}$  using the Bertsch-Pratt parametrisation, introduced in Section 2.4.2. The normalisation constant is fixed by the requirement  $C \rightarrow 1$  at large values of  $|\vec{q}|$  [88], where the correlation function is expected to flatten out at unity. Analogously to Equation (4.19), the experimental one-dimensional correlation function

$$C(q_{\text{inv}}) = \mathcal{N} \frac{A(q_{\text{inv}})}{B(q_{\text{inv}})}, \quad (4.20)$$

is generated by projecting Equation (4.18) onto the Lorentz-invariant relative momentum,

$$q_{\text{inv}} = \frac{1}{2} \sqrt{(\vec{p}_1 - \vec{p}_2)^2 - (E_1 - E_2)^2}, \quad (4.21)$$

with  $E_i = \sqrt{p_i^2 + m_i^2}$  and  $m_i$  ( $i = 1, 2$ ) are the total energies and the rest masses of the particles forming the pair, respectively. An example for the true two-particle distribution, the normalised mixed distribution and the correlation as function of the invariant relative momentum is plotted in Figure 4.17. Furthermore, one-dimensional projections of Equation (4.19) are constructed by projecting  $A(q_{\text{out}}, q_{\text{side}}, q_{\text{long}})$  and  $B(q_{\text{out}}, q_{\text{side}}, q_{\text{long}})$  onto one of the components  $q_{\text{out}}$ ,  $q_{\text{side}}$  or  $q_{\text{long}}$  and integrating over the other two directions within chosen limits:

$$C_{\text{proj}}(q_i) = \mathcal{N} \frac{\left[ \int_{q_{j,\text{min}}}^{q_{j,\text{max}}} \int_{q_{k,\text{min}}}^{q_{k,\text{max}}} A(q_{\text{out}}, q_{\text{side}}, q_{\text{long}}) \right]}{\left[ \int_{q_{j,\text{min}}}^{q_{j,\text{max}}} \int_{q_{k,\text{min}}}^{q_{k,\text{max}}} B(q_{\text{out}}, q_{\text{side}}, q_{\text{long}}) \right]}, \quad i, j, k = \{\text{out}, \text{side}, \text{long}\}. \quad (4.22)$$

Analogously, two-dimensional projections can be constructed, integrating only over one component of  $q_{\text{out}}$ ,  $q_{\text{side}}$  and  $q_{\text{long}}$ :

$$C_{\text{proj}}(q_i, q_j) = \mathcal{N} \frac{\left[ \int_{q_{k,\text{min}}}^{q_{k,\text{max}}} A(q_{\text{out}}, q_{\text{side}}, q_{\text{long}}) \right]}{\left[ \int_{q_{k,\text{min}}}^{q_{k,\text{max}}} B(q_{\text{out}}, q_{\text{side}}, q_{\text{long}}) \right]}, \quad i, j, k = \{\text{out}, \text{side}, \text{long}\}. \quad (4.23)$$

Worth to mention is that performing one- or two-dimensional projections by integrating just the correlation function (4.19) itself over the desired  $\vec{q}$

sub-range leads to incorrect values. But Equations (4.22) and (4.23) provide the exact way to do it (as also stated in appendix of [89]).

### 4.3.2 Pair selection

To fill the true distributions  $A(\vec{q})$  introduced in the previous section, the particles identified in Section 4.2.5 have to be paired. For all selected events of Section 4.1.5, a list of identified pions is created, separately for  $\pi^-$  and  $\pi^+$ . Then the pions in that list are paired with each other pion of the list and the pairs are stored in another list regarding not to collect pairs with contribution of the same tracks more than once. When all pairs within one event are collected, the next event follows and finally all true pairs are well arranged event-by-event. The pairs are stored with all necessary event and single particle track information for the subsequent analysis. Then the list of pairs is looped, where the relative momenta are calculated both, the invariantly and in the longitudinal co-moving system (LCMS), and filled in histograms, one-dimensional for the invariant distribution and three-dimensional for the LCMS frame using the coordinates  $q_{\text{out}}$ ,  $q_{\text{side}}$  and  $q_{\text{long}}$  as mentioned in the previous section. Moreover, the values of pair transverse momentum  $p_{t,12} = |\vec{p}_{t,1} + \vec{p}_{t,2}|$ , pair rapidity  $y_{12}$  and pair azimuthal angle relative to the event plane  $\Phi = \phi_{12} - \phi_{\text{EP}}$  are calculated, and for individually chosen intervals of them separate histograms are used. Later in the analysis a few histograms can be combined (e.g. all histograms of different values  $\Phi$  in the azimuthally integrated analysis, choosing a smaller or larger rapidity interval in  $y_{12}$ , etc.). In the present analysis, the intervals of pair transverse momentum have been explicitly chosen with a width of  $100 \text{ MeV}/c$  starting at  $0 \text{ MeV}/c$ . For  $\Phi$  eight equidistant intervals have been chosen with a width of  $45^\circ$ , where the first interval is located symmetrically around  $0^\circ$ . The pair rapidity is binned in intervals of 0.1, where the central one is located symmetrically around mid-rapidity  $y_{\text{cm}} = 0.74$ . The same differential treatment as on level of the histograms is done for the different centrality classes defined in Tables 4.1 and 4.2.

When calculating the relative momentum and decomposing into a chosen coordinate system (here:  $q_{\text{out}}$ ,  $q_{\text{side}}$ ,  $q_{\text{long}}$ ) one has to take into account the permutability of particles 1 and 2, i.e. the freedom of choosing the sign of  $\vec{q}$ . It allows to restrict the three-dimensional coordinate space to either the negative or the positive hemisphere of one explicit coordinate and rotate/mirror the  $q$ -vectors of the other hemisphere into the chosen one. Since the single particle tracks follow an implicit arrangement (due to the regularities applied in the DAQ, storing-algorithm in the DSTs or sorting after the tracking sector wise, etc.), they are not randomly listed. Hence the mentioned freedom is less a possibility, but more a necessity to avoid a biased pair distribution, see Figure 4.18 for illustration.

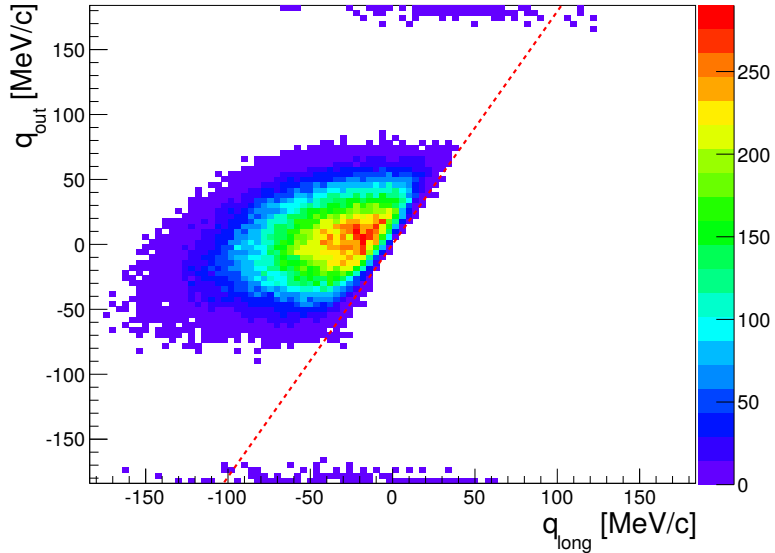


**Figure 4.18:**  $\pi^+\pi^+$  pair distribution from UrQMD as a function of  $q_{\text{out}}$  and  $q_{\text{long}}$  for small values of  $q_{\text{side}} < 10 \text{ MeV}/c$ , ignoring the permutability of particles 1 and 2. The red dashed line depicts the edge of the hemisphere with most of the entries. Data shown for exemplary chosen pair transverse momentum range of 200 to 300  $\text{MeV}/c$  and events within the centrality class 0-10 %.

### 4.3.3 Mixing

The combinatorial background is formed by taking pair-wise pions from different events. In this manner, it is excluded that the two particles are directly correlated to each other by quantum-statistical effects or the fundamental forces. A pointer moves through the list of all pairs with a constant step size controlled by a parameter  $i_{\text{step}}$  and collects all pairs along this way in a new array. Then all pions from the pairs of this new array are combined with each other forming the total sample of mixed pairs, wherein never two pions from the same event are combined. The parameter  $i_{\text{step}}$  is used to guarantee that in each phase space region at least ten times more mixed pairs are generated than true pairs are available. Thus the contribution of the combinatorial background to the statistical uncertainties is less than 5 %. Further,  $i_{\text{step}}$  is always chosen high enough to make sure that at maximum only one pair per event contributes to the event mixing. Even if the pions within the same event are not allowed to be combined, too large samples from one event can also bias the final distribution. Typical values of  $i_{\text{step}}$  are 150-200 for the most central events and 50-80 for the most peripheral

## 4. Analysis

---

ones. These numbers are reasonable, since the number of pairs scales with  $n(n - 1)/2$ , and the typical number  $n$  of pions per event is less than 10. However, one also has to take into account the different implicit single pion distribution event by event:

- different charged-particle multiplicities  $N_{\text{ch}}$ , directly correlated with the total pion production, belong to different impact parameters or fluctuations in the initial nucleonic state,
- different event-plane angles  $\phi_{\text{EP}}$  change the pion distributions in the detector-fixed coordinate system due to the collective motion modes of the pions, quantified, e.g., by elliptic flow,
- varying the primary event vertex in longitudinal, but also transverse direction, leads to slight differences in the angular distributions of acceptance and detecting efficiency of the pions.

The mentioned influences might change the shape of the distribution of all mixed pairs compared to the distribution of the true pairs and therefore disturb the baseline of the correlation function expected at unity. For that reason a couple of restrictions is applied to the mixed pairs:

- $|N_{\text{ch},1} - N_{\text{ch},2}| < 10$ ,
- $|\phi_{\text{EP},1} - \phi_{\text{EP},2}| < 30^\circ$  in the azimuthally integrated analysis, and  $|\phi_{\text{EP},1} - \phi_{\text{EP},2}| < 10^\circ$  for the analysis with azimuthal angle sensitivity,
- $|z_{\text{prim},1} - z_{\text{prim},2}| < 1.2 \text{ mm}$ ,

where the indices 1 and 2 refer to the different events the two pions belong to. Since the data set is already divided into classes of centrality, the cut on the difference of the charged particle multiplicities  $N_{\text{ch}}$  is of minor impact. More important is the cut on the reaction plane angle, which can be chosen coarse for azimuthally integrated central events, where the event plane resolution is quite low. But especially for peripheral events in the azimuthally dependent analysis, the difference should be low enough to keep additional uncertainties small. The cut on the primary vertex in  $z$  direction is especially important when considering inefficiencies due to the detector geometry. Details of that issue will be part of the next section. A cut on the transverse localisation of the primary vertex can be added, but turned out not that significant as the other selections. Finally, the cuts can not be set arbitrarily narrow, since the mixing statistics is limited at some point.

### 4.3.4 Accounting for non-physical correlations

Besides the Bose-Einstein (wave function symmetrisation) effect and final-state interactions related to strong and electromagnetic forces, introduced

in Section 2.3.1, further correlations are possibly observed, and one has to clarify either if they have a physical origin or if they appear only for technical reasons. A prominent candidate for physical long-range correlations, i.e. visible at larger values of  $|\vec{q}|$ , are global conservation laws [90]. The relative-momentum dependent spectrum of two particles is influenced by the total number of degrees of freedom of the initial  $N$  particle system. This effect becomes important in small systems, like  $p + p$  or  $e + e$ , but is negligible in symmetric heavy-ion collisions with gold or lead nuclei. More interesting are non-physical correlations emerging from an unappropriate treatment of the detector signals. These correlations may enter the correlation function at very low values of  $|\vec{q}|$  and disturb the quantum-statistical signal. Therefore such effects have to be removed.

Acceptance and efficiency losses are included in both, the true pair distributions and the mixed ones. However, there are losses of particle tracks caused by the presence of a secondary particles due to dead time of the detectors or just signal generations in one detector segment, which can not clearly be assigned to the one or the other or to both particle tracks. The probability of such losses depends on the localisation and the direction of the tracks inside the spectrometer. This effect increases with the total particle multiplicity and still applies to both, true and mixed distribution, but it becomes crucial, if it is related to the considered pair. In this case, pairs from the same event are affected, but mixed pairs are not, since the particles of them are temporally displaced. These losses are related to pairs with lower relative momenta and smaller opening angles in the laboratory system, therefore these problems are also known as close-track effects or close-track deficits. Their strength and range in the  $q$ -spectrum depend highly on the structure of the spectrometer. Therefore, different methods are used in different experiments to account for close-track effects. In the following, the important steps for their successful treatment are discussed.

### UrQMD Simulation data

The close-track deficit appears at low values of  $|\vec{q}|$  or  $q_{\text{inv}}$ , respectively, which is the same region where the quantum-statistical correlations and the final-state interactions are expected. For that reason, the simulated UrQMD data is useful, since it was tracked through the realistic detector simulation HGEANT and should therefore contain also the detector effects. On the other hand, the UrQMD simulations do not include final-state interactions and Bose-Einstein correlations, as mentioned in Section 3.7. The simulations are assumed therefore to act as a good indicator for the close-track effects. In the middle panel of Figure 4.19, the invariant correlation function is plotted (open red symbols) for a sample of the 5 % most central events. It matches the experimental correlation function at relative momenta above 50 MeV/ $c$ . For decreasing  $q_{\text{inv}}$ , the correlation function is steadily decreasing,

## 4. Analysis

---

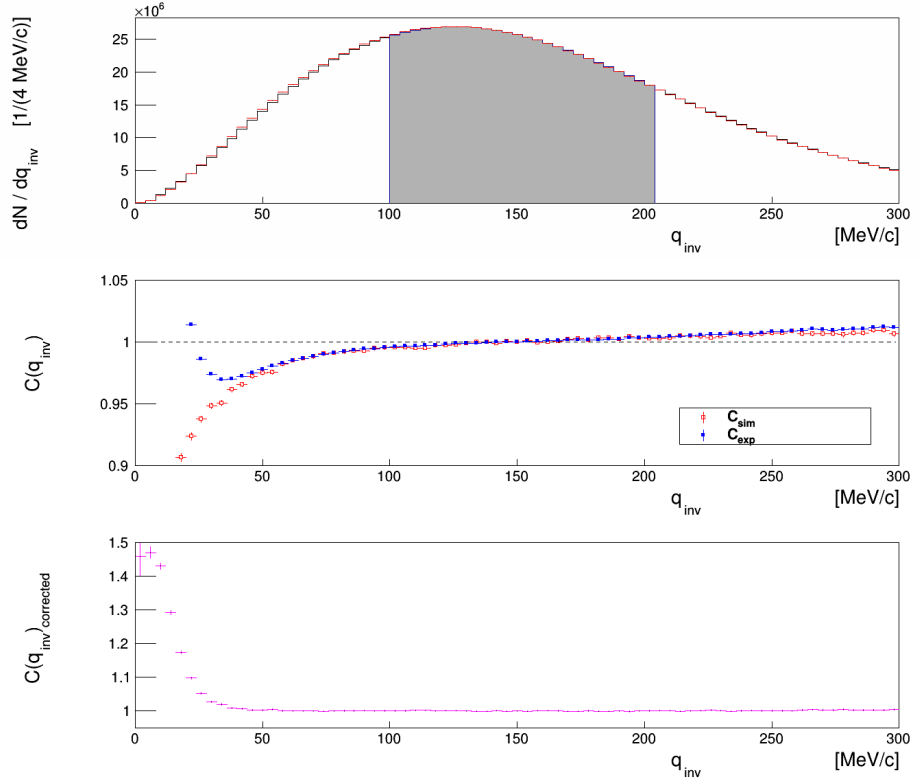


**Figure 4.19:** Top: Same as Figure 4.17, but for another data sample. Middle: Corresponding invariant correlation function (4.20) for experimental data (blue) and UrQMD+HGEANT simulation data (red). Bottom: Experimental correlation function divided by the simulated correlation function, yielding the so-called double-ratio correlation function. The physical correlations not included in the simulations remain at low values of  $q_{\text{inv}}$ .

as expected, since smaller relative momenta are correlated to smaller opening angles of the pairs, implying a higher probability of hitting the same sub-detector cells and reducing the two-track resolution.

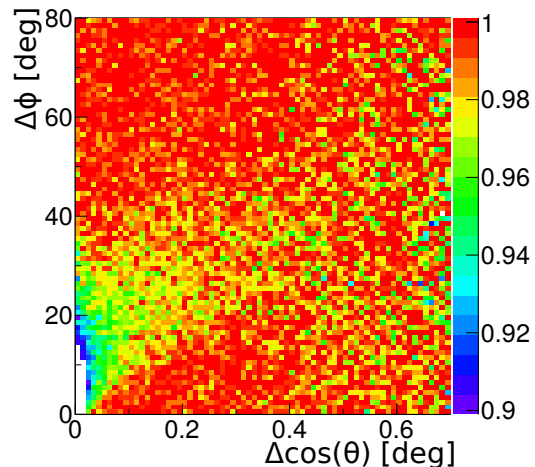
### Double-ratio method

The most simple way to account for these close-track deficits is to divide the experimental correlation function by the simulated one. The deficits caused by the finite efficiency and resolution of the detector are removed. Also the correction for finite momentum resolution is included (discussed more in detail in Section 4.4.2), since it enters both, the measured and the simulated particle distributions. Only the wanted physical correlations, namely the Bose-Einstein correlations and final-state interactions, remain

at low relative momenta, as shown in the lower panel of Figure 4.19. This procedure is called the double-ratio (DR) method and has been used, e.g. in [91]. However, the accuracy of the DR method is based on the assumption that the used simulation describes the experimental data precisely, especially at low relative momenta. Unfortunately, the sample of achievable simulated data in the present analysis was always less than the experimental data by a factor of about 20, which implicates that the statistical error of the final correlation function (and further derived quantities) is determined by the statistical uncertainty of the simulations. Following the error propagation of Poissonian distributions this ends up in an enhancement of the statistical uncertainty of the experimental DR correlation function by a factor of about 4.6.

### Opening-angle selection

**Figure 4.20:** Correlation function equivalent to Equations (4.19) and (4.20), but as function of the angle differences  $\Delta\phi$  and  $\Delta\cos(\theta)$  for UrQMD+HGeant simulation data.



Instead of using the double-ratio method for correcting the close-track deficits at low values of  $q_{\text{inv}}$  one can try to identify the properties of the paired pions which repeatedly show a bad resolution. Then one can extract them out of both the true and the mixed distribution to restore the baseline of the correlation function at unity.

The relative momentum of a pair is correlated to the opening angle between the two pions. Assuming the deficits origin from sub-detector inefficiencies, they should appear more frequently the closer the pair tracks are to each other in local position space. Therefore, the suppressed pair distribution at low values of  $q_{\text{inv}}$  compared to the mixed distribution should be visible also in the opening-angle dependent correlation function. Figure 4.20 displays the correlation function for  $\pi^-\pi^-$  pairs of the simulated data in dependence of

## 4. Analysis

---

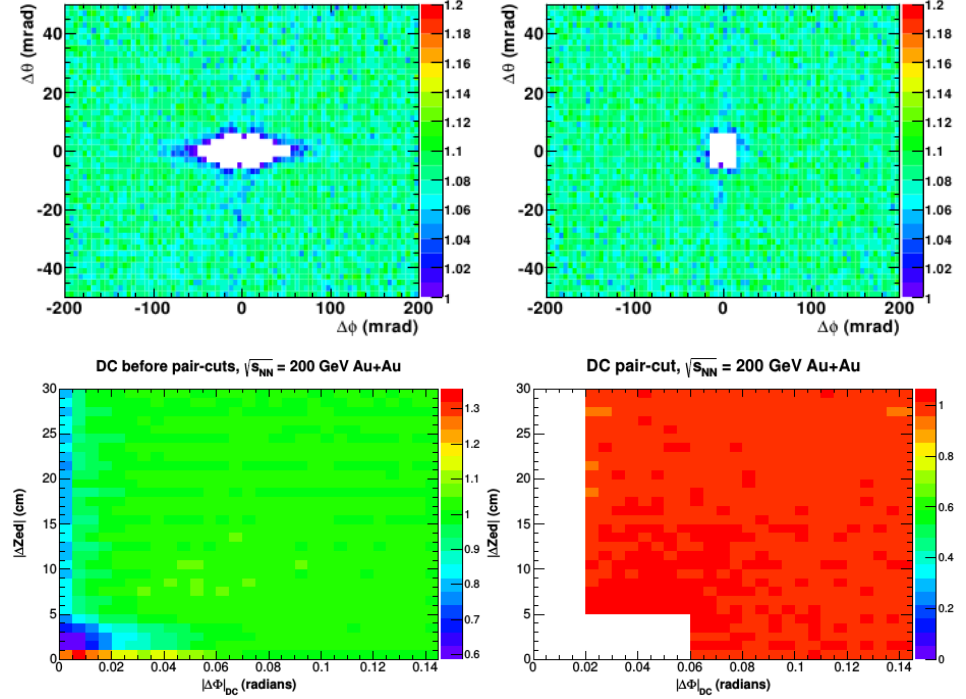


**Figure 4.21:** Examples for opening angle distributions of the correlation function from CERES [92] (top panels) and PHENIX [93] (bottom panels). For details see the text.

the angular difference between the pions in azimuthal direction (ordinate) and polar direction (abscissa), given by  $\Delta\phi = |\phi_1 - \phi_2|$  and  $\Delta\cos(\theta) = |\cos(\theta_1) - \cos(\theta_2)|$ . The correlation function is equal to one within statistical fluctuations over a wide range in  $\Delta\phi$  and  $\Delta\cos(\theta)$ . However, for small values of the angular differences a decrease of the correlation function below unity is visible. The reduction becomes stronger the smaller the angular differences are.

Similar investigations are done in HBT investigations of other experiments, e.g. at PHENIX [93] or CERES [92]. The first one is a collider experiment containing a cylindrically shaped time projecting chamber (TPC) as one main component for the particle identification. Therefore, cylindrical coordinates are more convenient, and instead of  $\Delta\cos(\theta)$  the difference in beam direction  $\Delta z$  is considered. The second one is also TPC based, but as it is a fixed target experiment, spherical coordinates are useful as well. However, in both examples it can be well distinguished between the 'good' area, where the correlation vanishes, and a 'bad' region, where a reduction in pairs resolvability is settled. By applying simple rectangle-shaped selection criteria the pair distributions are efficiently cleaned, cf. Figure 4.21. For

the present HADES data, this is not the case. Comparing with Figure 4.20, there is a region around  $\Delta \cos(\theta) < 0.05$  and  $\Delta\phi < 30^\circ$ , where larger reductions are visible. But besides this region there is a bigger triangle-shaped region with smaller, but still clearly visible deficits, separated from the region of unity by a virtual line between  $(0, 0^\circ)$  and  $(0.4, 40^\circ)$  in coordinates of  $(\Delta \cos(\theta), \Delta\phi)$ . The origin of this unusually shaped area of deficits is mainly related to the alignment within stereo angles of the MDC detectors mentioned in Section 3.3.2, which introduces a correlation between  $\Delta \cos(\theta)$  and  $\Delta\phi$  (mainly caused by the  $\pm 20^\circ$  and  $\pm 40^\circ$  wires, secondary smeared out by the merging of the considered quantities in spherical symmetry with the hexagonal symmetry of the sub-detectors). One could either apply a hard cut on the opening angles by parametrising the whole area of reductions by a triangular or trapezoidal form, or one applies only a soft cut of rectangular form choosing maximum values  $[\Delta \cos(\theta)]_{\max}$  and  $[\Delta\phi]_{\max}$ . In the first case, the part of discarded good resolved pion pairs containing the Bose-Einstein information at low relative momenta is too high. In the second case, still too many pairs enter the mixing distribution which are not resolvable within the same event and therefore disturb the correct shape of the correlation function.

### Pair topologies

**Figure 4.22:** Illustration of the considered pair topologies following [92]. Left: tracks which possibly tend to cross each other are referred as cowboys (CB). Right: tracks with increasing distance over flight time and no crossing are referred as sailors (SA).



The tracks of identical particles moving close to each other are deflected by the magnetic field nearly into the same direction. Whether the trajectories of them cross each other inside the spectrometer depends on the momentum difference and the initial emission angle at the target. Since the magnetic force acts mainly in transverse direction, the initial polar angle is of special interest. In [92] the idea has been introduced, to differentiate between two topologies of particle pairs, the one which tend to cross each other and the other one without crossing, considering an azimuthal projection on each other. The decision for selecting the one or the other is chosen accordingly to the impact of the magnetic field. Assuming the local differences

## 4. Analysis

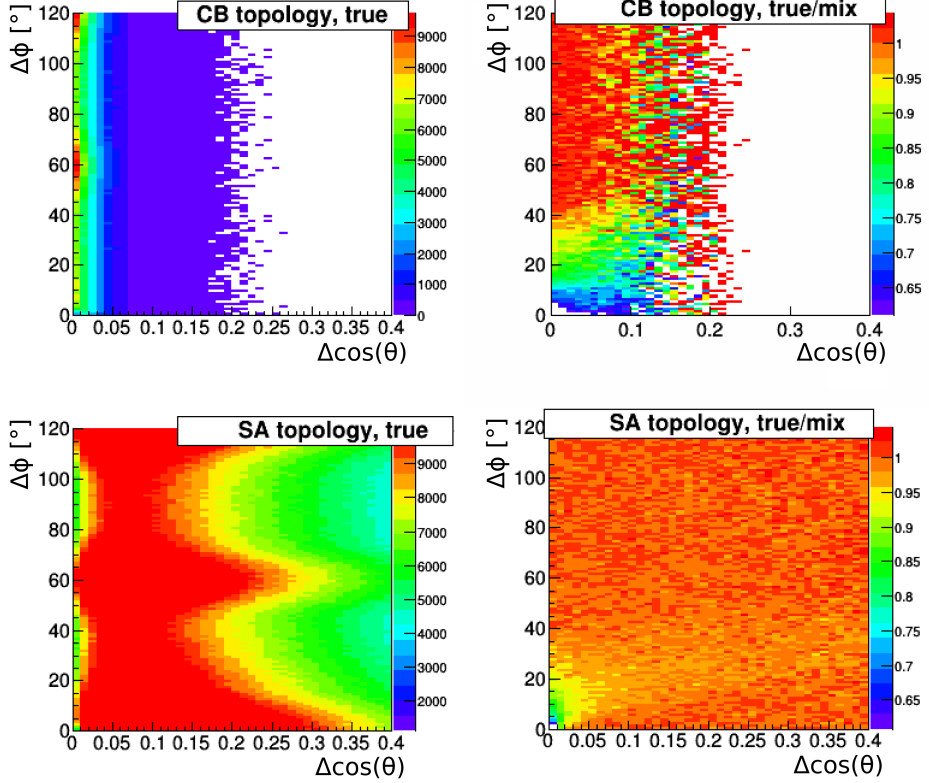


**Figure 4.23:** True pair distribution  $\frac{dN}{d\Delta\phi d\Delta\cos\theta}$  (left) and correlation function equivalent to Equations (4.19) and (4.20) (right) as a function of the opening angle differences  $\Delta\phi$  and  $\Delta\cos(\theta)$  for data from UrQMD+HGeant. Top panels represent pairs with cowboy (CB) topology, and bottom panels represent pairs with saylor (SA) topology following Equation (4.25).

of the strength of the magnetic field for particles moving closely together is very small, the faster particle “moves stiffer” through the field with smaller curvature and experiences less change of its polar angle. If a negatively charged particle with higher momentum is emitted closer to the beam axis, as compared to the other one, after passing the region of MDCs, the distance between the particles can only increase without a crossing of their trajectories. The other way around, if the particle with lower momentum is emitted closer to the beam axis, it is bent to higher final polar angle than the other one, and at some point the azimuthally projected trajectories may cross. Due to the shape of the particle tracks of the different topologies, the first one is called sailor (SA) and the latter one is called cowboy (CB)

topology, illustrated in Figure 4.22. To estimate these considerations taking into account all possible particle charges, the functional  $f_{SC}$  is defined,

$$f_{SC} = (Q_1 Q_2)(Q_2 p_2 - Q_1 p_1)(\theta_2 - \theta_1), \quad (4.24)$$

with  $Q_i$ ,  $\theta_i$  and  $p_i$  being the charge, the polar angle and the momentum of particle  $i = \{1, 2\}$ . If  $f_{SC}$  is larger than zero, the pair is assigned to the sailor topology; if  $f_{SC}$  is smaller than zero, it is considered to be in the cowboy topology. Tracks of pion pairs being considered as sailors along with Equation (4.24) are definitely not crossing each other. Contrary, the defined cowboy characteristic opens the possibility of crossing tracks. If the bending by the magnetic field changes the polar angle too less, or if the finitely sized spectrometer ends before the particle trajectories would merge each other, the pair should in principle be good resolvable. For that reason the topologies of sailors and cowboys are here defined a bit differently compared to [92], i.e. using additionally the information from the META detectors, which are the last sub-detectors in flight direction of the identified particles. The cells in both, the RPC detector and the TOF wall, are enumerated in transverse direction by an increasing number  $N^{\text{metacell}}$ . The notions of sailors and cowboys are kept and a new functional,  $f_{SC}^{\text{META}}$ , is defined,

$$f_{SC}^{\text{META}} = (N_2^{\text{metacell}} - N_1^{\text{metacell}})(\theta_2 - \theta_1), \quad (4.25)$$

defining similarly sailors if  $f_{SC}^{\text{META}}$  is larger than zero and cowboys if  $f_{SC}^{\text{META}}$  is smaller than zero. Figure 4.23 (right) shows the correlation function similarly to Figure 4.20, but split into the CB topology (top) and the SA topology (bottom), using the definition given by Equation (4.25). In addition, the left panels show the total true particle distributions as a function of  $\Delta \cos(\theta)$  and  $\Delta \phi$ . As expected, the CB pairs are located at small values of  $\Delta \cos(\theta)$ , since the bending power of the magnet is limited. Looking at the left panels one can clearly see the larger deficits for the CB topology at  $\Delta \phi$  smaller than  $40^\circ$  compared to the SA topology. However, for the sailor pairs still the triangular or trapezoidal shaped region of smaller reduction described in the last section is visible. This is not astonishing, since it was related to the alignment of the MDC detectors and, within the present consideration of pair topologies, no further restriction concerning the drift chambers has been applied. Finally, keeping only the sailor pairs and discarding the cowboy pairs would improve the quality of the correlation function with reasonably low loss of correlated pairs at low  $q_{\text{inv}}$ , but the remaining shortcomings are still significantly disturbing the correlation function, comparable to the effects mentioned above in the paragraph before.

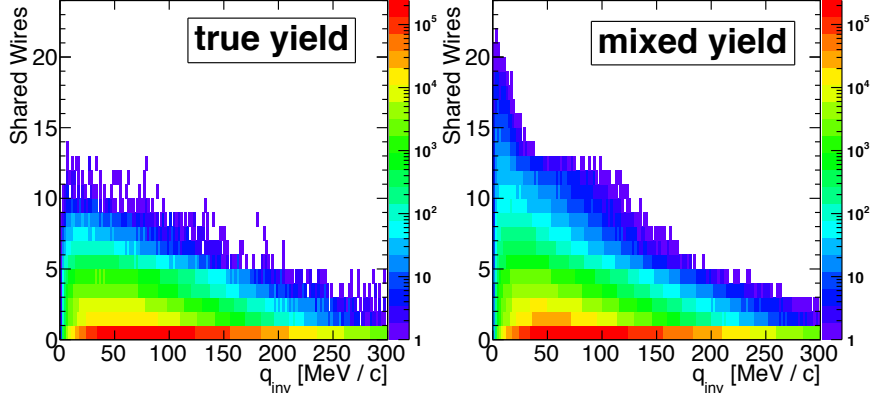


**Figure 4.24:** True (left) and mixed (right) pair distribution  $\frac{dN}{dN_{\text{wires}}^{\text{shared}} dq_{\text{inv}}}$  in dependence of  $q_{\text{inv}}$  and number of shared wires  $N_{\text{wires}}^{\text{shared}}$ , cf. text.

### Low-level data-driven pair cut

With the above findings, an investigation on the level of MDC wire layers seems to be inevitable. For that reason, for each particle per pair the hits in the 24 MDC layers (four planes and six layers per plane) are explicitly considered and compared to the hits of the partner track. A hit is counted if a fired wire in the corresponding layer contributes to the reconstruction of the particles track. The wires are sorted with consecutive numbers in transverse direction of their stereo angles.

Now it is checked layer-by-layer whether both tracks of a pair have hits belonging to the same wire. The total number of layers where this is the case is stored as number of shared wires  $N_{\text{wires}}^{\text{shared}}$ . Figure 4.24 displays the distribution over  $q_{\text{inv}}$  and  $N_{\text{wires}}^{\text{shared}}$  for true pairs (left) and for mixed pairs (right). Both distributions are most distinctive at smallest values of  $N_{\text{wires}}^{\text{shared}}$ , cp. the blue regions. While both distributions look very similar for relative momenta larger than  $150 \text{ MeV}/c$ , clear differences at smaller values are visible. Sharing too many wires at small relative momenta within the same event would mean that the two tracks are not resolvable separately, but merge to one track. The influence on the correlation function is illustrated in Figure 4.25, where the correlation function as a function of  $q_{\text{inv}}$ , as given by Equation (4.20), is plotted for simulated data with different selections on  $N_{\text{wires}}^{\text{shared}}$ . The black data points are drawn without further restriction (cp. Figure 4.19), the violet and the blue data points represent pairs with at most two or one shared wires, respectively, and in red the correlation function for pairs without shared wires is drawn. The increase of  $C(q_{\text{inv}})$  at low relative momenta with decreasing number of shared wires is remarkable. Comparing the red to the black data points, around 20 % of pion pairs with  $q_{\text{inv}}$  smaller than  $40 \text{ MeV}/c$  are discarded, but 89 % of the deficits in the range of

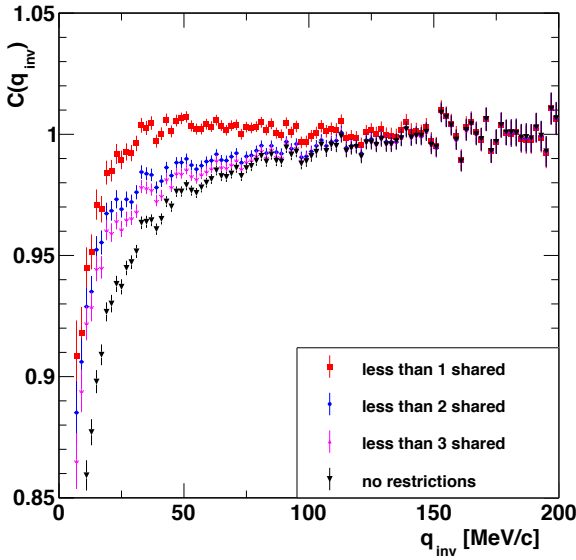


**Figure 4.25:** Correlation function (4.20) for several conditions on the number of shared wires  $N_{\text{wires}}^{\text{shared}}$ : no restriction (black), at most two (violet) or one (blue) and without shared wires (red).

10 to 100 MeV/ $c$  relative to the baseline are removed (considering the area between the data points of the correlation function and the virtual baseline fixed at large relative momenta).

Besides a small negative slope of the overall baseline, the distribution of the red symbols is flat down to around 35 MeV/ $c$  in  $q_{\text{inv}}$ . The remaining deficits at lower relative momenta are tried to be removed by further conditions on the wire hits of the particle tracks. The condition on shared wires is expected to work best for a situation where as many as possible layers with well defined fired wire per particle are available, since for layers without found hit no decision can be made. It was mentioned already in Section 4.2.1 that at least four of six wire planes per chambers have to be fired for acceptable single particle reconstruction. Therefore, it is possible that, in worst case, a pion pair has only eight layers contributing to  $N_{\text{wires}}^{\text{shared}}$ . In Figure 4.26 on the right side, the yield of pairs with  $N_{\text{wires}}^{\text{shared}} = 0$  is displayed as function of  $q_{\text{inv}}$  and the number of MDC layers  $N_{\text{layers}}^{\text{both}}$ , where both tracks have an attributed fired wire. A maximum of  $N_{\text{layers}}^{\text{both}}$  is found at 22 and an illustration of which layers are contributing to this number is shown on the left side of Figure 4.26. The resulting correlation functions  $C(q_{\text{inv}})$ , when setting lower limits on  $N_{\text{layers}}^{\text{both}}$ , are exhibited in Figure 4.27, again for a data sample from the UrQMD simulations. Black symbols are generated without any restriction, for all other colored data points  $N_{\text{wires}}^{\text{shared}}$  is set to zero. The violet sample covers the whole range of  $N_{\text{layers}}^{\text{both}}$ , while the blue points only include pairs with at least 22 layers with hits from both particles. Finally, the red data belongs to the ideal case, that is, each track of a pair was reconstructed with 24 well defined hits in the MDC layers without using twice any contributing fired wire. The

#### 4. Analysis

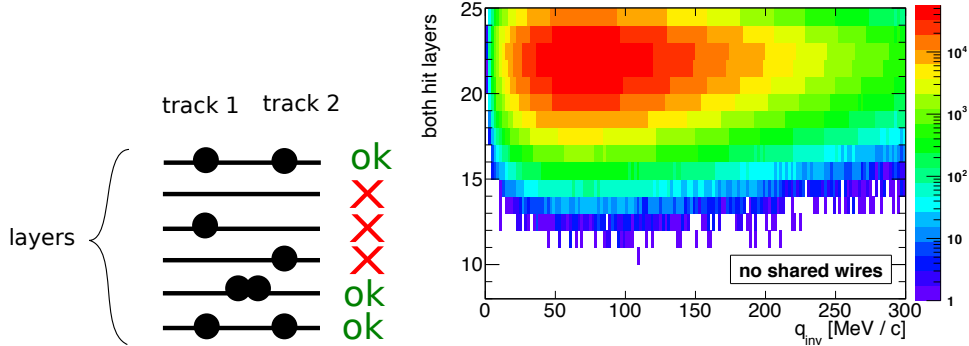


**Figure 4.26:** Left: Illustration of acceptable layers (marked by 'ok'), where both tracks of the pair have a registered hit (black circles), contributing to  $N_{\text{layers}}^{\text{both}}$  as described in the text. Right: True pair distribution over the  $q_{\text{inv}}\text{-}N_{\text{layers}}^{\text{both}}$  plane for the selection  $N_{\text{wires}}^{\text{shared}} = 0$ .

figure shows that making a rough selection on  $N_{\text{layers}}^{\text{both}}$ , whereat the maximum of the pair distribution is barely kept, delivers only a small improvement, comparing blue and violet data points. Applying an even harder cut may possibly restore the correlation function at low relative momenta completely, see the red data points. However, the large uncertainties caused by the tiny amount of remaining pairs does not allow to make a clear decision about that. Furthermore, the left over statistics is too low to move on with a meaningful investigation of the Bose-Einstein correlations.

Another ansatz would be to not only consider shared wires, but in addition a window of neighboring wires. One motivation for that idea is that particles can pass the MDC drift cell close to the boarder to the neighboring drift cell and may induce signals in either both cells or accidentally only in one of them. Another motivation is the finite accuracy of the specific event parameters in the event mixing operation, which leads to slightly different projected detector geometries visible by the pairs. The resulting smearing of the mixed distribution allows a couple of pairs to fulfil the selection on  $N_{\text{wires}}^{\text{shared}}$ , which would be not possible if the same particles are detected within the same event. A so called sliding wire window (SWW) is introduced consisting of an odd number, larger or equal one, describing how many wires around the fired wire of the first particle the hit of the second particle of the pair are excluded from giving a count to  $N_{\text{wires}}^{\text{shared}}$ . Explicitly, this means, if SWW has the number one, particle two is only forbidden to hit exactly the same wire as particle one. If SWW has the number three, then particle two is also forbidden to have a hit in two neighboring wires of the fired wire of particle one and, with increasing number of SWW by two, in addition the next neighboring wires are also vetoed. In the top panels of Figure 4.28 the sliding wire windows are illustrated, on the left for a width of three wires and

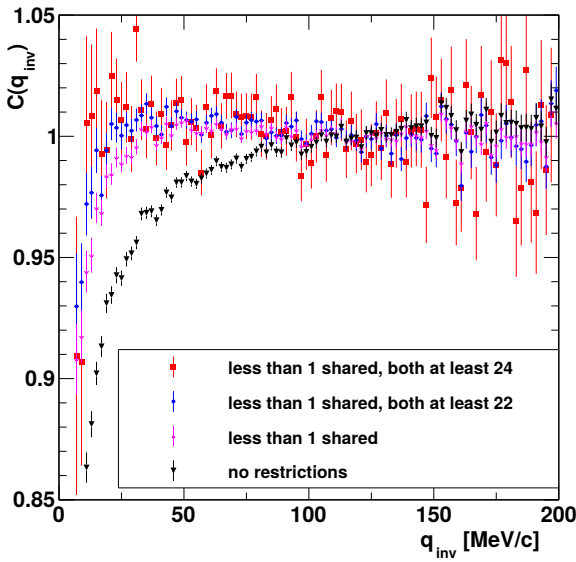


**Figure 4.27:** Correlation function (4.20) for several conditions on the number of layers with hits from both tracks  $N_{\text{layers}}^{\text{both}}$  for  $N_{\text{wires}}^{\text{shared}} = 0$ : no further condition (violet), at least 22 (blue) and 24 (red) counted layers. Black symbols show the initial case without restrictions on  $N_{\text{wires}}^{\text{shared}}$ .

on the right for five wires, always within one MDC layer. Associated with that, on bottom of Figure 4.28, the correlation functions with the applied sliding wire windows are plotted with red symbols. Additionally, in blue, the case of  $\text{SWW} = 1$  wire and in black the case without restrictions are plotted. For the results shown in the left plot with  $\text{SWW} = 3$ , the reduction of the remaining deficits between data points and baseline compared to the blue points is very effective. Within the error bars, the finally remaining deviation is smaller than 1% down to relative momenta of  $20 \text{ MeV}/c$  and less than 2% down to  $6 \text{ MeV}/c$ . For the sliding wire window of  $\text{SWW} = 5$ , a similar observation is made, and on a first glance the correlation function looks even more flat. The tiny overall negative slope turns into a marginal positive slope at large relative momenta. The statistical fluctuations at smallest values of  $q_{\text{inv}}$  increase, which indicates the stronger reduction of pion pairs in this region. Within this higher uncertainty it is not possible to state that the quality of the correlation function improves for the right plot when compared to the left one.

Note that a similar investigation has been introduced in [94] for the TPC based spectrometer in the STAR experiment with focus on both, merged and split tracks. Split tracks are tracks induced by one particle, but counted after data aquisition and track reconstruction as two particles. The treatment of the former is comparable to the explanations of this paragraph. The latter one was found not to play a significant role in HADES. The high number of required signals of fired wires per track (four wires per layer ends up in

#### 4. Analysis

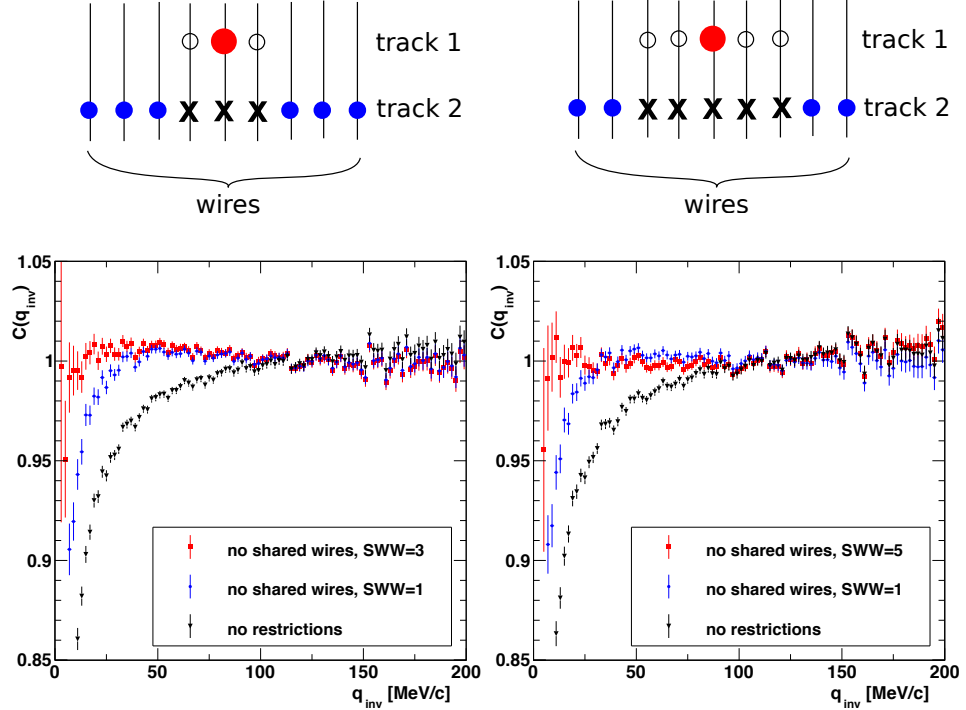


**Figure 4.28:** Top: Illustration of the sliding wire window (SWW) with width of three (left) and five (right) wires. A registered hit of track one (red circle) in one of the parallel aligned wires of one MDC layer restricts track two not to have a fired wire in a symmetric window around this wire (marked with crosses). Bottom: Invariant correlation function (4.20) for different selections: no restriction (black),  $N_{\text{wires}}^{\text{shared}} = 0$  (blue) and in addition SWW of size three (red, left panel) or SWW of size five (red, right panel), respectively.

at least 16 wires per track) makes it practically impossible to divide these hits for generating another one close by.

#### Remaining long-range correlations

Besides the previously discussed detector-based correlations related mainly to low relative momenta, also correlations at high relative momenta can be observed, visible as overall slope leading to deviations in the order of  $10^{-3} - 10^{-2}$  w.r.t. the baseline. For the correlation function  $C(q_{\text{inv}})$ , a positive slope at high  $q_{\text{inv}}$  is observed with magnitude between  $4 \times 10^{-5} c/\text{MeV}$  at high transverse momenta and  $1.4 \times 10^{-4} c/\text{MeV}$  at low transverse momenta. An example is shown in Figure 4.29. Such an observation is discussed in [95] as so called non-femtoscopic correlations and explained as broadening of the mixing yield due to a combination of collective pion flow

modes with preferred transverse direction and a finite event-plane resolution, which shifts small relative momenta slightly towards larger values. Unfortunately, this ends up in a correlation function with overall negative slope, which is opposite to the observation in Figure 4.29. A further experimental observation is that the slopes at high  $q_{\text{inv}}$  decrease, if the event mixing condition on the primary vertex,  $|z_{\text{prim},1} - z_{\text{prim},2}|$ , is changed to smaller distances or if an additional condition is set on the transverse directions,  $|x(y)_{\text{prim},1} - x(y)_{\text{prim},2}|$ , respectively. The combination of the finite resolution of the primary-vertex determination and event-to-event fluctuations passing the low-level data-driven pair cut leads to a reduced mixing pair yield at slightly higher values of  $q_{\text{inv}}$  compared to the true yield. This ends up in an increase of the correlation function with increasing relative momentum. This second mentioned effect is expected to dominate. Finally, one could decide to include this effects by a global slope or a second-order polynomial function in the subsequent fitting procedures.

### Final low-level detector cuts

To summarise the findings of the above paragraphs, the finally applied conditions on the pion pairs and the remaining relative statistics are listed:

- META cut: both pions must have hits in different META cells  
 $\rightarrow \sim 86\%$  remaining statistics,
- MDC cut I: no shared wires of the pions are allowed  
 $\rightarrow \sim 69\%$  remaining statistics,
- MDC cut II: no neighboring wires of shared wires of one pion are shared with the wires of the other pion (SWW = 3)  
 $\rightarrow \sim 59\%$  remaining statistics.

These so-called low-level close-track cuts are applied to both the distributions of true and mixed pairs (cf. Section 4.3.3).

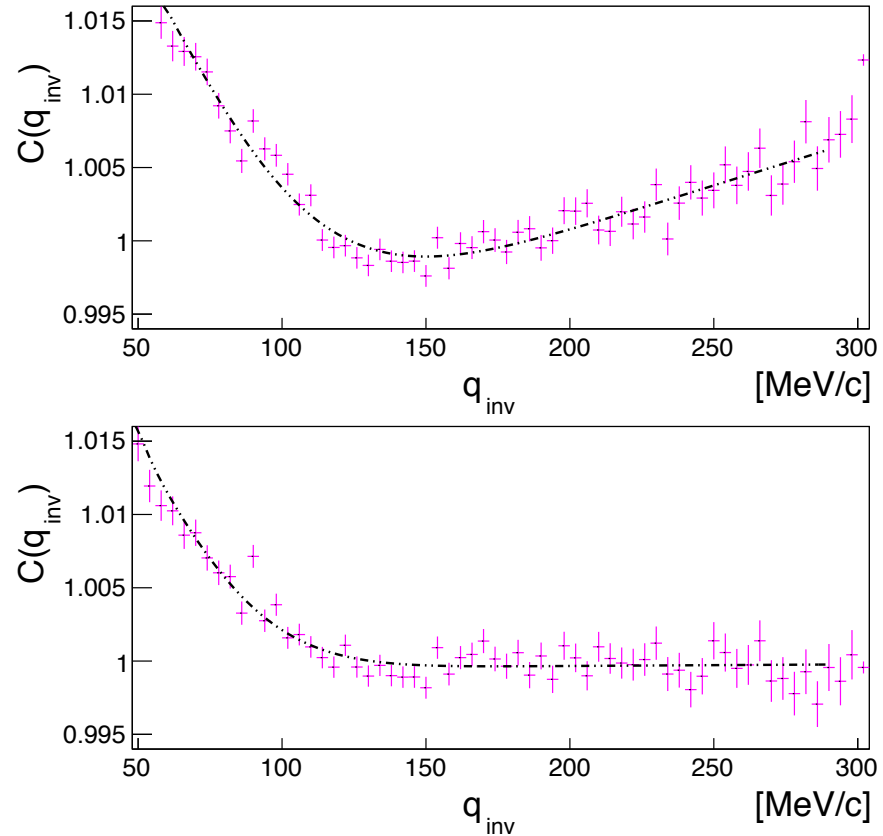


**Figure 4.29:** A zoom of the correlation function as a function of  $q_{\text{inv}}$ , at higher values of  $q_{\text{inv}}$ , for  $p_{t,12} \in [500, 600] \text{ MeV}/c$ . The Bose-Einstein signal is visible up to  $100 \text{ MeV}/c$ . Top: no condition on primary vertex in transverse direction; for larger relative momenta a linear trend with non-zero positive slope is observed. Bottom: primary vertex differences in  $x$  and  $y$  direction of mixed pairs required to be less than  $0.2 \text{ mm}$ ; no slope at high relative momenta visible. The black dashed-dotted curves are parametrisations for guiding the eyes.

## 4.4 Extracting the local space informations

The two-pion correlation signals are used to extract the geometrical properties like spatial extensions of the fireball region of the Au+Au collisions at particle freeze-out. Assuming a three-dimensional Gaussian source distribution as introduced in Section 2.4, one expects the experimental correlation function to have a Gaussian shape, affected by the final state interactions and eventually smeared by the finite relative momentum resolution of the detector set-up.

### 4.4.1 Two-particle correlation function including FSI

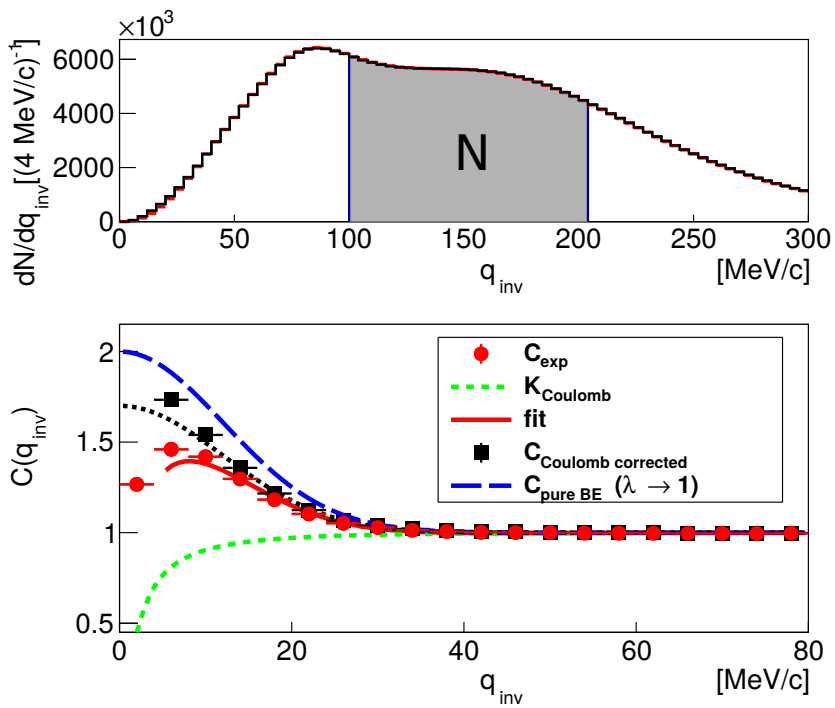


**Figure 4.30:** Top: true (black) and mixed (red) yields of pion pairs for  $p_{t,12} \in [200, 300] \text{ MeV}/c$  as a function of  $q_{\text{inv}}$ . The shaded region marked by 'N' depicts the region used for the normalisation. Bottom: corresponding correlation function, Equation (4.20), (red circles) fitted with Equation (4.26) (red line). The green dashed curve represents the separable final-state interaction Coulomb part. The black squares correspond to the Coulomb-corrected correlation function. The black dotted curve shows the fit function, Equation (4.26), after the Coulomb correction. The blue long-dashed curve gives the pure Bose-Einstein part, Equation (4.27), of the correlation function.

## 4. Analysis

---

After removing all the non-physical correlations discussed in some detail in Section 4.3.4, the experimental correlation functions Equations (4.19) and (4.20) should only differ from unity due to Bose-Einstein correlations (2.11) and final state interactions, mainly Coulomb interaction as discussed in Section 2.3. Following [38] the one-dimensional correlation function can be fit using

$$C(q_{\text{inv}}) = N [1 - \lambda_{\text{inv}} + \lambda_{\text{inv}} K_C(q_{\text{inv}}, R_{\text{inv}}) C_{\text{qs}}(q_{\text{inv}})], \quad (4.26)$$

$$C_{\text{qs}}(q_{\text{inv}}) = 1 + \exp(-(2q_{\text{inv}}R_{\text{inv}})^2), \quad (4.27)$$

with a second normalisation constant  $N$  and the incoherence parameter  $\lambda_{\text{inv}}$  introduced in Section 2.2.4.  $C_{\text{qs}}$  is the pure quantum-statistical part with a Gaussian form derived from Equation (2.15) assuming a Gaussian source distribution. It contains the invariant source size parameter  $R_{\text{inv}}$ , which can be seen as an average width of the area of homogeneity integrated over the whole emission duration. The two-particle Coulomb interaction factorises and is covered by  $K_C(q_{\text{inv}}, R_{\text{inv}})$ , calculated with Equation (2.24). Since the evaluation of the confluent hyper-geometrical function  $F$  has to be done numerically and is time consuming, the expression  $|\Phi^{\text{coul}}(\vec{r})|^2$  is evaluated only once on a grid of discrete values of  $q_{\text{inv}}$  and  $R_{\text{inv}}$  and stored in a two-dimensional histogram, which is later on used as a look-up table. The step size is fixed with  $1 \text{ c/MeV}$  in  $q_{\text{inv}}$  and  $1 \times 10^{-3} \text{ fm}$  in  $R_{\text{inv}}$ , which is always below the chosen interval size in relative momentum and much smaller than the typical uncertainties of HBT radius parameters. At the beginning the value of  $R_{\text{inv}}$  from the Coulomb correction histogram is set to  $6 \text{ fm}$ . After the first fit, it is adjusted to the value from the Bose-Einstein part (4.27). Then, the fit is repeated iteratively until the value of  $R_{\text{inv}}$  does not change by more than  $10^{-3} \text{ fm}$ . The three-dimensional correlation function (4.19) is fitted using the ansatz

$$C(q_{\text{out}}, q_{\text{side}}, q_{\text{long}}) = N [1 - \lambda_{\text{osl}} + \lambda_{\text{osl}} K_C(\hat{q}, R_{\text{inv}}) C_{\text{qs}}(q_{\text{out}}, q_{\text{side}}, q_{\text{long}})], \quad (4.28)$$

with the corresponding incoherence parameter  $\lambda_{\text{osl}}$  and again a second normalisation constant  $N$  (can be different from the  $N$  in Equation (4.26)). The Coulomb correction term  $K_C(\hat{q}, R_{\text{inv}})$  uses the former determined invariant HBT radius and the average invariant relative momentum  $\hat{q}$  depending on  $q_{\text{out}}$ ,  $q_{\text{side}}$  and  $q_{\text{long}}$ , which can be calculated by

$$\hat{q} = q_{\text{inv}}(q_{\text{out}}, q_{\text{side}}, q_{\text{long}}, \bar{k}_t) = \sqrt{q_{\text{out}}^2(1 - \beta_t^2) + q_{\text{side}}^2 + q_{\text{long}}^2}. \quad (4.29)$$

The transverse pair velocity  $\beta_t = 2\bar{k}_t/(E_1 + E_2)$  is calculated with the mean value of  $k_t$  for the chosen interval of pair transverse momenta. The Bose-Einstein part is separated and can be written as

$$C_{qs}(q_{\text{out}}, q_{\text{side}}, q_{\text{long}}) = 1 + \exp(-(2q_{\text{out}}R_{\text{out}})^2 - (2q_{\text{side}}R_{\text{side}})^2 - (2q_{\text{long}}R_{\text{long}})^2), \quad (4.30)$$

with the three HBT radii  $R_{\text{out}}$ ,  $R_{\text{side}}$  and  $R_{\text{long}}$ . Expression (4.30) is valid in the LCMS as long as it is integrated over all azimuthal angles of the pairs and a symmetric rapidity interval around mid-rapidity is considered. The functional form is used for the azimuthally integrated analysis with an interval of pair rapidity of  $y_{\text{cm}} \pm 0.35$ .

Actually, Equation (4.30) can be written in a more general way introduced already in Equation (2.38),

$$C_{qs} = 1 + \exp(-4 \sum_{i,j} q_i R_{ij} q_j), \quad (4.31)$$

where the indices  $i$  and  $j$  run over the three directions 'out', 'side' and 'long'. The three already introduced HBT radii are the diagonal components of this matrix representation  $R_{ij}$ , and additionally three non-diagonal HBT variances appear,  $R_{\text{out side}}^2$ ,  $R_{\text{out long}}^2$  and  $R_{\text{side long}}^2$ . The parameter  $R_{\text{out long}}^2$  can already have finite values in the azimuthally integrated investigation, if for example the rapidity distribution is not symmetric w.r.t. mid-rapidity. In the azimuthally dependent analysis all six HBT variances can have finite values and must be included in the fits applied to the correlation function.

From theoretical considerations, the parameters  $\lambda_{\text{inv}}$  and  $\lambda_{\text{osl}}$  should be equal unity for an ideal chaotic source. However, in practice the incoherence parameter enters with a value between zero and unity, as mentioned in Section 2.2.4. Contaminations of other particle species contributing to the reconstructed pion yields lead to a decrease of the BE amplitude, since the fraction of these particles have no quantum-statistical correlation with the pions. The purity of the pion yields in the used transverse momentum and rapidity range is between 97 and 99 %, intensively studied in [64] (p. 106). The influence of long-living pion-emitting resonances [48] with  $c\tau > 20$  fm (e.g.  $\eta$ ,  $\Sigma^0$ ,  $J/\psi$ , ...) producing an unresolvable spike at low values of  $q$  should be negligible at beam energies of around 1A GeV.

One can try to account for eventually long-range correlations mentioned in the penultimate paragraph of Section 4.3.4 by changing the normalisation in Equation (4.26) to  $N \rightarrow N' = N(1 + f(q_{\text{inv}}))$ , where the functional is in the simplest case linear,  $f(q_{\text{inv}}) = \alpha q_{\text{inv}}$ . This part is determined at higher values of  $q_{\text{inv}}$  and might improve the estimate of the baseline down to low relative momenta, which leads to a slight change of the fit parameters. This extension of Equation (4.26) has been used for example in [96]. Since the

## 4. Analysis

physical origin of the remaining slope is not completely clarified and the functional form  $f(q_{\text{inv}})$  is not necessarily the same at low and high values of  $q_{\text{inv}}$ , one should be careful when using the advanced term, i.e. one should treat deviations at most as contributions to the systematic uncertainties.

All fits with Equations (4.26) to (4.31) are performed using the *gMinuit* package included in the *ROOT* framework. The used estimators are both,  $\chi^2$  and maximum logarithmic likelihood, and both methods deliver the same fit parameters with the same statistical uncertainties. For more details on the minimisation procedures see Appendix A.1.

### 4.4.2 Finite relative momentum resolution



**Figure 4.31:** Scheme of the procedure used for determining the relative momentum resolution. Pion pairs are generated with the Pluto event generator being distributed in phase space comparable to the experimental distributions. The pairs are then tracked through HGeant to simulate acceptance, resolution, and efficiency of the detector.

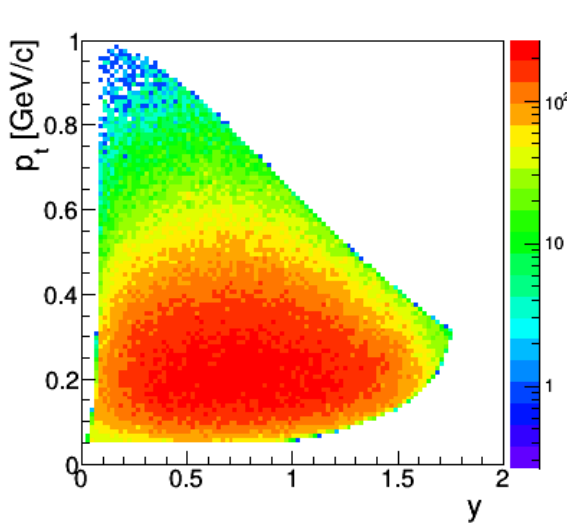


**Figure 4.32:** PLUTO phase space distribution of one of the pions for one million pion pairs. The value of the fireball temperature  $T$  is set to 200 MeV, the polar angle is restricted to  $[16^\circ, 88^\circ]$ , the transverse momentum to values larger than  $50 \text{ MeV}/c$  and the total momentum to values smaller than  $1 \text{ GeV}/c$ . The invariant relative momentum of all pairs is  $30 \text{ MeV}/c$

In Sections 3.3.2 and 3.4.1, the resolution of the detector components used for the particle identification has been mentioned. This causes a finite reso-

#### 4.4 Extracting the local space informations

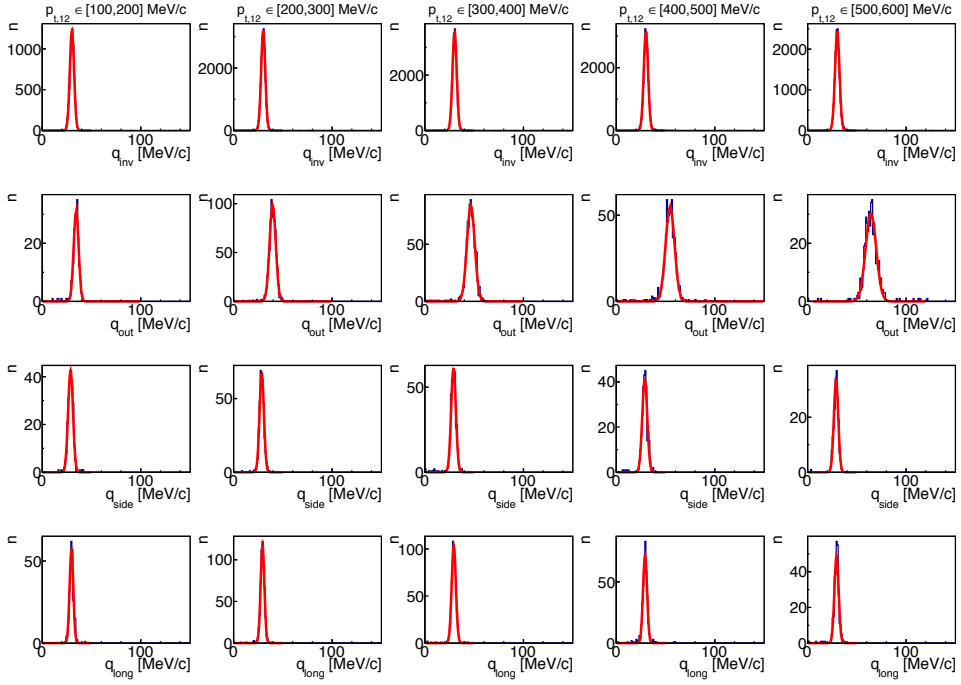


**Figure 4.33:** Relative momentum distributions as a function of  $q_{\text{inv}}$  (top row),  $q_{\text{out}}$  (second row),  $q_{\text{side}}$  (third row) and  $q_{\text{long}}$  (bottom row) for pion pairs generated with PLUTO with initial relative momentum of  $q_{\text{inv}} = 30 \text{ MeV}/c$  after tracking through HGeant. The distributions are plotted for different intervals of  $p_{t,12}$  (increasing from left to right) and fitted with Gaussians (red curves).

lution of the determined momenta of the identified pions. In [63] the phase-space dependent momentum resolution of HADES is discussed and exhibited in some detail. However, for the present analysis of two-particle correlation functions, one has to know the resolution of the relative momentum of both pions. For that reason, several ensembles of  $10^7$  pion pairs have been generated using the PLUTO event generator [97]. Each ensemble is characterised by a well defined relative momentum of the two pions. In PLUTO, this is achieved by creating a pseudo-particle with a fixed mass decaying into two pions. To get a statistical distribution like the typical HADES phase space distribution, compared to Figure 4.16, one can use the (inverse Boltzmann slope) temperature parameter  $T$  within the event generator. Setting its value to 200 MeV and setting limits for minimum and maximum polar angles and momenta, respectively, delivers a quite realistic phase-space distribution, see Figure 4.32. Then, the two-particle events are propagated through HGEANT, which imitates the acceptance, granularity (resolution), and efficiency of the whole HADES set-up. Afterwards, the momenta of the

#### 4. Analysis

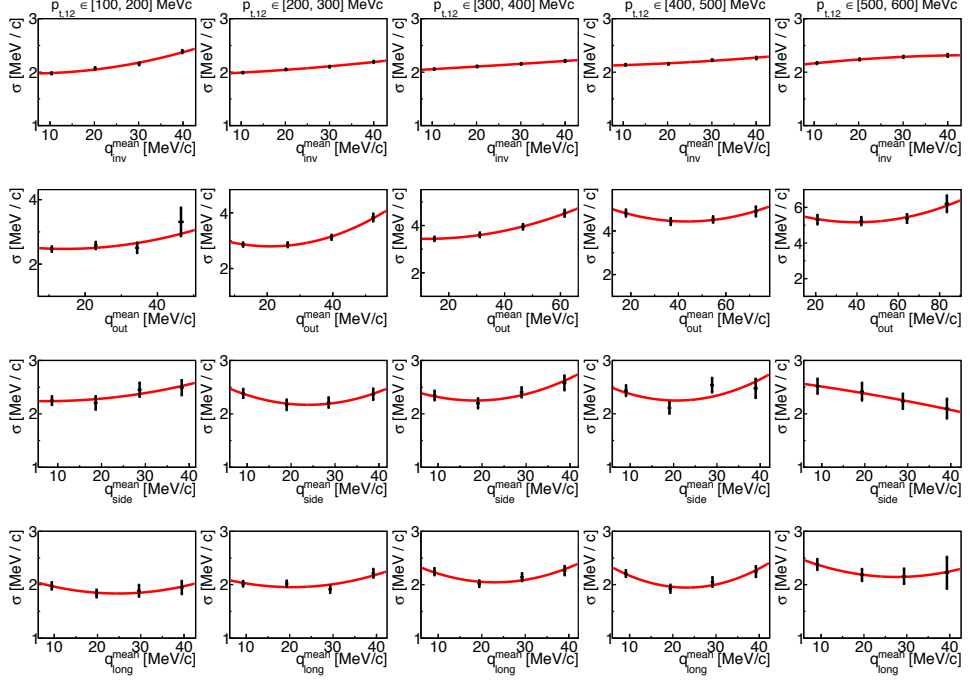


**Figure 4.34:** Relative momentum resolution in dependence of  $q_{\text{inv}}$  (top row),  $q_{\text{out}}$  (second row),  $q_{\text{side}}$  (third row) and  $q_{\text{long}}$  (bottom row) for different intervals of  $p_{t,12}$  (increasing from left to right) for  $\pi^-\pi^-$ . Red curves are parametrisations with a polynomial of second order.

pions can be reconstructed in the same way as for the experimental data. The relative momentum of each pair is calculated and the distributions of  $q_{\text{inv}}$ ,  $q_{\text{out}}$ ,  $q_{\text{side}}$  and  $q_{\text{long}}$  are compared to the initial values as plotted in Figure 4.33 exemplary for initial relative momentum of  $30 \text{ MeV}/c$ . These distributions are fitted with a standard Gaussian and the extracted width is taken as the relative momentum resolution. Repeating this for all intervals of  $p_{t,12}$  and all ensembles of initial relative momenta one gets the  $q$  and  $p_{t,12}$  dependent relative momentum resolution  $\sigma$  as plotted in Figure 4.34. Here, four ensembles for initial relative momenta  $q_{\text{inv}}^{\text{ini}} = \{10, 20, 30, 40\} \text{ MeV}/c$  have been used. The dependence of the relative momentum resolution on the initial relative momentum is small for nearly all  $p_{t,12}$  intervals and all directions. The distribution has been fitted with a second order polynomial of the form  $n_0 + m q_i + a q_i^2$ . Overall, a slight increase of  $\sigma$  with increasing  $q_{\text{inv}}^{\text{ini}}$  is visible. With the found parametrisations of the approximate Gaussian resolutions, one can correct the experimental correlation functions or the fit results, respectively. Below, three possible approaches how to do this are considered.

### Unfolding of the measured correlation function

The convolution of the correlation function with the finite relative momentum resolution can formally be written as

$$C_{\text{meas}}(q) = \int C_{\text{real}}(q') \mathcal{F}(q, q') dq', \quad (4.32)$$

with the measured (real) correlation function  $C_{\text{meas}}$  ( $C_{\text{real}}$ ), and the resolution function  $\mathcal{F}(q, q')$ , which here is a normalised Gaussian with  $q$ -dependent width given by the parametrisations of Figure 4.34. For a finite binning in  $q$ , the integral formula (4.32) can be translated into a matrix description,

$$C_{\text{meas}}(q_i) = M_{ij} \cdot C_{\text{real}}(q_j), \quad (4.33)$$

with the convolution matrix  $M_{ij}$ . The best and most accurate way of accounting for the finite relative momentum resolution would be to use the previously described procedure to fill the complete convolution matrix  $M_{ij}$  describing the smearing of the measured correlation function for the chosen binning. The task is then to invert  $M_{ij}$  and reconstruct the real correlation function,

$$C_{\text{real}}(q_i) = M_{ij}^{-1} \cdot C_{\text{meas}}(q_j). \quad (4.34)$$

This procedure is cumbersome, especially when considering the three-dimensional correlation function, and very time-consuming. With focus on the results and the knowledge, that the effect of the finite relative momentum resolution will be relatively small, a simplified approach is considered below.

### Gaussian subtraction

Since both the correlation signal  $C_{\text{qs}}$  and the relative momentum resolution are approximately Gaussian, and since a Gaussian convolution of a Gaussian function results also in a Gaussian function (see Appendix A.2) a consequence is in a very simple consideration

$$\sigma_{\text{true}}^2 = \sigma_{\text{meas}}^2 - \sigma_{\text{res}}^2, \quad (4.35)$$

where  $\sigma_{\text{res}}$  is the relative momentum resolution or the width of the Gaussian approximation to the resolution, respectively.  $\sigma_{\text{meas}}$  is the width of the Bose-Einstein part of the measured correlation signal and can be extracted from Equations (4.26) and (4.28) as

$$\sigma_{\text{meas},i} = \frac{197.327 \text{ fm MeV}}{\sqrt{8} R_i} \quad (i = \text{inv, out, side, long}). \quad (4.36)$$

## 4. Analysis

---

Inverting Equation (4.36) allows to calculate the unbiased HBT radii from the true Bose-Einstein correlation-width  $\sigma_{\text{true}}$ :

$$R_i = \frac{197.327 \text{ fm MeV}}{\sqrt{8} \sigma_{\text{meas},i}} \quad (i = \text{inv, out, side, long}). \quad (4.37)$$

However, both the superposition of the Bose-Einstein correlation signal with the non-Gaussian FSI Coulomb part and the appearance of non-diagonal HBT parameters in the exponent of Equation (4.31) disturb the validity of Equation (4.35). One has to check carefully, whether it can be used and how big the systematic uncertainties are compared to the exact treatment using Equation (4.34).

### Convolution of fit function

Instead of unfolding the measured correlation signal and fitting it with Equations (4.26) and (4.28) one can also imagine a convolution of the fit functions with the Gaussian momentum resolution and use these expressions for fitting the uncorrected correlation functions. This procedure is less cumbersome than the first approach, but treats the superposing Coulomb interaction and deviations due to finite non-diagonal HBT parameters correctly. The convolution of the fit functions is done numerically using a mesh of sufficiently large number of Gaussian nodes<sup>4</sup> for each direction. For the one-dimensional case ( $C(q_{\text{inv}})$  and 1D-projections of  $C(q_{\text{out}}, q_{\text{side}}, q_{\text{long}})$ ) this approach works very good, delivering correct results after a reasonable time. For the three-dimensional case, however, it turned out to be highly time-consuming, and fits could not be performed that comfortably, especially if one has a big amount of correlation functions in a multi-differential phase-space distribution.

However, it turned out that comparing this approach and the simple Gaussian subtraction approach described in the previous paragraph one finds the same relative momentum resolution correction in the order of several  $10^{-1}$  fm, while the difference between both methods is less by factor of ten, i.e. in the order of magnitude of  $10^{-2}$  fm only. This means, that finally the very simple Gaussian subtraction method can be used for correcting the finite relative momentum resolution of the three-dimensional correlation functions, while an additional 10 % systematic uncertainty enters the total amount of systematic uncertainties. Later on, it will turn out that this additional contribution is negligible when compared to the other systematic uncertainties.

---

<sup>4</sup>In numerical Gaussian integration procedures, nodes are essentially roots of an adequate polynomial, e.g. the Legendre polynomials.

### 4.4.3 Fit range

As obvious from Equations (4.26) and (4.28), the Bose-Einstein correlation signal and the final state interactions are located at low relative momenta and approaches unity for high relative momenta. Typically, the extracted radius parameters are in the range of 3 – 8 fm, which translates (using Equation (4.36)) into Bose-Einstein correlation widths not larger than 25 MeV/ $c$ . The upper limit of the fit range is chosen to 80 MeV/ $c$  to guarantee that the expected deviation between baseline and correlation function is less than 0.5 %. Changes of the fit parameters under variation of the upper fit limit are treated as systematic uncertainties. The lower limit of the fit range is not zero, but set to 6 MeV/ $c$ . It accounts for possible contributions from the strong FSI, mentioned in Section 2.3, and for remaining close-track deficits not caught by the cut introduced in Section 4.3.4. In the three-dimensional correlation function for each interval of  $q_{\text{out}}$ ,  $q_{\text{side}}$  and  $q_{\text{long}}$  it is checked, whether the corresponding value of  $q_{\text{inv}}$  calculated with Equation (4.29) is inside the chosen fit range. Otherwise, the outlying interval is excluded from the fit by setting the corresponding bin error in the histogram virtually to infinity.

### 4.4.4 Direct imaging: deviations from Gaussian sources

According to Equation (2.19), one could try to image the source in coordinate space by modelling and fixing the two-pion interaction and performing directly a Fourier transformation of the correlation function. With existing imaging codes [98–101] this can be done numerically for the one-dimensional correlation functions. However, there are still a lot of parameters to set (e.g. for constraining the shape of the outcoming source function, the limits at vanishing radius or large radii, respectively, etc.), and the calculations depend strongly on the considered range of  $q_{\text{inv}}$ , and the procedure becomes quite cumbersome when going to three dimensions. Exemplary results for the imaged source function  $S(r)$  are shown in Figure 4.35 for 5 % most central events and intervals of pair transverse momentum from 200 to 300 MeV/ $c$  (top left), 300 to 400 MeV/ $c$  (top right), 400 to 500 MeV/ $c$  (bottom left) and 500 to 800 MeV/ $c$  (bottom right). The red curves correspond to Gaussian distributions drawn with the parameters extracted from Equation (4.20) using the fit functions given by Equation (4.26). The blue curves are Gaussian fits to  $S(r)$  at small radii up to 15 fm. The figure shows that the Gaussian assumption of the source function is reasonable in leading order. It also shows that there are deviations from the Gaussian form, increasing with average transverse momentum of the considered pion pairs. The deviations are most obvious at larger values of  $r$ , corresponding to the range of lower  $q_{\text{inv}}$ . But also at low values of the source radius deviations are visible, corresponding to the larger relative momenta, especially for the

## 4. Analysis

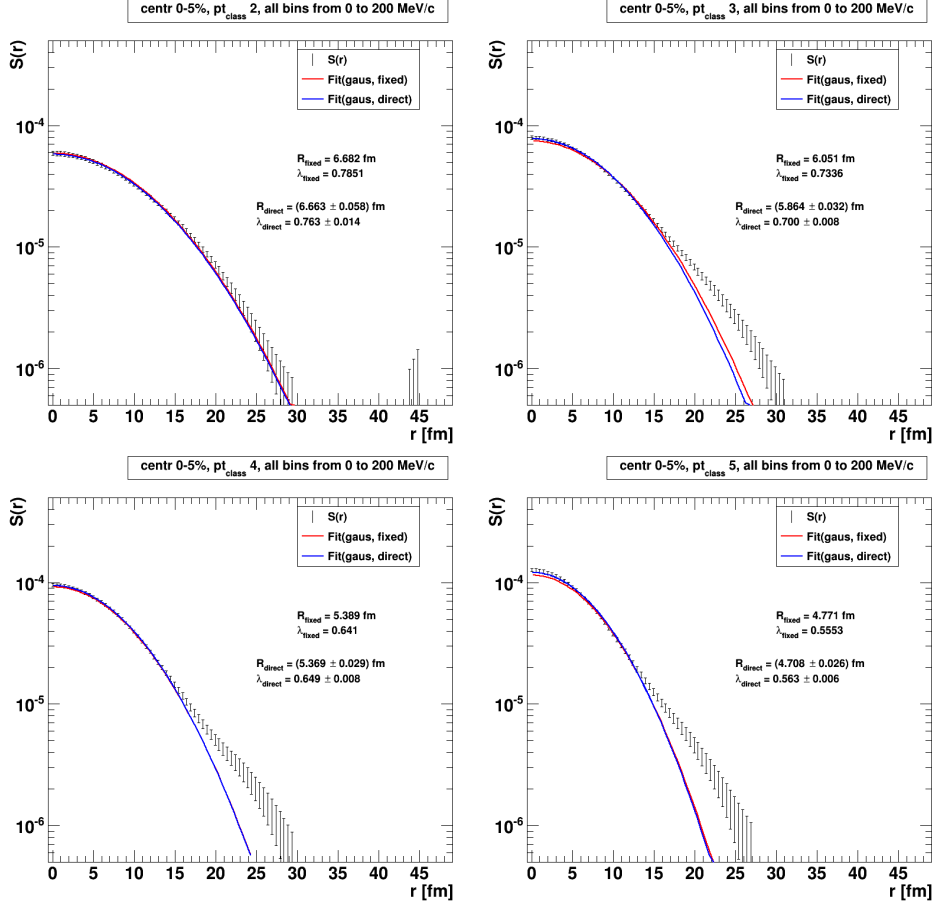


**Figure 4.35:** Source function  $S(r)$  constructed using the invariant correlation function and the imaging code *HBTprogs* from [98–100]. Results are for 5 % most central events and different intervals of pair transverse momentum. Blue curves represent Gaussian fits using the range of  $r \in [0, 15]$  fm, red curves are Gaussian distributions using the parameters from fits with Equation (4.26) applied directly to the invariant correlation function Equation (4.20).

largest transverse momentum window. Due to the logarithmic scale of the ordinate, the latter ones look smaller, but they are as significant as the tail-like structure at large radii.

A more detailed study of deviations from a Gaussian source shape goes beyond this thesis. Here, the focus is on an average Gaussian width of the fireball region, but three-dimentional in shape and multi-differentially investigating the dependence on centrality, transverse momentum, charge-sign, azimuthal angle relative to the reaction plane and rapidity. Albeit it should be mentioned that the high statistics of the HADES data would

allow such investigations. A lot of progress was achieved using Levy-stable distributions [102], which provide an easy extension of the Gaussian model and contains for example the more tail-like structure seen in Figure 4.35. At the moment, only PHENIX [96] provides published systematic studies on those non-Gaussian source shapes in heavy-ion collisions. Nonetheless, there exist preliminary results from STAR [103].

## 4.5 Including the azimuthal dependence

The azimuthal dependence of the HBT radius parameters can be used to get a more detailed picture of the three-dimensional shape of the area of homogeneity. Of special interest is the eccentricity of the transverse extension and a tilt of the particle emitting source relative to the beam axis.

### 4.5.1 Accounting for the explicit $\Phi$ dependence

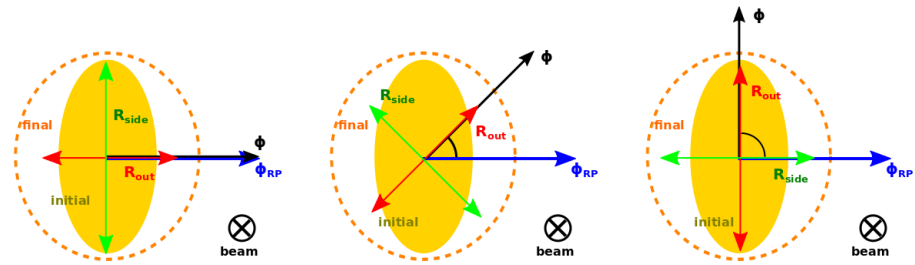


**Figure 4.36:** Illustration of the dependence of  $R_{\text{side}}$  and  $R_{\text{out}}$  on the azimuthal angle of the pair relative to the event plane  $\Phi = |\phi - \phi_{\text{RP}}|$  (from left to right  $0^\circ$ ,  $45^\circ$  and  $90^\circ$ ), following from the initial elliptic overlap region perpendicular to the beam direction (yellow shaded) of the Au+Au collision at finite impact parameter. For  $\Phi = 0^\circ$ ,  $R_{\text{side}}$  ( $R_{\text{out}}$ ) has a maximum (minimum) and decreases (increases) until  $\Phi = 90^\circ$ , where it has a minimum (maximum) and the other way around for larger angles.

As introduced in Section 2.4.3, the  $\Phi$  dependence of the six HBT variances deduced with Equation (4.31) originates mainly from a rotation of the pion-pair fixed out-side-long system relative to the reaction plane fixed  $xyz$  system. Metaphorically speaking, for a three-dimensional fireball with different extensions in  $x$  and  $y$  direction one can see a different picture, depending from which position relative to the event plane one is observing the collision,

## 4. Analysis

---

see Figure 4.36. This is the so-called explicit  $\Phi$  dependence which can be taken into account by using the following set of fit functions:

$$\begin{aligned}
R_{\text{out}}^2 &= \frac{1}{2}(S_{11} + S_{22}) + \frac{1}{2}(S_{22} - S_{11}) \cos 2\Phi + S_{12} \sin 2\Phi \\
&\quad - 2\beta_t(S_{01} \cos \Phi + S_{02} \sin \Phi) + \beta_t^2 S_{00}, \\
R_{\text{side}}^2 &= \frac{1}{2}(S_{11} + S_{22}) + \frac{1}{2}(S_{22} - S_{11}) \cos 2\Phi - S_{12} \sin 2\Phi, \\
R_{\text{out side}}^2 &= \frac{1}{2}(S_{22} - S_{11}) \sin 2\Phi + S_{12} \cos 2\Phi + \beta_t(S_{01} \sin \Phi - S_{02} \cos \Phi), \\
R_{\text{long}}^2 &= S_{33} - 2\beta_l S_{03} + \beta_l^2 S_{00}, \\
R_{\text{out long}}^2 &= (S_{13} - \beta_l S_{01}) \cos \Phi + (S_{23} - \beta_l S_{02}) \sin \Phi - \beta_t S_{03} + \beta_l \beta_t S_{00}, \\
R_{\text{side long}}^2 &= -(S_{13} - \beta_l S_{01}) \sin \Phi + (S_{23} - \beta_l S_{02}) \cos \Phi, \tag{4.38}
\end{aligned}$$

with the pair transverse velocity  $\beta_t$  and  $S_{\mu\nu}$  forming a  $4 \times 4$  matrix containing the information about the extension of the 3+1 dimensional ellipsoid of the region of homogeneity. When applying this set of equations to results taken in the LCMS at a small window around mid-rapidity ( $y = y_{\text{cm}}$ ) the longitudinal velocity  $\beta_l$  vanishes. The functions (4.38) are fitted to all six HBT parameters simultaneously and respect additionally the difference between  $R_{\text{side}}$  and  $R_{\text{out}}$  as stated in Equation (2.43). Due to symmetry constraints [104] within the present symmetric collision system of Au+Au and the consideration at mid-rapidity, the set of Equations (4.38) simplifies to

$$\begin{aligned}
R_{\text{out}}^2 &= \frac{1}{2}(S_{11} + S_{22}) + \frac{1}{2}(S_{22} - S_{11}) \cos 2\Phi + \beta_t^2 S_{00}, \\
R_{\text{side}}^2 &= \frac{1}{2}(S_{11} + S_{22}) + \frac{1}{2}(S_{22} - S_{11}) \cos 2\Phi, \\
R_{\text{out side}}^2 &= \frac{1}{2}(S_{22} - S_{11}) \sin 2\Phi, \\
R_{\text{long}}^2 &= S_{33} + \beta_l^2 S_{00}, \\
R_{\text{out long}}^2 &= S_{13} \cos \Phi, \\
R_{\text{side long}}^2 &= -S_{13} \sin \Phi. \tag{4.39}
\end{aligned}$$

However, keeping the full set (4.38) with all 10 components of  $S_{\mu\nu}$  allows to check for the validity of this combined fit and provides the opportunity to see influences of implicit  $\Phi$  dependences of the considered variances.

### 4.5.2 Finite event plane resolution

The sets of Equations (4.38) and (4.39) for fitting the oscillations of the measured azimuthally dependent variances are always evaluated at a certain

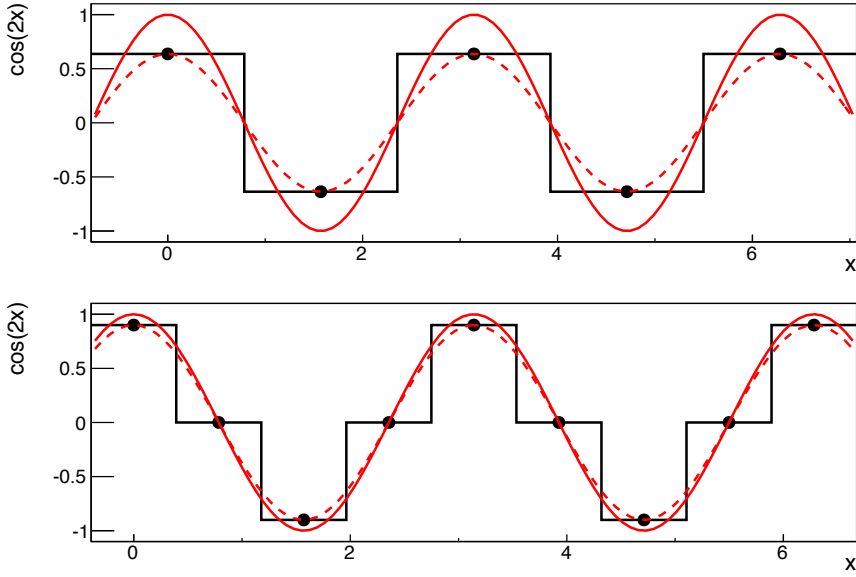


**Figure 4.37:** Illustration of the finite bin width effect acting on an oscillating function. The harmonic oscillation  $\cos(2x)$  (red solid curve) is sampled by four (eight) equal sized intervals in the upper (lower) panel within a total range of  $2\pi$ . The centers of the intervals (black dots) are used for reconstructing the oscillation (red dashed curves), which leads to a reduction of the amplitudes, taken into account by Equation (4.40).

value of  $\Phi$ . In practice, this is not always the case for the experimental data. On the one hand, the pairs of pions are divided in direction of  $\Phi$  into bins of finite size. Variances obtained for such bins are averaged values integrated over the bin range, but finally assigned to the weighted bin center. Figure 4.37 illustrates this effect acting on a harmonic oscillation. On the other hand, the range of  $\Phi$  is implicitly enlarged since the value of the reaction plane angle  $\phi_{RP}$  of the events is determined only up to a finite event plane resolution as introduced in Section 4.1.4. The correction of both, the finite reaction-plane resolution and the finite azimuthal bin width, is performed by using

$$R_{i,n}^{2,\text{corr}} = R_{i,n}^{2,\text{meas}} \frac{n \Delta/2}{F_n \sin(n \Delta/2)}, \quad (4.40)$$

where  $\Delta = \pi/4$  is the present  $\Phi$  bin width, and the quantity  $F_n = \langle \cos n \Delta \phi \rangle$  represents the  $n$ -th event-plane resolution as defined in Section 4.1.4 (see also Table 4.2). The measured Fourier coefficients  $R_{i,n}^{2,\text{meas}}$  are traced back to the underlying true coefficients  $R_{i,n}^{2,\text{corr}}$  of a Fourier expansion of the radius

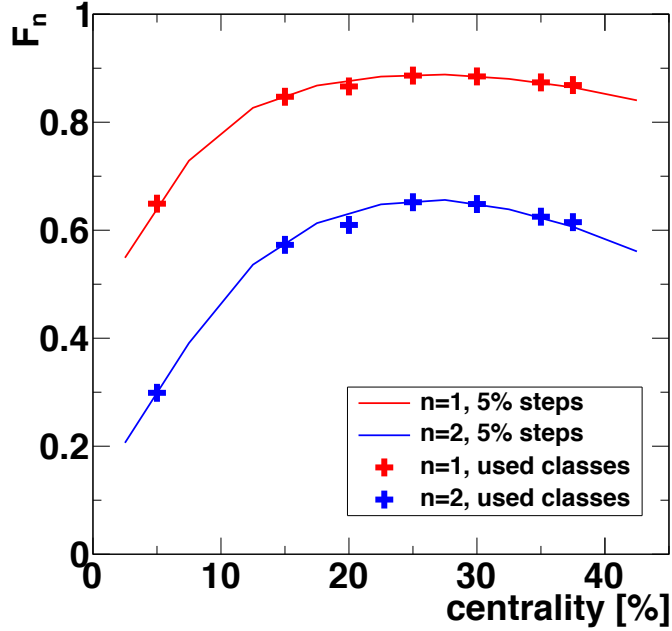


**Figure 4.38:** Event plane resolution  $F_n$  of 1<sup>st</sup> (red) and 2<sup>nd</sup> (blue) order calculated using Equations (4.7) and (4.8).

parameter  $R_i^2$  as defined by Equation (4.5). Practically, the matrix elements  $S_{ij}$  from Equations (4.38) and (4.39) or combinations of them appear as well-defined Fourier coefficients in front of an oscillation term  $\cos(n\Phi)$  or  $\sin(n\Phi)$ . They are corrected according to the order of oscillation they appear with:

$$(S_{22} + S_{11}), S_{00}, S_{33}, S_{03} \rightarrow \text{no correction}, \quad (4.41)$$

$$S_{01}, S_{02}, S_{13}, S_{23} \rightarrow 1^{\text{st}} \text{ order correction}, \quad (4.42)$$

$$(S_{22} - S_{11}), S_{12} \rightarrow 2^{\text{nd}} \text{ order correction}. \quad (4.43)$$

Figure 4.38 displays  $F_n$  for  $n = 1$  and  $n = 2$  as function of the collision centrality. The values of  $F_1$  and  $F_2$  for the four centrality classes investigated in the present analysis are given in table 4.2.

#### 4.5.3 Final observables in the RP-fixed coordinate system

The dynamics within the fireball after the collision at finite impact parameter causes the elliptic region of homogeneity to be not necessarily aligned with the beam axis and the impact parameter, i.e. a tilted source distribution is possible. A tilt pointing outwards the reaction plane is prohibited due to symmetry reasons. Therefore, only a tilt within this plane needs to

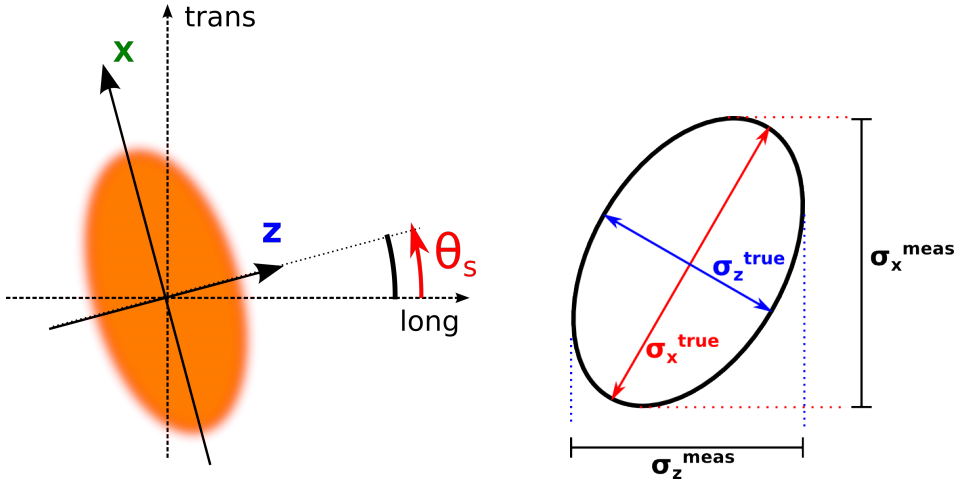


**Figure 4.39:** Left: Illustration of the finite tilt angle  $\theta_s$  of the ellipsoid within the reaction plane, defined between the  $z$  axis of the ellipsoid and the beam axis (long). Right: As consequence of the finite tilt angle, the smaller semi-axis tends to be measured too large and the larger semi-axis too small, respectively.

be considered. From Equations (4.38) and (4.40), the spatial tilt angle in the reaction plane can be calculated as

$$\theta_s = \frac{1}{2} \tan^{-1} \left( \frac{2S_{13}^{\text{corr}}}{S_{33}^{\text{corr}} - S_{11}^{\text{corr}}} \right), \quad (4.44)$$

which is defined as the angle between the beam axis and the  $z$  coordinate of the described ellipsoid in counterclockwise direction;  $\theta_s$  is determined modulo  $180^\circ$ , see Figure 4.39. Rotating  $S^{\text{corr}}$  by the angle  $-\theta_s$  around the  $y$  axis, i.e. applying the corresponding rotation matrix  $G_y(\theta_s)$ ,

$$S^{\text{diag}} = G_y^{-1}(\theta_s) S^{\text{corr}} G_y(\theta_s), \quad (4.45)$$

yields a diagonal tensor  $S^{\text{diag}}$  whose eigenvalues are the temporal and geometrical variances  $\sigma_t^2, \sigma_x^2, \sigma_y^2, \sigma_z^2$ .

A further handy variable for comparing the semi-axes of an ellipsoid relative to each other is the eccentricity. In this thesis, it is used to compare the in-plane extensions to the out-of-plane extension. The  $xy$ -eccentricity is defined by

$$\varepsilon_{xy} = \frac{\sigma_y^2 - \sigma_x^2}{\sigma_x^2 + \sigma_y^2}, \quad (4.46)$$

## 4. Analysis

---

and in similar manner the  $zy$ -eccentricity,

$$\varepsilon_{zy} = \frac{\sigma_y^2 - \sigma_z^2}{\sigma_y^2 + \sigma_z^2}. \quad (4.47)$$

Note that the coordinate system 'xzy' is reserved in the ongoing analysis for the alignment of the semi-axes of the ellipsoids of the fireball regions, where  $y$  points always outside the reaction plane, but  $x$  and  $z$  are exchangeable with respect to Equation (4.44), i.e. an interchange of the coordinates leads to a shift in  $\theta_s$  by  $\pm 90^\circ$ . This degree of freedom later on is removed by physical and logical constraints.

### 'Simplified' consideration without tilt

To improve the consideration of Section 4.5.1 one can use the full Fourier expansion of the azimuthal dependence and calculate the harmonic coefficients [60],

$$R_{ij,m}^c = \frac{1}{2\pi} \int_{-\pi}^{\pi} R_{ij}^2 \cos(m\Phi) d\Phi, \quad (4.48)$$

$$R_{ij,m}^s = \frac{1}{2\pi} \int_{-\pi}^{\pi} R_{ij}^2 \sin(m\Phi) d\Phi, \quad (4.49)$$

which include both, the explicit and the implicit  $\Phi$ -dependences. With fits including these harmonics up to order two, used for example in [17],

$$R_{\text{side}}^2 = R_{\text{side},0}^2 + R_{\text{side},1}^2 \cos(\Phi) + R_{\text{side},2}^2 \cos(2\Phi), \quad (4.50)$$

one is able to identify the approximate variances by

$$\begin{aligned} \sigma_x^2 &\approx \sigma_x'^2 = R_{\text{side},0}^2 - 2R_{\text{side},2}^2, \\ \sigma_y^2 &\approx \sigma_y'^2 = R_{\text{side},0}^2 + 2R_{\text{side},2}^2, \\ \sigma_z^2 &\approx \sigma_z'^2 = R_{\text{long},0}^2 \end{aligned} \quad (4.51)$$

and calculate the  $xy$ -eccentricity in simplified form as

$$\varepsilon_{xy} \approx \varepsilon'_{xy} = \frac{\sigma_y'^2 - \sigma_x'^2}{\sigma_y'^2 + \sigma_x'^2} = \frac{2R_{\text{side},2}^2}{R_{\text{side},0}^2}, \quad (4.52)$$

and the  $zy$ -eccentricity as

$$\varepsilon_{zy} \approx \varepsilon'_{zy} = \frac{\sigma_y'^2 - \sigma_z'^2}{\sigma_y'^2 + \sigma_z'^2} = 1 - \frac{2R_{\text{long},0}^2}{R_{\text{side},0}^2 + 2R_{\text{side},2}^2 + R_{\text{long},0}^2}. \quad (4.53)$$

Equations (4.52) and (4.53) require at least a small tilt angle  $\theta_s$ . Its effect is illustrated in Appendix B.6.

# 5 | Results

The presentation of the results is structured into three parts. First, the correlation functions are presented in general. After that, the extracted HBT parameters within the azimuthally integrated analysis are considered. Last, the azimuthally dependent HBT radius parameters and derived geometrical quantities are presented.

## 5.1 Correlation functions

In this section, the experimental correlation functions (4.19) and (4.20) are exhibited. While for the invariant two-pion distributions one can easily plot the correlation functions, for the three-dimensional case projections, either one- or two-dimensional given by Equations (4.22) and (4.23), respectively, have to be used. Although such projections can break the Gaussian form of the correlation signal and never should be used for fitting, they can somehow illustrate the quality of the experimental correlation functions and show potential sources of systematic uncertainties.

### 5.1.1 One-dimensional correlation function

In Figures 5.1 and 5.2, the invariant correlation function (4.20) for low values of  $q_{\text{inv}}$  between 0 and 100 MeV/c of the 10 % most central events are plotted. On the left side, the results for  $\pi^-\pi^-$  pairs are shown and on the right side the results for  $\pi^+\pi^+$  pairs, respectively. The panels belong to different intervals of pair transverse momentum  $p_{t,12}$  with increasing values in downwards direction, starting at 100 MeV/c on top of Figure 5.1 and ending at 900 MeV/c at bottom of Figure 5.2. All plots show clearly a correlation signal at lower values of  $q_{\text{inv}}$ , which flattens out towards unity for higher relative momenta. For the larger pair transverse momenta, the correlation (as deviation from unity) is visible up to values of  $q_{\text{inv}} \approx 50$  MeV/c, while for low  $p_{t,12}$  the enhancement of  $C(q_{\text{inv}})$  vanishes obviously already at  $q_{\text{inv}} \approx 40$  MeV/c for  $\pi^+\pi^+$  and at  $q_{\text{inv}} \approx 30$  MeV/c for  $\pi^-\pi^-$ , respectively. The red solid curves show the fits with Equation (4.26) to the experimental correlation function, which can be separated into the Coulomb part (green

## 5. Results

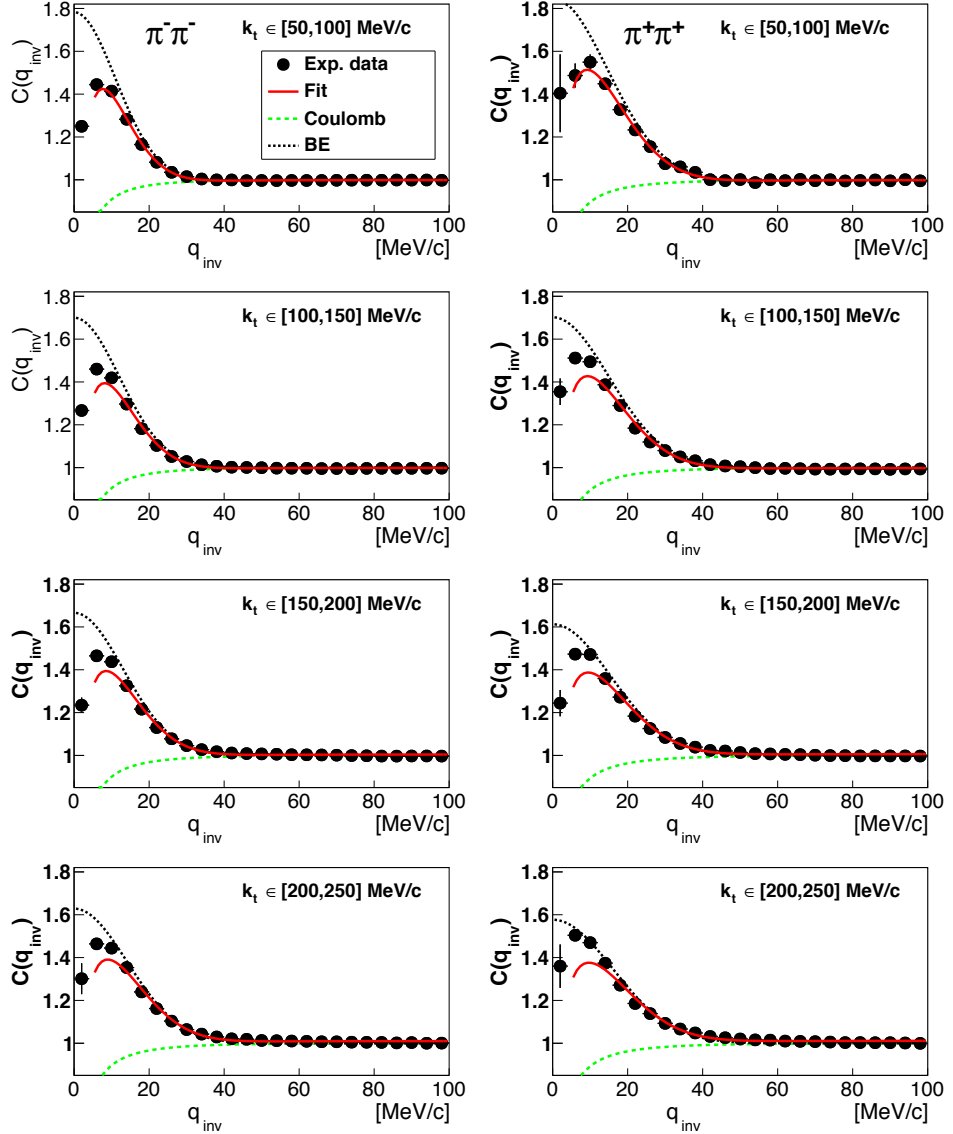


**Figure 5.1:** The correlation function  $C(q_{\text{inv}})$ , Equation (4.20), for  $\pi^-\pi^-$  (left panels) and  $\pi^+\pi^+$  (right panels) and transverse pair momenta  $p_{t,12}$  from 100 to 500 MeV/c (increasing from top to bottom) in the 0 – 10% centrality class. Black circles are experimental data, the red solid curve is a fit with Equation (4.26) containing the BE part (dotted black curve) and the Coulomb part (dashed green curve).

dashed curves) and the quantum-statistical Bose-Einstein part (dotted black curves). Apparently, the fit function describes the data quite good for values of  $q_{\text{inv}}$  larger than 15 MeV/c in all panels. However, for  $q_{\text{inv}} < 15$  MeV/c

## 5.1 Correlation functions

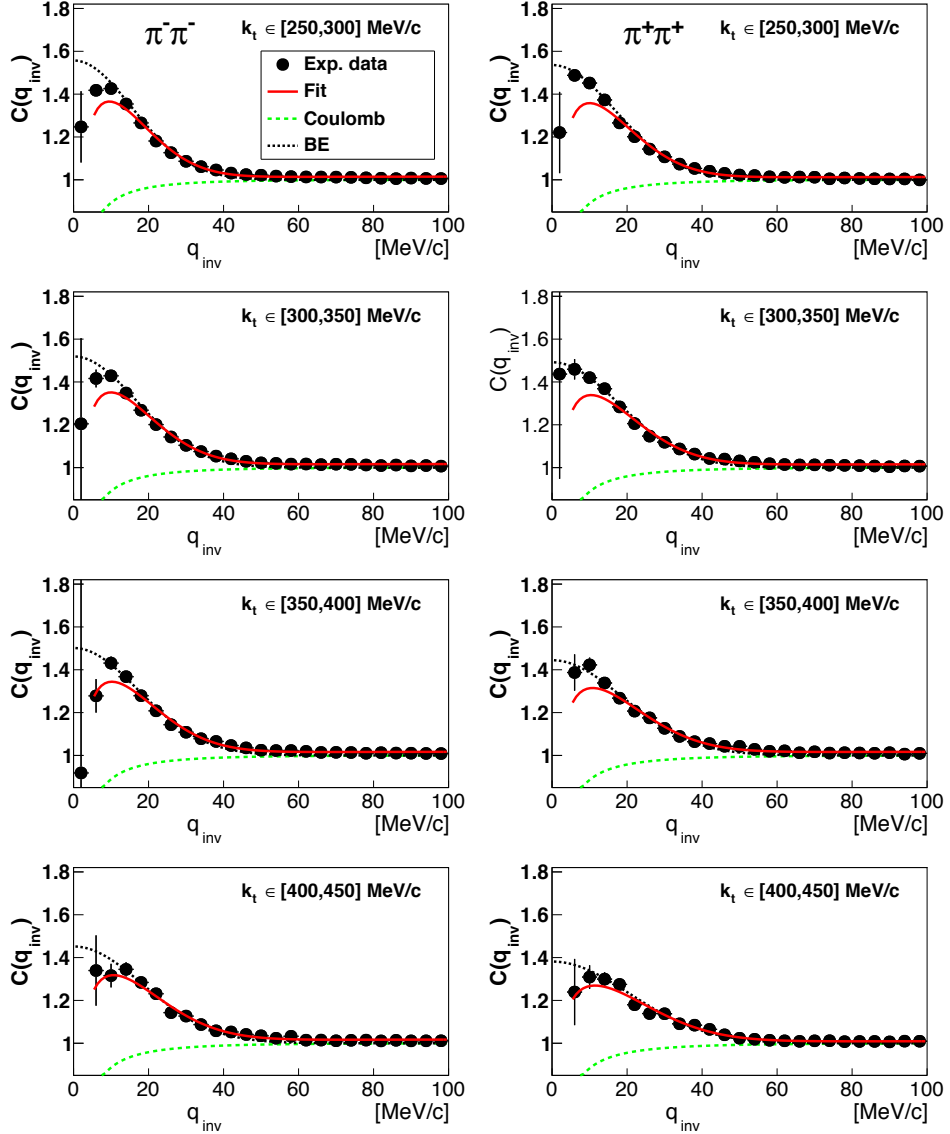


**Figure 5.2:** Same as Figure 5.1, but for  $p_{t,12}$  from 500 to 900 MeV/c (increasing from top to bottom).

only for the highest and the lowest exhibited interval of  $k_t = p_{t,12}/2$  the fit reproduces all the data points within their statistical uncertainties. For the other intervals, the fitted curves do slightly underestimate the data. This might hint at deviations from a Gaussian source, caused e.g. by a superposition of directly emitted thermal pions with contributions from pion emitting resonances like  $\Delta$ 's. But before one considers physical reasons for this non-Gaussian behaviour one should be sure on the fact that the source can have

## 5. Results

---

different extensions in the 3+1 space-time directions with highly varying widths. In this case, one can not expect to get a reasonable description of the source size by the one-dimensionally averaged invariant correlation function and one should step forwards and continue with the explicit three-dimensional consideration.

### 5.1.2 Three-dimensional correlation function

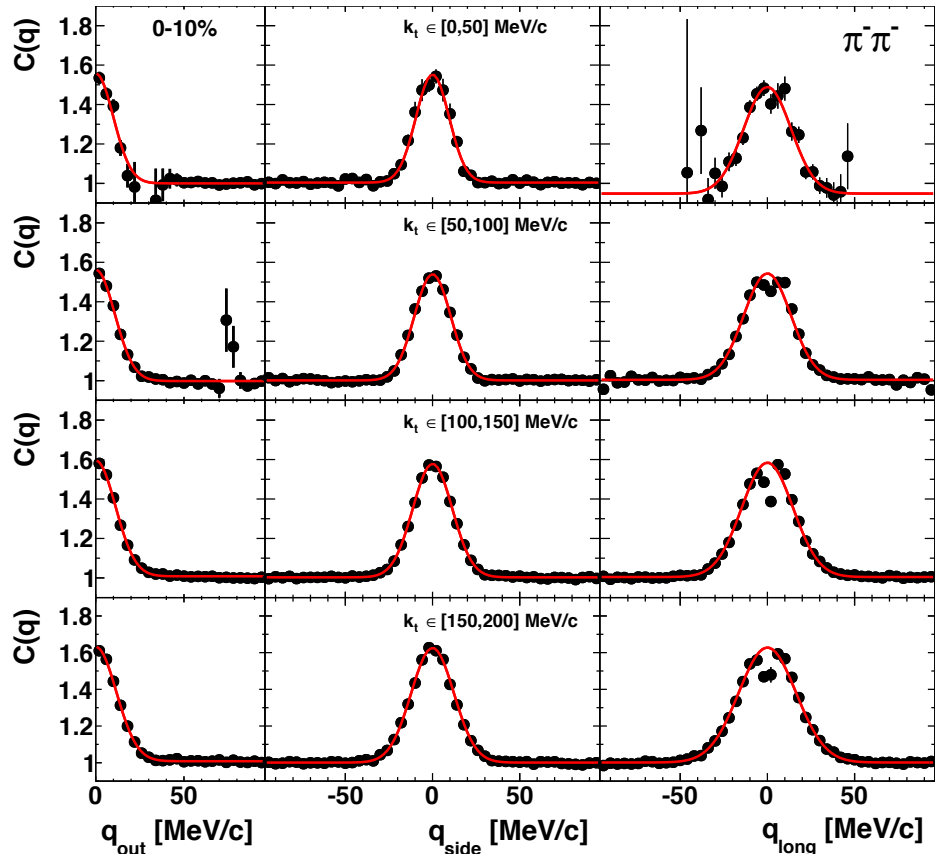


**Figure 5.3:** One-dimensional projections of the Coulomb-corrected three-dimensional correlation function  $C(q_{\text{out}}, q_{\text{side}}, q_{\text{long}})$  for  $\pi^-\pi^-$  and  $p_{t,12}$  from 0 to 400 MeV/c in the 0 – 10 % centrality class. The two other components of  $\vec{q}$  are integrated over the interval 0 to 12 MeV/c. The red curves depict Gaussian fits.

In Figures 5.3 and 5.4 one-dimensional projections (4.22) of the final-state Coulomb-corrected three-dimensional correlation function  $C(q_{\text{out}}, q_{\text{side}}, q_{\text{long}})$  are plotted in direction of  $q_{\text{out}}$  (left column),  $q_{\text{side}}$  (center column) and  $q_{\text{long}}$  (right column) for  $\pi^-\pi^-$  and  $p_{t,12}$  from 0 to 800 MeV/c in the 0 – 10 % centrality class. In Figure 5.5 the same is shown, but for  $\pi^+\pi^+$  and  $p_{t,12}$

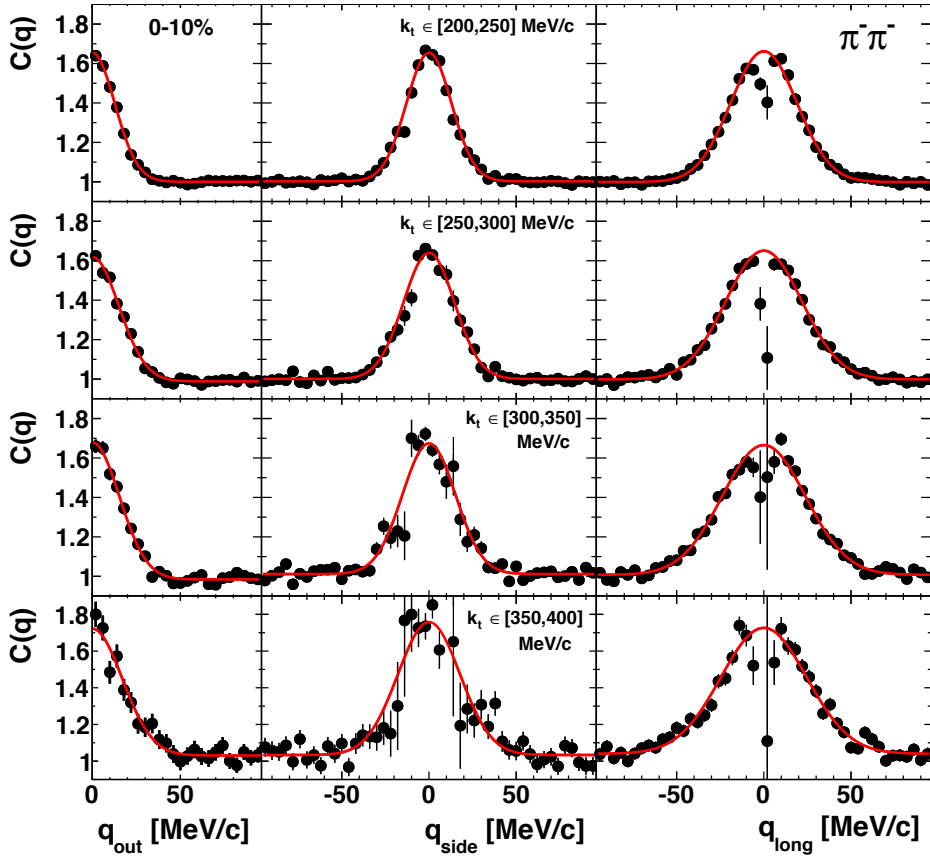


**Figure 5.4:** Same as Figure 5.3, but for  $p_{t,12}$  from 400 to 800 MeV/ $c$

from 100 to 800 MeV/ $c$ . The projections are formed by integrating the true and the mixed pair distributions  $A(\vec{q})$  and  $B(\vec{q})$  over two of the three relative distances from 0 to 12 MeV/ $c$ . The two-particle Coulomb contribution introduced in Section 2.3.1 was subtracted point by point according to Equations (4.28) to (4.30). The red curves are Gaussian fits to the bare projection data points. Except the points nearest to  $q_i = 0$  data is fitted quite well by these curves, supporting the assumption of a three-dimensional Gaussian correlation signal.

In Figures 5.6 and 5.7, two-dimensional projections (4.23) of the three-dimensional correlation function  $C(q_{\text{out}}, q_{\text{side}}, q_{\text{long}})$  are plotted (without Coulomb correction),  $q_{\text{out}}$  vs.  $q_{\text{side}}$  (left column),  $q_{\text{out}}$  vs.  $q_{\text{long}}$  (center column) and  $q_{\text{side}}$  vs.  $q_{\text{long}}$  (right column), for  $\pi^- \pi^-$  and  $p_{t,12}$  from 0 (top of Figure 5.6) to 800 MeV/ $c$  (bottom of Figure 5.7) for 0–10 % centrality. In Figures 5.8 and 5.9, the same is shown for  $\pi^+ \pi^+$  and  $p_{t,12}$  from 100 to 800 MeV/ $c$ . The projections are formed by integrating the true and the mixed distributions  $A(\vec{q})$  and  $B(\vec{q})$  over the corresponding third relative

## 5. Results

---

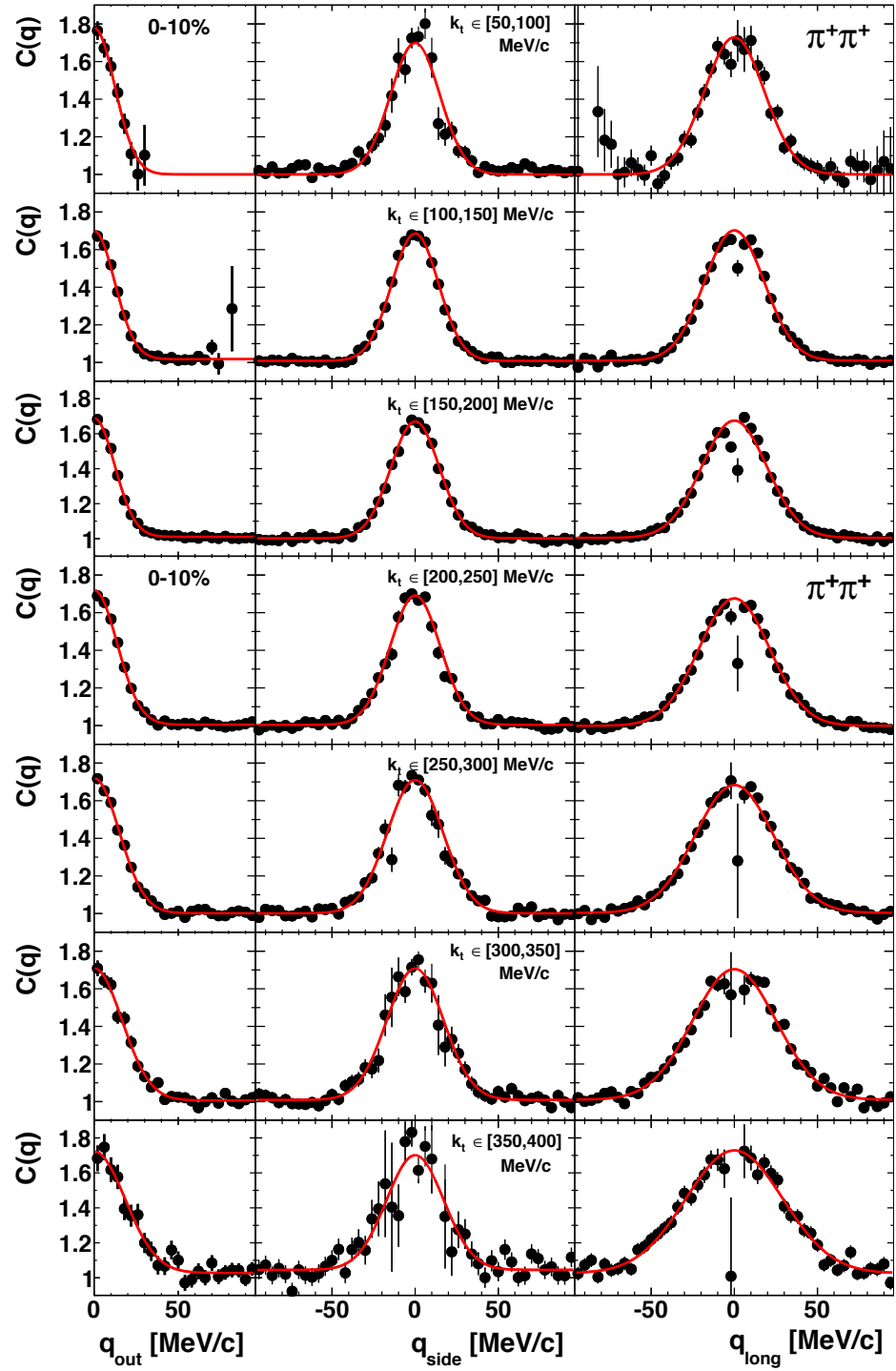


**Figure 5.5:** Same as Figure 5.3, but for  $\pi^+\pi^+$  and  $p_{t,12}$  from 100 to 800 MeV/c

## 5.1 Correlation functions

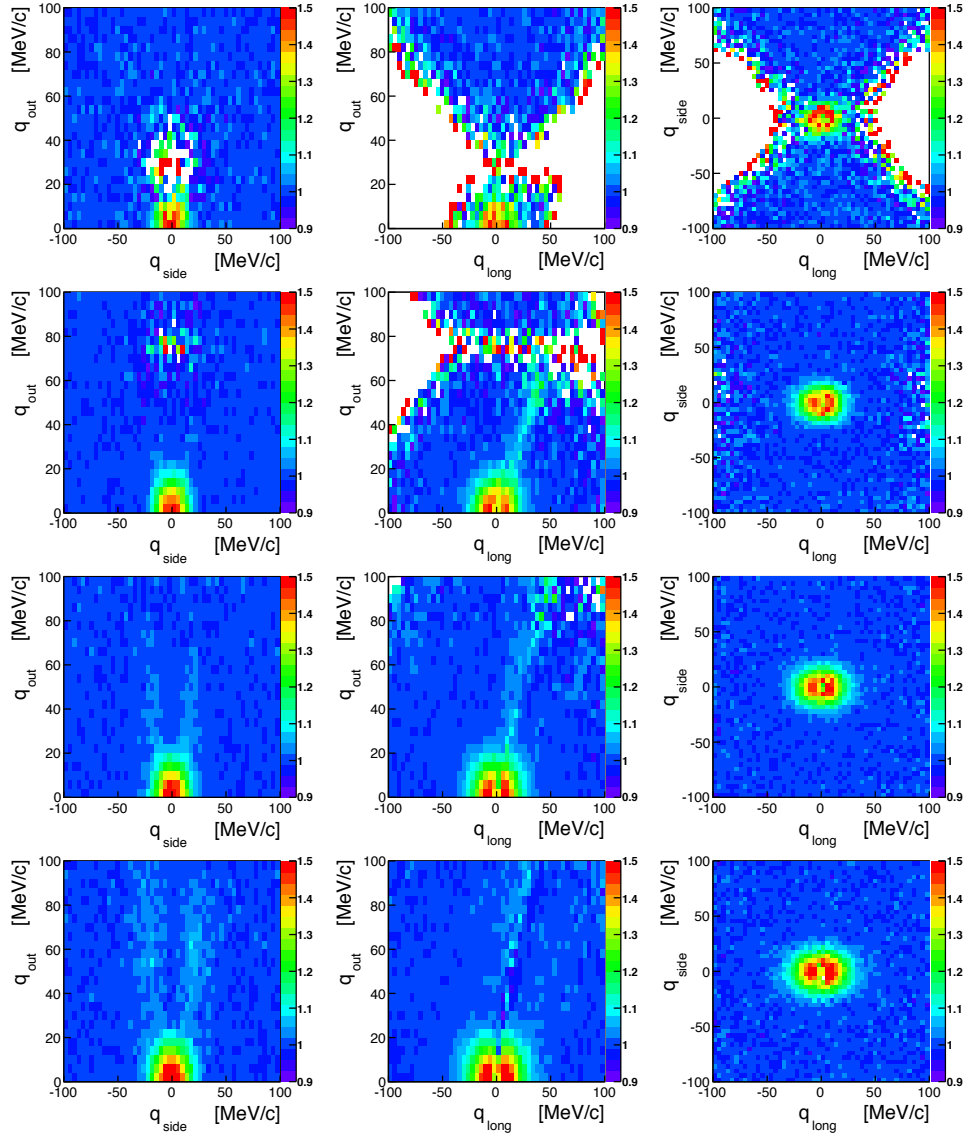


**Figure 5.6:** Two-dimensional projections of the three-dimensional correlation function  $C(q_{\text{out}}, q_{\text{side}}, q_{\text{long}})$  for  $\pi^-\pi^-$  and  $p_{t,12}$  from 0 to 400 MeV/c for 0 – 10 % centrality (left:  $q_{\text{out}}-q_{\text{side}}$  plane, middle:  $q_{\text{out}}-q_{\text{long}}$  plane, right:  $q_{\text{side}}-q_{\text{long}}$  plane). The third component of  $\vec{q}$  is integrated from 0 to 12 MeV/c.

distances from 0 to 12 MeV/c. The two-dimensional projections show a clear correlation signal at small values of  $|q_i|$  and mainly a flat distribution at higher values of  $|q_i|$ , typically at  $|q_i| > 50$  MeV/c. The maxima of the correlation signals are mostly not in the bins with smallest values of  $|q_i|$ , but one or two bins outside due to the underlying two-particle final-state

## 5. Results

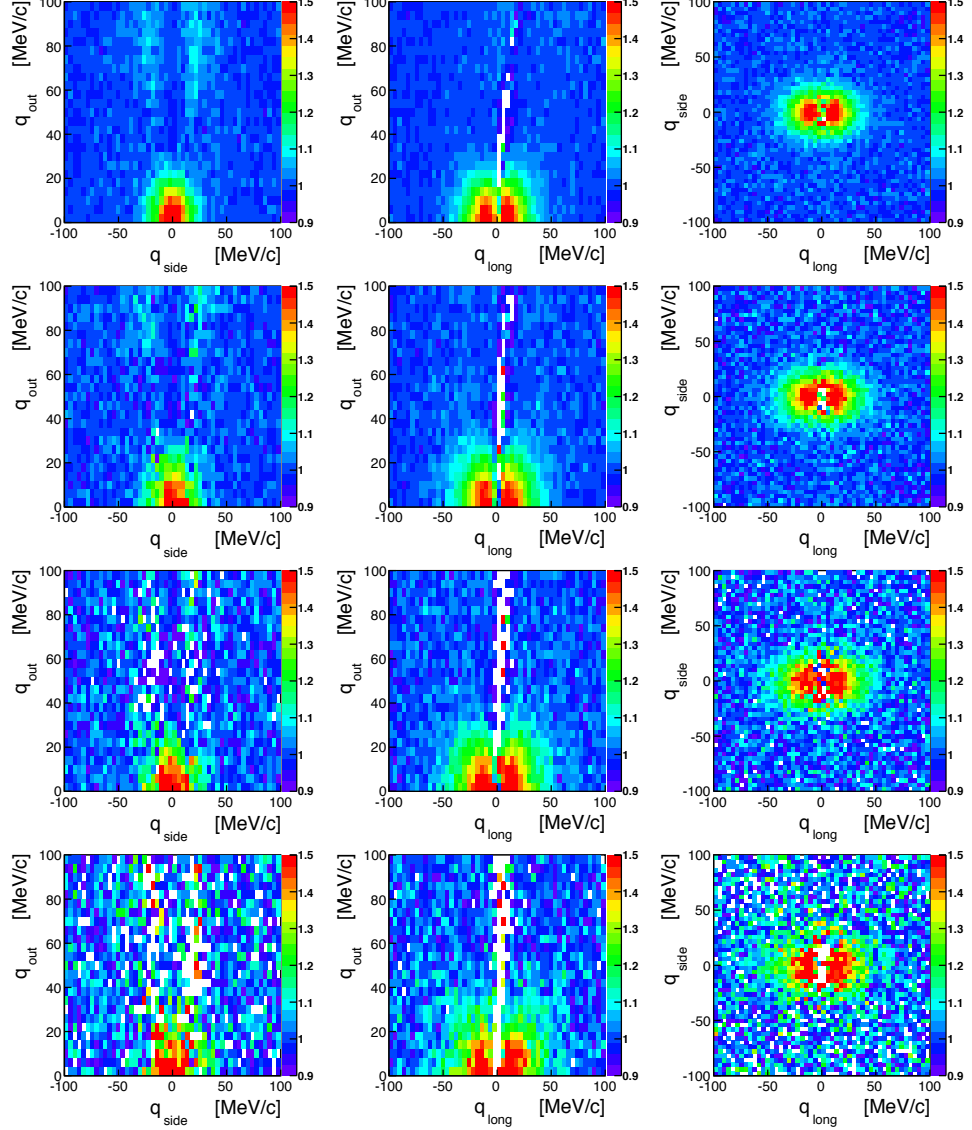


**Figure 5.7:** Same as Figure 5.6, but for  $p_{t,12}$  from 400 to 800 MeV/c

Coulomb repulsion, introduced in Section 2.3.1. However, there are at least two perturbations of the ideal picture of the correlation function. First, a region of vanishing pair statistics, visible at lower values of  $p_{t,12}$  and more intense in the  $\pi^+\pi^+$  plots, and secondly a line-shaped valley, visible in the left and central columns of Figures 5.6 to 5.9, changing its position slightly with  $p_{t,12}$ . This second perturbation is also obvious in Figures 5.3 to 5.5, prominent at low values of  $q_{\text{long}}$  and in the disappearing statistics of  $q_{\text{side}}$  at higher values of  $p_{t,12}$ . The first feature is explainable with the acceptance

## 5.1 Correlation functions

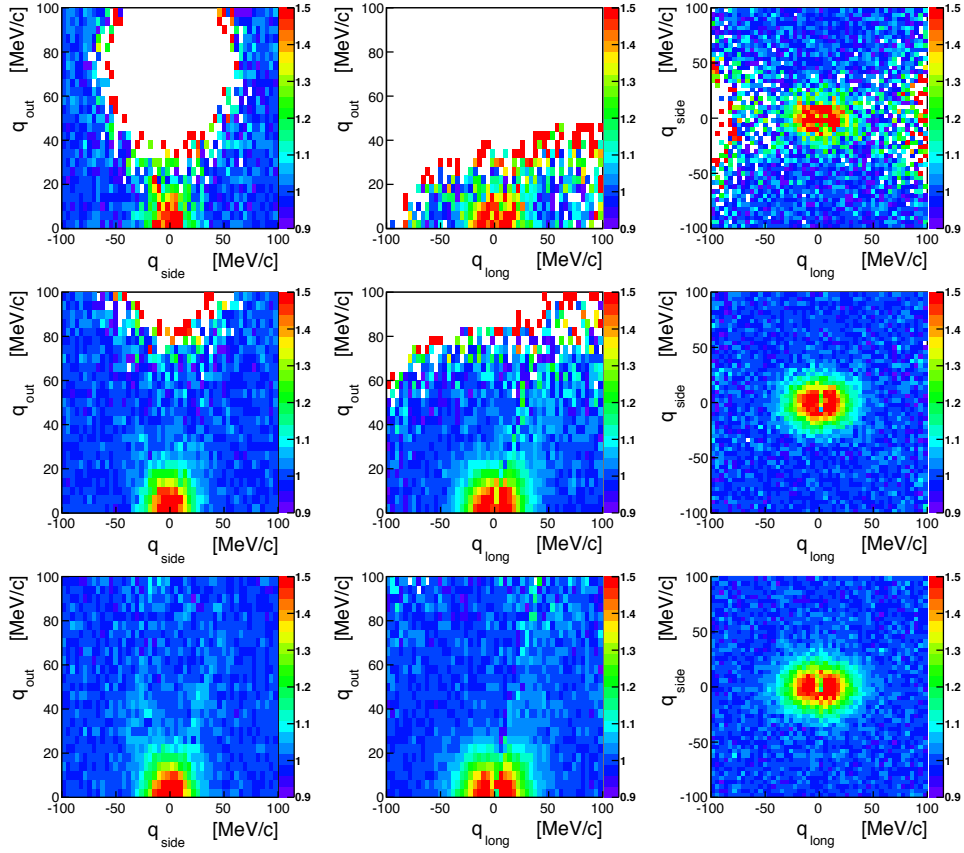


**Figure 5.8:** Same as Figure 5.6, but for  $\pi^+\pi^+$  and  $p_{t,12}$  from 100 to 400 MeV/c.

of the HADES set-up and a sharp cut in phase space of the pion pairs. As consequence one has to look carefully from one phase-space bin to the next, whether the region with the correlation signal is influenced and whether still a region with enough pair statistics for the normalisation is available. The second issue is related to the data-driven closed-pair cut introduced in Section 4.3.4 and again a sharp phase-space cut, e.g. in  $p_{t,12}$ , which leads to suppressed regions in the three-dimensional  $\vec{q}$ -space. Not visible in Figures 5.6 to 5.9 are the statistical errors of the data, which are more than a factor 2 higher in these critical regions, up to enormously high values for low statistics bins. That means, examining only the two-dimensional projections of  $C(q_{\text{out}}, q_{\text{side}}, q_{\text{long}})$  this issue is overestimated and has practically no influence on subsequent fits with Equation (4.28).

Figures 5.10 and 5.11 show two-dimensional projections of the three-dimensional correlation function  $C(q_{\text{out}}, q_{\text{side}}, q_{\text{long}})$  over the  $q_{\text{out}}$  vs.  $q_{\text{side}}$  plane (left column),  $q_{\text{out}}$  vs.  $q_{\text{long}}$  plane (center column) and  $q_{\text{side}}$  vs.  $q_{\text{long}}$  plane

## 5. Results

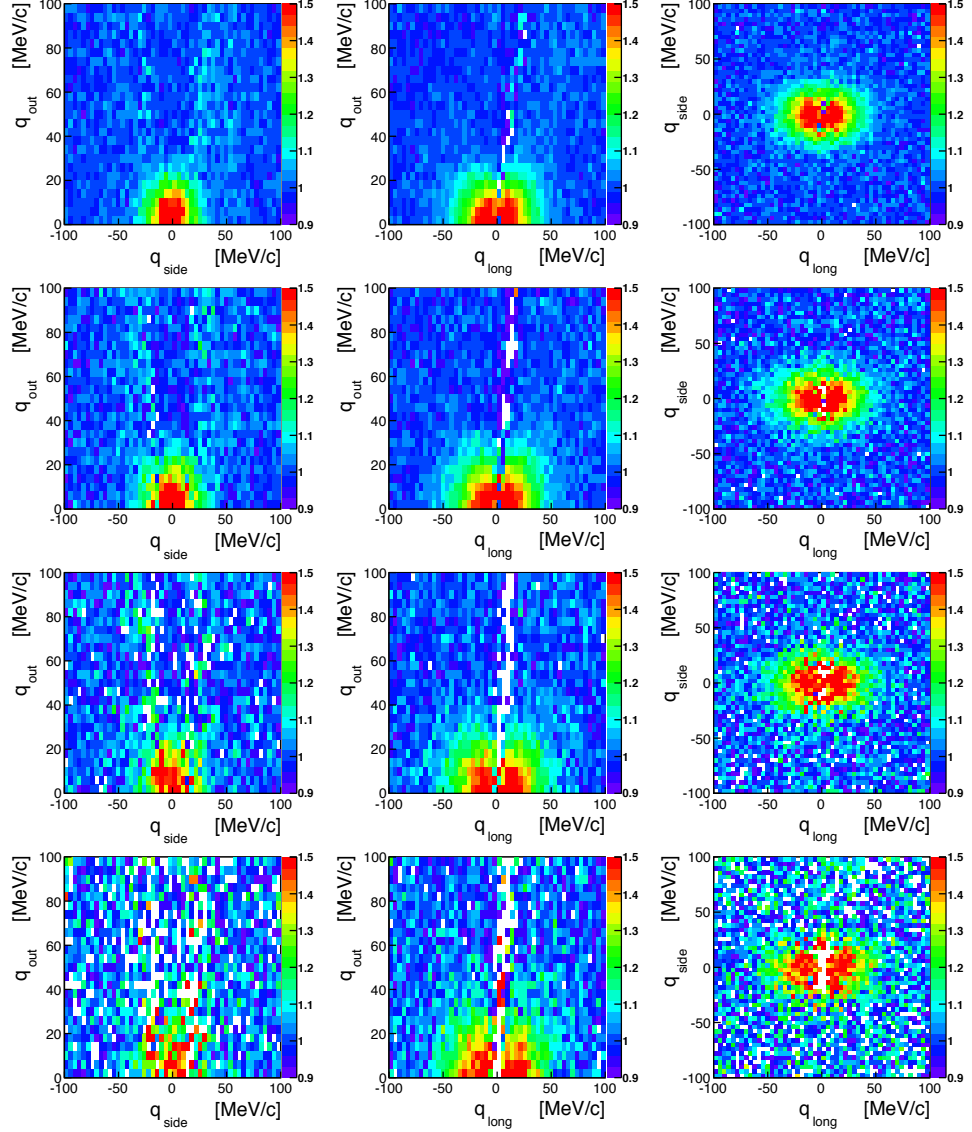


**Figure 5.9:** Same as Figure 5.8, but for  $p_{t,12}$  from 400 to 800 MeV/c

(right column), for  $\pi^-\pi^-$  integrated over  $p_{t,12}$  from 200 to 500 MeV/c for 0–10 % centrality for the eight  $\Phi$  bins defined in Section 4.3.2 (see figure captions for the actual intervals of  $\Phi$ ). Again, a flat distribution at higher values of  $|q_i|$  and a clear correlation signal at small values of  $|q_i|$  can be seen. Going from one projection to the next in direction of the azimuthal angle relative to the event plane  $\Phi$ , the elliptic correlation region changes smoothly its orientation. The above mentioned 2<sup>nd</sup> perturbation is even less visible here, since it is smeared out with respect to the larger  $p_{t,12}$  range.

## 5.1 Correlation functions

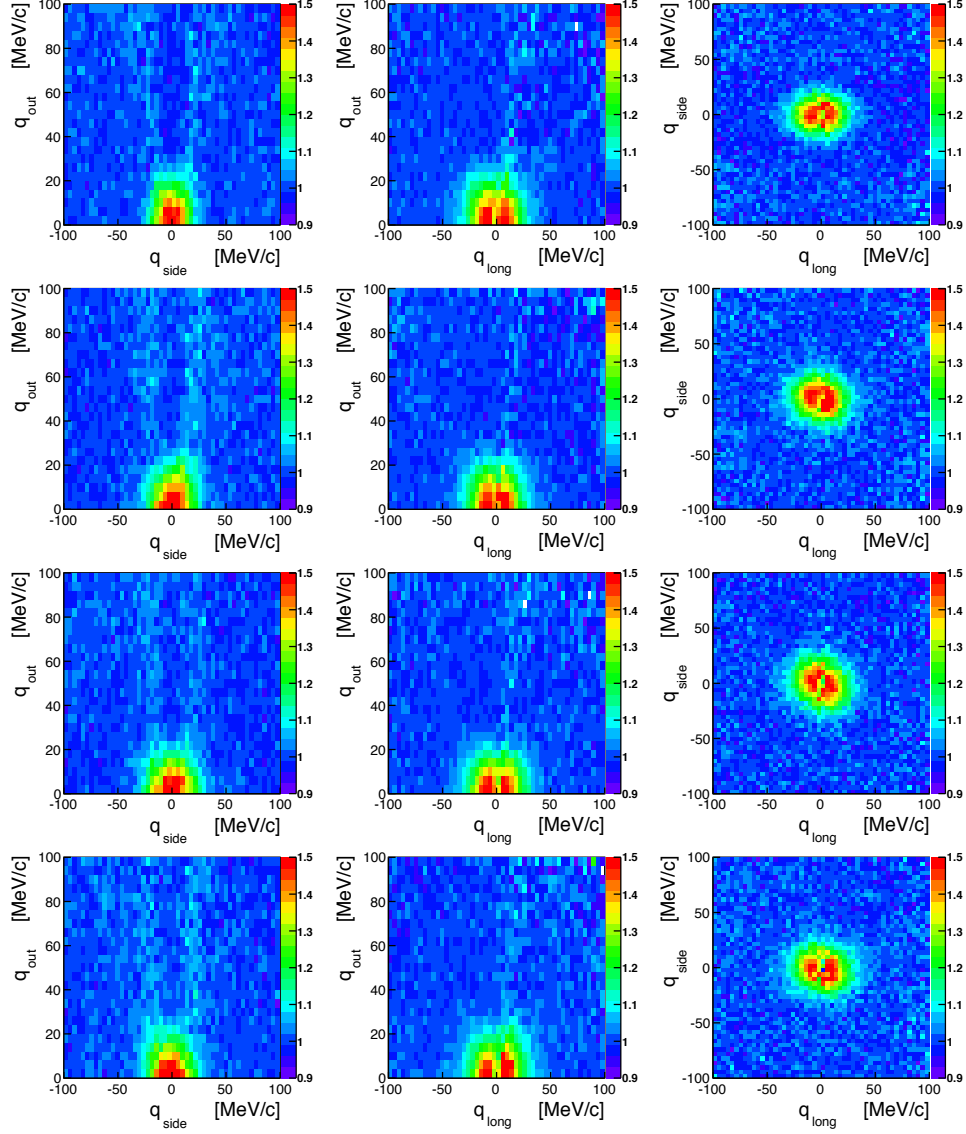


**Figure 5.10:** Two dimensional projections of the three-dimensional correlation function  $C(q_{\text{out}}, q_{\text{side}}, q_{\text{long}})$  for  $\pi^- \pi^-$  and  $p_{t,12}$  integrated from 200 to 500 MeV/c for 0 – 10 % centrality for mean azimuthal angles  $\Phi = \{0^\circ, 45^\circ, 90^\circ, 135^\circ\}$  (from top to bottom) relative to the event plane. The third component of  $\vec{q}$  is integrated over 0 to 12 MeV/c.

## 5. Results

---

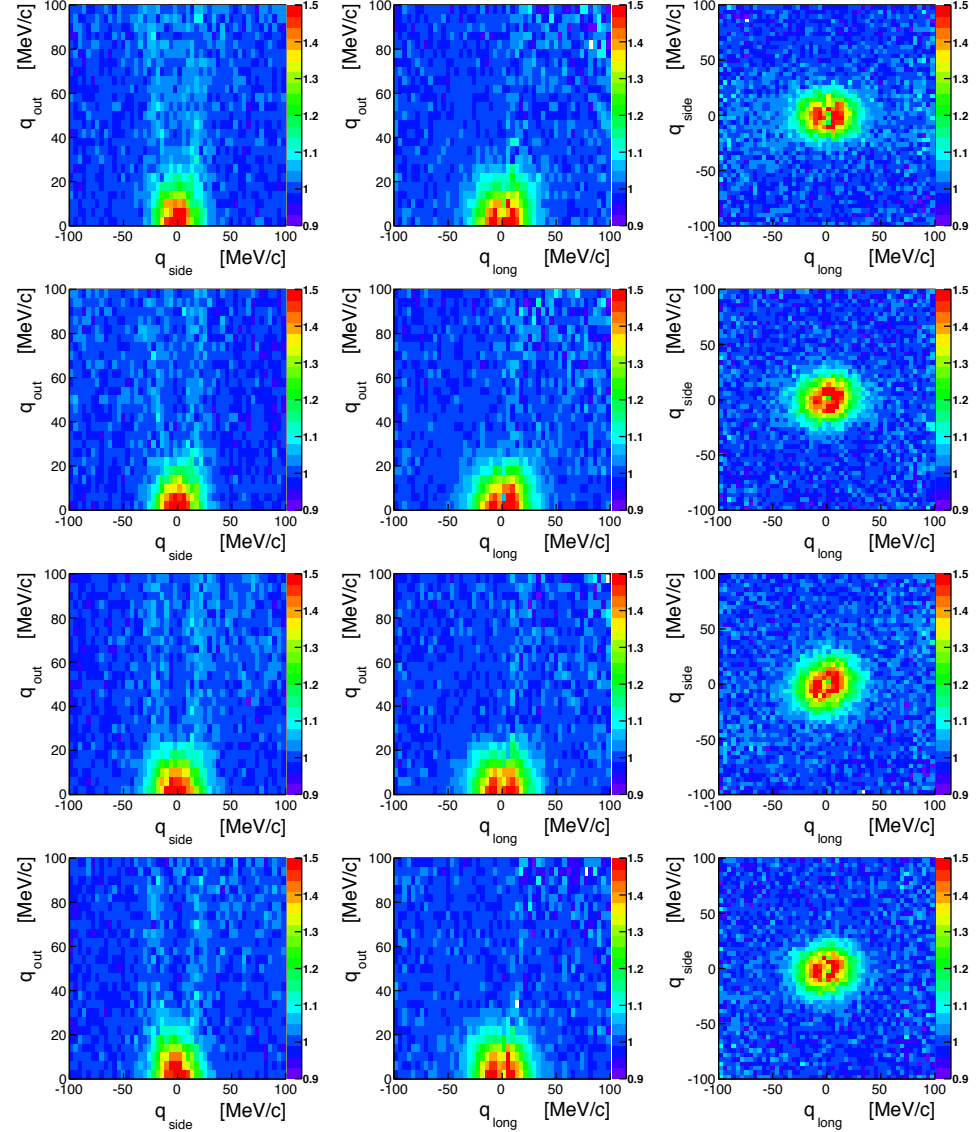


**Figure 5.11:** Same as Figure 5.10, but for mean azimuthal angles  $\Phi = \{180^\circ, 225^\circ, 270^\circ, 315^\circ\}$  (from top to bottom) relative to the event plane.

## 5.2 Azimuthally integrated correlations

In this section exclusively results of  $\Phi$ -integrated correlation functions are considered. Attention is payed to the dependence on  $p_{t,12}$  of the femtosopic radii  $R_{\text{inv}}$ ,  $R_{\text{out}}$ ,  $R_{\text{side}}$  and  $R_{\text{long}}$ , the scaling with centrality, differences related to the pion polarity and the comparison with results available at other beam energies.

### 5.2.1 Dependence on $p_{t,12}$ and centrality

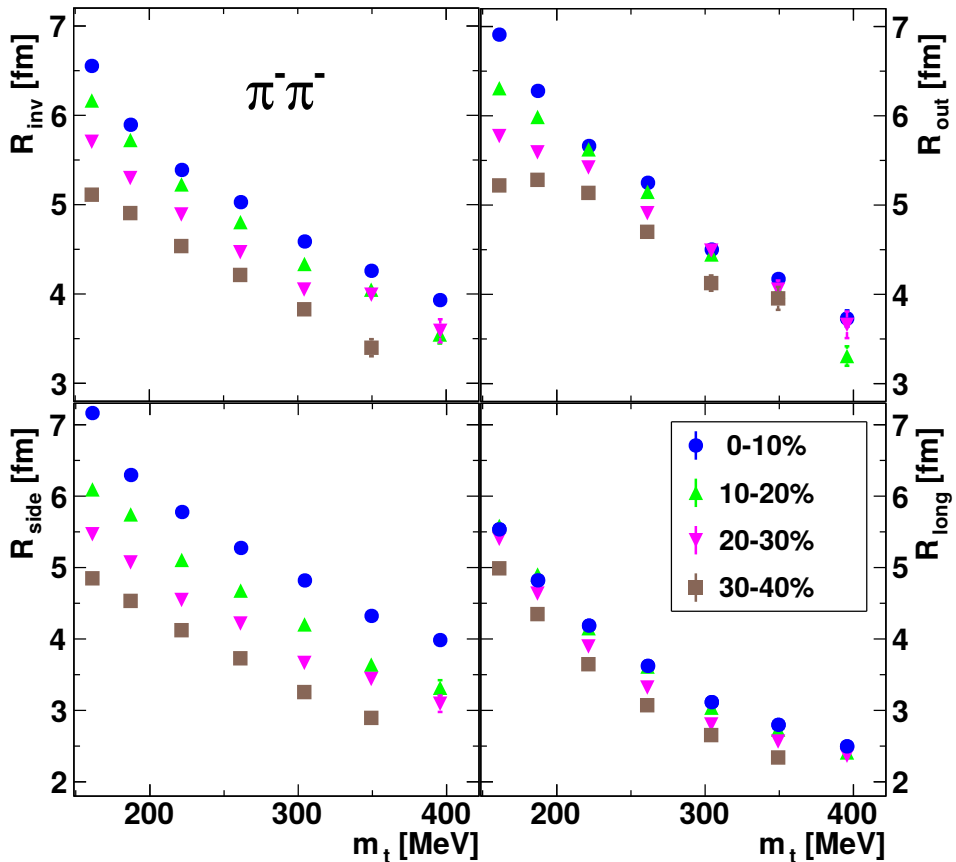


**Figure 5.12:**  $R_{\text{inv}}$  (top left),  $R_{\text{out}}$  (top right),  $R_{\text{side}}$  (bottom left) and  $R_{\text{long}}$  (bottom right) for  $\pi^- \pi^-$  and centrality classes 0 – 10 % (blue circles), 10 – 20 % (green up-pointing triangles), 20 – 30 % (violet down-pointing triangles), 30 – 40 % (brown boxes) in dependence on  $m_t = (k_t^2 + m_\pi^2)^{1/2}$ . Error bars contain only statistical uncertainties.

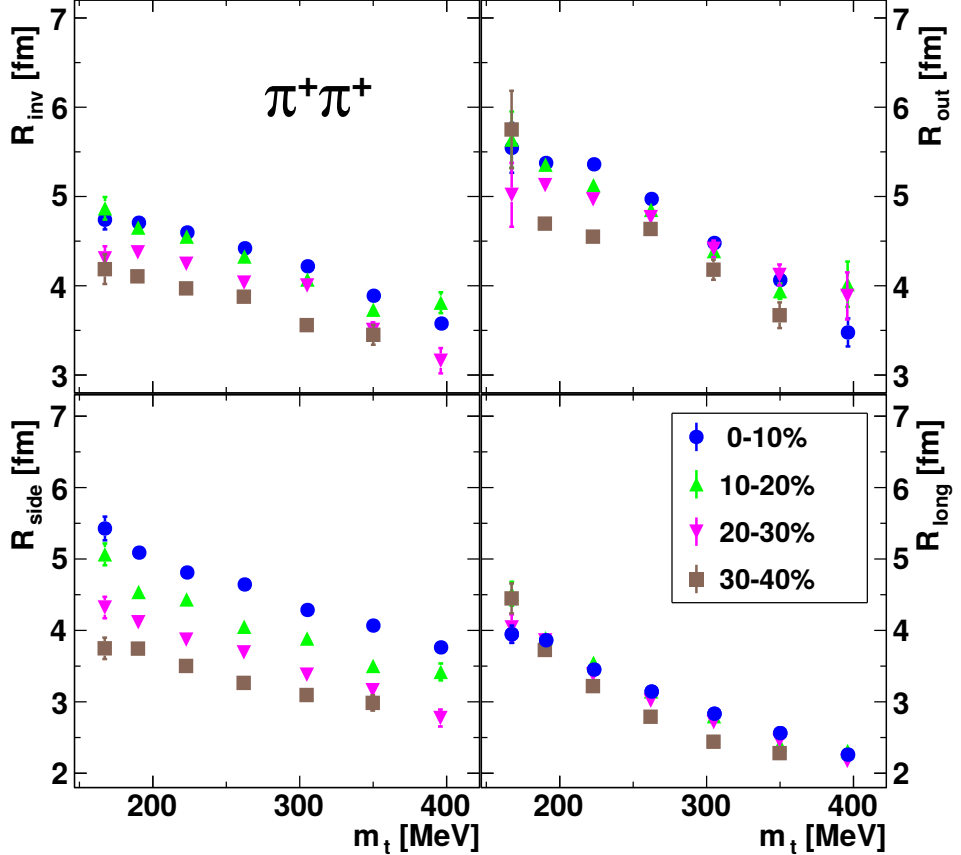


**Figure 5.13:** Same as Fig. 5.12, but for  $\pi^+\pi^+$ .

In the previous section, it has been shown that the correlation functions  $C(q_{\text{inv}})$  and  $C(q_{\text{out}}, q_{\text{side}}, q_{\text{long}})$  can be well fitted with Equations (4.26) and (4.28), i.e. pointing to a Gaussian correlation signal flattening out towards  $C = 1$  for large values of  $|q_i|$ . In Figure 5.12, the fit results of  $R_{\text{inv}}$ ,  $R_{\text{out}}$ ,  $R_{\text{side}}$  and  $R_{\text{long}}$  in dependence on  $m_t = (k_t^2 + m_\pi^2)^{1/2}$  are plotted for  $\pi^-\pi^-$  and four 10 % centrality classes within 0 – 40 %. All radii decrease with increasing values of  $m_t$  and for higher centrality. The spreading in direction of centrality is best visible in  $R_{\text{side}}$ . The overall hierarchy  $R_{\text{out}} > R_{\text{side}} > R_{\text{long}}$  can be observed, except for most central collisions and large values of  $m_t$ , where  $R_{\text{side}}$  almost equals  $R_{\text{out}}$  or can even be larger. The value of  $R_{\text{inv}}$  is always within the span of the values of  $R_{\text{out}}$ ,  $R_{\text{side}}$  and  $R_{\text{long}}$  and seems to give an average length of homogeneity. In Figure 5.13, the same as Figure 5.12, but for  $\pi^+\pi^+$  is plotted. The  $\pi^+\pi^+$  radii have the same trends w.r.t. the  $m_t$  dependence and centrality as the  $\pi^-\pi^-$  radii, but are found to be smaller.

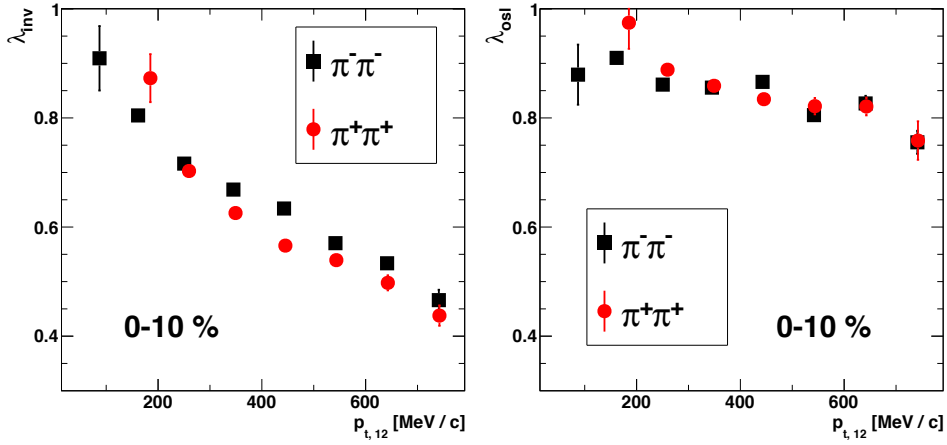


**Figure 5.14:**  $\lambda$  parameters from fits of Eq. (4.26) to  $C(q_{\text{inv}})$  (left) and Eq. (4.28) to  $C(q_{\text{out}}, q_{\text{side}}, q_{\text{long}})$  (right) as a function of  $p_{t,12}$  for  $\pi^- \pi^-$  (black boxes) and  $\pi^+ \pi^+$  (red circles) for 0 – 10 % centrality.

This charge-sign difference will be considered more in detail in Section 5.2.4. In Figure 5.14, the parameters  $\lambda_{\text{inv}}$  from the fit with Equation (4.26) (left panel) and  $\lambda_{\text{osl}}$  from the three-dimensional fit with Equation (4.28) (right panel) are plotted in dependence of  $p_{t,12}$  for the centrality 0 – 10 %. Black boxes belong to  $\pi^- \pi^-$  and red circles to  $\pi^+ \pi^+$  data. While  $\lambda_{\text{osl}}$  decreases only less with increasing values of  $p_{t,12}$  and has mainly values between 0.8 and 0.9,  $\lambda_{\text{inv}}$  displays a stronger dependence on  $p_{t,12}$  with values around 0.9 at low  $p_{t,12}$  decreasing down to values of about 0.45 for high transverse pair momenta. The deviations between  $\lambda_{\text{osl}}$  and  $\lambda_{\text{inv}}$  with increasing values of  $p_{t,12}$  are a hint at the failure of a Gaussian invariant correlation function ansatz for describing the extension of the homogeneity regions correctly. Already in the expression (4.29) one could see that, for  $\beta_t \rightarrow 1$ ,  $q_{\text{inv}}$  can be small, even if  $q_{\text{out}}$  is not small, and then  $R_{\text{inv}}$  may overestimate the average radius [105]. The trends of  $\pi^- \pi^-$  and  $\pi^+ \pi^+$  data are similar and mainly overlap with each other, but still there are a few points with a deviation of more than one sigma. One could argue for possible reasons for that, for instance anchored in charge-sign differences of the origins of a non-unique coherence parameter mentioned in Section 2.2.4. However, since Figure 5.14 does not include systematic errors, there is no substantial support for the conjecture of a difference between the  $\lambda$  parameters of  $\pi^- \pi^-$  and  $\pi^+ \pi^+$  data. Figure 5.15 shows the same data as Figures 5.12 and 5.13, but in dependence of the cubic root of the number of participants,  $A_{\text{part}}^{1/3}$ , for different values of  $p_{t,12}$  for  $\pi^- \pi^-$  (left column) and  $\pi^+ \pi^+$  (right column). All freeze-out radii follow mainly a linear trend in direction of  $A_{\text{part}}^{1/3}$ , as one would expect since  $A_{\text{part}}$  is supposed to be proportional to the freeze-out

## 5. Results

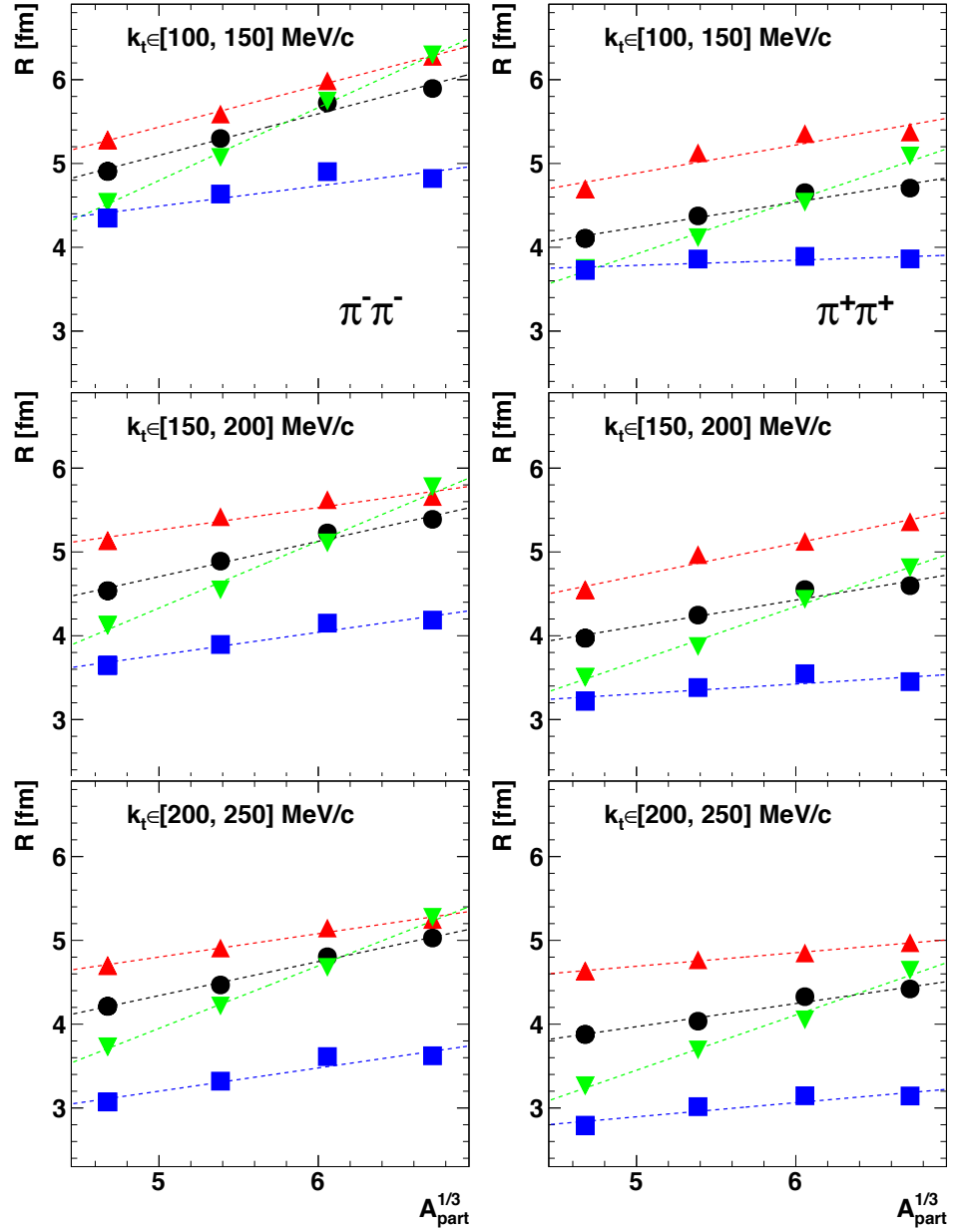


**Figure 5.15:**  $R_{\text{inv}}$  (black circles),  $R_{\text{out}}$  (red up-pointing triangles),  $R_{\text{side}}$  (green down-pointing triangles) and  $R_{\text{long}}$  (blue boxes) for  $\pi^- \pi^-$  (left panel) and  $\pi^+ \pi^+$  (right panel) for  $p_{t,12}$  from 200 to 300  $\text{MeV}/c$  (upper panels), 300 to 400  $\text{MeV}/c$  (middle panels), 400 to 500  $\text{MeV}/c$  (lower panels), as a function of the cubic root of the number of participants,  $A_{\text{part}}^{1/3}$ . Dashed lines are linear regressions to the data. Error bars contain only statistical uncertainties.

volume of the fireball. In all panels of Figure 5.15, it is clearly visible that  $R_{\text{side}}$  changes significantly with  $A_{\text{part}}^{1/3}$  and is therefore the most centrality dependent radius.

### 5.2.2 The cross-term $R_{\text{out long}}^2$ under variation of $y_{12}$

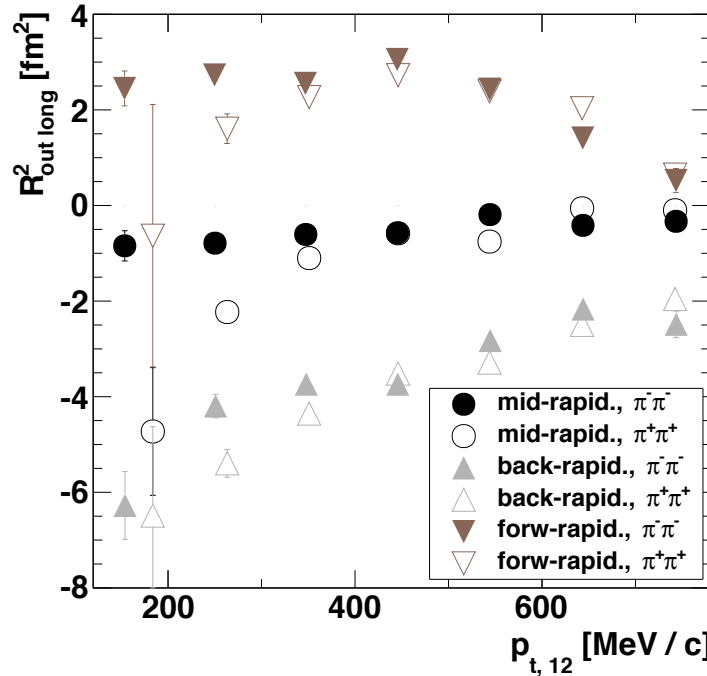


**Figure 5.16:** Cross-term  $R_{\text{out long}}^2$  from Equation (4.31) as a function of pair transverse momentum for 0 – 10 % centrality for  $\pi^- \pi^-$  (filled symbols) and  $\pi^+ \pi^+$  (open symbols). Black circles represent the rapidity window  $y_{12} \in [0.39, 1.09]$ , grey up-pointing triangles  $y_{12} \in [0.29, 0.69]$  and brown down-pointing triangles  $y_{12} \in [0.79, 1.19]$ , respectively.

In the previous section, only the diagonal HBT radius parameters of Equation (4.28) are shown, since at mid-rapidity all other components of  $R_{ij}$  should vanish due to symmetry constraints. In Figure 5.16 the non-diagonal parameter  $R_{\text{out long}}^2$  is exhibited for the 10% most central events in dependence on  $p_{t,12}$ . Filled symbols represent  $\pi^- \pi^-$  data and open symbols data of  $\pi^+ \pi^+$  pairs. The black circles are results for the above chosen window around mid-rapidity. In addition, the brown down-pointing triangles show results at forward-rapidity with values between 0.79 and 1.19 and the grey up-pointing triangles the results at backward-rapidity with values between 0.29 and 0.69, respectively. The values of  $R_{\text{out long}}^2$  are close to zero at mid-rapidity, while at forward rapidity, finite positive values and, at backward

## 5. Results

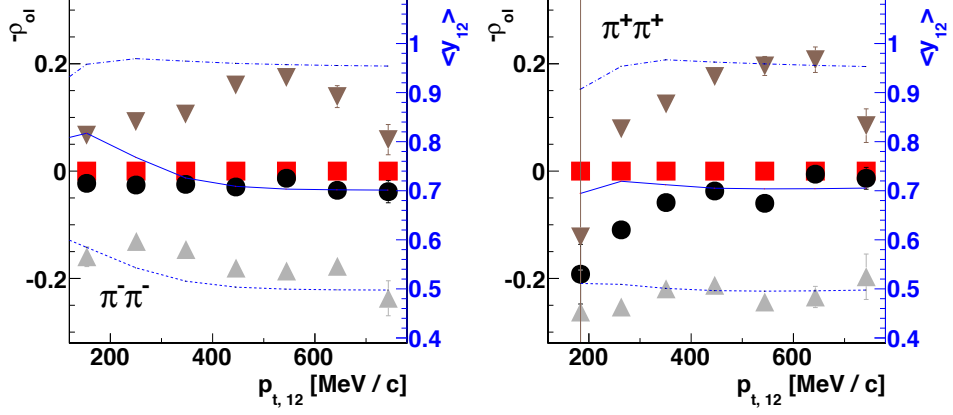


**Figure 5.17:** Correlation coefficient  $\rho_{\text{ol}}$ , defined in Equation (2.44), and the mean value of the chosen rapidity window (right scale) for  $\pi^-\pi^-$  (left panel) and  $\pi^+\pi^+$  (right panel) as a function of pair transverse momentum for 0 – 10 % centrality. Red squares represent fits without the cross-term  $R_{\text{out long}}^2$ ; other symbols and colors as in Figure 5.16. The blue curves belong to the rapidity intervals  $y_{12} \in [0.29, 0.69]$  (dashed),  $y_{12} \in [0.39, 1.09]$  (solid) and  $y_{12} \in [0.79, 1.19]$  (dashed-dotted).

rapidity, finite negative values are obtained. Although all pairs are boosted into the LCMS, where  $\beta_l$  of each pair vanishes, the mean value of the longitudinal velocity relative to mid-rapidity is finite. Therefore, Equation (2.41) delivers a positive value for  $R_{\text{out long}}^2$  at forward-rapidity and a negative value at backward-rapidity. There are only small differences between  $\pi^-\pi^-$  and  $\pi^+\pi^+$  data at high values of  $p_{t,12}$ , while at lower transverse momenta the data of  $\pi^+\pi^+$  pairs are significantly below those of  $\pi^-\pi^-$  pairs. To discuss the non-monotonous behaviour of  $R_{\text{out long}}^2$ , the linear correlation coefficient  $\rho_{\text{ol}}$  (2.44) is considered, exhibited in Figure 5.17. Colors and symbols are chosen in the same way as in Figure 5.16, and additional red boxes represent a vanishing correlation coefficient. The left panel belongs to  $\pi^-\pi^-$  and the right panel to  $\pi^+\pi^+$  pairs. In addition, the mean values of  $y_{12}$  in the chosen rapidity intervals at low values of  $\vec{q}$  are inserted as blue curves with the scale on the right side of the diagrams. The solid curve belongs to mid-rapidity, the dotted curve to backward rapidity, and the dashed curve to forward rapidity. If the average rapidity within the fixed rapidity intervals changes from one pair transverse momentum interval to the next one, one can expect that the values of  $\rho_{\text{ol}}$  or  $R_{\text{out long}}^2$ , respectively, are changing, too. Obviously, the trends of  $\rho_{\text{ol}}$  barely follow the trends of  $\langle y_{12} \rangle$ . However, taking a closer look one finds a correlation between them. If the correlation coefficient is constant or slightly decreasing one finds a clearly decreasing average pair rapidity like for the black circles and grey up-pointing triangles

in the  $\pi^-\pi^-$  panel of Figure 5.17. If  $\rho_{\text{ol}}$  is slightly increasing, like for backward rapidity of  $\pi^+\pi^+$  or forward rapidity of  $\pi^-\pi^-$  pairs, the dependences of  $p_{t,12}$  on  $\langle y_{12} \rangle$  are more or less negligible. Finally, for a strong increase at low values of  $p_{t,12}$ , visible in the trends of forward and mid-rapidity of  $\pi^+\pi^+$  pairs, one can see at least a small increase in the corresponding mean rapidity values. From this observations one can conclude that a correlation between  $\langle y_{12} \rangle$  and  $\rho_{\text{ol}}$  exists, but in addition something more affects the determination of  $R_{\text{out long}}^2$ , becoming significant especially at low values of  $p_{t,12}$ . Note that the diagonal HBT radius parameters depend only weakly on  $y_{12}$ . Setting  $R_{\text{out long}}^2$  explicitly to zero at mid-rapidity delivers no significant change of the HBT radius parameters, see Appendix B.1.

### 5.2.3 Other systematic influences

As visible for example in Figures 5.1 and 5.2, the fit functions (4.26) and (4.28) assuming a Gaussian source distribution do not perfectly match all experimental data points. Therefore, the fitted HBT parameters are affected by the choice of the fit intervals of the respective relative momentum quantities. To account for the possible fit-range dependence, a couple of variations has been applied to the fit range, listed in Table 5.1.

**Table 5.1:** Fit range variations in Equations (4.26) and (4.28) and possible constraints as well for generating Figures 5.18 to 5.20, used for systematic error investigations. In the three-dimensional case,  $q_{\text{inv}}$  is determined by Equation (4.29).

#	$q_{\text{inv}}^{\text{fit, min}}$ [MeV/c]	$q_{\text{inv}}^{\text{fit, max}}$ [MeV/c]	constraints
0	10	80	—
1	10	60	—
2	10	100	—
3	6	60	—
4	6	100	—
5	6	32	$C_{\text{norm}} = 1$
6	10	32	$C_{\text{norm}} = 1$

The results for  $R_{\text{inv}}$ ,  $R_{\text{out}}$ ,  $R_{\text{side}}$  and  $R_{\text{long}}$  are exhibited in Figure 5.18 for  $\pi^-\pi^-$  pairs and in Figure 5.19 for  $\pi^+\pi^+$  pairs, respectively. Apparently, the resulting fluctuations of the HBT radius parameters are small, typically within 0.1 to 0.3 fm. Only for  $R_{\text{inv}}$  of  $\pi^+\pi^+$  pairs, the changes are a bit larger, around 0.5 fm. This is the main contribution for the systematic uncertainties. Next to the fit range variations, a change of the pair rapidity interval is considered, one for backward-rapidity with  $y_{12} \in [0.39, 0.74]$  and one for forward-rapidity with  $y_{12} \in [0.74, 1.09]$ , depicted in Figures 5.18 and 5.19 as open downpointing triangles and open diamonds, respectively.

## 5. Results

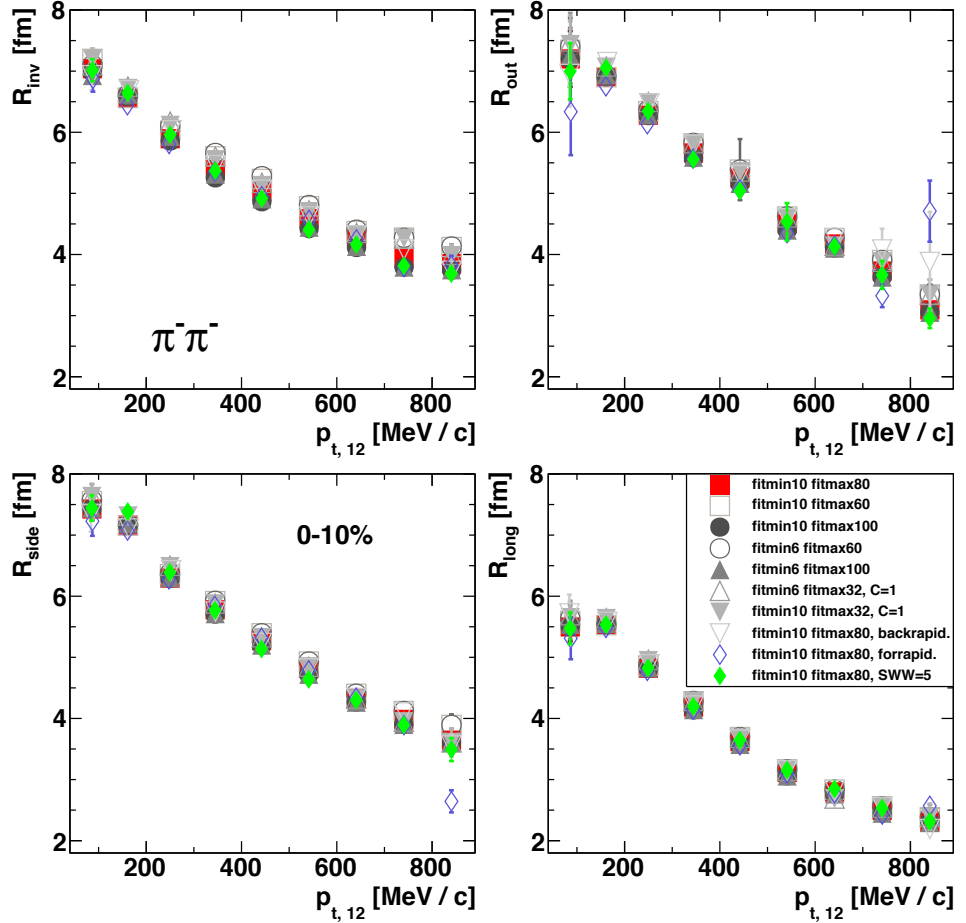


**Figure 5.18:** Systematic variations of the HBT radius parameters of the azimuthally integrated analysis in dependence of  $p_{t,12}$  for  $\pi^-\pi^-$  and 0 – 10 % centrality. In addition to the standard configuration (red filled boxes) the following settings are chosen: fit range of  $q_{\text{inv}}$  in units of  $\text{MeV}/c$  changed to [10,60] (open boxes), [10,100] (filled circles), [6,60] (open circles), [6,100] (filled up-pointing triangles), [6,32] (open up-pointing triangles), [10,32] (filled down-pointing triangles), where for the latter two ones an explicit condition is set on the second normalisation constant  $C = 1$ , see also Table 5.1. Open down-pointing triangles (open diamonds) denote a changed pair rapidity interval of [0.39,0.74] ([0.74,1.09]). Filled green diamonds belong to an increased sliding wire window (SWW) of size 5, see Section 4.3.4.

There are small differences compared to the interval which is symmetric around mid-rapidity, which can not be excluded by a physical motivation. However, due to the symmetry  $z \rightarrow -z$  in the LCMS, the HBT parameters in backward and forward rapidities should be the same if the intervals of  $y_{12}$

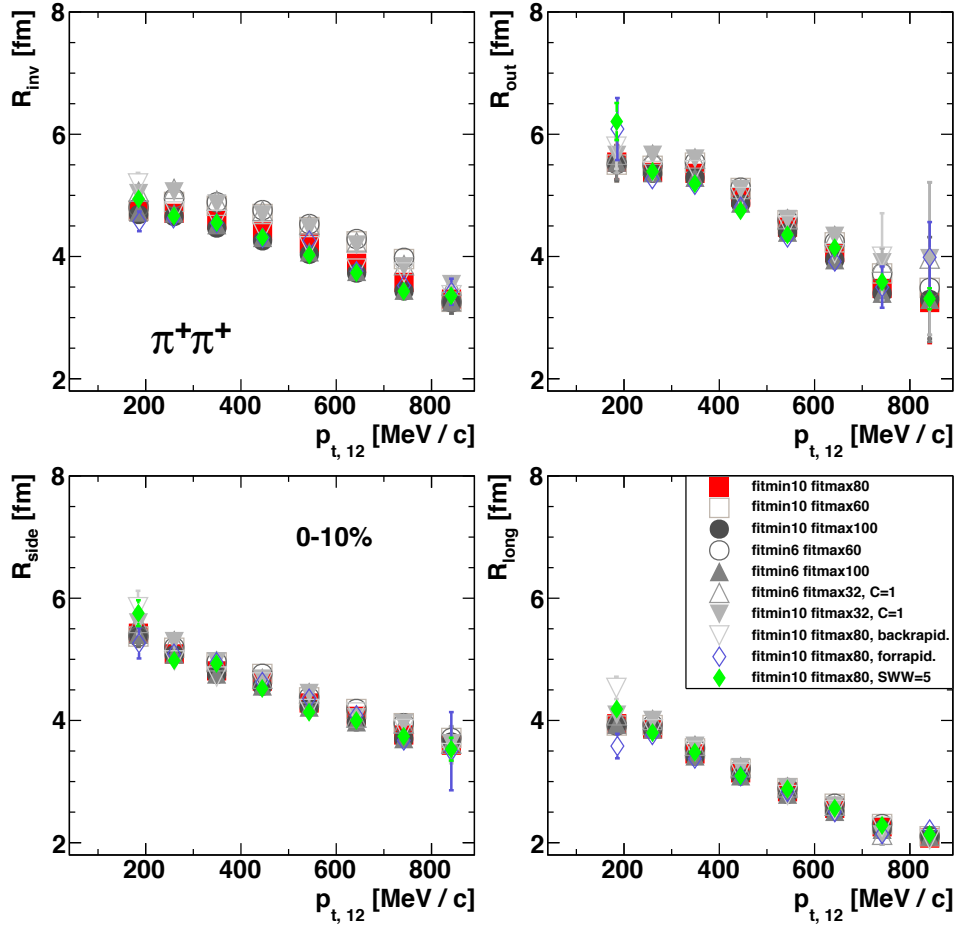
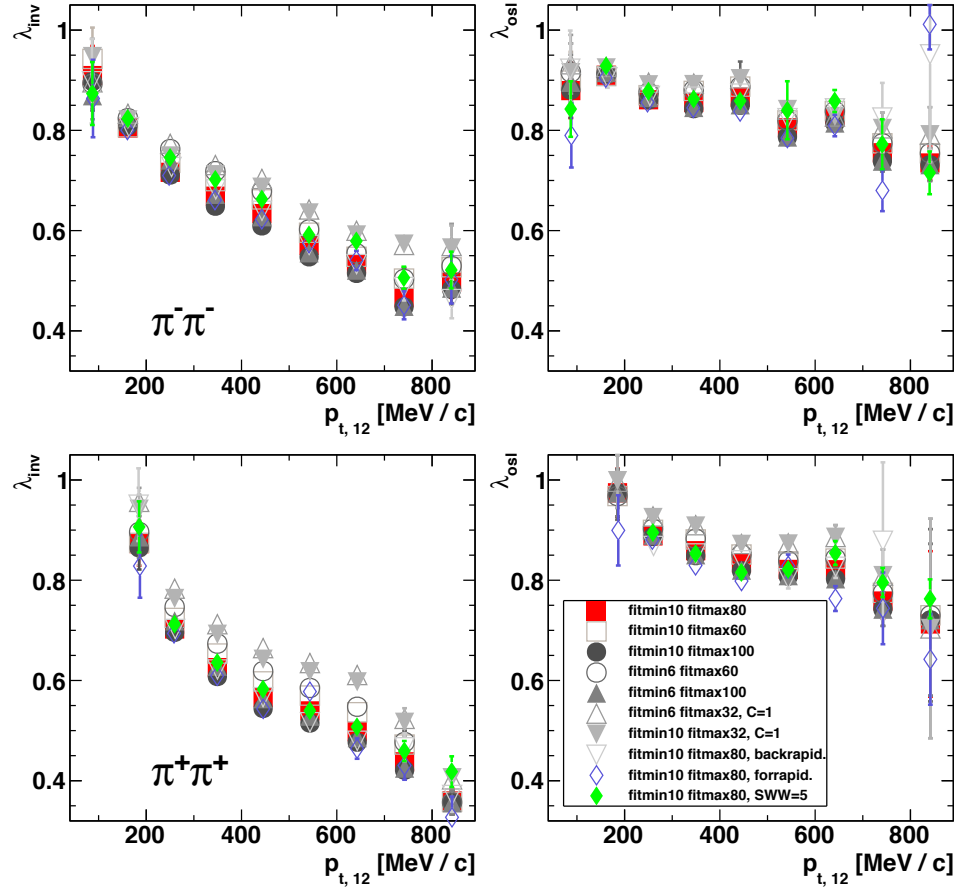


Figure 5.19: Same as Figure 5.18, but for  $\pi^+\pi^+$ .

are equally sized and the mean values of them relative to mid-rapidity are the same. For that reason, the differences of the HBT fit parameters within these two intervals off mid-rapidity are treated as further contribution to the systematic uncertainties. Typical systematic variations of the fit radii of  $0.03 - 0.1$  fm for  $R_{\text{inv}}$ ,  $R_{\text{side}}$  and  $R_{\text{long}}$  or  $0.03 - 0.2$  fm for  $R_{\text{out}}$ , respectively, are observed. The remaining green filled diamonds in Figures 5.18 and 5.19 belong to a variation of the size of the sliding wire window (SWW) introduced in Section 4.3.4, increased from three to five. The impact on the radii of this variation compared to the red filled boxes is very small (with values smaller 0.1 fm) and legitimates the usage of a selection on that quantity with SWW of size 3. The differences between SWW = 5 and SWW = 3 give a further contribution to the systematic uncertainties.

The influence of possible impurities entering the charged pion samples was tested with stronger cuts on the quality parameters of the particle identifi-

## 5. Results



**Figure 5.20:** Same as Figure 5.18, but for the parameters  $\lambda_{\text{inv}}$  (left panels) and  $\lambda_{\text{osl}}$  (right panels).  $\pi^-\pi^-$  ( $\pi^+\pi^+$ ) data is plotted in the top (bottom) row.

cation, see Section 4.2, i.e. by a  $\pm 30$  MeV mass window around the most probable pion mass. About two third of the pairs survived this cut. No systematic differences with respect to the full data sample are found within the statistical uncertainties. Varying  $R_{\text{inv}}$  in the Coulomb correction of Equations (4.26) and (4.28) results in systematic uncertainties of around  $\pm 0.01$  fm. The finite size of the  $q$  averaging intervals in Equation (4.29) yields systematic uncertainties of even smaller size. The uncertainty of the momentum resolution correction described in Section 4.4.2 appears to be an order of magnitude smaller than the absolute source radius shift, i.e. typical values of  $\pm 0.01 - 0.03$  fm are considered. For the fit of the azimuthally integrated three-dimensional correlation function, the slight differences of the results when switching on and off the 'out long' component in the fit function, see

Appendix B.1, are taken as further systematic uncertainty. Typically these differences are smaller than  $\pm 0.1$  fm.

In Figure 5.20 the above considerations are applied to the incoherence parameters  $\lambda_{\text{inv}}$  and  $\lambda_{\text{osl}}$  for both  $\pi^-\pi^-$  and  $\pi^+\pi^+$  pairs. Typical differences are  $\leq 0.1$  with a few outliers. Only for positive pion pairs, the differences for  $\lambda_{\text{inv}}$  are up to  $\pm 0.15$  with the main contributions coming from the smallest fit ranges in  $q_{\text{inv}}$ .

As an additional cross check, the stability of the results with respect to a reversed setting (for about 10 % of the beam time) of the magnetic field has been investigated. Within the larger statistical errors, the results for  $\pi^+\pi^+$  ( $\pi^-\pi^-$ ) in the reversed field are found identical to the  $\pi^+\pi^+$  ( $\pi^-\pi^-$ ) results, see Appendix B.2. Finally, all systematic error contributions are added quadratically. The values can be found as upper and lower labels in the second brackets in Tables D.1 and D.2 in Appendix D.

#### 5.2.4 Dependence on polarity for central collisions

In Section 5.2.1  $\pi^-\pi^-$  and  $\pi^+\pi^+$  results were shown separately. In Figure 5.21  $R_{\text{inv}}$ ,  $R_{\text{out}}$ ,  $R_{\text{side}}$  and  $R_{\text{long}}$  and the incoherence parameters  $\lambda_{\text{inv}}$  and  $\lambda_{\text{osl}}$  of both  $\pi^-\pi^-$  (red circles) and  $\pi^+\pi^+$  (black boxes) are plotted in dependence of  $m_t$  for 10 % most central collisions. The systematic uncertainties, discussed in Section 5.2.3, are added as hatched bands. A substantial charge-sign difference is visible in  $R_{\text{side}}$  and  $R_{\text{long}}$ , becoming larger for low values of  $m_t$  and smaller at high transverse momenta. Also  $R_{\text{inv}}$  shows this difference, but less significantly due to the larger systematic uncertainties. The effect is only visible in  $R_{\text{out}}$  at very low values of  $m_t$  and vanishes at intermediate and high transverse momenta. No significant charge-sign splitting is visible in the incoherence parameters, since the large systematic error bands overlap at all values of  $m_t$ . Applying Equation (2.29) to the polarity dependent freeze-out radii allows to construct the emission radii of pairs of two uncharged fiducial pions,  $\tilde{\pi}^0\tilde{\pi}^0$ , as

$$R_{\tilde{\pi}^0\tilde{\pi}^0}^2 \approx \frac{1}{2}(R_{\pi^+\pi^+}^2 + R_{\pi^-\pi^-}^2), \quad (5.1)$$

where  $R_{\tilde{\pi}^0\tilde{\pi}^0}$  is the initial source size shifted by the attracting (repulsing) effective Coulomb potential  $V_{\text{eff}}$  to  $R_{\pi^-\pi^-}$  ( $R_{\pi^+\pi^+}$ ), under the assumption that the HBT radius parameters are proportional to the inverse width of the correlation signal in relative momentum space. Furthermore,  $V_{\text{eff}}$  has to be small compared to the energy related to the transverse momentum,  $k_t c$ , of the considered pairs. Since the  $\pi^-\pi^-$  and  $\pi^+\pi^+$  data points have different bin centers of transverse momentum, the radii have been interpolated and each experimental point was compared to the interpolated value of the opposite polarity. It has been used both, a cubic spline and a linear interpolation, and differences of both curves are added to the uncertainties

## 5. Results

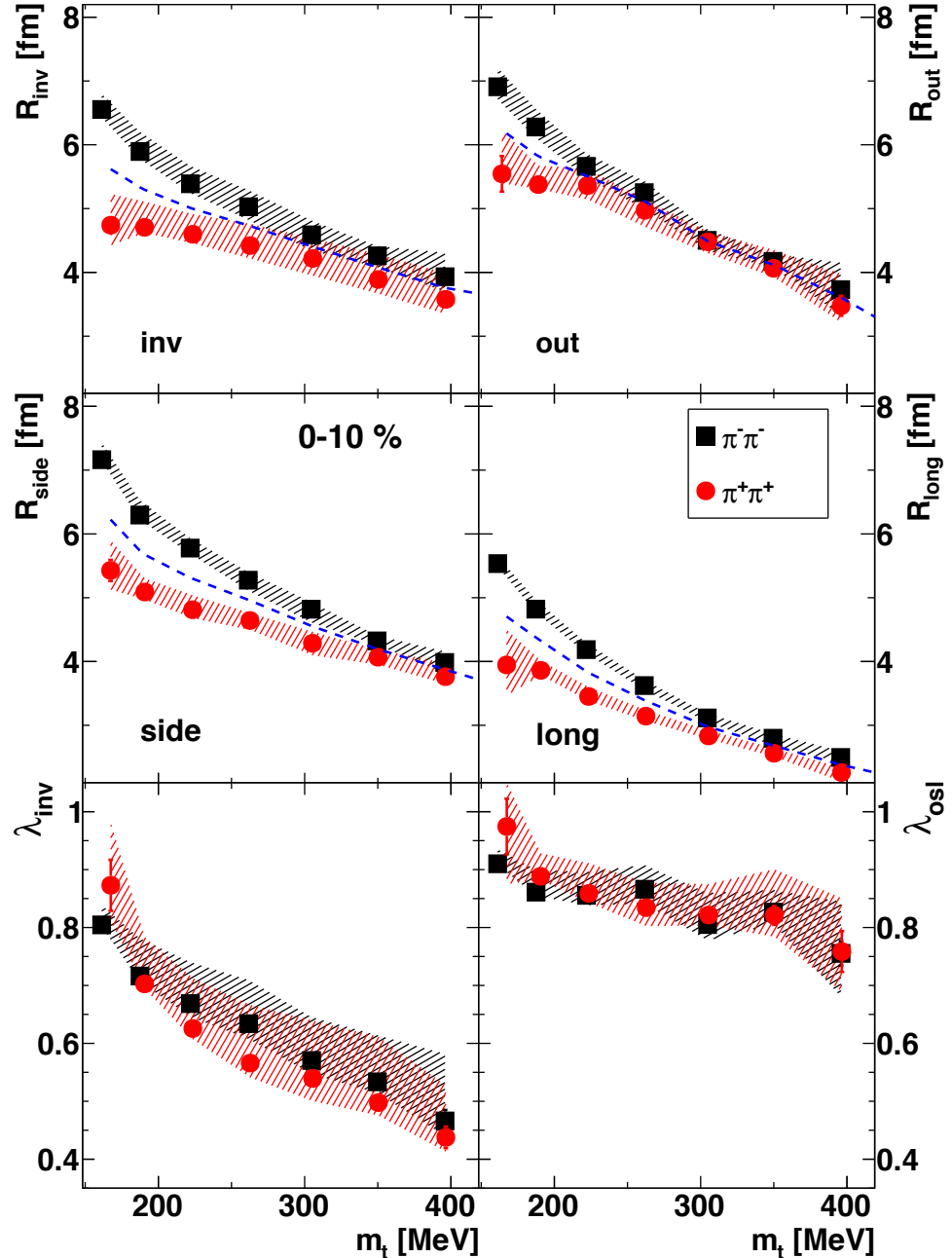


**Figure 5.21:** Source radii  $R_{\text{inv}}$  (top left),  $R_{\text{out}}$  (top right),  $R_{\text{side}}$  (center left),  $R_{\text{long}}$  (center right), as well as parameters  $\lambda_{\text{inv}}$  (bottom left) and  $\lambda_{\text{osl}}$  (bottom right) as function of  $m_t$  for  $\pi^-\pi^-$  (black boxes) and  $\pi^+\pi^+$  (red circles) in 0 – 10 % centrality. Error bars contain statistical errors, hatched bands denote systematic uncertainties. Blue dashed curves represent radii of constructed fiducial  $\tilde{\pi}^0\tilde{\pi}^0$ .

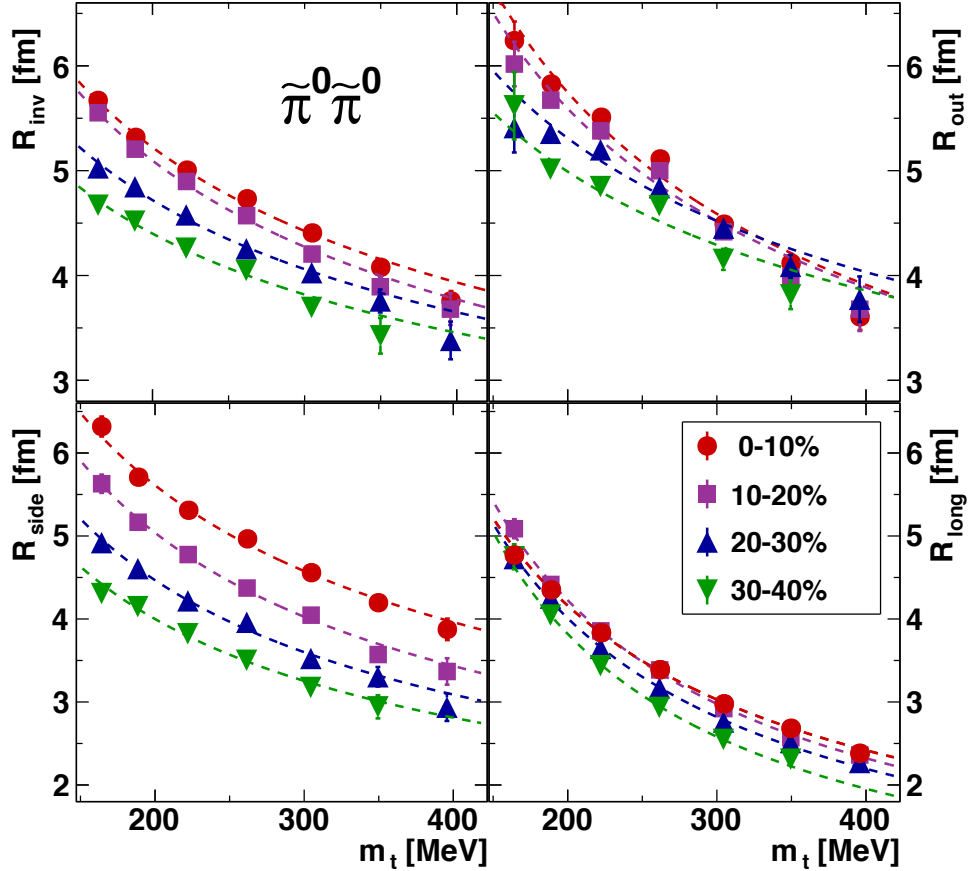


**Figure 5.22:** Source radii  $R_{\text{inv}}$  (top left),  $R_{\text{out}}$  (top right),  $R_{\text{side}}$  (bottom left) and  $R_{\text{long}}$  (bottom right) for centrality classes 0 – 10 % (red circles), 10 – 20 % (violet boxes), 20 – 30 % (blue up-pointing triangles), 30 – 40 % (green down-pointing triangles) in dependence on  $m_t = \sqrt{k_t^2 + m_\pi^2}$  for constructed fiducial  $\tilde{\pi}^0\tilde{\pi}^0$ . Dashed curves represent parametrisations with Equation (5.3).

of the derived quantities of Equation (5.1). The constructed  $\tilde{\pi}^0\tilde{\pi}^0$  radii are drawn as blue dashed curves in the four upper panels of Figure 5.21.

Accordingly, also the effective potential  $V_{\text{eff}}$  can be determined. From Equation (2.29) one derives

$$V_{\text{eff}}(m_t) = \frac{(m_t^2 - m_\pi^2)}{4m_t} \frac{(R_{\pi^-\pi^-}^2 - R_{\pi^+\pi^+}^2)}{R_{\tilde{\pi}^0\tilde{\pi}^0}^2}. \quad (5.2)$$

The values of  $V_{\text{eff}}$  were obtained with the same interpolation scheme as for the constructed  $\tilde{\pi}^0\tilde{\pi}^0$  radii. They can be found for all centrality classes in Appendix B.3.

## 5. Results

---

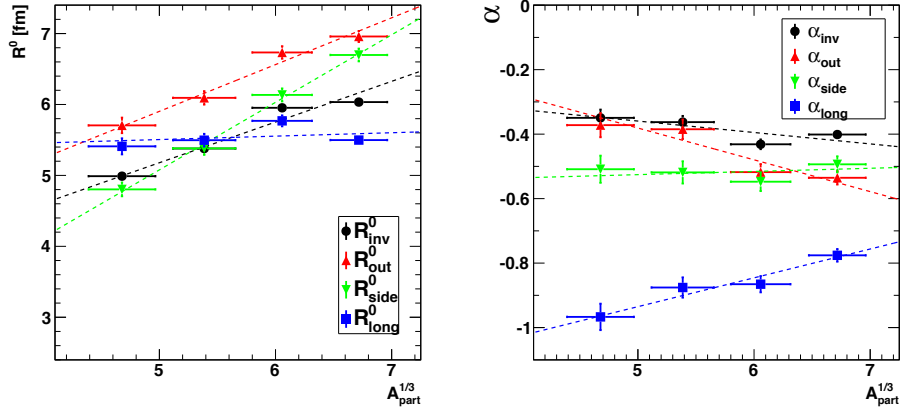


**Figure 5.23:** Fit parameters  $R_{i,0}$  (left panel) and  $\alpha_i$  (right panel) from Equation (5.3) applied to the data in Figure 5.22 in dependence on  $A_{\text{part}}^{1/3}$ ,  $i = \{\text{inv (black circles)}, \text{out (red up-pointing triangles)}, \text{side (green down-pointing triangles)}, \text{long (blue boxes)}\}$ . Dashed lines are straight-line fits to the data points.

Figure 5.22 exhibits the constructed  $\tilde{\pi}^0\tilde{\pi}^0$  radii in dependence of  $m_t$  for all considered centrality classes, similarly to Figures 5.12 and 5.13. The dashed lines represent a parametrisation with

$$R_i = R_{i,0} \left( \frac{m_t}{m_\pi} \right)^{\alpha_i}, \quad (5.3)$$

where  $i = \{\text{'inv'}, \text{'out'}, \text{'side'}, \text{'long'}\}$ . Equation (5.3) has been used previously in [94] as power law ansatz for  $R_{\text{out}}$ ,  $R_{\text{side}}$  and  $R_{\text{long}}$  fits. This power-law function ansatz delivers rather good fits of  $R_{\text{side}}$  and  $R_{\text{long}}$ , while for  $R_{\text{out}}$  it seems not to be the best choice. The fit parameters of Equation (5.3) are plotted in Figure 5.23:  $R_{i,0}$  in the left panel and  $\alpha_i$  in the right panel. Despite the fact that Equation (5.3) is not motivated from basic physical principles, one can discuss the parameters of this function.  $R_{i,0}$  increases with  $A_{\text{part}}^{1/3}$ , except for  $R_{\text{long}}$  in most central collisions, and can be used as rough approximation for  $R_i$  at  $k_t = 0$ , where dynamical effects vanish. The parameters  $\alpha_i$  are measures of the  $m_t$  slope of the freeze-out radii, where  $\alpha_{\text{side}} \approx -0.5$  is found for all centralities. This coincides with AMPT calculations performed at ultra-relativistic beam energies [3, 106]. The parameter  $|\alpha_{\text{long}}|$  is always larger than 0.5, increasing for more peripheral collisions with values between 0.78 and 0.96. The non-constancy of  $\alpha_{\text{long}}$  would indicate a non-constant longitudinal flow over different centralities. It can be interpreted with an increasing stopping power for more central collisions. In a similar investigation at  $\sqrt{s_{\text{NN}}} = 200 \text{ GeV}$  [94], the opposite case was

observed, i.e.  $\alpha_{\text{long}}$  was found to be constant and  $|\alpha_{\text{side}}|$  decreasing for more peripheral collisions. Overall, all values of  $\alpha_i$  were found to be smaller than those in the present investigation.

### 5.2.5 Interpretation of the $k_t$ dependence

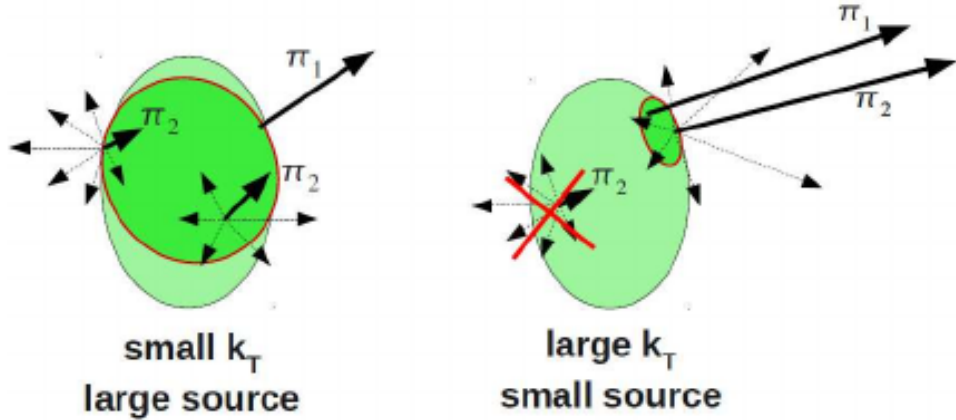


**Figure 5.24:** Illustration of the interplay of thermal motion and collective flow. Figure taken from [107]. See text for details.

A couple of possible reasons exists for the decrease of all HBT radii with increasing transverse momentum. The most prominent one is radial flow [3, 108], i.e. a directed collective motion of the pions emitted from the fireball. At least in transverse direction the collective flow is directly related to the pressure gradient and the viscosity of the hot and dense matter. It is superposed with the randomly distributed thermal motion of the pions, which is essential for detecting the Bose-Einstein signal as noted in Section 2.2.4. The magnitude of collective flow can be represented by the flow velocity  $v$  ( $v_t$  in transverse and  $v_l$  in longitudinal direction), while the thermal motion is quantified by the temperature  $T$ . In Figure 5.24, the influence of the flow on the measured radii is illustrated. A pion emitted from the fireball has locally a randomly distributed velocity direction, which is modified in dependence of the emission point by the collective flow vector pointing outward in radial direction. Two pions coming from different regions of the fireball can combine to small pair momentum and point into any direction, since the thermal motion might be strong enough to change the direction of emission. Large pair momenta are only achieved, if the pions pointing along each other origin from the same region of the fireball, since only then the contributions to the total momentum from the single pions are large enough. In principle, much more combinations for forming large and low pair momenta can be found, but only pion pairs with small relative

## 5. Results

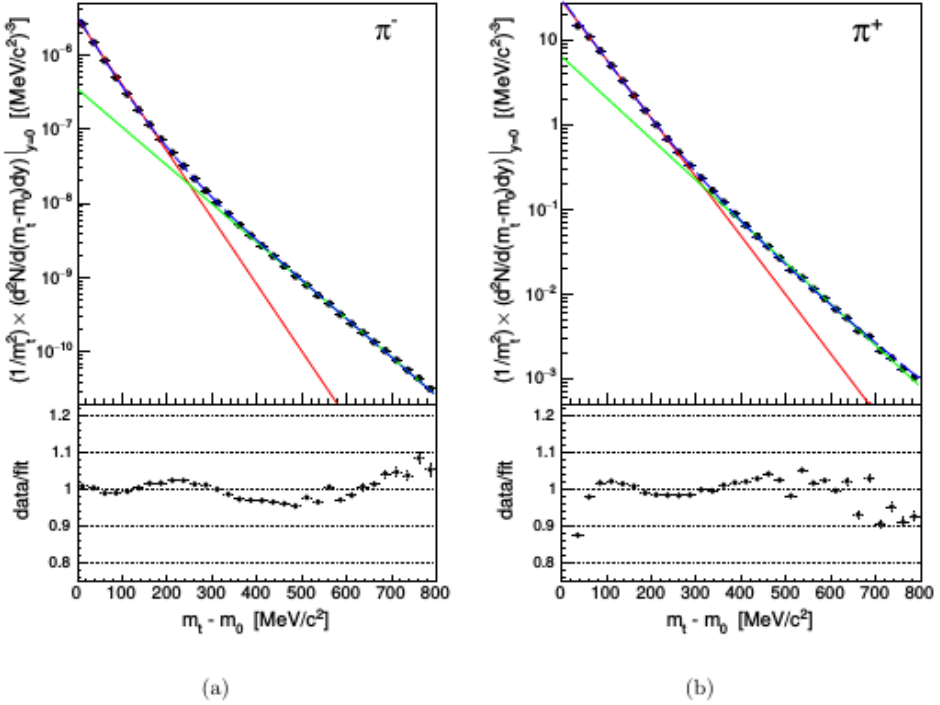


**Figure 5.25:** Acceptance- and efficiency-corrected transverse mass spectra of  $\pi^-$  (left) and  $\pi^+$  (right) at mid-rapidity. Blue curves represent a double-slope Boltzmann fit, red (green) lines denote the fraction of this fit function with larger (smaller) slope parameter. Figure taken from [83].

momentum moving into the same direction carry the wanted femtoscopy information delivering the source size. Furthermore, the mass of the particles affects the sensitivity to the dynamical changes of the momentum, i.e. heavier particles are more confined to the collective motion and less affected by the thermal one [108]. Therefore, one finds a scaling for the HBT radii with  $m_t = (k_t^2 + m^2)^{1/2}$ , proportional to the collective flow effects, which can be formally implemented, as e.g. in Equation (2.47), depending on the modelling of the source distribution. Fitting the  $m_t$  dependence of  $R_{\text{side}}$  in Figures 5.21 and 5.22 with the hydro-dynamically motivated expression (2.47) leads to values of  $\eta_t^2/T$  of about  $1 - 2 \times 10^{-2} \text{ MeV}^{-1}$  for  $\pi^-\pi^-$ ,  $\pi^+\pi^+$  and  $\tilde{\pi}^0\tilde{\pi}^0$ , when limiting the geometrical radius parameter  $R_G$  to reasonable values smaller than 20 fm. Inserting a typical kinetical freeze-out temperature of about  $60 - 70 \text{ MeV}$  [64, 109] leads to transverse flow velocities larger than  $0.7 - 0.8$ . These are quite large values compared to the values found in [109] ([64]) with  $v_t \sim 0.2(0.3) - 0.4$ . Furthermore, these large values interfere with the small-velocity expansions  $v_t \ll 1$  made in Section 2.5 for

obtaining e.g. Equation (2.47). A similar case occurs when fitting the  $m_t$  dependence of  $R_{\text{long}}$  with Equation (2.49), which do not match the whole data set, since the slope of the experimental data is too large. A fit with Equation (2.50) delivers a longitudinal flow velocity  $v_l$  close to unity, which points to an inconsistency of this fit function with a non-relativistic longitudinal expansion. Consequently, one has to state that radial or transverse flow can not explain the strong  $m_t$  dependence of the HBT radii alone.

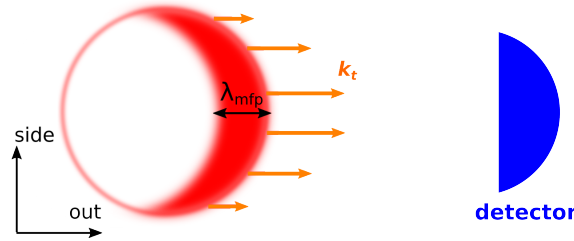


**Figure 5.26:** Illustration of the impact of a finite pion mean free path  $\lambda_{\text{mfp}}$  on the measurement of the source size. Only pions emitted from the sickle-like red area are detected, decreasing mainly the measured width in 'out' direction and increasing obviously the Gaussian width in 'side' direction.

A second possible reason for the decrease of the HBT radius parameters with increasing transverse momentum is the influence of resonance decay contributions with  $k_t$  dependent fractions. At beam energies of 1A GeV mainly  $\Delta$  resonances emit pions, since higher resonances have masses beyond the threshold of direct production. This contribution can be separated against the contribution of early or direct pions produced in a hotter phase of the evolution of the fireball with - by trend - higher momenta. For illustrating this statement, in Figure 5.25 the single particle yields of  $\pi^-$  and  $\pi^+$  mesons measured with HADES are distributed. They are well fitted with a Boltzmann-function (Eq. (3) in [83]) containing explicitly two fractions with two different slope parameters. The interpretation is that the fraction with the smaller slope parameter, i.e. with the higher temperature, represents the direct pions from the earlier stage, and the fraction with the larger slope (smaller temperature) belongs to the temporally delayed  $\Delta$ -decay pions with smaller transverse momentum. A similar picture exists at slightly higher beam energies within the measurements of E810 at AGS [110]. Taking now the ratio of direct pions relative to so-called decay pions,  $n_{\text{direct}}/n_{\text{decay}}$ , one obtains different values of that quantity at different values of  $m_t$  or  $k_t$ , respectively. Since the single particle yields are related to the observables of the two-particle correlation function via Equations (2.6) to (2.8) and (2.33), this two-slope behaviour ought to be implicitly included e.g. in the  $k_t$ -dependence of  $R_{\text{side}}$  and  $R_{\text{long}}$ . Applying with brute force this ansatz

## 5. Results

---

of two Boltzmann slopes within a pion emitting source containing explicitly two fractions, one obtains formulae for source distributions and radii,

$$S(x, p) = S^{\text{dec}}(x, p) + S^{\text{dir}}(x, p), \quad (5.4)$$

$$\begin{aligned} R_i(k_t) = \langle \tilde{x}_i \rangle(k_t) &= \frac{\int d^4x x_i (S^{\text{dec}}(x, k_t) + S^{\text{dir}}(x, k_t))}{\int d^4x (S^{\text{dec}}(x, k_t) + S^{\text{dir}}(x, k_t))} \\ &= [\text{partial integration, substitutions}] \\ &= \frac{R_{i,\text{dec}}(k_t) P_1^{\text{dec}}(k_t) + R_{i,\text{dir}}(k_t) P_1^{\text{dir}}(k_t)}{P_1^{\text{dec}}(k_t) + P_1^{\text{dir}}(k_t)}, \end{aligned} \quad (5.5)$$

with two implicit HBT radius parameters per explicit parameter,  $R_{i,\text{dec}}$  and  $R_{i,\text{dir}}$ , weighted with the single particle distributions. Note that a more refined treatment should be implemented already on the level of the correlation function  $C(\vec{q})$ , fitting explicitly with  $R_{i,\text{dec}}$  and  $R_{i,\text{dir}}$ . A consideration taking also into account the decay widths of the resonances can be found in [111]. However, Equation (5.5) illustrates the impact of resonance decay contributions to the slopes of the  $m_t$ -dependent HBT radii. Since it is the most obvious effect besides radial flow being able to generate a sufficiently large  $m_t$  slope, one can state that the transverse momentum dependence of the HBT radius parameters is given at least partly by the corresponding fraction of decay pions and direct pions. The fraction of early emitted direct pions is larger at high values of  $k_t$  and the fraction of later emitted  $\Delta$ -decay pions is larger at small values of  $k_t$ . As a last consequence, the HBT radii inherit this intrinsic time dependence, meaning radii obtained at higher transverse momentum are correlated with earlier times of the fireball evolution and the other way round (also supported by the findings of [112]).

For a quantitative treatment one should be able to combine collective flow, resonance contributions and the charge-sign dependence of Section 5.2.4 in an appropriate formalism, since Equation (2.29) needs not necessarily to factorise into a form like Equation (5.5). Finally, the possibility of the influence of the finite mean free path of the pions,  $\lambda_{\text{mfp}}$ , in the hot and dense matter should be considered. If  $\lambda_{\text{mfp}}$  is in or below the order of magnitude of the source extension then the fireball has to be considered as partly opaque with the emission points of pions shifted more to the surface. From this consideration, a slight increase of  $R_{\text{side}}$  and a significant decrease of  $R_{\text{out}}$  can be expected [50, 113]. When studying  $R_{\text{side}}$  this can be seen as small systematic uncertainty. However, especially for the difference of  $R_{\text{side}}$  and  $R_{\text{out}}$ , the opaqueness can have a crucial impact.<sup>1</sup>

---

<sup>1</sup>To make a decision of how large the effect of opaqueness is, in [114] the usage of the YKP parametrisation is suggested, since there the influence of  $\lambda_{\text{mfp}}$  is highest in one given direction.

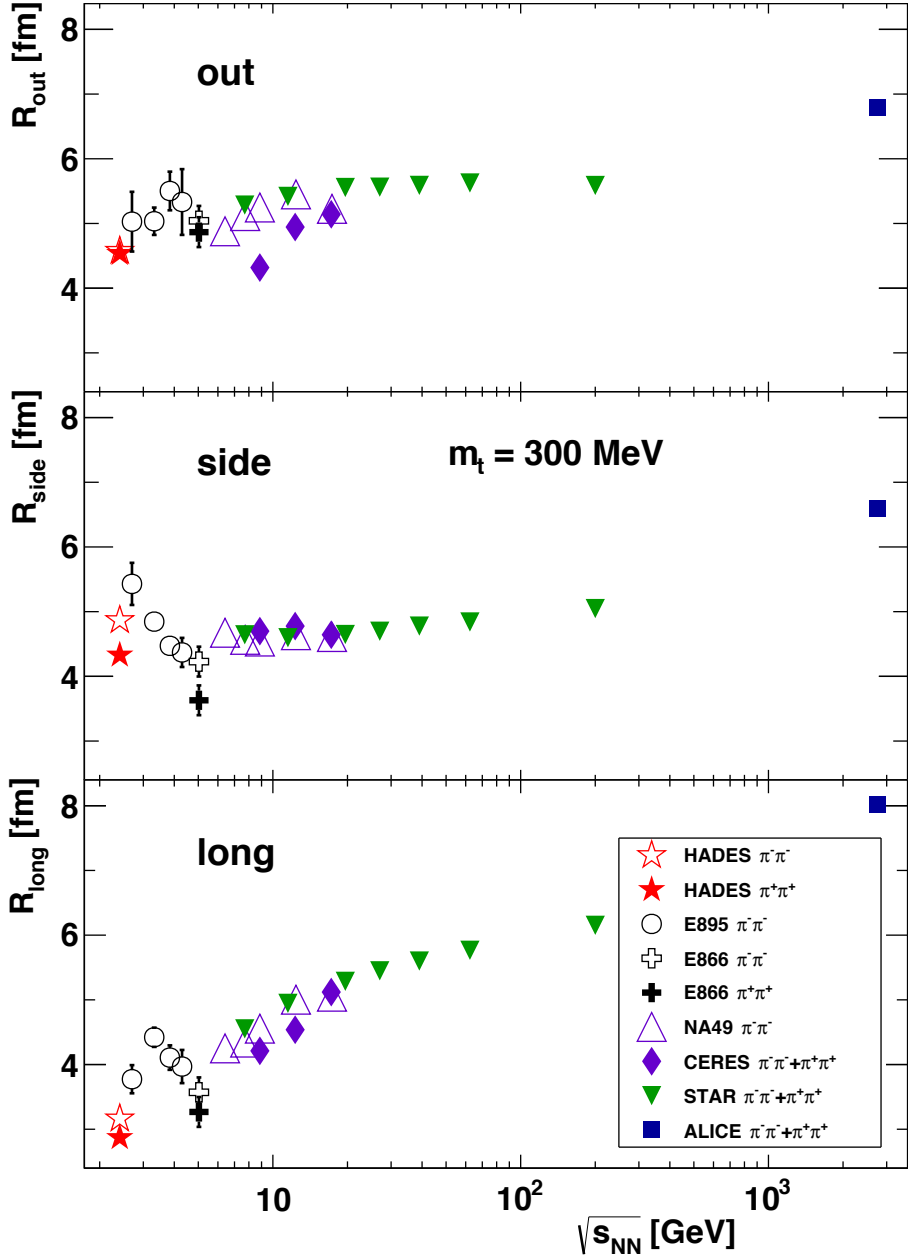


**Figure 5.27:** Excitation function of  $R_{\text{out}}$  (upper panel),  $R_{\text{side}}$  (central panel), and  $R_{\text{long}}$  (lower panel) for  $\pi^-\pi^-$  and  $\pi^+\pi^+$  with  $m_t = 300$  MeV in central collisions of Au + Au, Pb + Au or Pb + Pb. Squares represent data by ALICE ( $\pi^+\pi^+$ ) [18], full triangles STAR ( $\pi^-\pi^-+\pi^+\pi^+$ ) [17], diamonds are for CERES ( $\pi^-\pi^-+\pi^+\pi^+$ ) [15], open triangles are for NA49 ( $\pi^-\pi^-$ ) [16], open circles are  $\pi^-\pi^-$  data by E895 [13], and open (full) crosses involve  $\pi^-\pi^-$  ( $\pi^+\pi^+$ ) data of E866 [14], respectively. HADES data for  $\pi^-\pi^-$  ( $\pi^+\pi^+$ ) are given as open (full) stars.

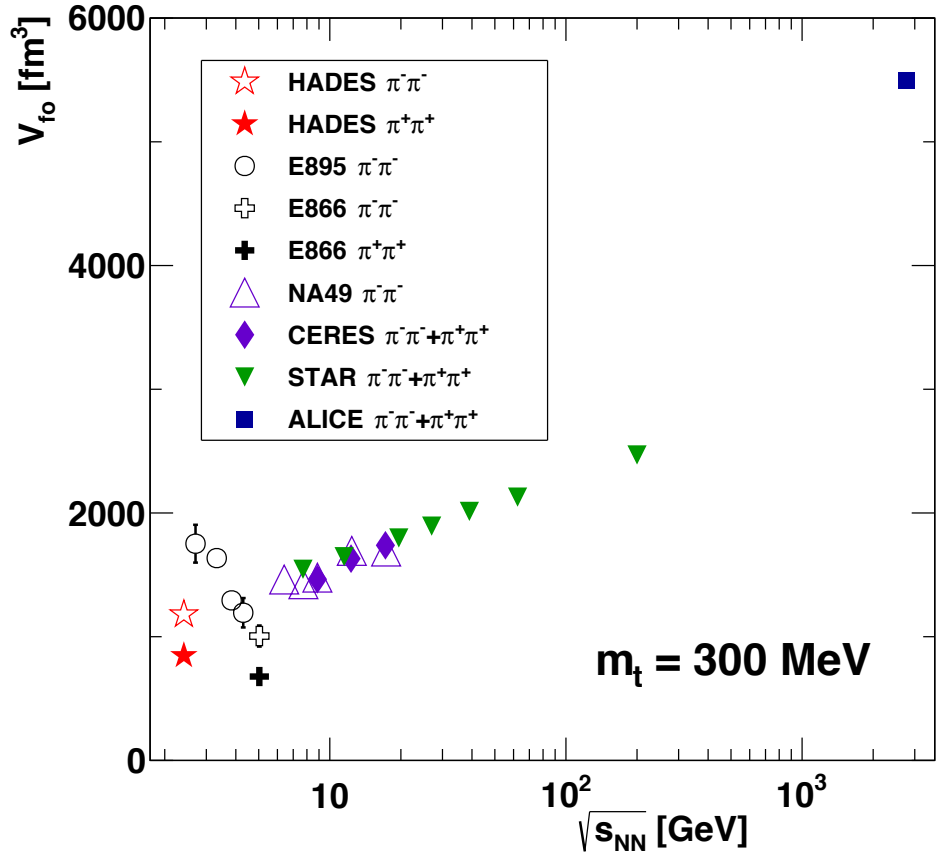


**Figure 5.28:** Same as Figure 5.27, but for the approximate freeze-out volume  $V_{\text{fo}}$  according to Equation (5.6).

### 5.2.6 Excitation functions

In the previous sections 5.2.1 and 5.2.4, multi-differential freeze-out radii are presented, depending highly on transverse momentum, centrality and polarity of the pion pairs. Now, this data can be compared to femtoscopy radii from other experiments at higher beam energies to study excitation functions. Figure 5.27 displays  $R_{\text{out}}$  (top),  $R_{\text{side}}$  (middle) and  $R_{\text{long}}$  for central (0 – 10 %) collisions in dependence on  $\sqrt{s_{\text{NN}}}$ . The data is taken from Au+Au, Pb+Au and Pb+Pb collisions. All shown radius parameters have been obtained by interpolating the existing measured data points to the same transverse mass of  $m_t = 300$  MeV ( $k_t = 265$  MeV/c). The statistical uncertainties are properly propagated and quadratically added with the differences of linear and cubic spline interpolations. Extrapolations were not necessary at this  $m_t$  value. Corresponding excitation functions at other

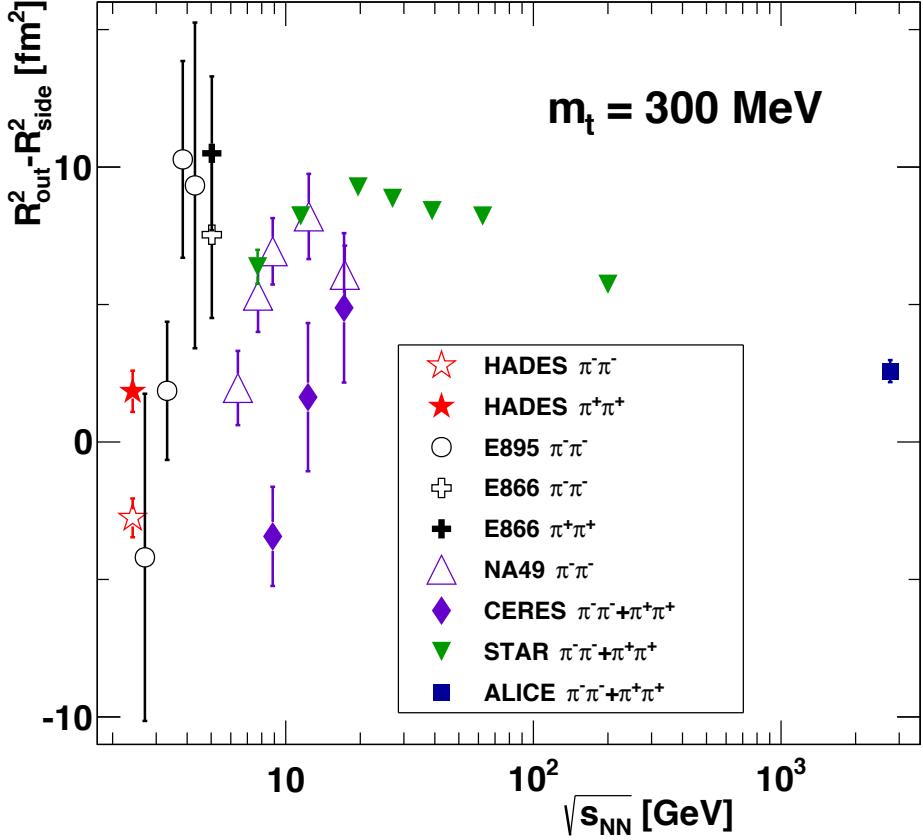


**Figure 5.29:** Same as Figure 5.27, but for the quantity  $R_{\text{out}}^2 - R_{\text{side}}^2$ .

transverse masses show similar dependencies [115, 116]. Surprisingly,  $R_{\text{out}}$  and  $R_{\text{side}}$  vary hardly more than 40 % over three orders of magnitude in center-of-mass energy. Only  $R_{\text{long}}$  exhibits a systematic increase by about a factor of two when going in energy from SIS18 via AGS, SPS, RHIC to LHC. Note that in the excitation functions of ref. [17] not all, (on particular, AGS) data points were properly corrected for their  $k_t$  dependence.

The excitation function of the approximate freeze-out volume,

$$V_{\text{fo}} = (2\pi)^{3/2} R_{\text{side}}^2 R_{\text{long}}, \quad (5.6)$$

for central collisions is given in Figure 5.28. Note that this definition of a three-dimensional Gaussian volume does not incorporate  $R_{\text{out}}$ , since this length is potentially extended due to a finite value of the aforementioned emission duration. From the above HADES data, a volume of about  $850 \text{ fm}^3$

## 5. Results

---

for constructed fiducial  $\pi^0\bar{\pi}^0$  pairs is estimated. This volume of homogeneity steadily increases with beam energy, but appears merely a factor four larger at LHC. Extrapolating  $V_{\text{fo}}$  to  $k_t = 0$  yields a value of about  $3.900 \text{ fm}^3$ . The excitation function of  $R_{\text{out}}^2 - R_{\text{side}}^2$  for an average transverse momentum of the pion pairs of  $k_t = 265 \text{ MeV}/c$  in central collisions is shown in Figure 5.29. Up to now almost all measurements below  $10 \text{ GeV}$  beam energy are characterized by large errors and scatter sizeably. The new HADES data show that the difference of the source parameters in the transverse plane almost vanishes at low collision energies. Since this quantity is related to the emission duration  $\Delta\tau$  in leading order via (compare Equation (2.43))

$$\beta^2(\Delta\tau)^2 \approx R_{\text{out}}^2 - R_{\text{side}}^2, \quad (5.7)$$

one would conclude that, in the  $1 \text{ A GeV}$  beam energy region, the observed pions are emitted into free space during a short time span of less than a few  $\text{fm}/c$ . However, also the opaqueness of the source affects  $R_{\text{out}}^2 - R_{\text{side}}^2$ , discussed in Section 5.2.5 and illustrated in Figure 5.26, which could cause it to become negative, thus compensating the positive contribution from the emission time [50]. It should also be emphasized that, with increasing available energy, this quantity reaches a local maximum at  $\sqrt{s_{\text{NN}}} \sim 20 - 30 \text{ GeV}$  and afterwards decreases towards zero at LHC energies.

## 5.3 Azimuthally dependent correlations

In this section the full results of azimuthally sensitive correlation functions in the 'osl'-system are considered. Furthermore, derived quantities with respect to the reaction-plane fixed 'xyz'-system are presented and compared to observations of other experiments at higher beam energies.

### 5.3.1 Oscillations of the femtoscopic variances

In Figure 5.30, the fit results applying Equations (4.28) and (4.31) to the azimuthally sensitive correlation functions are displayed, as a function of the azimuthal angle relative to the event plane  $\Phi$  for five intervals of transverse momenta of  $\pi^-\pi^-$  for  $10 - 30\%$  centrality. In the left panels, the diagonal variances  $R_{\text{out}}^2$ ,  $R_{\text{side}}^2$  and  $R_{\text{long}}^2$  (from top to bottom) are plotted. All these squared radii display a systematic dependence of  $k_t$ , in accordance to the trends of Figure 5.12.  $R_{\text{out}}^2$  and  $R_{\text{side}}^2$  show clearly oscillations, while  $R_{\text{long}}^2$  is constant apart a few fluctuations, the more for lower values of  $k_t$ . In the right panels the non-diagonal variances  $R_{\text{out side}}^2$ ,  $R_{\text{out long}}^2$  and  $R_{\text{side long}}^2$  (from top to bottom) are plotted. They show also clear oscillations:  $R_{\text{out side}}^2$  with two cycles and  $R_{\text{out long}}^2$  and  $R_{\text{side long}}^2$  with one cycle within  $2\pi$ . The amplitudes of all oscillations are larger for smaller values of  $k_t$  in accordance with the correspondingly larger diagonal radii. The curves represent global fits with

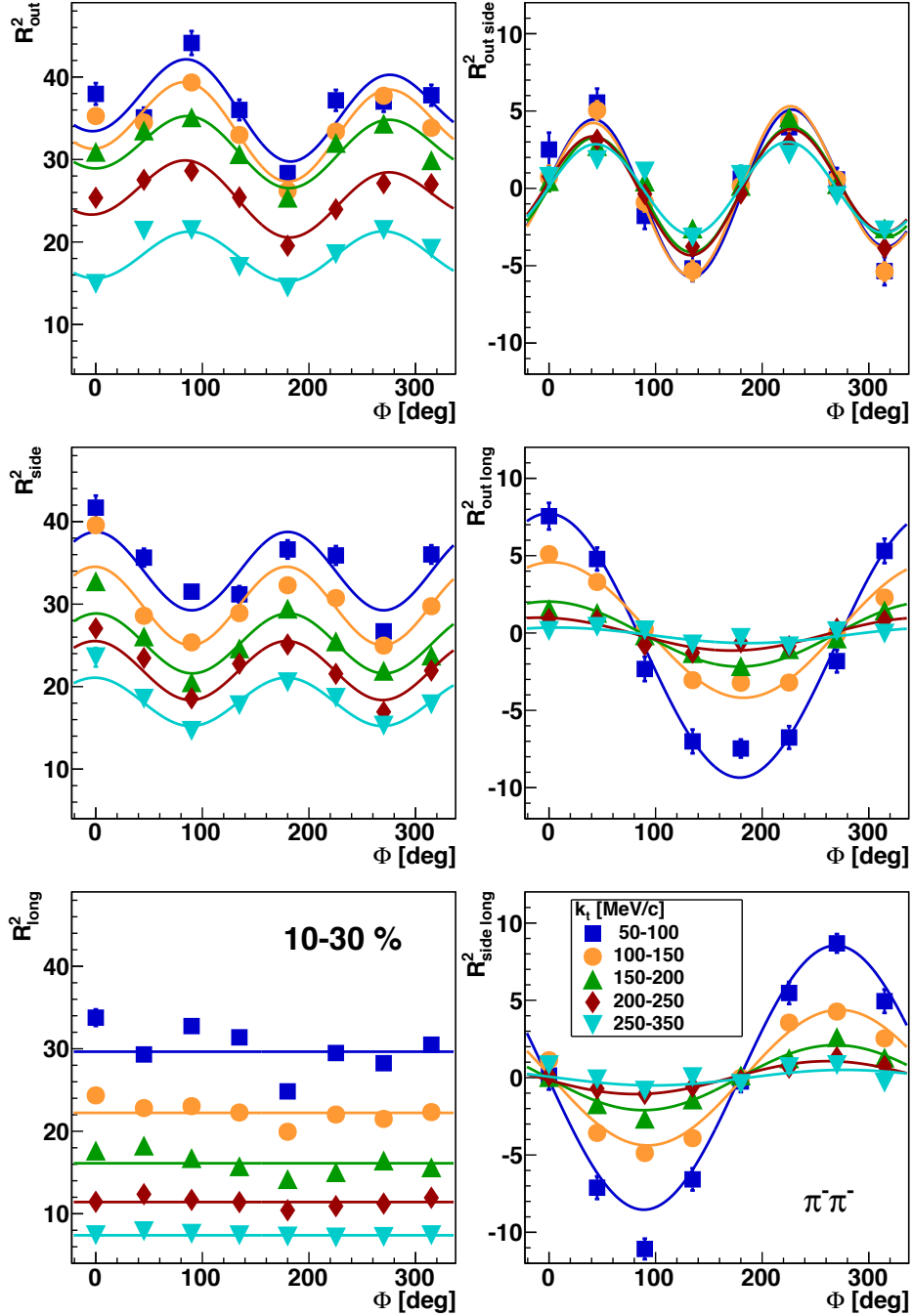


**Figure 5.30:** HBT radius parameters  $R_{\text{out}}^2$  (top left),  $R_{\text{side}}^2$  (middle left),  $R_{\text{long}}^2$  (bottom left),  $R_{\text{out side}}^2$  (top right),  $R_{\text{out long}}^2$  (middle right) and  $R_{\text{side long}}^2$  (bottom right) resulting from the fit of Eqs. (4.28) and (4.31) to the three-dimensional correlation functions for  $\pi^- \pi^-$  for different values of  $k_t$  and centrality 10 – 30 % as a function of  $\Phi$ . Error bars include only statistical uncertainties. Full curves represent global fits with Equation (4.38).

## 5. Results

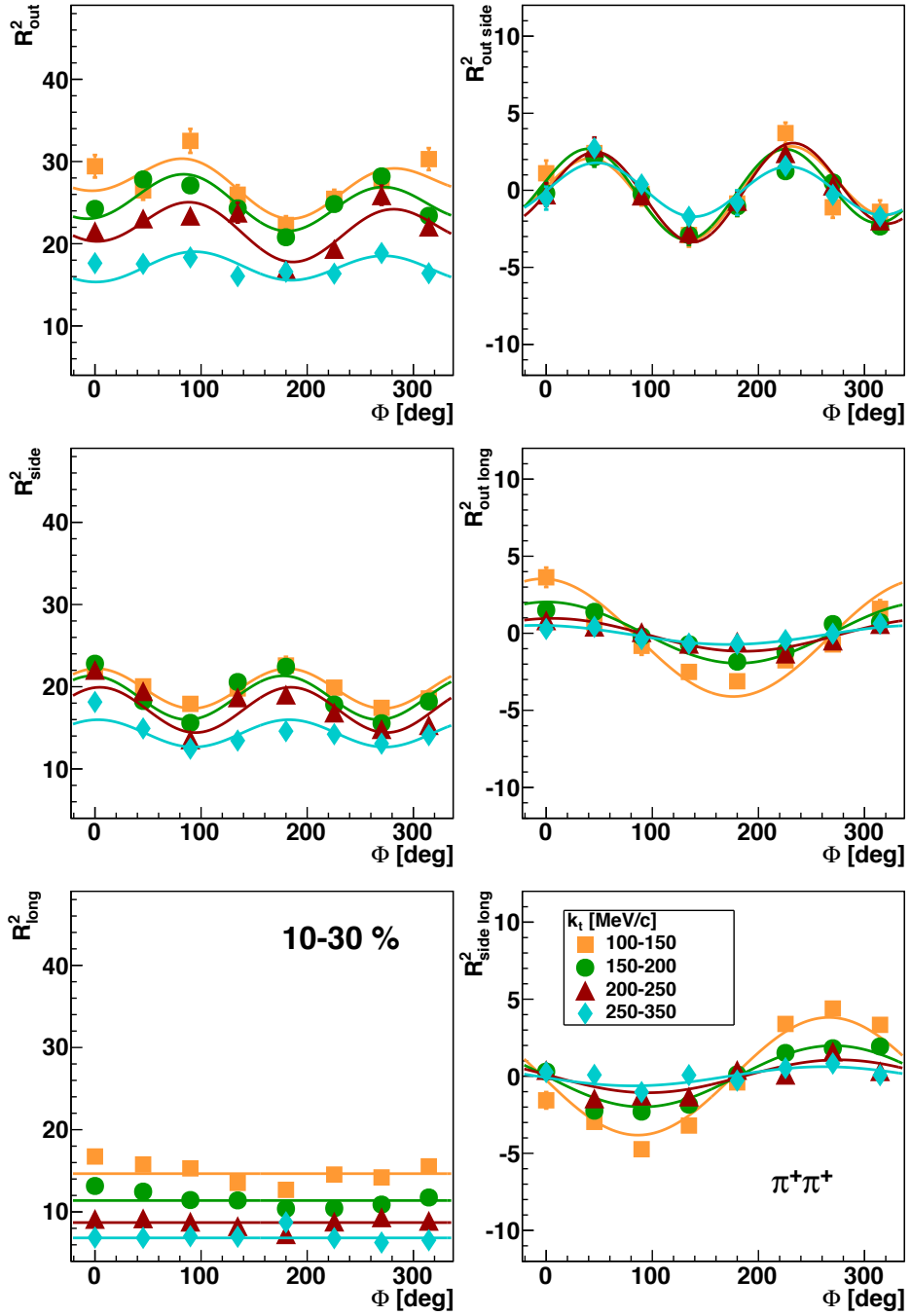
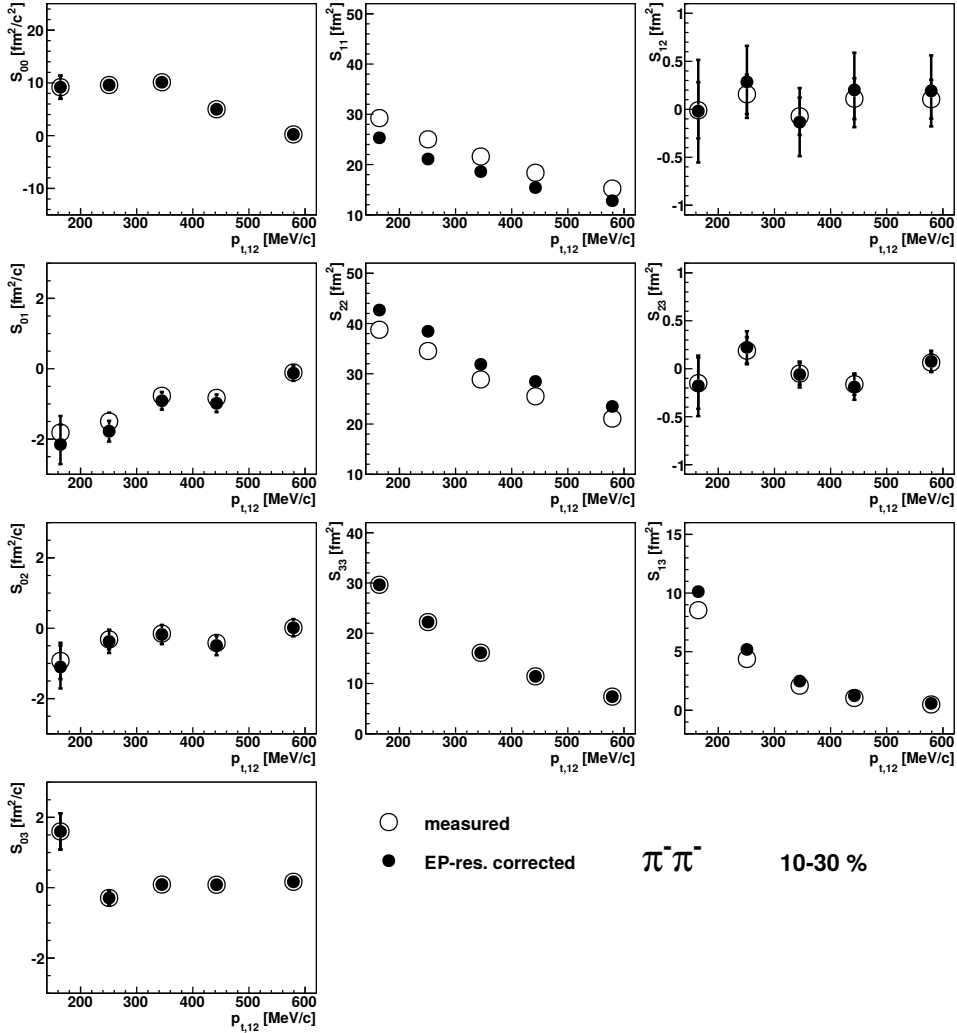


Figure 5.31: Same as Figure 5.30, but for  $\pi^+\pi^+$ .

Equation (4.38) to the six variances, i.e. the combined set of fit functions is fitted to all data points of all panels for each value of  $k_t$  simultaneously. While for the lowest  $k_t$  intervals some fluctuations are visible, for the higher

### 5.3 Azimuthally dependent correlations



**Figure 5.32:** The ten independent fit parameter  $S_{\mu\nu}$  from Equation (4.38) as function of pair transverse momentum  $p_{t,12}$  for  $\pi^-\pi^-$  for 10 – 30 % centrality. Temporal components are on the left column, diagonal (non-diagonal) pure spatial components on the middle (right) column. Open circles are the direct outcome from the fits, full circles are EP-resolution corrected according to Equation (4.40).

ones the fit describes the data quantitatively very good. Overall all fits describe the trends also quite good. In Figure 5.31, the same is shown for  $\pi^+\pi^+$ . Since the pair statistics is significantly smaller for positive pions, data points are only available for four classes of  $k_t$  starting at 100 MeV/c. While the absolute values of the diagonal variances are smaller and change less with  $p_{t,12}$ , compared to  $\pi^-\pi^-$ , the non-diagonal variances and the oscillation

## 5. Results

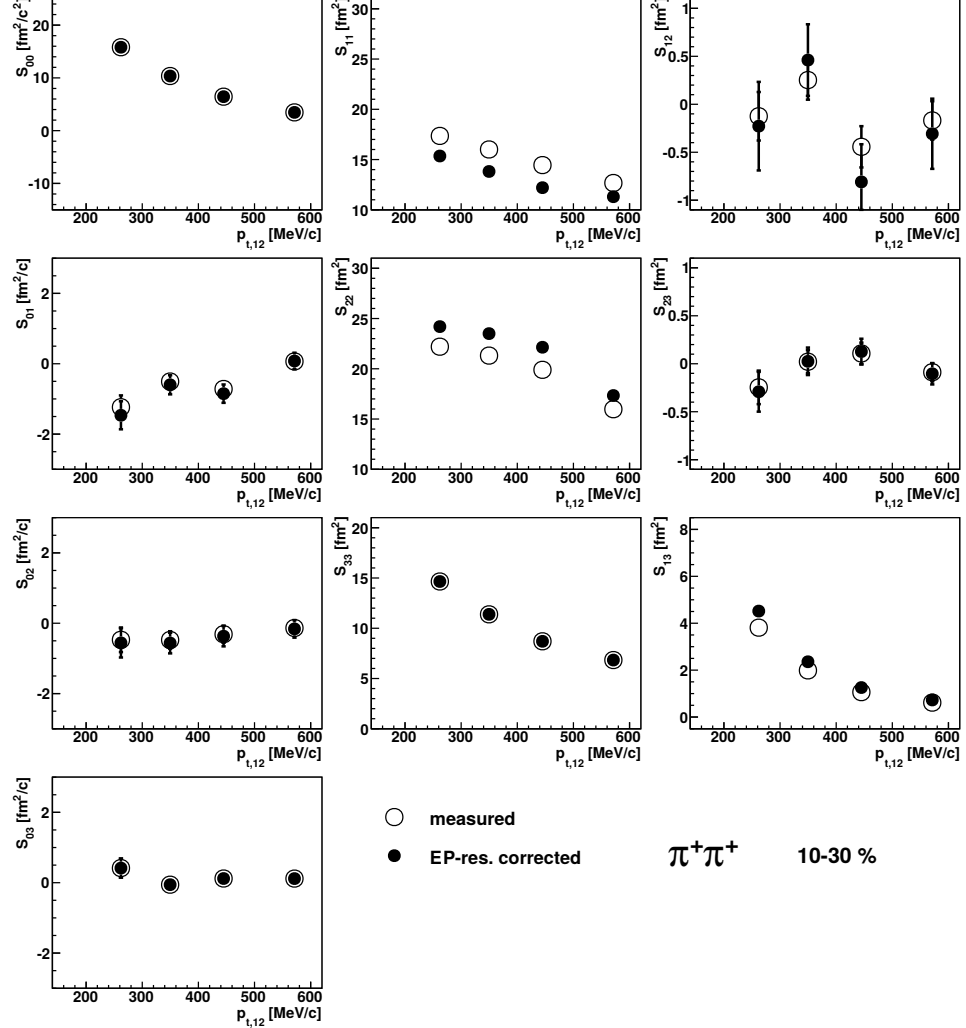


**Figure 5.33:** Same as Figure 5.32, but for  $\pi^+\pi^+$ .

amplitudes of all variances are very similar. Apart from a few fluctuations the fit reproduces the data again quite good.

The fit parameters of Equation (4.38) from the global fits are exhibited in Figure 5.32 for  $\pi^-\pi^-$  and in Figure 5.33 for  $\pi^+\pi^+$ , respectively. In the left column from top to bottom, the temporal element  $S_{00}$  and the spatio-temporal elements  $S_{01}$ ,  $S_{02}$  and  $S_{03}$  are displayed; in the middle column, the spatial diagonal elements  $S_{11}$ ,  $S_{22}$  and  $S_{33}$  are listed, and in the right column, the spatial non-diagonal elements  $S_{12}$ ,  $S_{23}$  and  $S_{13}$  are exhibited. Open circles are for the values coming directly from the combined fit, the filled smaller circles are the event-plane resolution corrected values according to Equation (4.40). Only the elements  $S_{00}$ ,  $S_{11}$ ,  $S_{22}$ ,  $S_{33}$  and  $S_{13}$  are significantly different from zero, as already expected from symmetry constraints,

see Equation (4.39).  $S_{12}$  and  $S_{23}$  are mostly zero within one standard deviation and vanish completely within two standard deviations for both,  $\pi^-\pi^-$  and  $\pi^+\pi^+$ . The same statement is valid for  $S_{03}$ , except one outlier at the smallest value of  $p_{t,12}$  for  $\pi^-\pi^-$ , which is in the range of three standard deviations around zero. For  $S_{01}$  and  $S_{02}$ , the case is a bit different. Even if  $S_{02}$  vanishes again within two standard deviations, all values are found to be smaller or at least equal to zero without fluctuations into the positive area. The same case occurs for  $S_{01}$ , but the difference to zero is even larger, up to five standard deviations for  $\pi^-\pi^-$ . Despite the fact that the absolute values are still small compared to  $S_{00}$ ,  $S_{11}$  or  $S_{22}$ , this might be a hint for an implicit  $\Phi$  dependence of the source function. Following [104] it could be a reflection of the spatial manifestation of elliptic flow. Since  $S_{00}$ ,  $S_{33}$  and  $S_{03}$  are not influenced by azimuthal oscillations, they are also not affected by the event-plane resolution. The correction is biggest for  $S_{11}$  and  $S_{22}$  and enters with opposite sign, that means,  $S_{22}$  is (like all other affected elements) enlarged, while  $S_{11}$  is reduced. Therefore the right handling of this correction is most important for derived quantities, where the difference of both elements is used, e.g. the  $xy$ -eccentricity, see Equation (4.46). Worth to mention is that  $S_{11}$  and  $S_{22}$  are determined by the trends of  $R_{\text{out}}^2$ ,  $R_{\text{side}}^2$  and  $R_{\text{out side}}^2$ , which means that even a drastic fluctuation in one of the HBT parameters can be compensated by the other ones, which makes the corresponding elements of  $S_{\mu\nu}$  much more stable and their values more reliable. The same reasoning holds for  $S_{13}$ , which is determined by the oscillation of  $R_{\text{out long}}^2$  and  $R_{\text{side long}}^2$ .

The values inferred from Figures 5.32 and 5.33 are employed to calculate with Equation (4.44) the tilt angle  $\theta_s$  within the reaction plane and to use it for tilting back the measured ellipsoid of the fireball region, as described in Section 4.5.3. In Figure 5.34, the geometrical variances  $\sigma_x$ ,  $\sigma_y$  and  $\sigma_z$  (left column), which are the semi-axes of the upstanding ellipsoid, are plotted. In the right column, the tilt angle  $\theta_s$  (top), the eccentricities  $\varepsilon_{xy}$  (middle, see Equation (4.46), filled symbols) and  $\varepsilon_{zy}$  (middle, see Equation (4.47), open symbols), and the emission duration  $\sigma_t$  (bottom) are exhibited. Black boxes represent  $\pi^-\pi^-$  data and red squares the data of  $\pi^+\pi^+$ . In leading order, the trends of  $\sigma_x$ ,  $\sigma_y$  and  $\sigma_z$  are similar compared to  $R_{\text{side}}$  and  $R_{\text{long}}$  in the azimuthally integrated analysis, see Figures 5.12 and 5.13. The variances decrease with  $p_{t,12}$  and one finds the hierarchy  $\sigma_y > \sigma_x > \sigma_z$ , i.e. a three-dimensional almond-shape. Furthermore, the gap between the values of  $\pi^-\pi^-$  and  $\pi^+\pi^+$  is clearly visible, which is related to the Coulomb potential of the charged participants, similar to what was discussed in Section 5.2.4. Probably, also the charged spectators contribute to the charge-sign dependence of these geometrical variances, since there are more spectators for peripheral and semi-peripheral collisions than for central collisions, and they are close-by due to short evolution times of the fireball expected at SIS energies. In contrast, the tilt angle  $\theta_s$  shows no dependence on the polarity of

## 5. Results

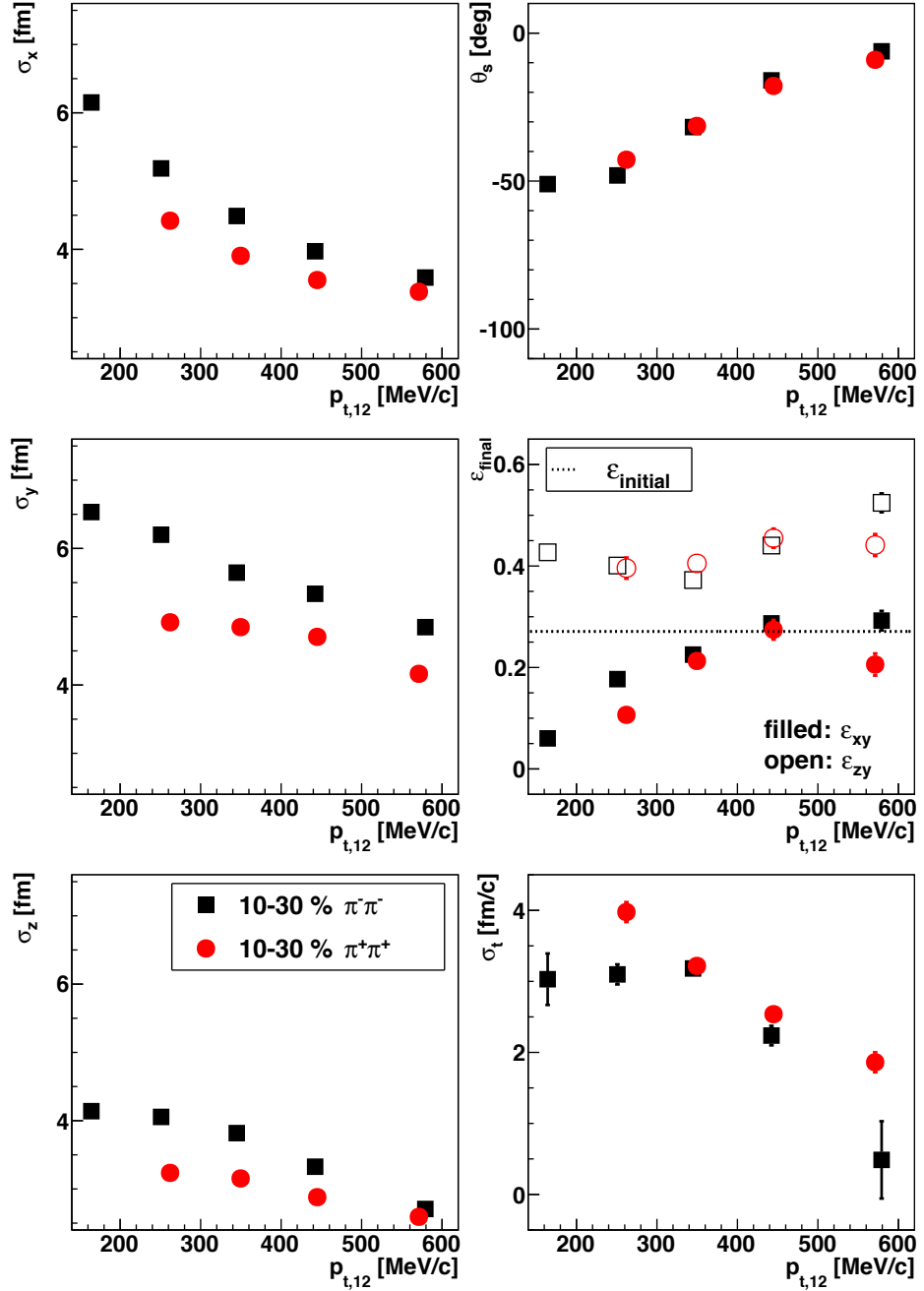


**Figure 5.34:** The spatial semi-axes (left panels), the tilt angle w.r.t. the beam axis in the reaction plane (Eq. (4.44), top right), the  $xy$ -eccentricity (full, Eq. (4.46)) and the  $zy$ -eccentricity (empty, Eq. (4.47), middle right) and the emission duration  $\sigma_t$  (bottom right) of the Gaussian emission ellipsoid of  $\pi^- \pi^-$  (boxes) and  $\pi^+ \pi^+$  (circles) as function of transverse momentum for 10 – 30 % centrality. Error bars include only statistical uncertainties. The dotted line (to be compared to  $\varepsilon_{xy}$ ) represents the initial nucleonic eccentricity derived from Glauber simulations.

the pion pairs. It has negative values, which means that the tip of the longer semi-axes in the  $xz$  plane is pointing to the spectators. The tilt angle has its largest magnitude at the small values of  $p_{t,12}$ , increases smoothly with  $p_{t,12}$  and tends to vanish at high pair transverse momenta. The eccentricities depend also only less on the polarity of the pion pairs. Only for the smallest and the largest values of  $p_{t,12}$ , a small difference is present, but not more than two standard deviations. The  $xy$ -eccentricity is always positive; it is small for small values of  $p_{t,12}$  and increases for large transverse momenta up to the initial eccentricity  $\varepsilon_{\text{ini}}$ , which was extracted from Glauber simulations, depicted as dashed line in Figure 5.34 (right middle panel). The  $zy$ -eccentricity is only less dependent on  $p_{t,12}$ ; it is almost constant around 0.4 for low transverse momenta and seems to increase slightly with higher values of  $p_{t,12}$ . The emission duration  $\sigma_t$ , identified with  $\sqrt{S_{00}}$ , decreases with increasing transverse momenta. A significant charge-sign difference is visible only at small values of  $p_{t,12}$  (smaller than 300 MeV/c).

### 5.3.2 Excitation functions

The results of the previous section can be compared to the experimental findings of other experiments at different beam kinetic energies and  $\sqrt{s_{\text{NN}}}$ , respectively.

#### Comparison with E895@AGS

In Figure 5.35, results of this work are compared to results from E895 [19] for  $\pi^-\pi^-$  correlations in dependence on  $\sqrt{s_{\text{NN}}}$ . In the left column from top to bottom,  $\sigma_x$  (red),  $\sigma_y$  (green) and  $\sigma_z$  (blue), in the right column from top to bottom  $\theta_s$  (black),  $\varepsilon_{xy}$  and  $\varepsilon_{zy}$  (blue filled and red open, one panel) and  $\sigma_t$  (violet) are displayed. Error bars include only statistical uncertainties. Data from E895 is given for a large interval of  $k_t$  from 0 to 400 MeV/c with average value  $\bar{k}_t = 110$  MeV/c of small pair relative momenta. Accordingly, HADES data points are taken from linear interpolations at  $p_{t,12} = 220$  MeV/c of the dependences shown in Figure 5.34. The trends of  $\sigma_x$ ,  $\sigma_y$  and  $\sigma_z$  are smooth, and the values are decreasing with larger values of  $\sqrt{s_{\text{NN}}}$ . When compared with the excitation function for central  $\phi$ -integrated results (see Figure 5.27), this seems a bit misleading, since it was emphasized that there is no rising of the radii with lower beam energy. However, one should take into account that here only  $\pi^-\pi^-$  data is compared and that the influence of the central Coulomb potential is very large at such small values of  $k_t$ , compare also with Figure 5.21. Fixing the interval of  $k_t$  as been done by E895, delivers for HADES an average transverse momentum of  $\bar{k}_t \approx 150$  MeV/c and corresponding results are plotted as boxes. Except  $\sigma_x$ , the semi-axes at this slightly larger transverse momentum describe also good the curvature of the AGS trends. For  $\theta_s$ ,  $\varepsilon_{xy}$  and  $\varepsilon_{zy}$ , one finds also very smooth trends

## 5. Results

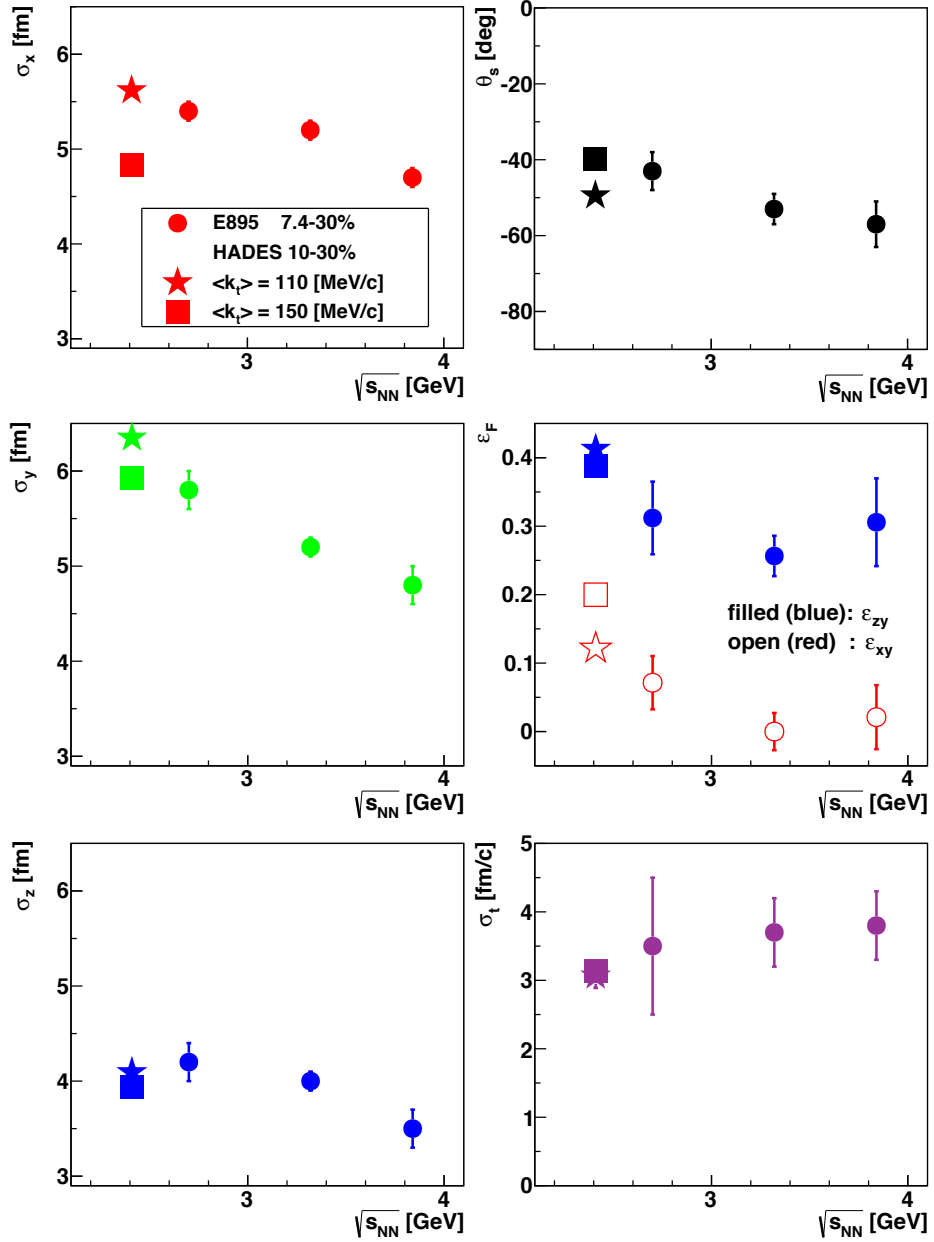


**Figure 5.35:** The spatial principal axes (left column), the tilt angle w.r.t. the beam axis in the reaction plane (see Equation (4.44), top right), the  $xy$ -eccentricity (empty) and the  $zy$ -eccentricity (filled symbols, Equations (4.46) and (4.47), right middle) and the emission duration  $\sigma_t$  (bottom right) of the Gaussian emission ellipsoid for  $\pi^-\pi^-$  as function of  $\sqrt{s_{NN}}$  for semi-peripheral Au + Au collisions. Circles represent data of E895 at AGS [19] for 7.4 – 30 % centrality at average  $k_t$  of 110 MeV/c, HADES data interpolated to this value of  $k_t$  using the data of Figure 5.34 is given by stars. Boxes represent HADES interpolated data at  $k_t = 150$  MeV/c. Error bars include only statistical uncertainties.

with decreasing values for higher values of  $\sqrt{s_{\text{NN}}}$ . The same holds finally for  $\sigma_t$ , but increasing with  $\sqrt{s_{\text{NN}}}$ . Looking at  $\theta_s$ , the box fits even better into the trend of E895 than the star, indicating that the higher transverse momenta are the more reliable ones. However, the uncertainties of the HADES data are by a significant factor smaller than those from E895 data, therefore a possible kink of  $\theta_s$  is not reliably confirmable when comparing with the published value of  $\bar{k}_t = 110 \text{ MeV}/c$ .

### Eccentricities

Unfortunately, E895 is the one and only experiment which provides published results from a comparable analysis considering tilt angles  $\theta_s$ , although there is work in progress at STAR [117]. Going to higher energies one can compare  $\varepsilon_{xy}$  and  $\varepsilon_{zy}$  with those extracted with the simplified form of Equations (4.52) and (4.53), under the assumption that  $\theta_s$  is small. In Figure 5.36, the values of  $\varepsilon_{xy}$  ( $\varepsilon_{zy}$ ) from Figure 5.35 are kept as blue open (filled) symbols, stars are again HADES data points and circles represent data from E895. In addition, data of CERES at SPS [20] (diamonds), STAR at RHIC [17] (triangles), and ALICE at LHC [21] (boxes) are included; open symbols are calculated using Equation (4.52) and filled symbols using Equation (4.53). If data was available only for the more narrow centrality classes 10 – 20 % and 20 – 30 % (especially for ALICE) it has been averaged over both. Since all data  $\sqrt{s_{\text{NN}}} \geq 7 \text{ GeV}$  is not available at the same value of  $k_t$  of  $110 \text{ MeV}/c$  as for E895, different colors are chosen for the presentation, and corresponding HADES points are added. The CERES data is given at an average value of  $k_t$  of  $230 \text{ MeV}/c$  (colored in green). STAR and ALICE data is available over a wide range in  $k_t$  starting at around  $260 \text{ MeV}/c$ . Since in [17, 118] a study of  $\varepsilon_{\text{final}}$  has been done using  $\bar{k}_t = 310 \text{ MeV}/c$ , this value is kept here for having a better comparison, using black color. The long- (short-) dashed colored curves are 'guiding-eyes' curves with a parametrisation  $a \exp[-b \log(\sqrt{s_{\text{NN}}})] + c$  without direct physical motivation. Overall, both eccentricities decline monotonously for all considered values of  $k_t$ . The variation of the data points for higher values of  $\sqrt{s_{\text{NN}}}$ , i.e. larger than  $10 \text{ GeV}$ , is relatively low as compared to the variations at smaller energies. The values of  $\varepsilon_{zy}$  are always larger than those of  $\varepsilon_{xy}$ . The arrow on the ordinate gives the final eccentricity  $\varepsilon_{\text{final}}$  extracted from Glauber simulations for HADES energies, which decreases slightly over three orders of magnitude in  $\sqrt{s_{\text{NN}}}$  from 0.271 to 0.224. In [17, 118] the larger eccentricity  $\varepsilon_{zy}$  (there defined as  $\varepsilon_{xy}$ ) is associated with the initial eccentricity  $\varepsilon_{\text{ini}}$ , while in the present work  $\varepsilon_{xy}$  is linked to  $\varepsilon_{\text{ini}}$ , which becomes clear following the systematics in  $p_{t,12}$  (and in centrality, see the next section). This indicates a crossing of trends in the region of  $\sqrt{s_{\text{NN}}} = 4 – 7 \text{ GeV}$ . A hint for that is visible at the lowest data points of STAR at  $7.7 \text{ GeV}$ , where  $\varepsilon_{xy}$  seems to be a bit above the overall trend and  $\varepsilon_{zy}$  a bit below. However, this is most properly related

## 5. Results

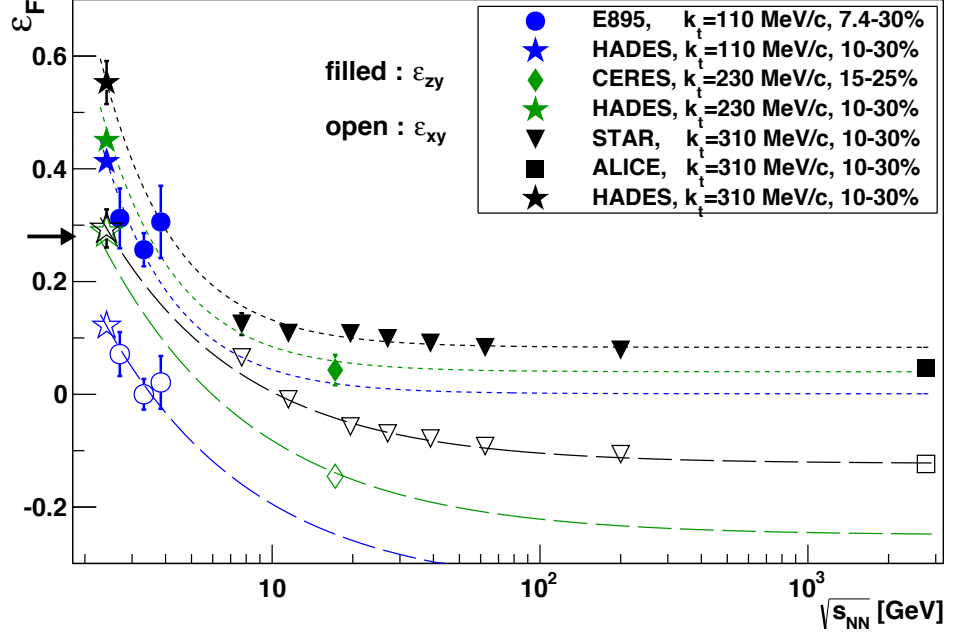


**Figure 5.36:** Excitation function of the approximate  $\pi^- \pi^-$  freeze-out eccentricity for semi-peripheral Au + Au, Pb + Au, or Pb + Pb collisions. Stars are HADES  $\pi^- \pi^-$ -data for three different transverse momentum regions with average values of  $\bar{k}_t = 110, 230$ , and  $260$  MeV/c. Filled (open) symbols represent  $\epsilon_{zy}$  ( $\epsilon_{xy}$ ); for details see the text. The circles, diamonds, triangles, and squares are corresponding data by E895 at AGS [19], CERES at SPS [20], STAR at RHIC [17], and ALICE at LHC [21], respectively. The arrow on the ordinate denotes the approximate (not constant) value of  $\epsilon_{ini}$ , the dashed curves are for guiding the eyes without physical motivation. Error bars include only statistical uncertainties.

to the fact that  $\theta_s$  is not anymore small enough for the simple consideration yielding Equations (4.52) and (4.53). This idea is also supported by [119], where UrQMD model calculations confirm the trend of  $\epsilon_{zy}$  in Figure 5.36 and indicate that for the lowest STAR energies the tilt angle  $\theta_s$  has already values significantly different from  $0^\circ$  and  $90^\circ$ , respectively. A few illustrations concerning this particular aspect can be found in Appendix B.6.

### Emission duration $\Delta\tau$

The values of  $\sigma_t$  from the lower right panel of Figure 5.35 can be identified with the freeze-out duration  $\Delta\tau$ , which can be calculated by using Equations (2.43) and (5.7) in an azimuthally integrated analysis. By replacing  $R_{out}$  by  $R_{out,0}$  and  $R_{side}$  by  $R_{side,0}$  comparable values can be determined for the azimuthally dependent analysis of STAR, ALICE and CERES. The

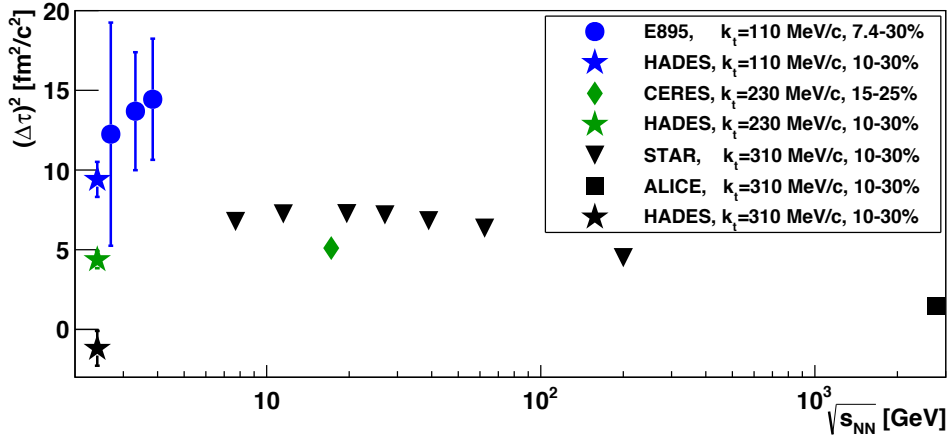


**Figure 5.37:** Excitation function of the squared emission duration, either directly taken from the corresponding fit parameter of the spatial correlation tensor,  $\sigma_t^2 = S_{00}$  (cf. Equation (4.38)), or derived from the difference of the 'out' and 'side' radii,  $(\Delta\tau)^2 = (R_{\text{out}}^2 - R_{\text{side}}^2)/\langle\beta_t^2\rangle$ , for semi-peripheral (10 – 30 %) Au + Au, Pb + Au, or Pb + Pb collisions. Stars are HADES  $\pi^-\pi^-$  data of  $\sigma_t^2$  for three different transverse momentum regions with average values of  $\bar{k}_t = 110, 230$ , and  $310 \text{ MeV}/c$ . The circles are corresponding  $\sigma_t^2$  data by E895 at AGS [19]. The diamond, triangles and square represent data of  $(\Delta\tau)^2$  by CERES at SPS [20], STAR at RHIC [17], and ALICE at LHC [21], respectively. Error bars include only statistical uncertainties.

squared results are exhibited in Figure 5.37 in dependence on  $\sqrt{s_{\text{NN}}}$ . Colors and symbols belong to the same experiments and values of  $k_t$  as in Figure 5.36. Considering the black triangle data points one finds a weak local maximum at  $\sqrt{s_{\text{NN}}} \approx 10 - 20 \text{ GeV}$ . For larger and lower energies,  $(\Delta\tau)^2$  decreases, the HADES value even becomes negative. As already discussed in Section 5.2.6, this is a hint that the measure of Equation (2.43) is highly influenced by momentum-space correlations, the finite pion mean-free path [50], or other similar aspects. A strong  $k_t$  dependence is not only visible for HADES: Continuing the trend of blue symbols with  $k_t = 110 \text{ MeV}/c$  from low energies to higher ones and comparing with the black symbols, one finds that  $(\Delta\tau)^2$  decreases with higher transverse momentum. Only the CERES data point is an outlier in this systematics, which is a direct consequence of the systematics of  $R_{\text{out}}$  in the azimuthal integrated analysis in Figure 5.27, where the CERES values are slightly below the overall trend. Although Figure 5.37 considers only  $\pi^-\pi^-$  data, the charge-sign of the pion pairs is important at low energies, especially at low values of  $k_t$ . Comparing with Figures 5.32 and 5.33 one finds that the HADES value for  $\pi^+\pi^+$  is up to  $10 \text{ fm}^2/c^2$  larger at  $k_t = 110 \text{ MeV}/c$ , which means that the freeze-out

## 5. Results

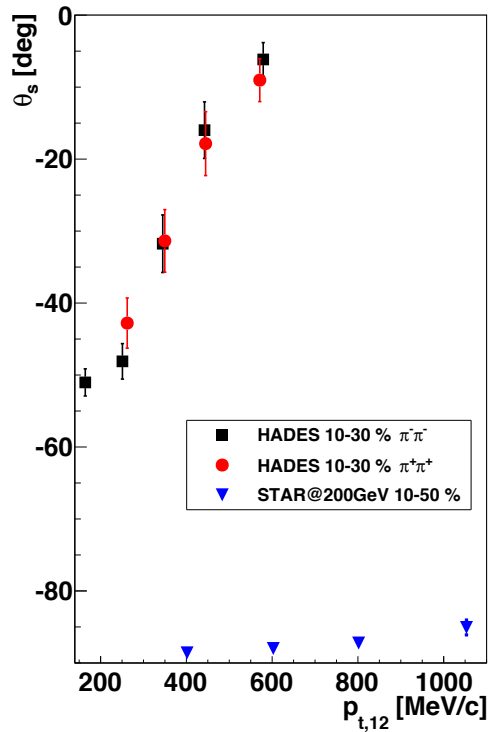
---

duration is not affected by this Coulomb effect and can be about  $5 \text{ fm}^2/c^2$  higher.

However, regarding Figures 5.36 and 5.37 it turned out that the results obtained for HADES match very good the existing systematics. Especially in view of previously existing compilations [17, 119], the  $k_t$ -differential data of this thesis helps to connect the data points from E895, CERES, STAR and ALICE and acts as a key to combine them in one picture.

### Tilt angle $\theta_s$

**Figure 5.38:** Available published and preliminary data for the tilt angle  $\theta_s$  in dependence on  $p_{t,12}$  for semi-peripheral collisions of Au+Au. Error bars include only statistical uncertainties.



The experimental values of E895 plotted in Figure 5.35 are the only published data of the tilt angle  $\theta_s$ . Preliminary data is available only from STAR at  $\sqrt{s_{\text{NN}}} = 200 \text{ GeV}$  for 10 – 50 % centrality [117, 120]. The dependence on centrality was found to be small at that energy and therefore one can compare it with the HADES data for 10 – 30 % centrality. In Figure 5.38, the  $p_{t,12}$  dependence of  $\theta_s$  is plotted. The tilt angles obtained by STAR deviate only less from  $-90^\circ$ . For all data sets a decrease of the tilt magnitude with increasing transverse momentum is visible. At  $p_{t,12} = \mathcal{O}(600 \text{ MeV}/c)$ , the ellipsoids of homogeneity from both, STAR and HADES, show no tilt relative to the beam axis. Indeed, they have opposite orientations w.r.t. the larger semi-axis within the reaction plane. Metaphorically spoken the ellipsoid is upright at HADES energy and lying flat at STAR energy. One

can assume that the gap between the plotted dependencies can be filled with data extracted at energies between SIS18 and the highest RHIC energy. This assumption is supported by UrQMD calculations [119], predicting a smooth transition of the tilt angle over three orders of magnitude in beam energy.

### Semi-axes and volume of homogeneity

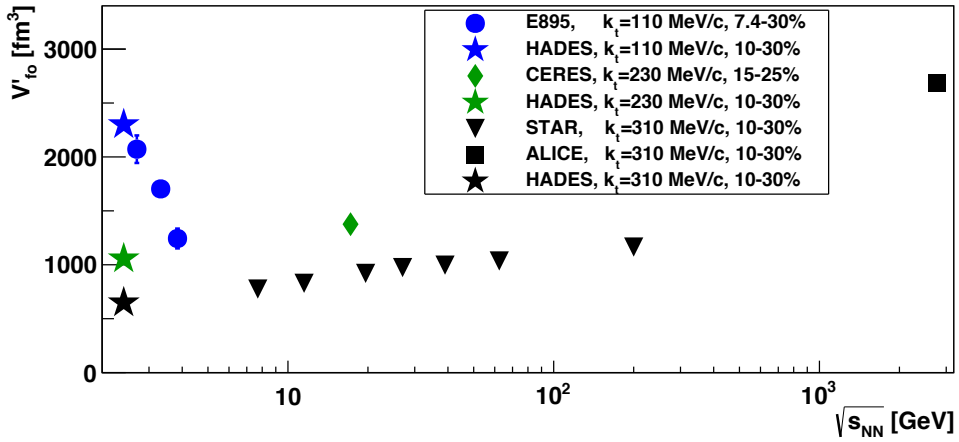


**Figure 5.39:** Excitation function of the volume of homogeneity  $V'_{\text{fo}}$  according to Equation (5.8) as a function of  $\sqrt{s_{\text{NN}}}$ . Symbols and colors are the same as in Figure 5.37. Error bars include only statistical uncertainties.

Last but not least, the three semi-axes  $\sigma_x$ ,  $\sigma_y$  and  $\sigma_z$  ( $\sigma_x'$ ,  $\sigma_y'$  and  $\sigma_z'$  from Equation (4.51), respectively) and the resulting volume of homogeneity,

$$V'_{\text{fo}} = (2\pi)^{3/2} \sigma_x \sigma_y \sigma_z, \quad (5.8)$$

are discussed as a function of  $\sqrt{s_{\text{NN}}}$ , see Figure 5.39 with colors and symbols the same as in Figure 5.37. For large values of available  $k_t$ , one finds a smooth increase of  $V'_{\text{fo}}$  for changing  $\sqrt{s_{\text{NN}}}$  over three orders of magnitude from HADES over STAR up to ALICE (black symbols for  $k_t = 310 \text{ MeV}/c$ ). A comparable slope of  $V'_{\text{fo}}(\sqrt{s_{\text{NN}}})$  is found when comparing the two HADES and CERES data points at medium transverse momentum ( $k_t = 230 \text{ MeV}/c$ , green symbols). However, at small values of  $k_t$  the volume of homogeneity is strongly decreasing with energy, e.g. in the region from 2 – 4 GeV by more than a factor of two ( $k_t = 230 \text{ MeV}/c$ , blue symbols). Since in this excitation function again only negative charged pions are considered, the effective volume – unbiased by the Coulomb potential of participants and spectators – is expected slightly reduced. Using the corresponding semi-axes of  $\pi^+ \pi^+$  as input for Equation (5.8) one gets a value of  $V'_{\text{fo}}$  which is about  $1000 \text{ fm}^3$  lower

## 5. Results

---

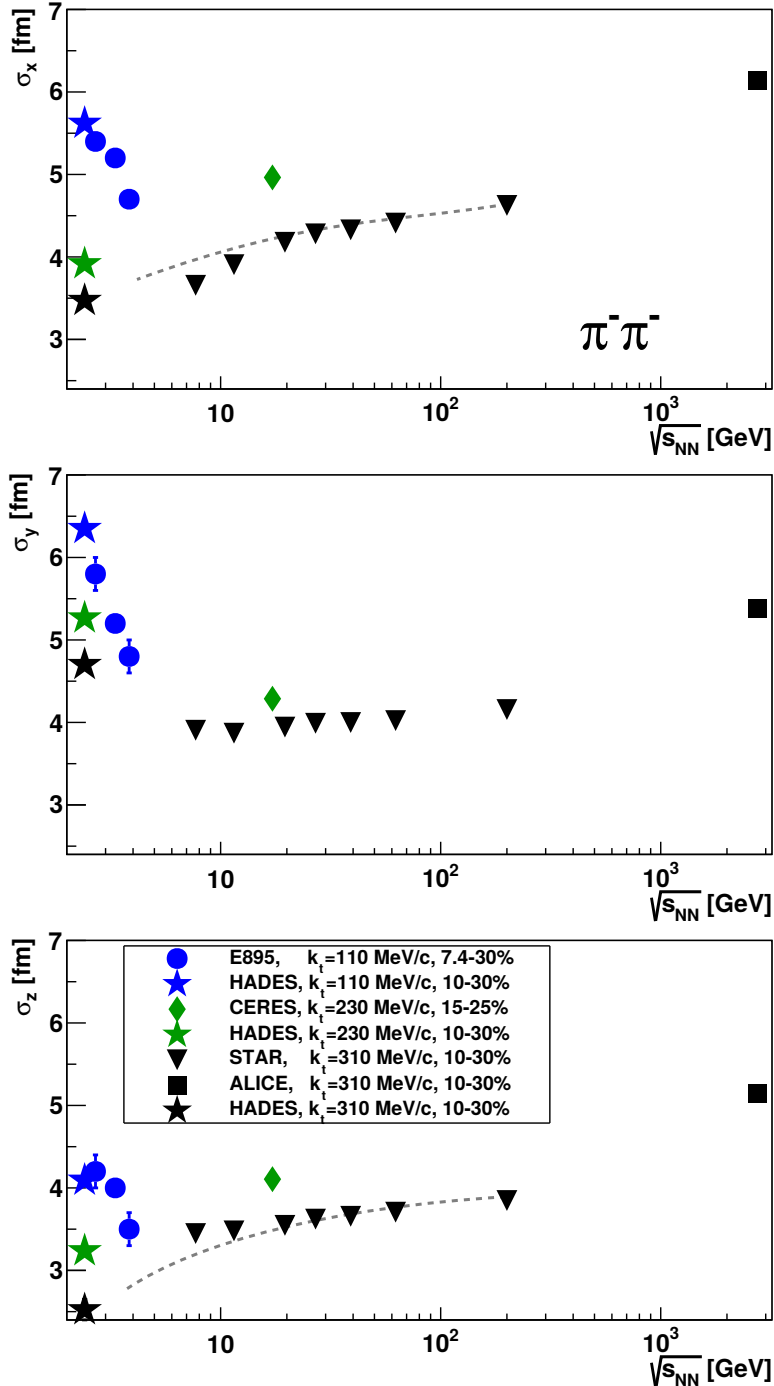


**Figure 5.40:** Excitation function of the semi-axes  $\sigma_x$  (upper panel),  $\sigma_y$  (middle panel) and  $\sigma_z$  (lower panel) as a function of  $\sqrt{s_{\text{NN}}}$ . Symbols and colors are the same as in Figure 5.37. Values are taken from Figure 5.35 (Equation (4.51)) for  $\sqrt{s_{\text{NN}}}$  lower (higher) than 5 GeV. Dashed guiding-eye curves represent trends if possible tilt angles  $\theta_s$  are taken into account. Error bars include only statistical uncertainties.

than the value of  $V'_{\text{fo}}$  obtained for  $\pi^-\pi^-$ . This means the unbiased volume is about  $500 - 600 \text{ fm}^3$  smaller compared to what is displayed in Figure 5.39. This is still larger than the E895 volume at highest beam energy. Since one can expect that all AGS data points are also affected by the charge-sign effect, the negative slope of the trajectory through the blue points is not explainable with Coulomb potential effects alone (, at most the half). However, contrary to what was found in Figure 5.28 for central collisions, HADES confirms the trend of E895 very good for semi-peripheral collisions, supposed the chosen value of  $\bar{k}_t = 110 \text{ MeV}/c$  is correct. This decreasing trend is found simultaneously for all three semi-axes, exhibited in Figure 5.40 ( $\sigma_x$  upper,  $\sigma_y$  middle, and  $\sigma_z$  lower panel), which means that there is no preferred direction of the fireball expansion at lower energies. This is different for the higher transverse momenta. Considering  $k_t = 310 \text{ MeV}/c$ ,  $\sigma_x$  and  $\sigma_z$  increase very smoothly with  $\sqrt{s_{\text{NN}}}$ , although there are small shifts at lowest energies of STAR due to a possible disregard of the tilt angle  $\theta_s$ , i.e. missing major-axis transformation (see also Appendix B.6). In contrast,  $\sigma_y(\sqrt{s_{\text{NN}}})$  is decreasing first, acquires a local minimum at about  $10 \text{ GeV}$ , and then starts to increase smoothly up to ALICE energies, similar as in the other two directions. This observation is confirmed by the comparison of HADES and CERES data points at  $k_t = 230 \text{ MeV}/c$ , where  $\sigma_x$  and  $\sigma_z$  of HADES are smaller than that of CERES at lower energy, but  $\sigma_y$  is larger. This is the most interesting point here, since it could be seen as geometrical manifestation of the so called 'squeeze-out', i.e. a strong out-of-plane particle emission around mid-rapidity in the early stage of the collision observed at low beam energies. At beam energies smaller than  $10 \text{ GeV}$ , the region of homogeneity tends to expand more out of the reaction plane, while at energies higher than  $20 \text{ GeV}$ , the expansion continues equally distributed in all three spatial directions, although the in-plane elliptic flow at high beam energies [121] might cause  $\sigma_y$  to increase a bit less than  $\sigma_x$  and  $\sigma_z$  at next-to-leading order. Finally, these findings also complement quite well Figure 5.27, bearing in mind the different centralities. This also highlights the advantage of an azimuthally sensitive analysis compared to the  $\Phi$ -integrated investigation. While  $R_{\text{side}}$  as quadratic average of  $\sigma_y$  and  $\sigma_x$  (and partially an admixture of  $\sigma_z$ , dependent on  $\theta_s$ ) was found to be almost independent of  $\sqrt{s_{\text{NN}}}$  (except at LHC energies), it turned out that this is due to the counterbalance of rising  $\sigma_y$  by decreasing  $\sigma_x$  or  $\sigma_z$ , respectively. Furthermore,  $R_{\text{long}}$ , which shows the largest dependence on  $\sqrt{s_{\text{NN}}}$ , can be related to  $\sigma_x$  at high energies and with  $\sigma_z$  at low energies, under the condition of vanishing  $\theta_s$  (as in the case at large values of  $k_t$ ), and as a mixture of both semi-axes in regions of  $\sqrt{s_{\text{NN}}}$  and  $k_t$ , where a sufficiently large tilt angle must not be ignored.

### 5.3.3 Dependence on centrality

After studying the transverse momentum dependence and the excitation function of the spatial parameters of the three-dimensional source model for semi-peripheral collisions, the systematics in classes of centrality is considered.

#### Spatial parameters

In Figure 5.41, the semi-axes  $\sigma_x$ ,  $\sigma_y$  and  $\sigma_z$ , the tilt angle  $\theta_s$  and the out-of-plane eccentricities  $\varepsilon_{xy}$  and  $\varepsilon_{zy}$  for  $\pi^-\pi^-$  are displayed similarly to Figure 5.34, but here for different classes of centrality. Red circles correspond to 0 – 10 %, violet boxes to 10 – 20 %, blue up-pointing triangles to 20 – 30 %, cyan diamonds to 25 – 35 % and green down-pointing triangles to 30 – 45 %. The trends of all source extensions change systematically with centrality: the more central the collision is the larger is the deduced source size. Furthermore, the source sizes are decreasing with higher values of  $p_{t,12}$ , which is best seen in  $\sigma_x$ , where the slope is the steepest. In  $\sigma_y$  and  $\sigma_z$ , the slope is larger for more central collisions, while for most peripheral collisions,  $\sigma_z$  seems to be almost independent of  $p_{t,12}$ . The tilt angle in the reaction plane seems to vanish for all centralities at large transverse momenta, i.e.  $\theta_s = 0^\circ$  or  $-90^\circ$ , respectively. It is always negative, which means that the source ellipsoid is tilted to the front, i.e. inside the reaction plane the larger semi-axis points into the direction of the spectators. The magnitude of the tilt becomes largest at lowest transverse momenta. For all centralities, the  $xy$ -eccentricity increases with higher values of  $p_{t,12}$ , seems to vanish at very low transverse momenta, and reaches at highest measurable  $p_{t,12}$  the corresponding value of the initial eccentricity  $\varepsilon_{\text{ini}}$ , the latter one depending on the impact parameter of the collision and derived from Glauber Monte-Carlo simulations. The more peripheral the collision is the more pronounced are the overall trends of  $\varepsilon_{xy}$ . The  $zy$ -eccentricity does not show a clear dependence on  $p_{t,12}$  or centrality of the collisions. It varies a bit at low transverse momenta and seems to increase at higher values. For more central collisions,  $\varepsilon_{zy}$  becomes on average smaller, and in general its values are larger than those of  $\varepsilon_{xy}$ . The point of centrality 25 – 35 % at highest value of  $p_{t,12}$  is to be considered as an outlier.

In Figure 5.42, the same systematics is plotted for  $\pi^+\pi^+$ . Due to the reduced pair statistics by a factor of about 5, there are less data points compared to  $\pi^-\pi^-$ . Overall, the values of the semi-axes are smaller compared to  $\pi^-\pi^-$ , which has to be addressed to the Coulomb force of participants and spectators, similar as introduced in Section 5.2.4. The decrease with higher transverse momenta is weaker compared to  $\pi^-\pi^-$ , and the separation of the trends in the dependence on centrality is not visible that clear anymore. In general, the observation of larger source extensions for more

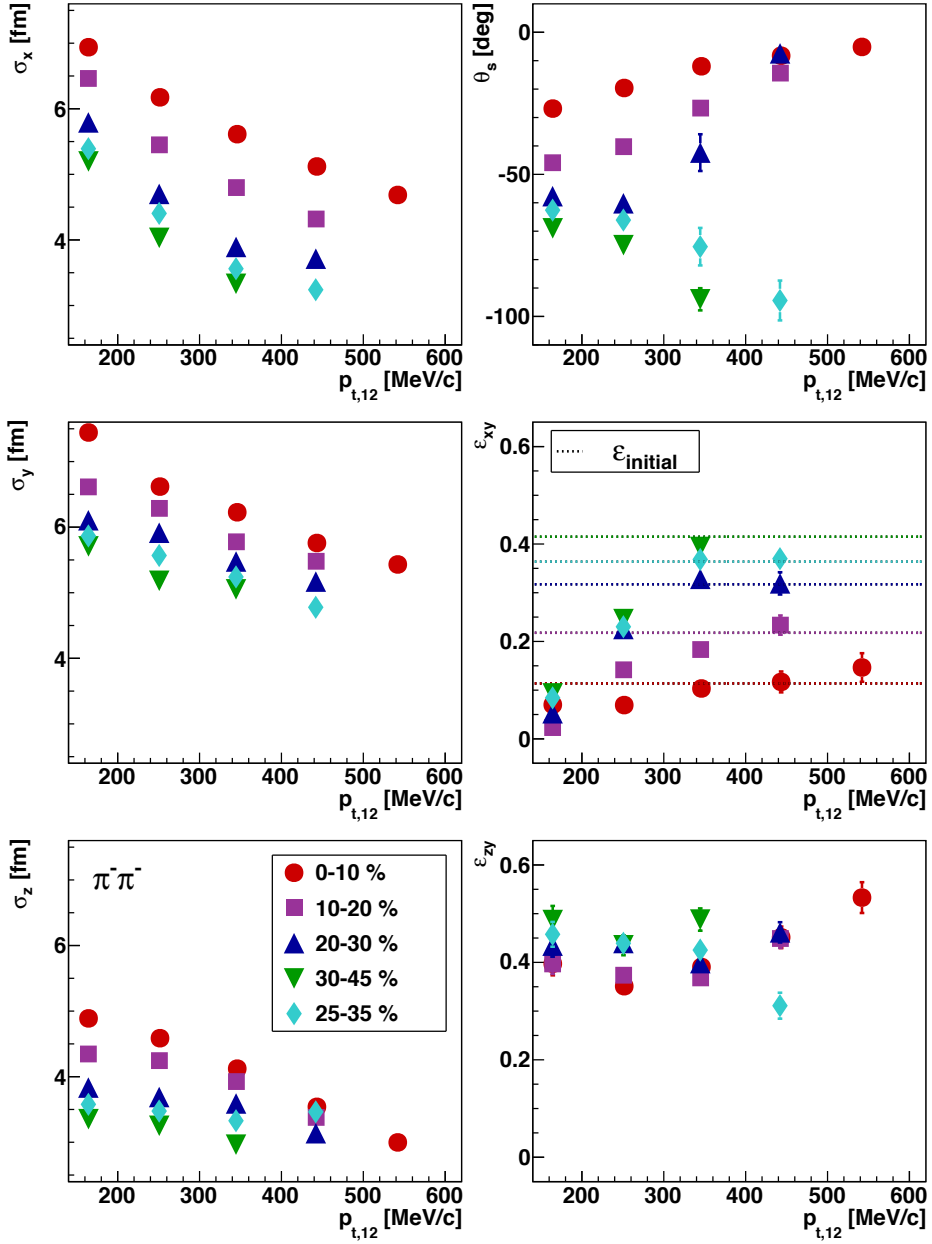


**Figure 5.41:** The spatial semi-axes (left columns), the tilt angle w.r.t. the beam axis in the reaction plane (Equation (4.44), top right), the  $xy$ -eccentricity (Equation (4.46), right middle) and the  $zy$ -eccentricity (Equation (4.47), bottom right) of the Gaussian emission ellipsoid of  $\pi^+\pi^-$  as function of transverse momentum for 0 – 10 % (circles), 10 – 20 % (boxes), 20 – 30 % (up-pointing triangles), 25 – 35 % (diamonds), and 30 – 45 % (down-pointing triangles), respectively. Error bars include only statistical uncertainties. Dotted lines represent the initial nucleonic eccentricities for the corresponding centrality classes derived from Glauber simulations.

## 5. Results

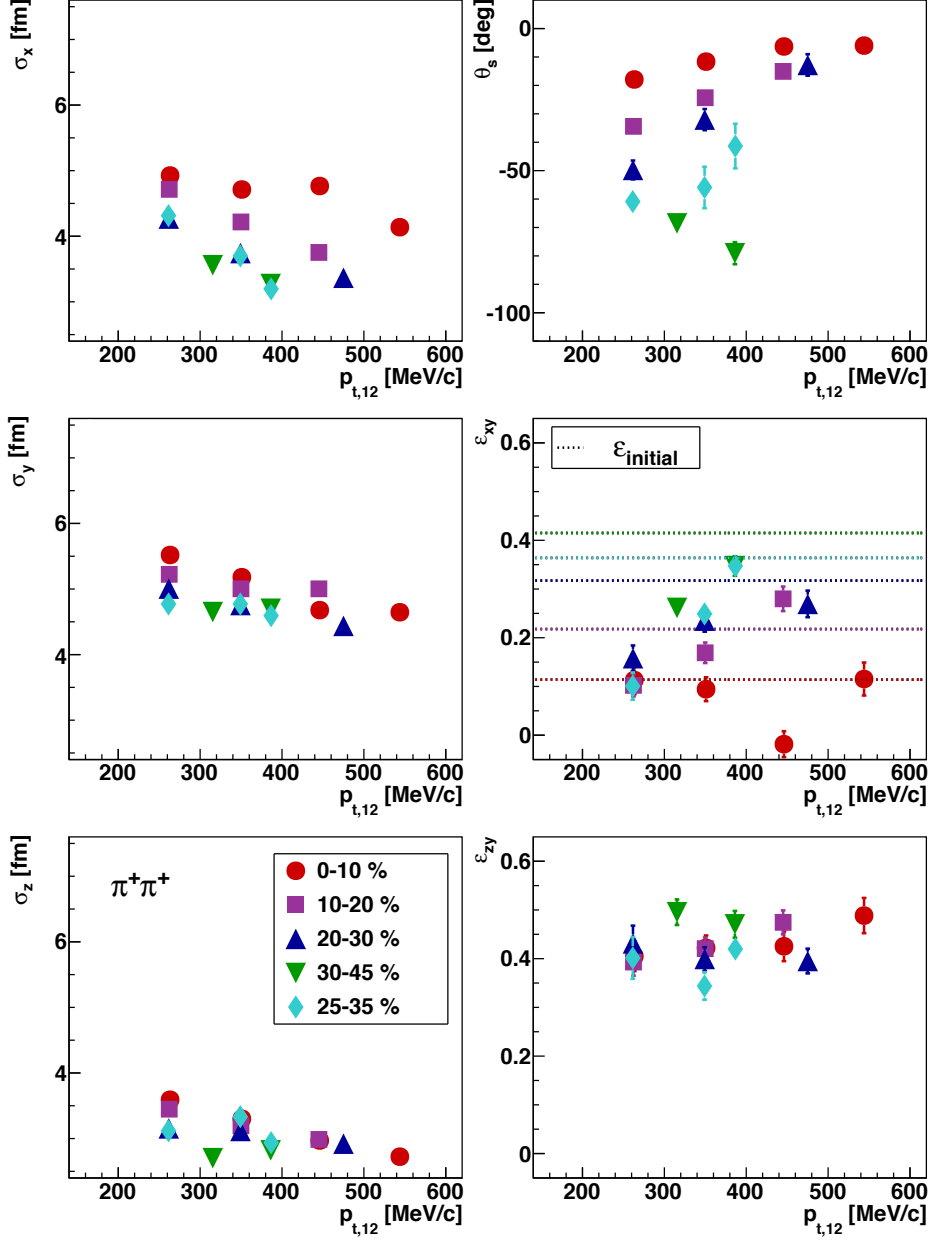
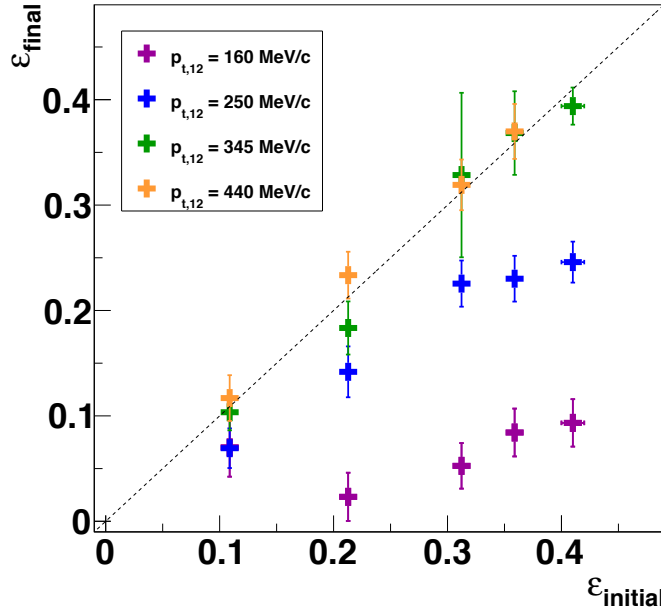


Figure 5.42: Same as Figure 5.41, but for  $\pi^+\pi^+$ .

central collisions does not longer apply. This is also a consequence of the central Coulomb potential introduced in Section 2.3.2, which has a larger influence at lower transverse momenta. Comparing with Equation (2.29) one finds a flattening of the decreasing  $p_{t,12}$ -slopes for  $\pi^+\pi^+$  and a compression of data points in direction of centrality with respect to the smaller effective Coulomb potential in more peripheral collisions, see Appendix B.3. The



**Figure 5.43:** Final eccentricity  $\varepsilon_{\text{final}}$  ( $xy$ -eccentricity) plotted against initial nucleonic eccentricity  $\varepsilon_{\text{ini}}$  derived from Glauber simulations for different values of pair transverse momenta of negatively charged pion pairs. The dashed line depicts  $\varepsilon_{\text{final}} = \varepsilon_{\text{ini}}$ . Error bars include only statistical uncertainties.

trends of the tilt angle are similar as in Figure 5.41 for all centrality classes, which confirms the statement already made w.r.t. Figure 5.34 that  $\theta_s$  shows no significant dependence on the pion polarity. Also the  $zy$ -eccentricity has, similar to  $\pi^-\pi^-$ , no clear trend. For all measured transverse momenta and centrality classes it has values of about  $0.4 \pm 0.1$ . The  $xy$ -eccentricity for semi-peripheral collisions is again increasing with  $p_{t,12}$ , but does not reach the corresponding values of  $\varepsilon_{\text{ini}}$  like for  $\pi^-\pi^-$ . For the central collisions ( $0 - 10\%$ ), there is almost no dependence on transverse momentum, and  $\varepsilon_{xy}$  is approximately the same as the initial value from Glauber calculations. There are two special points breaking the specified systematics of  $\varepsilon_{xy}$ : the points for centralities  $0 - 10\%$  and  $10 - 20\%$  at about  $p_{t,12} = 440 \text{ MeV}/c$ . The reduction of the red point might be a consequence of the charge-sign difference of  $\sigma_x$  and  $\sigma_y$ , since  $\sigma_y$  has a wider gap between  $\pi^-\pi^-$  and  $\pi^+\pi^+$  values over the whole range of  $p_{t,12}$ , while for  $\sigma_x$  this gap appears only at lower transverse momenta and vanishes already at exactly this position of  $p_{t,12} = 440 \text{ MeV}/c$ . The upward shift of the violet box at this transverse momentum is not that clear and it might be an outlier.

One should comment here on the arrangement of the data points. Due to the freedom in the coordinate-system definition, the tilt angle, defined as

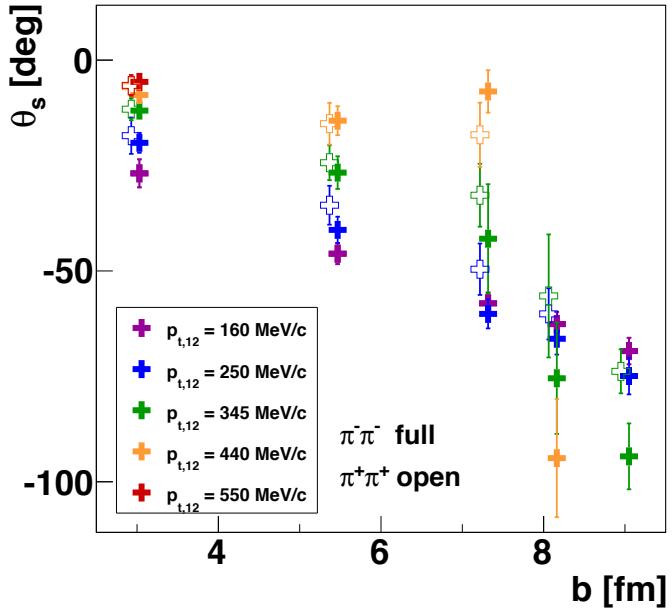


**Figure 5.44:** Tilt angle  $\theta_s$  in dependence on the impact parameter  $b$  derived from Glauber simulations for different values of pair transverse momenta. Filled (open) crosses denote  $\pi^- \pi^-$  ( $\pi^+ \pi^+$ ) pairs; for better visibility data points are shifted slightly to the right (left).

the angle between the  $z$  coordinate (directed along the shortest principal axis in our case) and the beam direction, can be changed from  $\theta_s$  to  $\theta_s - 90^\circ$ , while  $\sigma_x$  and  $\sigma_z$  (and accordingly  $\varepsilon_{xy}$  and  $\varepsilon_{zy}$ ) interchange, see the comment at the end of Section 4.5.3. Thus, there are quite some possibilities of arranging the data points in Figures 5.41 and 5.42 relative to each other. The arrangement of the data was chosen such that both dependences, on transverse momentum and on centrality, show smooth trends, i.e. no alternating series of data points exist. Furthermore, smaller values of  $|\theta_s|$  for more central collisions are ensured, as one would expect from the collision geometry. However, at more peripheral collisions and large values of  $p_{t,12}$ , a different configuration is conceivable, i.e. requiring  $\theta_s = 0$  at high transverse momenta, which becomes relevant here only for the data points at  $p_{t,12} = 440 \text{ MeV}/c$  and centrality  $25 - 35\%$  for  $\pi^- \pi^-$ . Within the statistical and systematic uncertainties in this analysis one is not able to decide which arrangement is the better one. An illustration with overlapping transverse momentum intervals can be found in Appendix B.4. Note also that near  $p_{t,12} = 400 \text{ MeV}/c$  and for centralities larger than 20%,  $\sigma_x$  and  $\sigma_z$  are about the same size, which disturbs the picture of a well defined tilt angle, possibly represented by large uncertainties of this quantity.

In Figure 5.43, the final eccentricity, meanwhile the  $xy$  eccentricity, is related to the initial nucleonic eccentricity  $\varepsilon_{\text{ini}}$  derived from Glauber simulations. Different colors represent different mean values of  $p_{t,12}$ . The dependencies are nicely ordered in direction of pair transverse momenta. At small values of  $p_{t,12}$  the final eccentricity becomes smallest and the shape of the emission ellipsoid in the  $xy$  plane is close to a circle. For increasing transverse momenta,  $\varepsilon_{\text{final}}$  becomes larger, and at large transverse momenta the source eccentricity derived from the present identical-pion HBT analysis recovers the initial eccentricity. This can be interpreted as an temporal evolution with an anti-correlation of  $k_t$  and time, i.e. high transverse momenta are related more to the early stage of the fireball evolution and low transverse momenta to the later stage. It confirms the discussion made in Section 5.2.5.

To study the centrality dependence of the tilt angle in more detail, Figure 5.44 displays  $\theta_s$  for  $\pi^-\pi^-$  (full symbols) and  $\pi^+\pi^+$  (open symbols) pairs as function of the impact parameter  $b$ , see Table 4.2, for different average transverse momentum values. No charge-sign difference is observed in the centrality dependence of  $\theta_s$ . While for lower momenta the magnitude of  $\theta_s$  is proportional to  $b$ , this dependence gets weaker with increasing pair transverse momentum until the tilt is close to zero for the highest momentum classes. A crucial change happens at impact parameter  $b \approx 8 \text{ fm}$ , where the hierarchy in direction of transverse momentum is flipped, i.e. the tilt angle decreases with increasing values of  $p_{t,12}$ . A more detailed study of this critical point can be found in Appendix B.4. With the interpretation of anti-correlated transverse momentum and evolution time of the fireball one estimates an elliptic region of homogeneity without tilt at the early stage and the highest magnitude of  $\theta_s$  at the final stage.

### Volume of homogeneity and comparison to azimuthally integrated results

The volume of homogeneity  $V_{\text{fo}}$  in the azimuthally dependent analysis is calculated using Equation (5.8), which is the exact expression for a model with three-dimensional ellipsoid with three independent semi-axes and Gaussian density distribution. In Figure 5.45,  $V_{\text{fo}}$  is exhibited by filled symbols for four different centrality classes in dependence on  $p_{t,12}$ . Black boxes represent data of  $\pi^-\pi^-$  and red circles those of  $\pi^+\pi^+$ . One finds the strong dependence of the volume on the transverse momentum and also the dependence on the charge of the pion pairs. The latter one becomes weaker the more peripheral the collisions are, which implies that the charge-sign splitting is more related to the central Coulomb potential, i.e. the bulk charge of the participants, than to the Coulomb effect of the spectators. The exact three-dimensional volume model can be compared to the corresponding values of the azimuthally integrated analysis, calculated with Equation (5.6) and depicted as open symbols. On a first glance they match good to each

## 5. Results

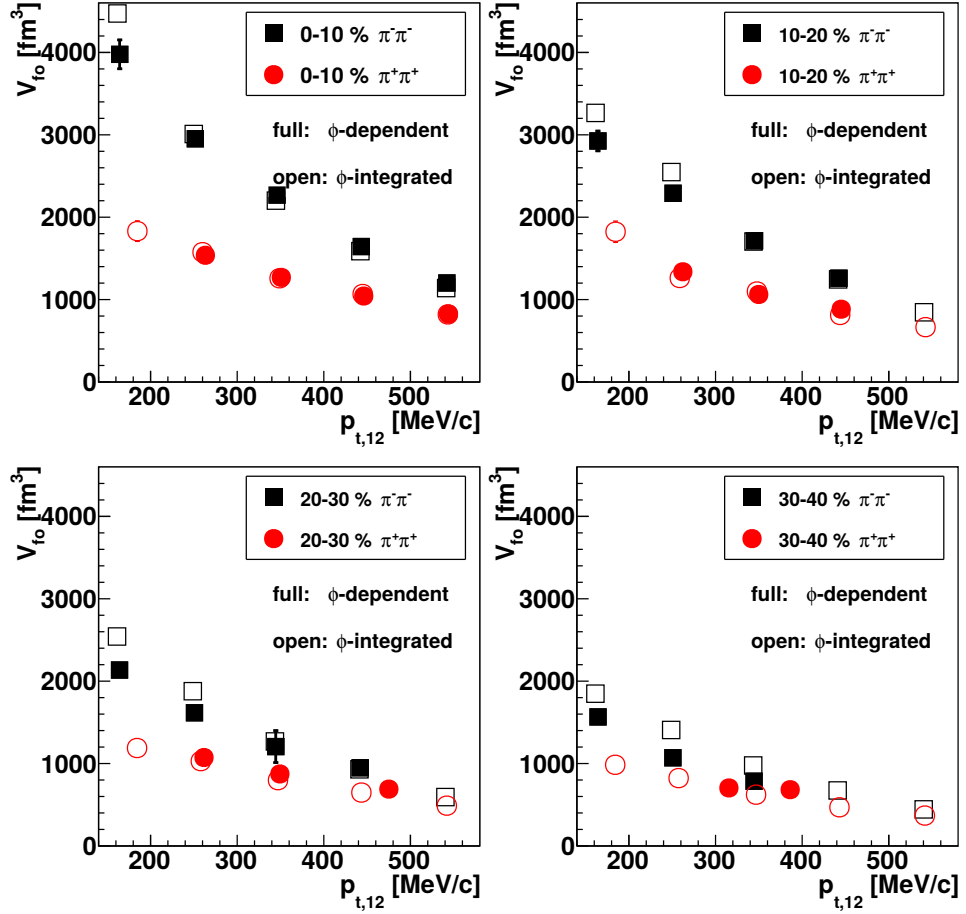


**Figure 5.45:** Comparison of the freeze-out volumes calculated with Equation (5.8) (full symbols) and using the azimuthally integrated approximation given by Equation (5.6) (empty symbols) for different centralities (top left: 0 – 10 %, top right: 10 – 20 %, bottom left: 20 – 30 %, bottom right: 30 – 40 %) for  $\pi^-\pi^-$  (black boxes) and  $\pi^+\pi^+$  (red circles) in dependence on pair transverse momentum.

other. For  $\pi^+\pi^+$ , almost no deviations are visible, but for  $\pi^-\pi^-$  the values of the azimuthally integrated analysis become larger than the others with decreasing transverse momenta. The deviations rise up to 10 – 20 %. Since Equation (5.6) does not account for the tilt angle  $\theta_s$ , and because  $R_{\text{side}}$  is taken as the average of  $\sigma_x$  and  $\sigma_y$ , it is clear that one could not always expect a coincidence of the results of both expressions. In Appendix B.7 the expected deviations are quantified in more detail.

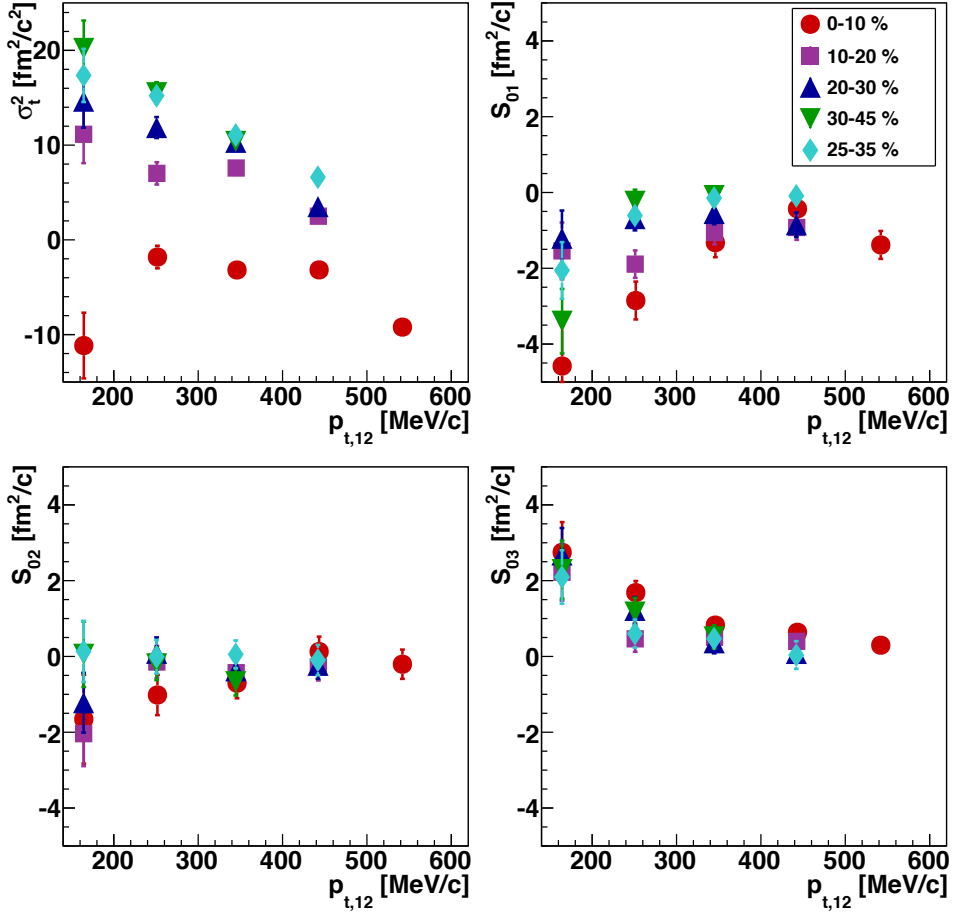


**Figure 5.46:** Temporal ( $S_{00}$ , respectively  $\sigma_t^2$ ) and spatio-temporal components ( $S_{01}$ ,  $S_{02}$ ,  $S_{03}$ ) of fits with Equation (4.38) to the six freeze-out variances  $R_{ij,i \neq j}^2$  ( $i, j = \text{'out', 'side', 'long'}$ ) for  $\pi^- \pi^-$  in dependence on pair transverse momentum for centralities of 0 – 10 % (circles), 10 – 20 % (boxes), 20 – 30 % (up-pointing triangles), 25 – 35 % (diamonds) and 30 – 45 % (down-pointing triangles). Error bars include only statistical uncertainties.

### Temporal parameters

The temporal components  $S_{00}$ ,  $S_{01}$ ,  $S_{02}$  and  $S_{03}$  derived from the set of equations (4.38) are exhibited in Figure 5.46 for pairs of negative pions in dependence on  $p_{t,12}$ . Different colors denote different classes of centrality. The diagonal component  $S_{00}$  is related to  $\sigma_t^2$ . Similarly as shown in Figure 5.32,  $\sigma_t^2$  is mainly decreasing with increasing pair transverse momentum for all centralities. Especially for 0 – 10 % centrality, the values of  $\sigma_t^2$  become negative, which makes the definition as a squared duration difficult to

## 5. Results

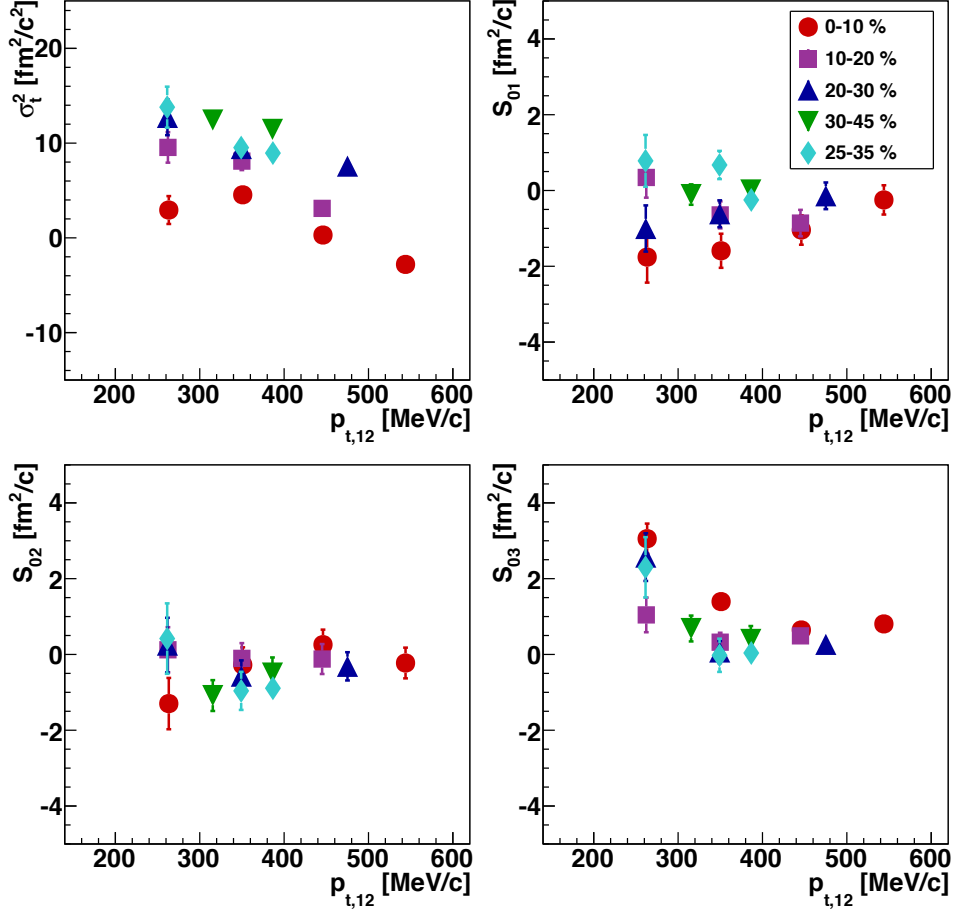


**Figure 5.47:** Same as Figure 5.46, but for  $\pi^+\pi^+$ .

understand. In Section 5.2.5, the influence of opacity has been discussed, and in [50] it was shown that the influence of an opaque source on the measured source extensions increases with increasing transverse momentum. As illustrated in Figure 5.26,  $R_{\text{out}}$  decreases and  $R_{\text{side}}$  increases as a result of a finite pion mean free path, resulting in a reduced value of  $\sigma_t^2$  according to Equation (5.7). Furthermore, the temporal components are also influenced by the Coulomb potential of the participants and spectators. For that reason the data of  $\pi^-\pi^-$  should be considered together with those of  $\pi^+\pi^+$  pairs, exhibited in Figure 5.47. Adding the quadratic values of both polarities and looking at the average values one finds at small transverse momenta the values of  $\sigma_t \approx 1 \text{ fm}/c$  for central collisions, for details see Appendix B.5. The temporal extension of the source is increasing for more peripheral collisions, visible for both pairs of negative and positive pions. Considering again the

quadratic averaged values of both polarities one finds  $\sigma_t \approx 3 - 4 \text{ fm}/c$  for semi-peripheral collisions at low values of  $p_{t,12}$ , see again Appendix B.5.

Caused by the symmetry constraints [104], implemented in Equation (4.39), the non-diagonal temporal elements  $S_{01}$ ,  $S_{02}$  and  $S_{03}$  should vanish. Obviously, these elements are small and mostly close to zero. However, especially at small transverse momenta trends are visible departing from zero.  $S_{01}$  and  $S_{02}$  are slightly decreasing for decreasing values of  $p_{t,12}$ , while  $S_{03}$  is increasing. This behaviour is visible in both figures, Figures 5.46 and 5.47, for  $\pi^-\pi^-$  and  $\pi^+\pi^+$  pairs. Although the statistical uncertainties of data points of different centrality classes are overlapping, the amplitude of this deviation from zero becomes larger for more central collisions. The increase of  $S_{03}$  with lower transverse momenta confirms the consideration in Section 5.2.2, since the expression of  $R_{\text{out long}}^2$  in the set of equations (4.38) can be identified with  $-S_{03}$  when ignoring the explicit dependence on  $\Phi$ . As discussed already w.r.t. Figures 5.32 and 5.33 within the centrality class of 10 – 30 %, the non-vanishing elements  $S_{01}$  and  $S_{02}$  can indicate an implicit  $\Phi$  dependence, which may arise as consequence of elliptic flow. However, in the chosen approach the non-vanishing non-diagonal matrix elements imply a systematic inadequacy. Differences between the results when fitting with Equation (4.39) and those of the fits performed with Equation (4.38) are added to the systematic uncertainties.

## 5. Results

---

# 6 | Conclusion and Outlook

In this thesis the two-particle correlation function of identically charged pions emitted from the fireball in Au+Au collisions at  $\sqrt{s_{\text{NN}}} = 2.41 \text{ GeV}$  was investigated. With the technique of intensity interferometry the area of homogeneity was imaged. A multi-differential analysis has been done to uncover the underlying physics and to initiate the visualisation of the pion-emitting source.

## Summary

The data was taken with the HADES setup in April 2012 with gold projectiles with 1.23AGeV kinetic energy impinging on a gold target. A high quality and high statistics data set of more than two billion events for investigating 0 – 45 % of the most central collisions was obtained. The pions were paired with each other per event and distributed as function of relative momenta. A detector based close-track selection on the level of hits in the sub-detectors was elaborated for the HADES setup, to account for the deficits of unresolvable pion pairs. A combinatorial background was formed by pairing pions from different events with similar event characteristics, and the correlation functions were constructed as the normalised ratio of true and mixed pair distributions. The invariant one-dimensional and three-dimensional correlation functions in the 'out-side-long' system were studied. The Bose-Einstein correlation signals were fitted with a Gaussian form, taking into account the mutual Coulomb interaction of the pairs. The extracted HBT radius and the incoherence parameters were studied in dependence on pair transverse momenta, centrality, charge sign of the pions, rapidities, and pair azimuthal angles relative to the event plane. From the azimuthal dependence of the HBT radius parameters, the temporal and geometric variances of the presumed ellipsoidal region of homogeneity, as well as a tilt angle relative to the beam axis were extracted. The results were compared to existing experimental data at other beam energies. Various excitation functions were studied.

In the explicit azimuthally integrated analysis an increase of the source parameters  $R_{\text{inv}}$ ,  $R_{\text{out}}$ ,  $R_{\text{side}}$  and  $R_{\text{long}}$  linear with  $A_{\text{part}}^{1/3}$  was found. This conforms with a linear dependence of the volume of homogeneity at freeze-out on

## 6. Conclusion and Outlook

---

the number of participants  $A_{\text{part}}$ . A decrease of all HBT radii with increasing pair transverse momenta was observed, which was found in experiments at higher energies, too, and is usually explained with space-momentum correlations due to radial flow. Nonetheless, the slope of these  $k_t$  dependencies was found steeper than models including radial or transversal flow can predict. Therefore, at least a part of this dependency is related for instance to resonance decay contributions of short-living resonances like  $\Delta$ 's. This hypothesis is supported by two-slope pion single-particle distributions within the same HADES data set, assigning direct thermal pions to higher transverse momenta and resonance-decay pions to lower ones. A substantial difference has been observed between the HBT radii of  $\pi^-\pi^-$  and  $\pi^+\pi^+$  pairs, becoming largest at low values of transverse momenta. While this charge-sign difference is small in  $R_{\text{out}}$ , it becomes clearly visible for the other radii. Especially for  $R_{\text{side}}$  and  $R_{\text{long}}$ , where the systematic uncertainties are comparably small, the gap is reasonably non-neglectable. It is noteworthy that such a significant difference in  $\pi^-\pi^-$  and  $\pi^+\pi^+$  HBT data has never been reported before. If there was any difference, it was covered by statistical and systematic uncertainties. This charge-sign splitting was assigned to a central Coulomb potential, i.e. the Coulomb force of the positively charged participant region, dominated by the initial number of protons in the spatial overlap region. Also, the influence of the positively charged spectators can contribute to this effect. This Coulomb potential leads to a shift in the relative momentum spectrum of the pairs and obviously to apparently smaller  $\pi^+$  and larger  $\pi^-$  sources, respectively. A simple formula was derived to account for this shift, delivering the length of homogeneity of constructed fiducial uncharged pion pairs and an effective Coulomb potential. The effective potentials have values of about 12 MeV. However, for a more precise treatment, all these effects (collective flow, resonance decay contributions, Coulomb potential from participants and spectators), complemented by a possible finite pion mean free path, should be combined in one consistent framework to obtain a measure for the real size of the pion source. With the experimental data provided here this task can be addressed to theoreticians. The comparison of the radii  $R_{\text{out}}$  and  $R_{\text{side}}$  with corresponding values obtained by other experiments over three orders of magnitude in  $\sqrt{s_{\text{NN}}}$  shows a very weak dependence on the beam energy. Only  $R_{\text{long}}$  increases by slightly more than a factor two when comparing the HADES data at the lower energy edge with the ALICE data at the higher one. Furthermore, the HADES radii are in good agreement with the extrapolated trends of RHIC and SPS data down to lower energies (except  $R_{\text{out}}$  from CERES), but do not confirm the increasing trend in  $R_{\text{side}}$  and  $R_{\text{long}}$  as indicated by the AGS data. This structure becomes even more visible in the excitation function of the volume of homogeneity at freeze-out. A similar compilation already exists [17], where the opposite trend of the AGS data was even more pronounced, but without taking care of comparing values at the same mean value of trans-

---

verse momentum. The compilation of this thesis moderates this structure and gives the hint that a part of it arises from the influence of the central Coulomb potential, manifestly not affecting the HBT radii at larger beam energies.

The HBT radius parameters in the azimuthally dependent analysis showed clearly the oscillations expected from symmetry considerations, allowing the extraction of the spatio-temporal semi-axes of the emission ellipsoid and the tilt angle within the reaction plane. As never done before, the dependence on pair transverse momentum, centrality and pion polarity was studied simultaneously. For the semi-axes  $\sigma_x$ ,  $\sigma_y$  and  $\sigma_z$ , the same qualitative trends were observed as in the azimuthally integrated analysis for  $R_{\text{out}}$ ,  $R_{\text{side}}$  and  $R_{\text{long}}$ . A three-dimensional almond shape with  $\sigma_y > \sigma_x > \sigma_z$  was found. The eccentric source in the  $xy$  plane matches at high transverse momenta the initial participant overlap region and becomes more circular at low values of transverse momentum. The magnitude of the tilt angle becomes highest at low transverse momenta and vanishes at very large ones. This can be interpreted as a temporal evolution, with the early stage of the fireball imaged with higher transverse momenta and the final stage visible when going to low momenta. Furthermore, the tilt angle showed no dependence on the charge sign of the pions, and its magnitude increases with increasing impact parameter, as one would expect from geometric considerations.

The comparison with the results of azimuthally sensitive analyses available at other beam energies showed a very nice confirmation of the existing trends. Again, it was emphasised to compare data points only at the same mean value of transverse momentum. In that sense, variables like  $\sigma_x$ ,  $\sigma_y$ ,  $\sigma_z$ ,  $\sigma_t$ ,  $V_{\text{fo}}$ ,  $\varepsilon_{xy}$  or  $\varepsilon_{zy}$  from E895, CERES, STAR and ALICE can be combined in a meaningful way with the HADES results acting as a link. From the observed trends, hints for a non-vanishing tilt angle at lowest STAR energies were found. The separation of the two transversely expanding directions shows an out-of-plane extension increasing with decreasing beam energies, not visible in an azimuthally integrated analysis. The freeze-out duration was found to be small at a level of about  $\Delta\tau \approx 0 - 1 \text{ fm}/c$  for central (0 – 10 %) collisions and  $\Delta\tau \approx 3 - 4 \text{ fm}/c$  for semi-peripheral collisions up to 45% centrality. In contrast to previous findings,  $\Delta\tau$  becomes non-negative for all centrality classes when considering both,  $\pi^-\pi^-$  and  $\pi^+\pi^+$ , and extracting it at low transverse momentum only.

## Outlook

The presented dependencies of the HBT radius parameters on pair transverse momentum and centrality are ready to be compared to adequate theoretical approaches treating the known dynamic effects. Thus, transport models, like UrQMD or iQMD, can be tested by comparing their output with the observables presented here. The found experimental dependencies can be

## 6. Conclusion and Outlook

---

used to adjust sensitive parameters within the models. From that hopefully one can learn more about the equation of state or other parameters entering implicitly the transport or explicitly the hydrodynamical approaches in the  $1A$  GeV energy regime.

From the excitation functions presented in this thesis, a high interest arises for the energy range above HADES up to  $\sqrt{s_{NN}}$  of about 10 GeV. The energy dependencies of  $R_{\text{side}}$  and  $R_{\text{long}}$  reported by E895@AGS as well as the appearance of a finite tilt angle have to be studied. Also, the influence of the central nucleonic Coulomb potential on the HBT radii and derived quantities has to be clarified in this energy range by a differential  $\pi^-\pi^-$  and  $\pi^+\pi^+$  investigation. Fortunately, a couple of facilities exists, which aim at studying the physics of heavy-ion collisions in this energy region. In the following three promising facilities are picked out. First, the already started STAR Fixed-Target (FT) program should be mentioned, which uses the existing facility at RHIC, inserting a 1 mm thick gold target at one edge of the spectrometer. A test run in 2014 already provided 1.3 million events at  $\sqrt{s_{NN}} = 4.5$  GeV, the full run starting in 2018 covers the range from 3.0 to 7.7 GeV. Secondly, there are the BM@N fixed-target and MPD collider experiments at the NICA facility, covering the energy range for heavy-ions of 2.0 to 3.5 GeV and 2.7 to 11 GeV, respectively. While the former one is already going to start operation with a gold beam in 2021, MPD plans to start with the physical program in 2023. Thirdly, SIS100 at the FAIR facility will provide HADES and the CBM experiments with a gold beam of up to  $11A$  GeV, which allows to study the energy range of  $\sqrt{s_{NN}}$  between 2.7 and 5 GeV. Although the latter one will not start operating before 2025, the CBM experiment will be able to reach interaction rates of up to  $10^{10}$  Hz, delivering unprecedented high statistics of Au+Au (or other  $A + A$ ) data. Finally, the HADES beam time with the system Ag+Ag@ $1.65A$  and  $1.23A$  GeV performed successfully in March 2019 should be mentioned, providing more than twice as much recorded events compared to the Au+Au HADES experiment. With this data a complementary system size dependence of the HBT radius parameters can be studied, which is linked directly to the central Coulomb potential, the centrality dependence and the impact of collective flow. The almost finished HADES upgrade with an electromagnetic calorimeter will allow to detect direct photons from the collisions. With that it might be possible to perform additionally a two-photon HBT analysis, useful for a comparison with the two-pion results and for investigating of the source of probes not strongly interacting with the surrounding hadronic environment.

# Appendix



# A | Details on analysis

## A.1 Minimisation procedures

For finding the best set of parameters (and their uncertainties) of a function describing a couple of data points, the *gMinuit* package included in the *ROOT* framework is used. Different choices for the so called 'estimator', which is the part to be minimised, are possible. Below, two common estimators are described in view of the essential part of this thesis, i.e. fitting correlation functions.

### A.1.1 Least $\chi^2$ method

Within the least  $\chi^2$  method, the sum of squared differences between a given data set with  $N$  entries and a fit function, weighted by the Gaussian statistical uncertainties of the data points, is formed,

$$\chi^2 = \sum_{i=0}^N \frac{(C_{\text{exp},i} - C_{\text{model}})^2}{(\Delta C_{\text{exp},i})^2} \Big/ \sum_{i=0}^N \frac{1}{(\Delta C_{\text{exp},i})^2}, \quad (\text{A.1})$$

and normalised by the sum of weights.  $C_{\text{exp},i}$  is the  $i$ -th experimental data point,  $\Delta C_{\text{exp},i}$  the corresponding statistical error, and  $C_{\text{model}}$  a fit function with a couple of parameters. The method works for Poisson-distributed quantities. However, a correlation function  $C = A/B$  formed by two Poisson distributions  $A$  and  $B$  is not necessarily itself Poisson-distributed, especially at low statistics.

### A.1.2 Maximum-likelihood method

Within the Maximum-Likelihood method one tries to minimise the conditional probability of a quantity in dependence on other defective quantities. It is used to bypass the problem that  $C$  as ratio of  $A$  and  $B$  is not Poisson-

## A. Details on analysis

---

distributed and Gaussian error propagation is only valid for large numbers of  $A$  and  $B$ . One starts with the following formalism [122]:

$$P(A) = \frac{\bar{A}^A e^{-\bar{A}}}{A!}, \quad P(B) = \frac{\bar{B}^B e^{-\bar{B}}}{B!}, \quad (\text{A.2})$$

$$P(C|AB) = \int \int d\mu d\nu \frac{\mu^A e^{-\mu}}{A!} \frac{\nu^B e^{-\nu}}{B!} \delta(C - \mu/\nu), \quad (\text{A.3})$$

$$= \frac{C^A}{A!B!} \frac{(A+B+1)!}{(C+1)^{A+B+2}}. \quad (\text{A.4})$$

Here,  $P(A)$  is the Poisson distribution for number of events  $A$ ,  $P(C|AB)$  is the conditional probability of  $C$  in dependence on  $A$  and  $B$  and  $\bar{A}$  and  $\bar{B}$ , or  $\mu$  and  $\nu$ , respectively, are the mean values of the single Poisson distributions. The likelihood function  $\chi_{\text{ML}}^2$  is defined as twice the negative logarithm of the conditional probability,

$$\chi_{\text{ML}}^2 = -2 \ln \left[ P(C|AB) \right] \quad (\text{A.5})$$

$$\approx -2 \left[ A \ln \left( \frac{C(A+B)}{A(C+1)} \right) + B \ln \left( \frac{A+B}{B(C+1)} \right) \right]. \quad (\text{A.6})$$

Its value summed over all entries has to be minimised. Here, one uses the property that the logarithm of a function has the same monotonicity as the function itself. For deriving the approximation (A.6) one uses the formula of Stirling ( $\ln(n!) \approx n \ln n - n$ ) keeping only leading terms. This estimator is correct as long as one has the same amount of entries for  $A$  and  $B$ . If instead  $B > A$ , the  $\delta$  distributions change,  $\delta(C - \mu/\nu) \rightarrow \delta(C - N\mu/\nu)$ , where  $N$  is a normalisation constant equivalent to Equation (4.20), treated as exact value without uncertainty compared to the yields  $A$  and  $B$ . The likelihood function changes to

$$\begin{aligned} \chi_{\text{ML}(B>A)}^2 = -2 & \left[ A \ln \left( \frac{C(A+B+1)}{A(C+N)} \right) + B \ln \left( \frac{A+B+1}{B(C/N+1)} \right) \right. \\ & \left. + \ln \left( \frac{A+B+1}{N(1+C/N)^2} \right) - 1 \right], \quad (\text{A.7}) \end{aligned}$$

$$\approx -2 \left[ A \ln \left( \frac{C(A+B)}{A(C+N)} \right) + B \ln \left( \frac{A+B}{B(C/N+1)} \right) \right]. \quad (\text{A.8})$$

In the investigations of the correlation function in this thesis, both estimators, Equations (A.1) and (A.8), were used, obtaining similar results with the same statistical uncertainties.

## A.2 Gaussian convolution

In this section, expressions for the Gaussian convolution discussed in Section 4.4.2 are derived. The HBT radius parameters  $R_i$  are translated back into Gaussian widths  $\sigma_i$  in relative momentum space (as given by the expression (4.36)),

$$\sigma_i = \frac{197.327 \text{ fm MeV}}{\sqrt{8} R_i}. \quad (\text{A.9})$$

The convolution is given in one dimension by

$$h(x) = \int_{-\infty}^{\infty} dx' f(x') g(x - x'), \quad (\text{A.10})$$

$$f(x) = 1 + \lambda e^{-\frac{x^2}{2\sigma_f^2}}, \quad (\text{A.11})$$

$$g(x) = \frac{1}{\sqrt{2\pi}\sigma_g} e^{-\frac{x^2}{2\sigma_g^2}}, \quad (\text{A.12})$$

$$(\text{A.13})$$

with  $f(x)$  being the initial Bose-Einstein signal of interest,  $g(x)$  the relative momentum resolution and  $h(x)$  the measured convoluted signal. Evaluating  $h(x)$  leads to

$$h(x) = \int_{-\infty}^{\infty} g(x - x') dx' + \frac{\lambda}{\sqrt{2\pi}\sigma_g} \int_{-\infty}^{\infty} e^{-(\frac{1}{2\sigma_f^2} + \frac{1}{2\sigma_g^2})x'^2 + \frac{(2xx' - x'^2)}{2\sigma_g^2}}, \quad (\text{A.14})$$

$$= 1 + \frac{\lambda}{\sqrt{\frac{\sigma_g^2}{\sigma_f^2} + 1}} e^{-\frac{x^2}{2} \frac{1}{\sigma_g^2 + \sigma_f^2}}, \quad (\text{A.15})$$

$$:= 1 + \lambda_h e^{-\frac{x^2}{2\sigma_h^2}}, \quad (\text{A.16})$$

$$(\text{A.17})$$

where the measured HBT parameters  $\lambda_h$  and  $\sigma_h^2$  can be identified as functions of  $\lambda$ ,  $\sigma_f^2$  and  $\sigma_g^2$ . The resulting expressions for the initial parameters are

$$\lambda = \frac{\lambda_h}{\sqrt{1 - \frac{\sigma_g^2}{\sigma_h^2}}}, \quad (\text{A.18})$$

$$\sigma_f^2 = \sigma_h^2 - \sigma_g^2. \quad (\text{A.19})$$

## A. Details on analysis

---

Extending this scheme to three dimensions is straightforward, if no non-diagonal HBT radii are considered:

$$f(x) = 1 + \lambda e^{-\frac{x^2}{2\sigma_{f,x}^2}} e^{-\frac{y^2}{2\sigma_{f,y}^2}} e^{-\frac{z^2}{2\sigma_{f,z}^2}}, \quad (\text{A.20})$$

$$\lambda = \frac{\lambda_h}{\sqrt{1 - \frac{\sigma_{g,x}^2}{\sigma_{h,x}^2}} \sqrt{1 - \frac{\sigma_{g,y}^2}{\sigma_{h,y}^2}} \sqrt{1 - \frac{\sigma_{g,z}^2}{\sigma_{h,z}^2}}}, \quad (\text{A.21})$$

with the abbreviations

$$\sigma_{f,x}^2 = \sigma_{h,x}^2 - \sigma_{g,x}^2, \quad (\text{A.22})$$

$$\sigma_{f,y}^2 = \sigma_{h,y}^2 - \sigma_{g,y}^2, \quad (\text{A.23})$$

$$\sigma_{f,z}^2 = \sigma_{h,z}^2 - \sigma_{g,z}^2. \quad (\text{A.24})$$

Considering the three-dimensional convolution with one additional non-diagonal element  $\sigma_{xz}$  yields

$$f(x) = 1 + \lambda e^{-\frac{x^2}{2\sigma_{f,x}^2}} e^{-\frac{y^2}{2\sigma_{f,y}^2}} e^{-\frac{z^2}{2\sigma_{f,z}^2}} e^{-\frac{2xz}{2\sigma_{f,xz}^2}}, \quad (\text{A.25})$$

$$\lambda_h = \frac{\lambda}{\sqrt{1 + \frac{\sigma_{g,y}^2}{\sigma_{f,y}^2}} \sqrt{(1 + \frac{\sigma_{g,x}^2}{\sigma_{f,x}^2})(1 + \frac{\sigma_{g,z}^2}{\sigma_{f,z}^2}) - \frac{\sigma_{g,x}^2 \sigma_{g,z}^2}{\sigma_{xz}^4}}}, \quad (\text{A.26})$$

$$\sigma_{h,xz}^2 = \sigma_{xz}^2 \left[ \left(1 + \frac{\sigma_{g,x}^2}{\sigma_x^2}\right) \left(1 + \frac{\sigma_{g,z}^2}{\sigma_z^2}\right) - \frac{\sigma_{g,x}^2 \sigma_{g,z}^2}{\sigma_{xz}^4} \right] \quad (\text{A.27})$$

$$= \sigma_{xz}^2 \left[ 1 + \frac{\sigma_{g,x}^2}{\sigma_x^2} + \frac{\sigma_{g,z}^2}{\sigma_z^2} + \sigma_{g,x}^2 \sigma_{g,z}^2 \left( \frac{1}{\sigma_x^2 \sigma_z^2} - \frac{1}{\sigma_{xz}^4} \right) \right], \quad (\text{A.28})$$

$$\sigma_{h,y}^2 = \sigma_{f,y}^2 + \sigma_{g,y}^2, \quad (\text{A.29})$$

$$\sigma_{h,x}^2 = (\sigma_x^2 + \sigma_{g,x}^2) \left[ 1 + \frac{1}{\frac{\sigma_{g,x}^2}{\sigma_x^2} \left( \left( \frac{\sigma_{xz}^2}{\sigma_x^2} + \frac{\sigma_{xz}^2}{\sigma_{g,x}^2} \right) \left( \frac{\sigma_{xz}^2}{\sigma_z^2} + \frac{\sigma_{xz}^2}{\sigma_{g,z}^2} \right) - 1 \right) - 1} \right], \quad (\text{A.30})$$

$$\sigma_{h,z}^2 = (\sigma_z^2 + \sigma_{g,z}^2) \left[ 1 + \frac{1}{\frac{\sigma_{g,z}^2}{\sigma_z^2} \left( \left( \frac{\sigma_{xz}^2}{\sigma_x^2} + \frac{\sigma_{xz}^2}{\sigma_{g,x}^2} \right) \left( \frac{\sigma_{xz}^2}{\sigma_z^2} + \frac{\sigma_{xz}^2}{\sigma_{g,z}^2} \right) - 1 \right) - 1} \right]. \quad (\text{A.31})$$

$$(\text{A.32})$$

One defines a term  $\omega^2$  by

$$\omega_{x(z)}^2 := \frac{1}{\frac{\sigma_{g,z}^2}{\sigma_{x(z)}^2} \left( \left( \frac{\sigma_{xz}^2}{\sigma_x^2} + \frac{\sigma_{xz}^2}{\sigma_{g,x}^2} \right) \left( \frac{\sigma_{xz}^2}{\sigma_z^2} + \frac{\sigma_{xz}^2}{\sigma_{g,z}^2} \right) - 1 \right) - 1}, \quad (\text{A.33})$$

which is used as a control parameter. If  $\omega_{x(z)}^2$  is very small, given mainly by  $\sigma_{f,xz}^2 \gg \sigma_{g,x}^2, \sigma_{g,z}^2$ , the expressions Equations (A.21) to (A.24) remain the same for the  $\lambda$  parameter and the three diagonal HBT radius parameters as well. The non-diagonal element  $\sigma_{xz}^2$  follows as

$$\sigma_{f,xz}^2 = \frac{\sigma_{h,xz}^2}{(1 + \frac{\sigma_{g,x}^2}{\sigma_x^2})(1 + \frac{\sigma_{g,z}^2}{\sigma_z^2})}. \quad (\text{A.34})$$

This formalism can be extended to three non-diagonal elements by using Equation (4.31) in the fits of the correlation functions, going along with three control parameters defined in the spirit of Equation (A.33). In the practical evaluations within this thesis, these control parameters were always small enough to keep the introduced formalism.

## A. Details on analysis

---

## B | Further systematics

### B.1 $R_{\text{out long}}^2$ in $\Phi$ -integrated analyses

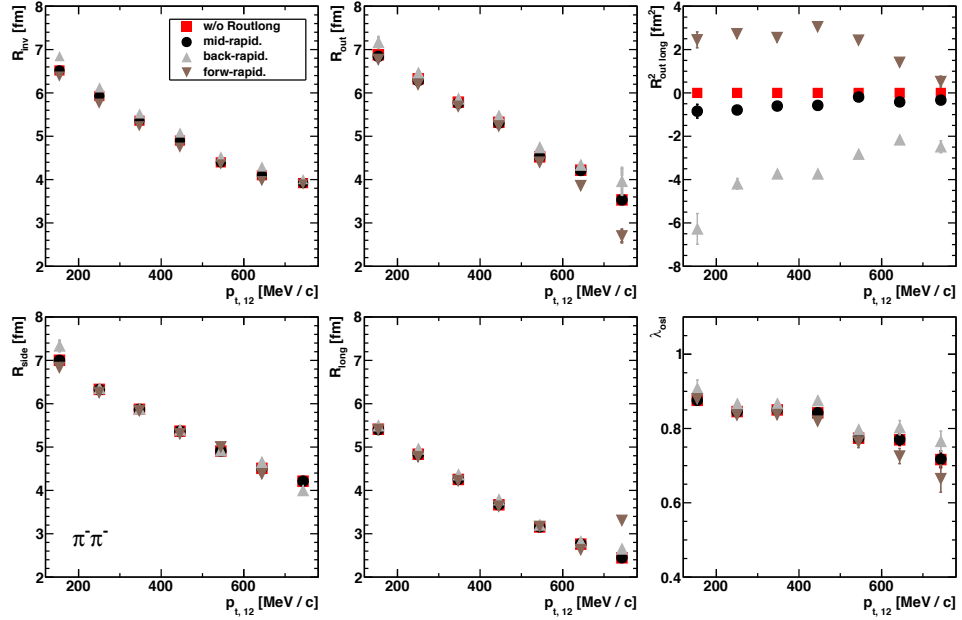


**Figure B.1:** HBT radius parameters and  $\lambda_{\text{osl}}$  of the azimuthally integrated analysis in dependence on  $p_{t,12}$  for  $\pi^-\pi^-$  and 0 – 10 % centrality and different intervals of pair rapidity: [0.29,0.69] (grey up-pointing rectangles), [0.39,1.09] (black circles), [0.79,1.19] (brown down-pointing rectangles). Red boxes show results at mid-rapidity setting explicitly  $R_{\text{out long}}^2 = 0$ . Error bars contain only statistical uncertainties.

In Figure B.1, the  $\pi^-\pi^-$  HBT radius parameters  $R_{\text{inv}}$ ,  $R_{\text{out}}$ ,  $R_{\text{side}}$ ,  $R_{\text{long}}$ , the non-diagonal variance  $R_{\text{out long}}^2$  and parameter  $\lambda_{\text{osl}}$  for 0 – 10 % centrality in dependence on  $p_{t,12}$  are shown. Red boxes represent results fitted without and black circles with  $R_{\text{out long}}^2$  in the fit. Grey up-pointing triangles denote results obtained for a changed rapidity window of  $y_{12} \in [0.29, 0.69]$  and

## B. Further systematics

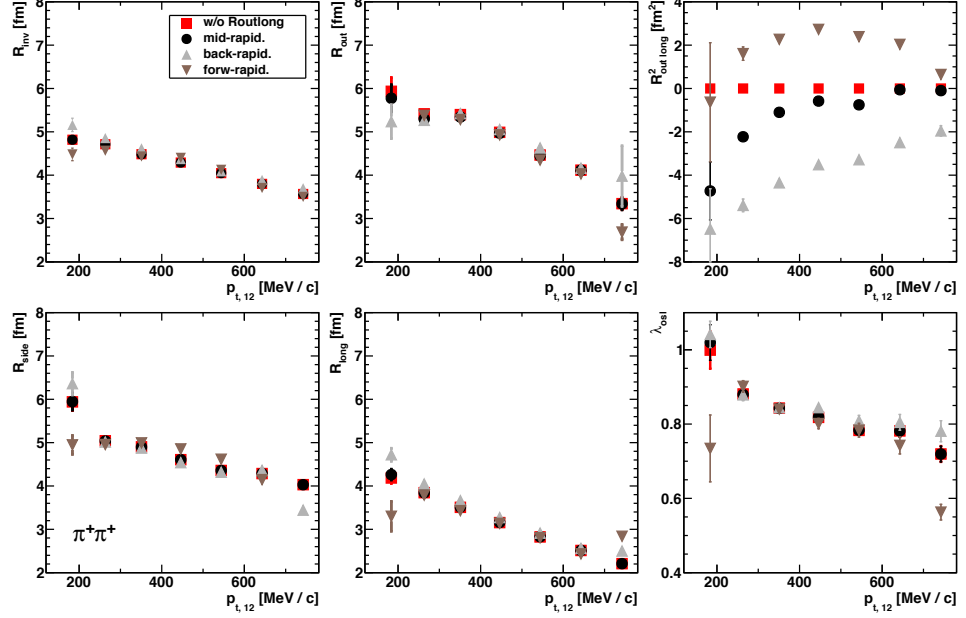


**Figure B.2:** Same as Figure B.1, but for  $\pi^+\pi^+$ .

brown down-pointing triangles for  $y_{12} \in [0.79, 1.19]$ . The plots show that the HBT radius parameters hardly depend on the choice of  $y_{12}$  and are not influenced by switching on or off the term  $R_{\text{out long}}^2$  in the three-dimensional fits of the azimuthally integrated analysis. The same is shown for  $\pi^+\pi^+$  pairs in Figure B.2. Here only at lowest values of  $p_{t,12}$ , where statistics becomes an issue, differences in direction of  $y_{12}$  are visible. Also, a strong decrease of  $R_{\text{out long}}^2$  is observable at low transverse momenta for all rapidity bins. A possible relation to a non-symmetric rapidity range has been discussed in Section 5.2.2.

## B.2 Results for reversed magnetic field

The last two measuring days of the Au+Au beam time were reserved for a measurement with reversed field, i.e. the direction of the polarity of the magnetic field was inverted. In this configuration, negatively charged particles are deflected into direction of the beam axis and positively charged particles away from it. In Figure B.3, results derived with the normal magnetic field configuration are compared to the observables from the inverse configuration for the azimuthally integrated analysis. For both  $\pi^-\pi^-$  and  $\pi^+\pi^+$  pairs, a very good confirmation of the  $p_{t,12}$  dependencies of  $R_{\text{inv}}$ ,  $R_{\text{out}}$ ,  $R_{\text{side}}$ ,  $R_{\text{long}}$  and the  $\lambda$  parameters was found for the centrality 0 – 10 %. The statistical uncertainties of the reversed-field results are larger compared to

### B.3 Effective potentials

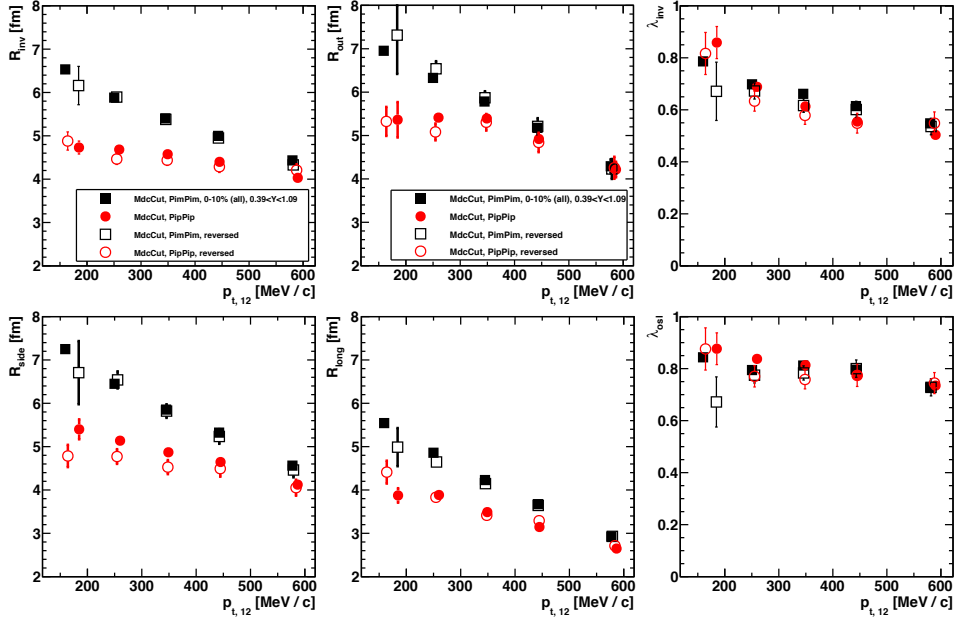


**Figure B.3:** HBT radius parameters and  $\lambda$  parameters of the azimuthally integrated analysis in dependence on  $p_{t,12}$  for  $\pi^-\pi^-$  (black boxes) and  $\pi^+\pi^+$  (red circles) and 0 – 10 % centrality. Open symbols represent reversed-field data (magnetic field with same strength, but opposite direction), filled symbols display data for normal magnetic field configuration. Error bars contain only statistical uncertainties.

the normal field results, the latter ones are derived from a factor of ten larger statistics. The accordance of the trends excludes a technical insufficiency as explanation of the charge-sign difference of  $\pi^-\pi^-$  and  $\pi^+\pi^+$  results and substantiates further the found influence of the central Coulomb potential.

### B.3 Effective potentials

In Figure B.4, the effective Coulomb potential  $V_{\text{eff}}$  (in the plots denoted by  $V_{\text{coul}}$ ) is exhibited, extracted with Equation (5.2). Due to the real geometry, the derived formula is inadequate for the 'out' direction, and the obtained values of  $V_{\text{eff}}$  based on  $R_{\text{out}}$  definitely underestimate the potential. Furthermore, the effective potential has a contribution both from the participant region and from the spectators. Identifying the obtained values with a central Coulomb potential is therefore more reliable for central collisions. All values at small transverse mass are significantly influenced by the non-static proton distribution during the collision evolution and after the freeze-out. The protons carry the main charge contributing to the effective potential and move in average outwards, describable with an inverse Boltzmann slope

## B. Further systematics

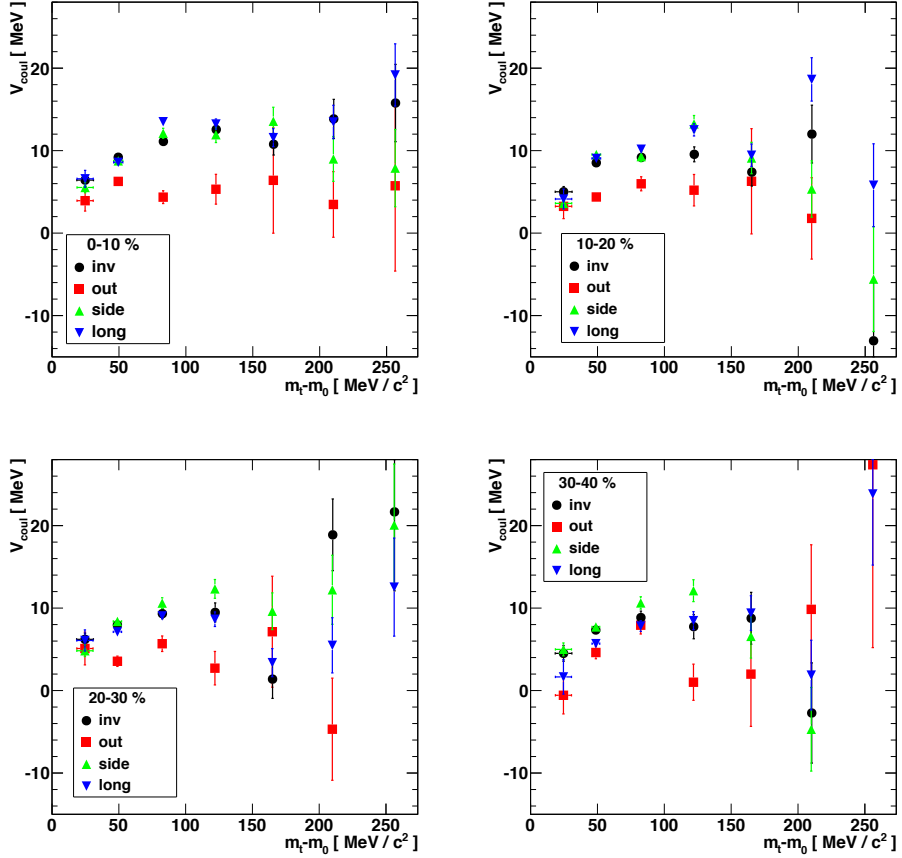


**Figure B.4:** Effective Coulomb potentials extracted with Eq. (5.2) using  $R_{\text{inv}}$  (black circles),  $R_{\text{out}}$  (red boxes),  $R_{\text{side}}$  (green up-pointing triangles) and  $R_{\text{long}}$  (blue down-pointing triangles) for centralities of 0 – 10 % (top right), 10 – 20 % (top left), 20 – 30 % (bottom left) and 30 – 40 % (bottom right), respectively. Error bars contain only statistical uncertainties.

parameter of 130 MeV when not including explicitly the collective flow [64]. Especially the low-energy pions are not able to pass by all the protons. Using the ansatz of [123] one can correct for this, finding a change only for the data points at the two lowest values of transverse mass.

In [124] a Coulomb potential of about 10 MeV at pion kinetic energy around 200 MeV (measured in center-of-mass frame) is reported for central collisions. This is conform with the effective potentials in Figure B.4 extracted at the values of  $m_t - m_0 = 200$  MeV. Overall, for central collisions, the effective potential extracted via  $R_{\text{inv}}$ ,  $R_{\text{side}}$  and  $R_{\text{long}}$  amounts about 12 MeV. This is not in agreement with the systematic studies of [123], where a Coulomb potential of  $V_C = 27$  MeV is predicted from an analysis of inclusive single-pion

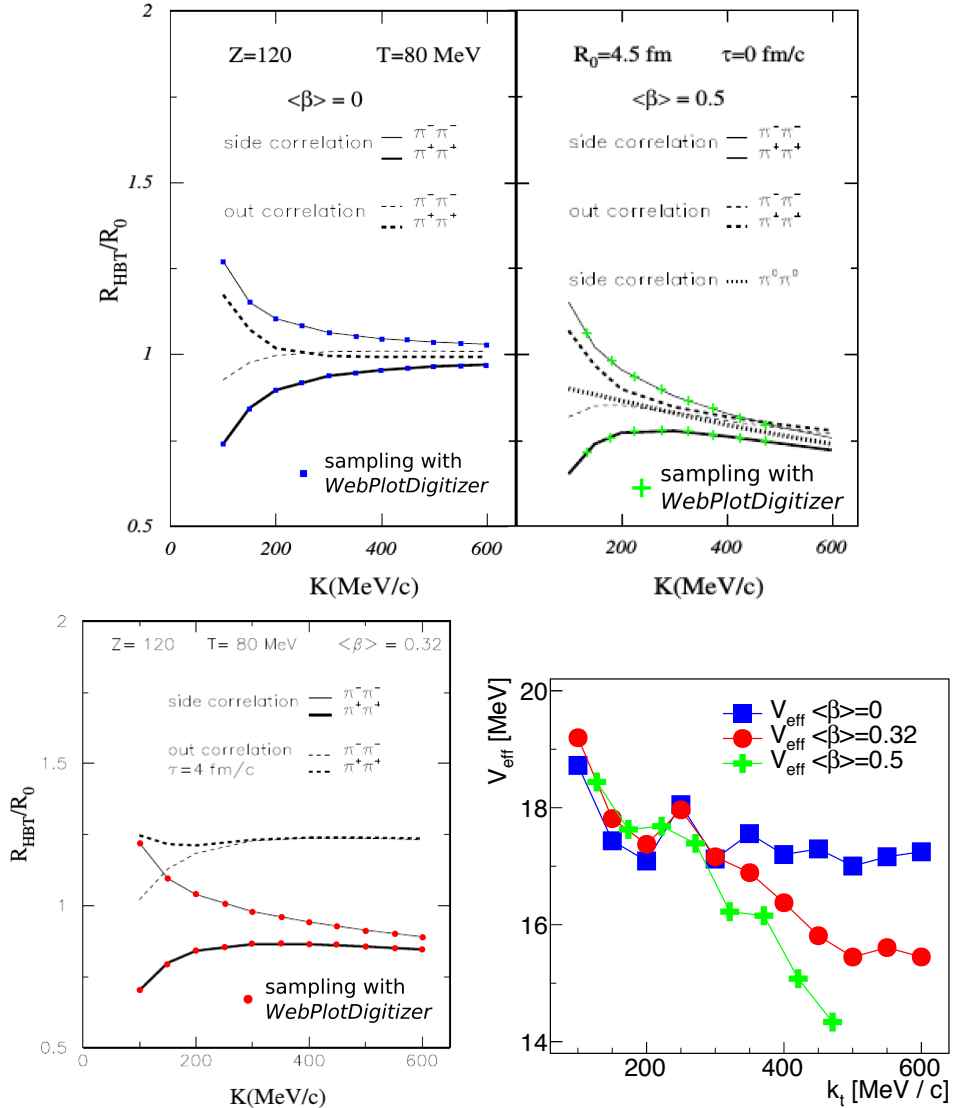


**Figure B.5:** Applying Equation (5.2) to the calculated curves of  $R_{\text{side}}$  from [50] (top and bottom left). Red circles correspond to a mean radial-flow velocity  $\langle\beta\rangle = 0.32$ , green crosses to  $\langle\beta\rangle = 0.5$ , and blue boxes represent the case without radial flow. Data points were extracted with *WebPlotDigitizer* (<https://apps.automeris.io/wpd/>). The initial Gaussian radius is  $R_0 = 4.47$  fm, and the corresponding initial Coulomb potential is 26.4 MeV. The extracted effective Coulomb potentials  $V_{\text{eff}}$  are exhibited in the bottom right.

phase space distributions for heavy-ion collisions with a projectile kinetic energy of  $1.23A$  GeV.

## B. Further systematics

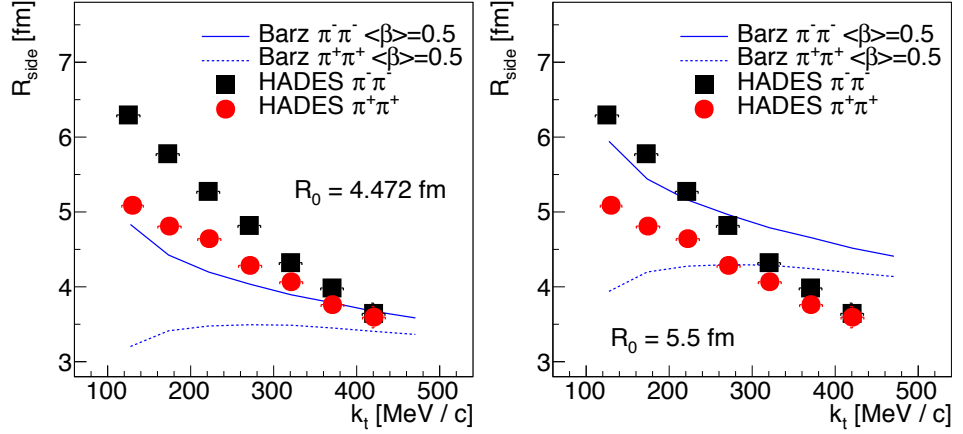


**Figure B.6:** Comparing calculations of  $R_{\text{side}}$  from [50] to experimental data of Figure 5.21. Calculated values of [50] (blue curves) are scaled with  $R_0 = 4.47 \text{ fm}$  ( $R_0 = 5.5 \text{ fm}$ ) in the left (right) panel.

A comparison with calculations from [50] is shown in Figure B.5. The calculations were performed inserting a Gaussian shaped central Coulomb potential in the pion wave functions with the value of 26.4 MeV at the Gaussian initial radius  $R_0 = 4.5 \text{ fm}$ , see [50]. Results for  $R_{\text{side}}$  and  $R_{\text{out}}$  are available for different settings of an average radial flow velocity  $\langle \beta \rangle$ . The relation (5.2) was applied to the calculated curves of  $R_{\text{side}}$  for a couple of sampling points. The obtained values of  $V_{\text{eff}}$  are plotted in the lower right panel as a function of  $k_t$ . Apparently, the effective potentials decrease with increasing transverse momentum when switching on a radial collective motion. This fits into the picture illustrated by Figures 1.3 and 5.24 of observing regions of homogeneity with a smaller volume and moving towards the surface of the fireball for increasing  $k_t$ . If the average emission points of the pions are located more outside of the fireball volume, the effective potential becomes weaker. Ignoring the influence of radial flow, an effective potential of about 17 – 18 MeV is obtained, significantly different from the initial value. This puts into perspective that either Equation (5.2) does not precisely enough uncover the real situation and has to be extended, or – besides the explanation introduced in Section 2.3.2 – another effect contributes to the deduced different extents of the area of homogeneity of  $\pi^- \pi^-$  and  $\pi^+ \pi^+$  pairs. For that reason, a more appropriate consideration (as discussed in Section 5.2.5) has to be done to obtain realistic values of the Coulomb potential of the fireball.

Figure B.6 compares the experimental data of  $R_{\text{side}}$  shown already in Figure 5.21 with the calculated curves from [50]. In the left plot, the actual parameter  $R_0 = 4.5 \text{ fm}$  has been used for scaling the calculated results to the experimental ones. Obviously, the charge-sign splitting deduced from exper-

imental data is not that large. Nonetheless, the trends of the data and the calculations of [50] match only at highest transverse momenta and become very different at low values of  $k_t$ . In the right plot, the scaling parameter was chosen as  $R_0 = 5.5$  fm, which causes the trends to match (accidentally) at medium  $k_t$ . However, the charge-sign difference becomes apparently larger, since one can not account for the implicitly weaker Coulomb potential when increasing the extension of the source by just changing  $R_0$  alone.

## B.4 Tilt angle systematics

At the end of Section 4.5.3, the freedom of interchanging the coordinates  $x$  and  $z$  was mentioned, with a corresponding shift of  $\theta_s$  by  $90^\circ$ , which allows a couple of arrangements of the  $k_t$  and centrality dependent data. The final arrangement depends on the chosen constraints. In the standard analysis, the most important requirement of getting a smooth trend was chosen, together with smaller  $|\theta_s|$  for more central collisions. For this standard scenario, results are displayed in Figure B.7 for 24 – 34 % and in Figure B.8 for 26 – 36 % centrality. All exhibited dependences show a very smooth behaviour and especially  $\theta_s$  follows nicely a curve within the high statistical uncertainty of a possible outlier. However, the crucial point of this standard scenario is that the trend of  $\theta_s$  for high transverse momenta and centralities more peripheral than 25 – 35 % does not point in direction of zero, as observed for more central collisions. Therefore one could think of an alternative scenario, where explicitly a vanishing tilt angle at high transverse momenta is required, exhibited in Figure B.9 for 26 – 36 % centrality. All trends, except for  $\theta_s$ , are very smooth in this scenario, too. For the trend of the tilt angle a 'knee'-like structure is visible around  $p_{t,12} = 350$  MeV/ $c$ . Even if this structure disturbs the smoothness of the  $p_{t,12}$  dependency, one can argue, that this 'knee' is already visible at more central collisions (compare with Figure B.7).

In Figure B.10, the tilt angle is plotted as a function of the impact parameter  $b$  for different mean values of  $p_{t,12}$ . In the standard scenario on the left side, smooth trends are visible up to a critical value of  $b \approx 8$  fm, where the orientation of the tilt evolution with  $p_{t,12}$  changes the direction. In the alternative scenario on the right side for all values of transverse momentum, smooth trends are observed, though the green data points at 300–350 MeV/ $c$  are clearly crossing the other trends of the data points at lower values of  $p_{t,12}$ . In Figure B.11 the final eccentricity, also called the  $xy$  eccentricity, is plotted in dependence on the initial eccentricity  $\varepsilon_{\text{ini}}$ . The additional data points of the overlapping bins in  $p_{t,12}$  and centrality fit very nicely into the previous systematics of Figure 5.43 and complete the picture. Clearly visible is that the final eccentricity reaches its maximum not at highest transverse momenta, but slightly before that and seems to decrease again for higher

## B. Further systematics

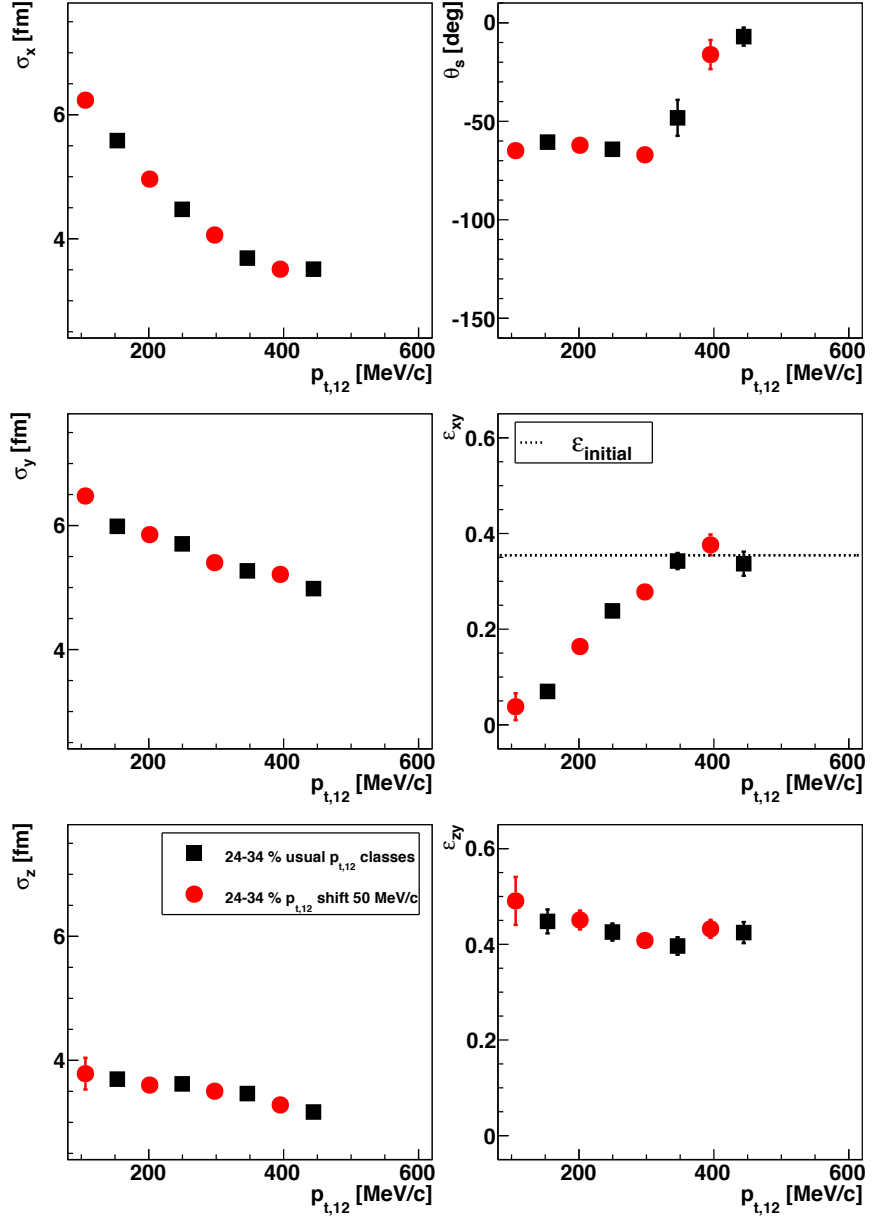


**Figure B.7:** The spatial principal axes (left column), the tilt angle w.r.t. the beam axis in the reaction plane (Equation (4.44), top right), the  $xy$  eccentricity (Equation (4.46), middle right) and the  $yz$  eccentricity (Equation (4.46), bottom right) of the Gaussian emission ellipsoid of  $\pi^-\pi^-$  as function of pair transverse momentum for 24 – 34 % centrality. Data of standard intervals of  $p_{t,12}$  (black boxes) and that shifted by 50 MeV/c (red circles) is separated. Error bars include statistical uncertainties only. The dotted line depicts the initial nucleon eccentricity from Glauber simulations.

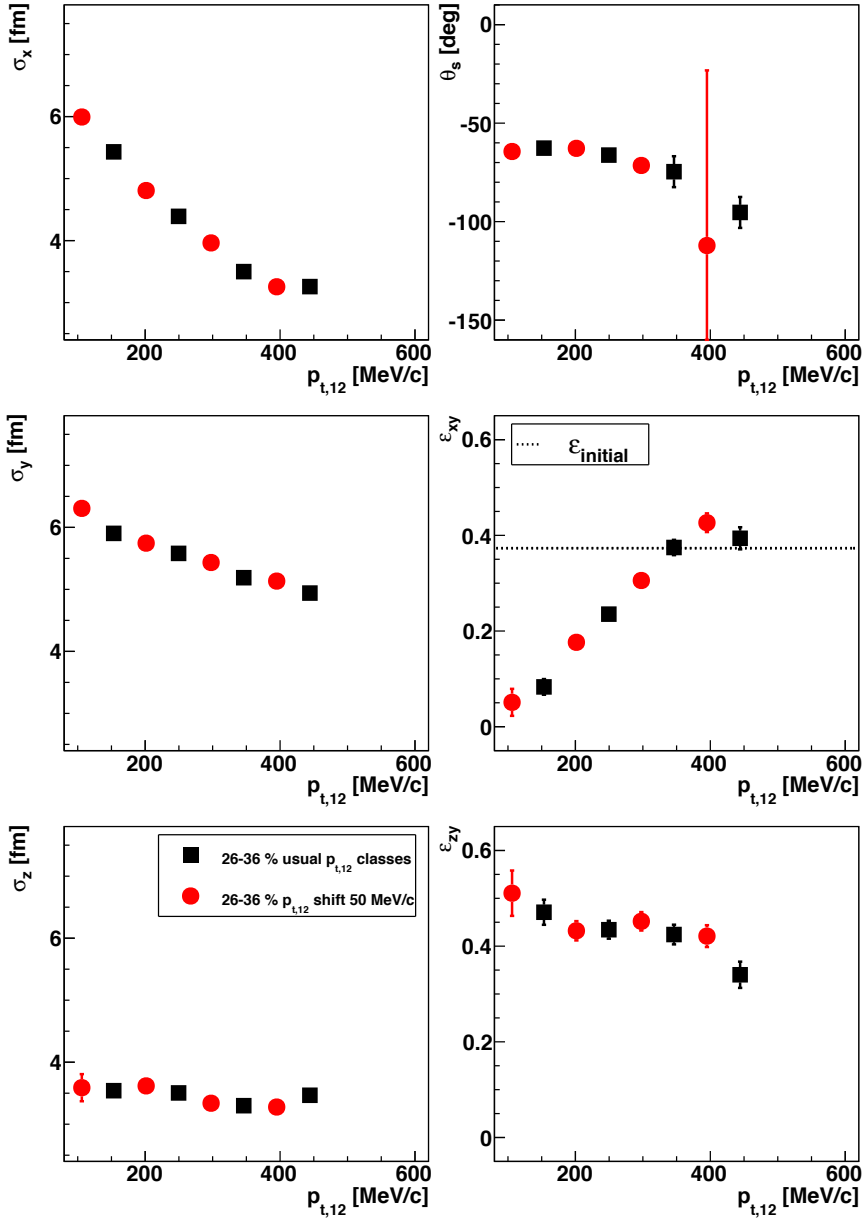


**Figure B.8:** Same as Figure B.7, but for 26 – 36 % centrality.

values of  $p_{t,12}$ . Note that here only  $\pi^-\pi^-$  data is considered. The standard scenario in the left panel only differs from the alternative scenario in the right panel in the yellow data points at high initial eccentricities. Here, the alternative scenario shows smoother trends without outliers within the statistical uncertainties.

## B. Further systematics

---

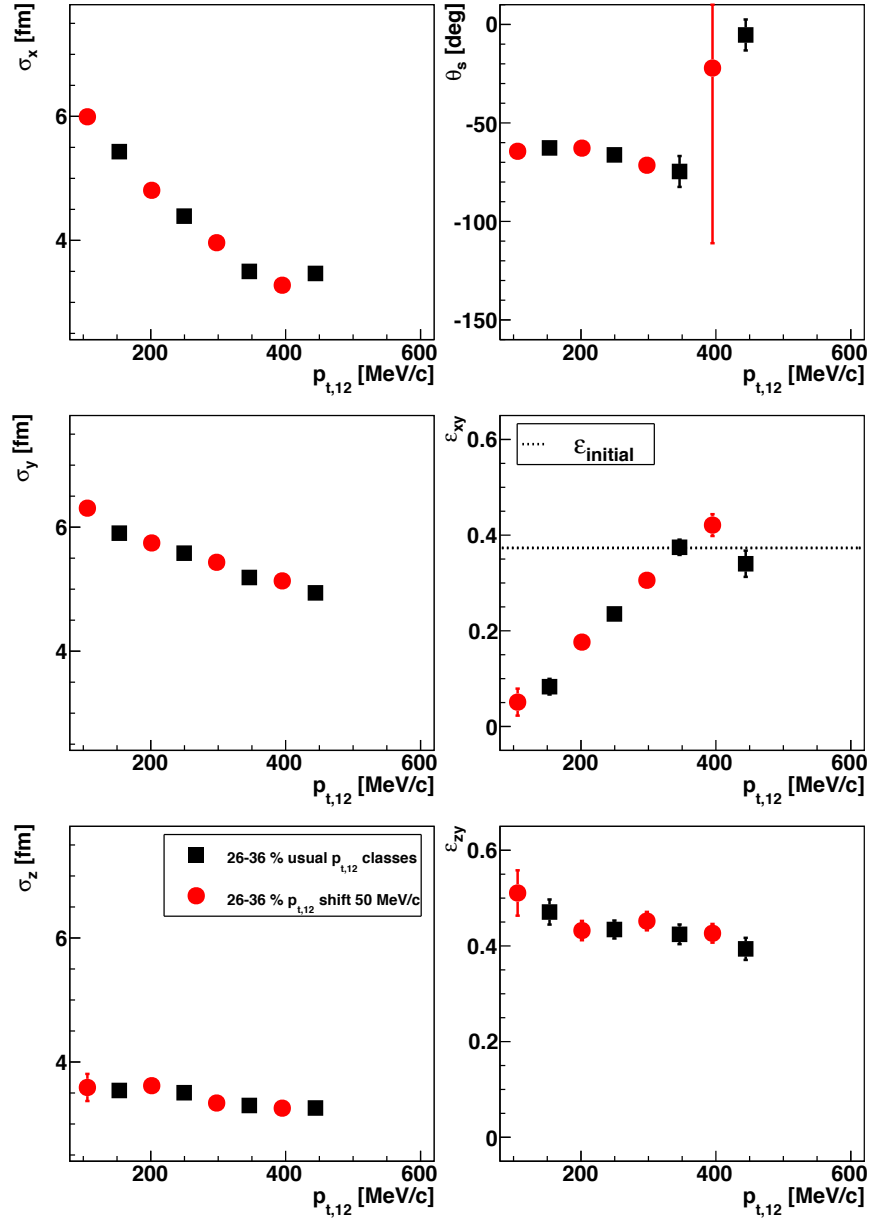


**Figure B.9:** Same as Figure B.7, but for 26–36% centrality and the alternative scenario described in the text.

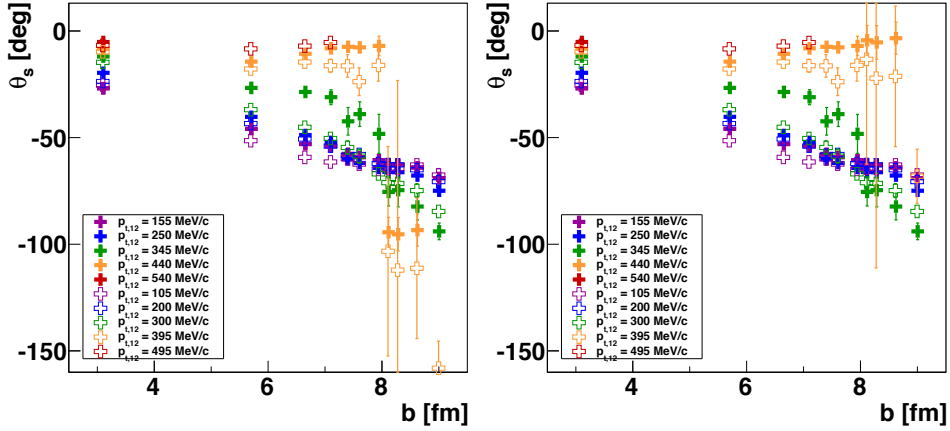


**Figure B.10:** Tilt angle  $\theta_s$  in dependence of the impact parameter  $b$ , the latter one derived from Glauber simulations, for  $\pi^- \pi^-$  pairs and different values of pair transverse momenta. Left panel represents the standard scenario, while in the right panel the arrangement of the data follows an alternative scenario with details are given in the text. Error bars include only statistical uncertainties.

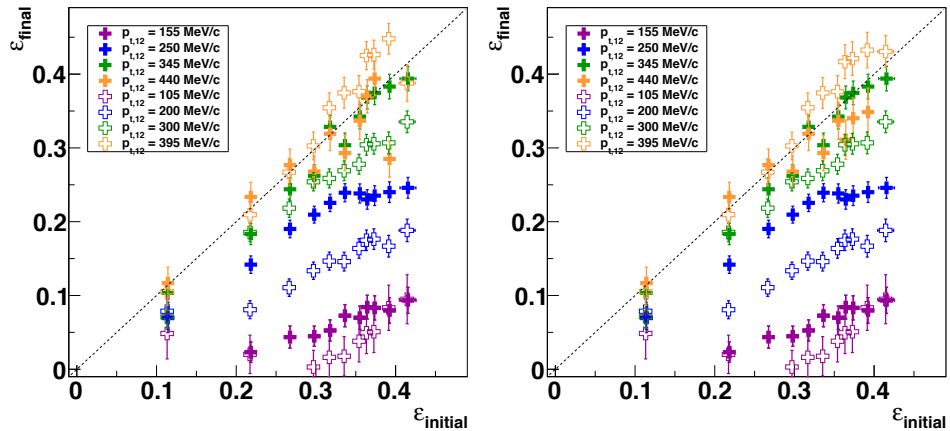


**Figure B.11:** Final eccentricity  $\varepsilon_{\text{final}}$  ( $xy$  eccentricity) plotted against initial nucleon eccentricity  $\varepsilon_{\text{ini}}$  derived from Glauber simulations for different values of pair transverse momenta of negatively charged pion pairs. Left panel represents the standard scenario, while in the right panel the arrangement of the data follows an alternative scenario with details are given in the text. The dashed line denotes  $\varepsilon_{\text{final}} = \varepsilon_{\text{ini}}$ . Error bars include only statistical uncertainties.

## B.5 Charge-sign corrected extensions of the emission ellipsoid

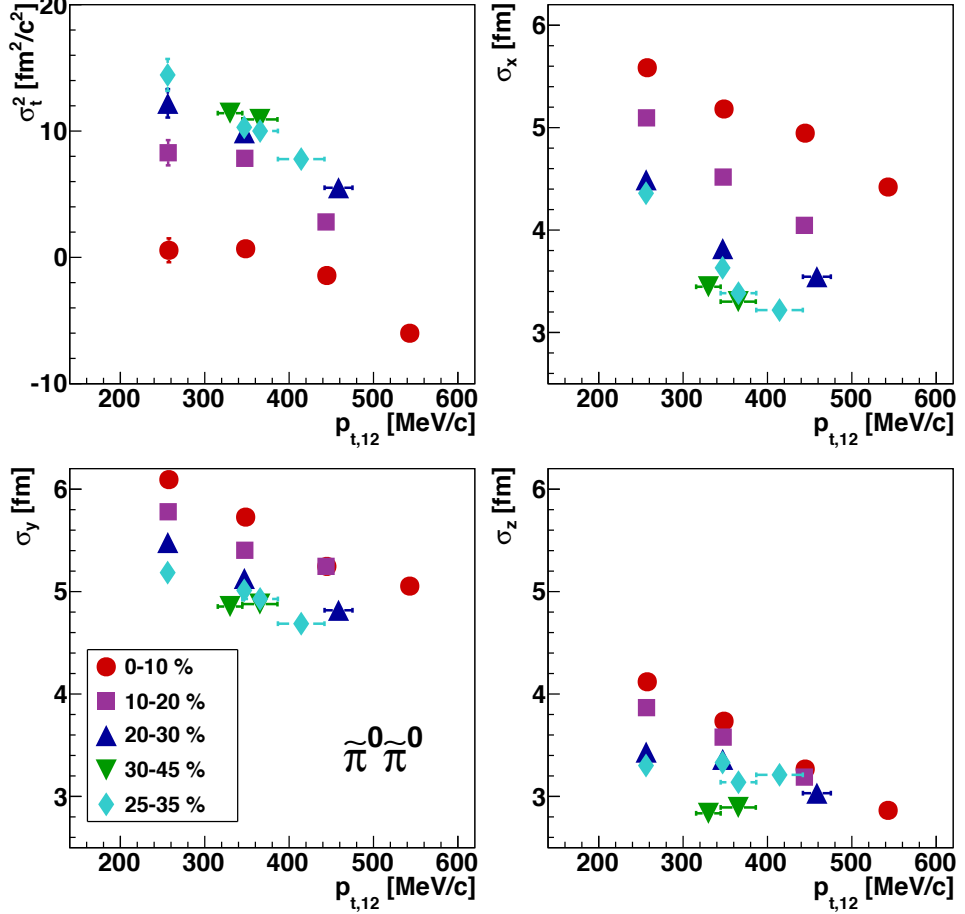


**Figure B.12:** Constructed charge-sign corrected temporal and spatial variances according to Equation (B.1) for different centralities in dependence on  $p_{t,12}$ :  $\sigma_t^2$  (top left),  $\sigma_x$  (top right),  $\sigma_y$  (bottom left) and  $\sigma_z$  (bottom right). Error bars include only statistical uncertainties.

With the most simple assumption, the charge-sign dependence of the azimuthally dependent data can be corrected using a similar form like Equation (2.29),

$$\sigma_{\tilde{\pi}^0\tilde{\pi}^0}(k_t) \approx \frac{1}{2} \left( \sigma_{\pi^-\pi^-}^2(k_t) + \sigma_{\pi^+\pi^+}^2(k_t) \right). \quad (\text{B.1})$$

Since results for  $\sigma_{\pi^-\pi^-}^2$  and  $\sigma_{\pi^+\pi^+}^2$  are obtained at different values of mean  $k_t$ , a window of  $\Delta p_{t,12} = 60 \text{ MeV}/c$  is defined. Then, each semi-axis from  $\pi^+\pi^+$  data is compared to all values of the same semi-axis from  $\pi^-\pi^-$  data within

the same centrality class. If the difference in  $p_{t,12}$  of a pair of semi-axes is smaller than  $\Delta p_{t,12}$ , Equation (B.1) is applied delivering a value for  $\sigma_{i, \tilde{\pi}^0 \tilde{\pi}^0}^2$ . The real difference in  $p_{t,12}$  of the corresponding values of  $\sigma_{\pi^- \pi^-}^2$  and  $\sigma_{\pi^+ \pi^+}^2$  is added to the uncertainties. The results obtained for  $\sigma_{\tilde{\pi}^0 \tilde{\pi}^0}^2$  according to the data points shown in Figures 5.41, 5.42, 5.46 and 5.47 are exhibited in Figure B.12. Obviously, the semi-axis in  $x$  direction within the reaction plane depends strongest on centrality. But the most interesting observation is that, at low transverse momenta, the time component  $\sigma_t$  has positive values for all classes of centrality. Identifying the values at smallest values of  $p_{t,12}$  with the squared freeze-out duration one obtains  $\Delta t \approx 0\text{--}1 \text{ fm}/c$  for most central collisions and  $\Delta t \approx 3\text{--}4 \text{ fm}/c$  for the semi-peripheral collisions achievable in this analysis.

## B.6 Eccentricity - different calculations

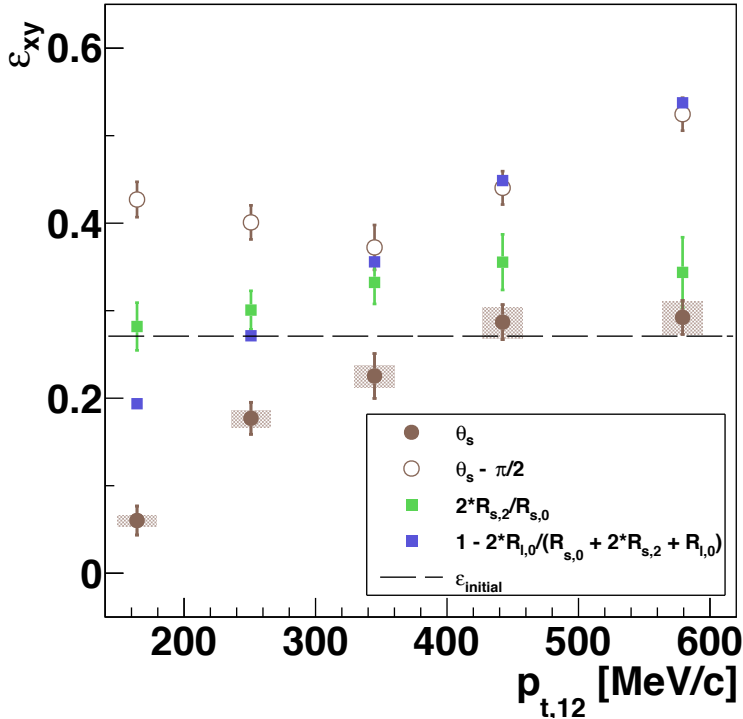


**Figure B.13:** Final eccentricity  $\epsilon_{xy}$  in dependence on  $p_{t,12}$  for  $\pi^- \pi^-$  for 10 – 30 % centrality. Filled (open) brown circles represent  $\epsilon_{xy}$  ( $\epsilon_{zy}$ ) calculated with Equation (4.46) (Equation (4.47)). Green (blue) boxes are for the values calculated with Equation (4.52) (Eq. (4.53)). The black dashed line gives the initial eccentricity  $\epsilon_{\text{ini}}$  determined from GlauberMC simulations.

Figure B.13 shows the final eccentricity in dependence on  $p_{t,12}$  for  $\pi^-\pi^-$  for 10 – 30 % centrality. The brown filled circles represent the eccentricity  $\varepsilon_{xy}$  calculated with Equation (4.46), the open brown circles are for  $\varepsilon_{zy}$  calculated using Equation (4.47), which is equivalent to  $\varepsilon_{xy}$ , if the tilt angle  $\theta_s$  is shifted by 90° and the directions  $x$  and  $z$  are exchanged (compare with Equation (4.44)). The green (blue) boxes give the values for  $\varepsilon_{xy}'$  ( $\varepsilon_{zy}'$ ) calculated with the simplified formula Equation (4.52) (Equation (4.53)). The figure illustrates the influence of  $\theta_s$  on the different ways of calculating the eccentricities. While for all brown data points the tilt of the ellipsoid is treated accurately, the simplified formulae of Equations (4.52) and (4.53) require a vanishing tilt angle and therefore the boxes deviate strongly from the circles for values of  $p_{t,12}$ , where  $\theta_s$  is clearly non-zero, see top right panel of Figure 5.34. At high values of  $p_{t,12}$ , deviations are small, and boxes and circles are the same within their uncertainties. At around  $p_{t,12}$  values of 300 MeV/c, the trajectories of the colored boxes cross each other, as expected, since there the magnitude of the tilt angle reaches 45°. For lower values of  $p_{t,12}$ , the approximate  $xy$ -eccentricity is even larger than the

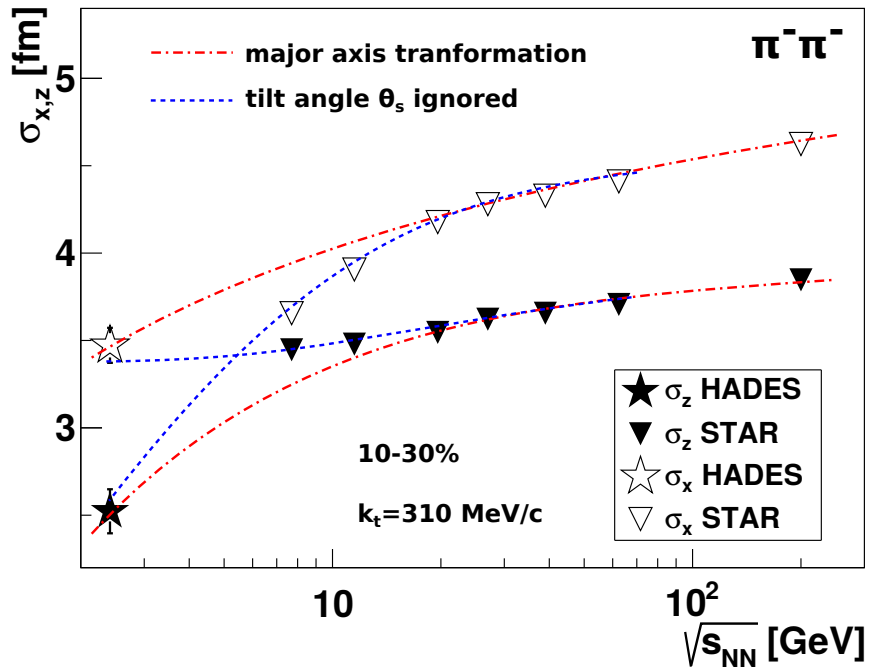


**Figure B.14:**  $\sigma_x$  ( $\sigma_z$ ) of  $\pi^-\pi^-$  pairs as a function of  $\sqrt{s_{NN}}$  for  $\bar{k}_t = 310$  MeV/c and 10 – 30 % centrality. Red dashed-dotted curves indicate the correct trends when determining  $\theta_s$  and performing a major-axis transformation. Blue dashed curves show the trends obtained when ignoring a finite tilt angle.

approximate  $zy$ -eccentricity. If one could extend this trends to a region, where  $|\theta_s| = 90^\circ$ , the complete and the simplified formalism would describe exactly the opposite kind of eccentricity. Note that part of the deviations between green boxes and filled circles also could come from the fact that for the approximation only  $R_{\text{side}}$  is taken into account, while for the description with the complete formalism the oscillations of  $R_{\text{side}}^2$ ,  $R_{\text{out}}^2$  and  $R_{\text{outside}}^2$  are considered simultaneously.

In Figure B.14, the above discussed aspect is illustrated by comparing  $\sigma_x$  and  $\sigma_z$  as function of  $\sqrt{s_{\text{NN}}}$ . The trends from STAR, calculated with Equation (4.51), can be extended by eye to the HADES energy, depicted as blue dashed curves. These extensions match the HADES data points, which correspond to a vanishing tilt angle shifted by  $90^\circ$  compared to the STAR data points at highest energies, see Figure 5.38. Extracting the tilt angle  $\theta_s$  and performing the major-axis transformation one could expect that the data points follow the trend given by the red dashed-dotted curves, where the open (filled) triangles match the open (filled) stars. This indicates that, for the two lowest energies available from STAR, a finite tilt of the ellipsoid must be present, which is significantly different from  $0^\circ$  modulo  $90^\circ$ .

## B.7 Volume calculation

In this section, the difference between Equation (5.6) and Equation (5.8) is quantified with respect to (i) the finite eccentricity transverse to the beam and (ii) the finite tilt angle  $\theta_s$ .

### Finite eccentricity $\varepsilon_{xy}$ ( $\theta_s = 0$ )

In Equation (5.6) one assumes that  $R_{\text{side}}^2 = \sigma_x \sigma_y$ , which is exact for  $\varepsilon_{xy} = 0$ . For a finite  $xy$ -eccentricity and neglecting any influence of the tilt angle  $\theta_s$ , one finds

$$\sigma_x^2 = R_{\text{side}, 0}^2 (1 - \varepsilon_{xy}), \quad (\text{B.2})$$

$$\sigma_y^2 = R_{\text{side}, 0}^2 (1 + \varepsilon_{xy}), \quad (\text{B.3})$$

$$\rightarrow \sigma_x^2 \sigma_y^2 = R_{\text{side}, 0}^4 (1 - \varepsilon_{xy}^2), \quad (\text{B.4})$$

$$\sigma_x \sigma_y = R_{\text{side}, 0} \sqrt{1 - \varepsilon_{xy}^2}, \quad (\text{B.5})$$

$$(\varepsilon_{xy}^2 \ll 1) \rightarrow \sigma_x \sigma_y \approx R_{\text{side}, 0}^2 \left( 1 - \frac{\varepsilon_{xy}^2}{2} \right). \quad (\text{B.6})$$

Identifying  $R_{\text{side}} \approx R_{\text{side}, 0}$ , which is disturbed only slightly by a non-homogeneous phase-space weighting in direction of  $\Phi$  (elliptic flow and higher order flow modes), there remains the leading order term  $(1 - \frac{\varepsilon_{xy}^2}{2})$  for small values of  $\varepsilon_{xy}$ . If the eccentricity is smaller than 0.2, this causes a deviation

## B. Further systematics

---

of less than 2%. For relatively large values of  $\varepsilon_{xy}$ , such as 0.4, it can cause already a deviation by 8%.

### Finite tilt angle $\theta_s$ ( $\varepsilon_{xy} = 0$ )

A finite tilt of the ellipsoid within the  $xz$ -plane causes the larger semi-axis to appear a bit smaller and the smaller semi-axis to appear a bit larger when projected onto the transverse and longitudinal axes relative to the beam. Then one is interested in the difference between  $\sigma_x \sigma_z$  and  $R_{\text{side}} \sqrt{1 - \varepsilon_{xy}} R_{\text{long}}$ . For simplicity  $\varepsilon_{xy}$  can be set to zero. Reducing the matrix formalism to two dimensions one gets

$$G_y^\dagger(\theta_s) S G_y(\theta_s) = \begin{pmatrix} \cos \theta_s & -\sin \theta_s \\ \sin \theta_s & \cos \theta_s \end{pmatrix} \begin{pmatrix} \sigma_x & 0 \\ 0 & \sigma_z \end{pmatrix} \begin{pmatrix} \cos \theta_s & \sin \theta_s \\ -\sin \theta_s & \cos \theta_s \end{pmatrix} \quad (\text{B.7})$$

$$= \begin{pmatrix} \cos^2 \theta_s \sigma_x^2 + \sin^2 \theta_s \sigma_z^2 & \cos \theta_s \sin \theta_s (\sigma_x^2 - \sigma_z^2) \\ \cos \theta_s \sin \theta_s (\sigma_x^2 - \sigma_z^2) & \cos^2 \theta_s \sigma_z^2 + \sin^2 \theta_s \sigma_x^2 \end{pmatrix}, \quad (\text{B.8})$$

which means that, one measures in the azimuthally integrated analysis the diagonal terms only:

$$R_{\text{side}}^2 R_{\text{long}}^2 = (\cos^2 \theta_s \sigma_x^2 + \sin^2 \theta_s \sigma_z^2) (\cos^2 \theta_s \sigma_z^2 + \sin^2 \theta_s \sigma_x^2), \quad (\text{B.9})$$

$$= \cos^2 \theta_s \sin^2 \theta_s (\sigma_x^4 + \sigma_z^4) + (\cos^4 \theta_s + \sin^4 \theta_s) \sigma_x^2 \sigma_z^2, \quad (\text{B.10})$$

$$= \cos^2 \theta_s \sin^2 \theta_s (\sigma_x^2 + \sigma_z^2)^2 + (\cos^2 \theta_s - \sin^2 \theta_s)^2 \sigma_x^2 \sigma_z^2. \quad (\text{B.11})$$

Inserting certain values for  $\theta_s$  into Equation (B.11) one finds

$$\theta_s = 0 (90)^\circ : \quad R_{\text{side}} R_{\text{long}} = \sigma_x \sigma_z, \quad (\text{B.12})$$

$$\theta_s = 45^\circ : \quad R_{\text{side}} R_{\text{long}} = \frac{\sigma_x^2 + \sigma_z^2}{2}, \quad (\text{B.13})$$

$$\theta_s = 30 (60)^\circ : \quad R_{\text{side}} R_{\text{long}} = \sqrt{\frac{3}{16} (\sigma_x^2 + \sigma_z^2)^2 + \frac{1}{4} \sigma_x^2 \sigma_z^2}. \quad (\text{B.14})$$

This means, if  $\theta_s$  vanishes ( $0^\circ$  or  $90^\circ$ ), there remains the trivial exact case. With rising tilt, a deviation appears scaling with  $(\sigma_x^2 + \sigma_z^2)/2$ , which becomes largest at  $\theta_s = 45^\circ$ . Of course, if  $\sigma_x = \sigma_z$  holds, there remains also the exact case, since a circle has no well-defined tilt angle. The relative deviation for the most extreme case  $\theta_s = 45^\circ$  can be quantified as

$$\left( \frac{\sigma_x^2 + \sigma_z^2}{2} - \sigma_x \sigma_z \right) / \sigma_x \sigma_z = \frac{(\sigma_x - \sigma_z)^2}{2 \sigma_x \sigma_z}. \quad (\text{B.15})$$

If the ratio of  $\sigma_x$  and  $\sigma_z$  is, for example, 3/2 the deviation calculated with Equation (B.15) is 8.3% (the same for  $\theta_s = 30^\circ$  gives only a deviation of 3.2%).

# C | Explicit models for the source distribution

## C.1 Three-dimensional Gaussian source with flow

A simple Gaussian parametrisation for a cylindrically symmetric fireball is given in [62]:

$$S(x, k) = \frac{1}{4\pi^2 R_G^2 L_G \Delta\tau} C_1(k) e^{-ku(x)/T - \rho^2/2R_G^2 - z^2/2L_G^2 - (t-\tau_0)^2/(\Delta\tau)^2} \quad (\text{C.1})$$

with linear radial velocity profile,

$$u(x) = \left[ 1 + \frac{1}{2} \left( \frac{v_t \rho}{R_G} \right)^2 + \frac{1}{2} \left( \frac{v_l z}{L_G} \right)^2, \frac{v_t x}{R_G}, \frac{v_t y}{R_G}, \frac{v_l z}{L_G} \right], \quad (\text{C.2})$$

and the transverse coordinate  $\rho^2 = x^2 + y^2$ . The geometrical extensions of the fireball are given by  $R_G$  in transverse direction and  $L_G$  in longitudinal direction,  $\tau_0$  is the freeze-out time and  $\Delta\tau$  denotes the freeze-out duration. The freeze-out temperature  $T$  is also referred to as the inverse slope parameter of the single particle spectra.

According to Equations (2.33) and (2.41) one obtains the following expressions for the HBT radii (terms  $\propto v_{\{R,L\}}^4$  ignored):

$$R_{\text{side}}^2 = \frac{R_G^2}{1 + \frac{v_t^2 m_t}{T}}, \quad (\text{C.3})$$

$$R_{\text{out}}^2 = \frac{R_G^2}{1 + \frac{v_t^2 m_t}{T}} + \beta_t^2 (\Delta\tau)^2, \quad (\text{C.4})$$

$$R_{\text{long}}^2 = \frac{L_G^2}{1 + \frac{v_l^2 m_t}{T}} + \beta_l^2 (\Delta\tau)^2, \quad (\text{C.5})$$

$$R_{\text{out long}}^2 = \beta_l \beta_t (\Delta\tau)^2. \quad (\text{C.6})$$

Note that  $(\Delta\tau)^2$  can be eliminated, and for finite longitudinal velocity  $\beta_l \neq 0$  one gets

$$R_{\text{out}}^2 = R_{\text{side}}^2 + \frac{\beta_t}{\beta_l} R_{\text{out long}}^2 \Rightarrow \frac{\beta_t}{\beta_l} = \frac{R_{\text{side}}^2 - R_{\text{out}}^2}{R_{\text{out long}}^2}, \quad (\text{C.7})$$

$$R_{\text{long}}^2 = \frac{L_G^2}{1 + \frac{\beta_l^2 m_t}{T}} + \frac{\beta_l}{\beta_t} R_{\text{out long}}^2. \quad (\text{C.8})$$

This formalism might be a good starting point for describing heavy-ion collisions at beam energies in the order of  $1 A$  GeV in the deep Landau scenario and delivers the common basic expressions for  $R_{\text{side}}$  and  $R_{\text{out}}$ . However, the high pressure gradients in longitudinal directions can end up in relativistic flow velocities, which break the series expansion when calculating e.g.  $R_l^2$ .

## C.2 Boost-invariant blast-wave

In ultra-relativistic heavy ion collisions at very large beam energies (achieved e.g. at LHC), so-called boost-invariant sources are used for modelling the source function  $S(x, k)$ . The longitudinal flow velocity is set to  $v_l = z/t$  (Bjorken scaling), and the finite source extension in beam direction  $\Delta\eta$  is assumed to be uncovered with the parametrisation by Milne coordinates which employ the proper time  $\tau = \sqrt{t^2 - z^2}$  and the rapidity  $\eta = \frac{1}{2} \ln(\frac{t+z}{t-z})$ . Then the source parametrisation reads [62]

$$S(x, k) = \frac{\tau_0}{(2\pi)^3 \tau} m_t \cosh(\eta - y) e^{-\frac{ku(x)}{T}} e^{-\rho^2/2R_G^2 - \eta^2/2(\Delta\eta)^2} H(\tau), \quad (\text{C.9})$$

$$H(\tau) = \frac{1}{\sqrt{2\pi\Delta\tau^2}} e^{-(\tau-\tau_0)^2/(2\Delta\tau^2)}, \quad (\text{C.10})$$

$$u(x) = \left[ \cosh \eta \sqrt{1 + \frac{v_t^2 \rho^2}{R_G^2}}, \frac{v_t x}{R_G}, \frac{v_t y}{R_G}, \sinh \eta \sqrt{1 + \frac{v_t^2 \rho^2}{R_G^2}} \right], \quad (\text{C.11})$$

with  $\rho^2 = x^2 + y^2$ , the radial flow velocity  $v_t$ , transverse source radius  $R_G$ , freeze-out temperature  $T$  and the freeze-out time  $\tau_0$ . For the  $m_t$  dependence of the HBT radii one finds

$$R_{\text{out}}^2 = \frac{R_G^2}{1 + v_t^2 m_t / T} + (\beta_t \Delta\tau)^2, \quad (\text{C.12})$$

$$R_{\text{side}}^2 = \frac{R_G^2}{1 + v_t^2 m_t / T}, \quad (\text{C.13})$$

$$R_{\text{long}}^2 = \begin{cases} \tau_0^2 \frac{T}{m_t} & \text{w/o transverse flow, LO, } m_t \gg T, \\ \tau_0^2 \frac{T}{m_t} \frac{K_2(m_t/T)}{K_1(m_t/T)} & \text{w/o transverse flow, NLO,} \\ \tau_0^2 \frac{T}{m_t} \frac{1}{1 + \frac{T}{m_t} (\frac{1}{\Delta\eta^2} - 1)} & \text{with transverse flow, LO,} \end{cases} \quad (\text{C.14})$$

with the Bessel functions  $K_1$  and  $K_2$ . Note, that  $k$  and  $u$  in Equation (C.9) are four-vectors and  $ku$  is the scalar product.



# D | Data summary tables

In the following, the data summary tables of various quantities are provided.

## D.1 Azimuthally integrated

**Table D.1:** Source parameters resulting from fits with Equations (4.26) and (4.28) for  $\pi^-\pi^-$  pairs in dependence on centrality and average transverse momentum  $\bar{k}_t$ . Values in the 1st (2nd) brackets represent the corresponding statistical (systematic) errors in units of the last digit of the respective quantity.

centrality %	$\bar{k}_t$ MeV/c	$R_{\text{inv}}$ fm	$\lambda_{\text{inv}}$	$R_{\text{out}}$ fm	$R_{\text{side}}$ fm	$R_{\text{long}}$ fm	$\lambda_{\text{osl}}$
0-10	43	7.03(23)( <sup>+17</sup> <sub>-10</sub> )	0.904(84)( <sup>+42</sup> <sub>-38</sub> )	7.03(60)( <sup>+31</sup> <sub>-8</sub> )	7.44(27)( <sup>+23</sup> <sub>-1</sub> )	5.50(34)( <sup>+21</sup> <sub>-2</sub> )	0.872(74)( <sup>+59</sup> <sub>-0</sub> )
0-10	81	6.54(4)( <sup>+20</sup> <sub>-0</sub> )	0.801(12)( <sup>+28</sup> <sub>-0</sub> )	6.88(9)( <sup>+17</sup> <sub>-1</sub> )	7.15(10)( <sup>+16</sup> <sub>-1</sub> )	5.53(5)( <sup>+11</sup> <sub>-1</sub> )	0.904(19)( <sup>+38</sup> <sub>-2</sub> )
0-10	125	5.88(2)( <sup>+28</sup> <sub>-4</sub> )	0.710(7)( <sup>+59</sup> <sub>-6</sub> )	6.22(5)( <sup>+23</sup> <sub>-6</sub> )	6.27(6)( <sup>+21</sup> <sub>-1</sub> )	4.81(3)( <sup>+15</sup> <sub>-0</sub> )	0.848(11)( <sup>+36</sup> <sub>-1</sub> )
0-10	172	5.37(2)( <sup>+28</sup> <sub>-7</sub> )	0.662(7)( <sup>+21</sup> <sub>-6</sub> )	5.59(6)( <sup>+26</sup> <sub>-8</sub> )	5.75(5)( <sup>+15</sup> <sub>-13</sub> )	4.17(2)( <sup>+15</sup> <sub>-5</sub> )	0.840(12)( <sup>+40</sup> <sub>-18</sub> )
0-10	221	5.01(3)( <sup>+17</sup> <sub>-17</sub> )	0.628(9)( <sup>+26</sup> <sub>-3</sub> )	5.16(10)( <sup>+18</sup> <sub>-9</sub> )	5.26(6)( <sup>+8</sup> <sub>-13</sub> )	3.61(3)( <sup>+12</sup> <sub>-5</sub> )	0.847(19)( <sup>+17</sup> <sub>-17</sub> )
0-10	271	4.57(4)( <sup>+22</sup> <sub>-17</sub> )	0.565(12)( <sup>+74</sup> <sub>-24</sub> )	4.69(34)( <sup>+16</sup> <sub>-13</sub> )	4.80(8)( <sup>+11</sup> <sub>-10</sub> )	3.11(3)( <sup>+11</sup> <sub>-6</sub> )	0.836(62)( <sup>+43</sup> <sub>-24</sub> )
0-10	321	4.25(6)( <sup>+15</sup> <sub>-15</sub> )	0.530(18)( <sup>+20</sup> <sub>-20</sub> )	4.27(11)( <sup>+12</sup> <sub>-8</sub> )	4.32(9)( <sup>+8</sup> <sub>-12</sub> )	2.80(5)( <sup>+8</sup> <sub>-11</sub> )	0.846(26)( <sup>+15</sup> <sub>-15</sub> )
0-10	370	3.91(10)( <sup>+35</sup> <sub>-14</sub> )	0.462(27)( <sup>+10</sup> <sub>-19</sub> )	3.84(27)( <sup>+12</sup> <sub>-12</sub> )	3.95(13)( <sup>+14</sup> <sub>-8</sub> )	2.50(7)( <sup>+15</sup> <sub>-5</sub> )	0.776(57)( <sup>+57</sup> <sub>-20</sub> )
0-10	420	3.84(15)( <sup>+25</sup> <sub>-11</sub> )	0.494(44)( <sup>+73</sup> <sub>-15</sub> )	3.04(19)( <sup>+25</sup> <sub>-4</sub> )	3.57(19)( <sup>+25</sup> <sub>-12</sub> )	2.33(9)( <sup>+18</sup> <sub>-0</sub> )	0.725(52)( <sup>+68</sup> <sub>-3</sub> )
10-20	43	6.08(23)( <sup>+28</sup> <sub>-15</sub> )	0.734(75)( <sup>+82</sup> <sub>-31</sub> )	4.82(73)( <sup>+69</sup> <sub>-26</sub> )	6.24(24)( <sup>+14</sup> <sub>-12</sub> )	5.73(39)( <sup>+37</sup> <sub>-13</sub> )	0.740(72)( <sup>+30</sup> <sub>-30</sub> )
10-20	81	6.16(4)( <sup>+9</sup> <sub>-0</sub> )	0.770(13)( <sup>+28</sup> <sub>-0</sub> )	6.29(8)( <sup>+8</sup> <sub>-3</sub> )	6.09(8)( <sup>+8</sup> <sub>-3</sub> )	5.57(6)( <sup>+8</sup> <sub>-0</sub> )	0.849(18)( <sup>+17</sup> <sub>-0</sub> )
10-20	125	5.71(3)( <sup>+22</sup> <sub>-2</sub> )	0.702(9)( <sup>+50</sup> <sub>-1</sub> )	5.94(5)( <sup>+17</sup> <sub>-1</sub> )	5.73(5)( <sup>+11</sup> <sub>-0</sub> )	4.89(3)( <sup>+11</sup> <sub>-0</sub> )	0.829(12)( <sup>+26</sup> <sub>-1</sub> )
10-20	172	5.21(3)( <sup>+22</sup> <sub>-7</sub> )	0.666(9)( <sup>+61</sup> <sub>-10</sub> )	5.57(6)( <sup>+17</sup> <sub>-2</sub> )	5.09(5)( <sup>+12</sup> <sub>-2</sub> )	4.14(3)( <sup>+12</sup> <sub>-1</sub> )	0.845(13)( <sup>+34</sup> <sub>-31</sub> )
10-20	221	4.78(4)( <sup>+24</sup> <sub>-13</sub> )	0.629(12)( <sup>+79</sup> <sub>-19</sub> )	5.06(10)( <sup>+17</sup> <sub>-7</sub> )	4.66(6)( <sup>+6</sup> <sub>-6</sub> )	3.60(3)( <sup>+8</sup> <sub>-4</sub> )	0.868(20)( <sup>+14</sup> <sub>-14</sub> )
10-20	270	4.32(5)( <sup>+25</sup> <sub>-11</sub> )	0.585(16)( <sup>+88</sup> <sub>-17</sub> )	4.62(33)( <sup>+15</sup> <sub>-11</sub> )	4.19(8)( <sup>+10</sup> <sub>-7</sub> )	3.03(4)( <sup>+6</sup> <sub>-4</sub> )	0.885(65)( <sup>+49</sup> <sub>-19</sub> )
10-20	320	4.03(8)( <sup>+19</sup> <sub>-10</sub> )	0.529(25)( <sup>+100</sup> <sub>-19</sub> )	4.11(13)( <sup>+23</sup> <sub>-23</sub> )	3.62(10)( <sup>+30</sup> <sub>-9</sub> )	2.73(6)( <sup>+11</sup> <sub>-9</sub> )	0.827(31)( <sup>+81</sup> <sub>-18</sub> )
10-20	370	3.52(14)( <sup>+60</sup> <sub>-4</sub> )	0.435(35)( <sup>+5</sup> <sub>-18</sub> )	3.37(23)( <sup>+44</sup> <sub>-15</sub> )	3.27(15)( <sup>+14</sup> <sub>-2</sub> )	2.43(8)( <sup>+38</sup> <sub>-2</sub> )	0.736(53)( <sup>+33</sup> <sub>-10</sub> )
20-30	43	5.62(22)( <sup>+27</sup> <sub>-13</sub> )	0.821(86)( <sup>+56</sup> <sub>-19</sub> )	4.22(74)( <sup>+18</sup> <sub>-12</sub> )	5.49(22)( <sup>+27</sup> <sub>-2</sub> )	5.76(44)( <sup>+55</sup> <sub>-1</sub> )	0.790(80)( <sup>+108</sup> <sub>-4</sub> )
20-30	81	5.69(4)( <sup>+16</sup> <sub>-0</sub> )	0.745(14)( <sup>+34</sup> <sub>-0</sub> )	5.76(8)( <sup>+16</sup> <sub>-7</sub> )	5.46(7)( <sup>+9</sup> <sub>-7</sub> )	5.39(6)( <sup>+17</sup> <sub>-0</sub> )	0.823(18)( <sup>+22</sup> <sub>-0</sub> )
20-30	125	5.28(3)( <sup>+24</sup> <sub>-2</sub> )	0.701(10)( <sup>+48</sup> <sub>-2</sub> )	5.56(5)( <sup>+20</sup> <sub>-0</sub> )	5.06(5)( <sup>+13</sup> <sub>-0</sub> )	4.62(4)( <sup>+16</sup> <sub>-0</sub> )	0.822(12)( <sup>+29</sup> <sub>-0</sub> )
20-30	172	4.87(3)( <sup>+22</sup> <sub>-9</sub> )	0.670(10)( <sup>+52</sup> <sub>-13</sub> )	5.37(6)( <sup>+16</sup> <sub>-3</sub> )	4.53(5)( <sup>+13</sup> <sub>-2</sub> )	3.89(3)( <sup>+12</sup> <sub>-2</sub> )	0.851(14)( <sup>+34</sup> <sub>-4</sub> )
20-30	221	4.45(4)( <sup>+24</sup> <sub>-13</sub> )	0.622(14)( <sup>+81</sup> <sub>-19</sub> )	4.84(10)( <sup>+10</sup> <sub>-6</sub> )	4.21(6)( <sup>+9</sup> <sub>-4</sub> )	3.32(4)( <sup>+5</sup> <sub>-3</sub> )	0.861(21)( <sup>+16</sup> <sub>-10</sub> )
20-30	270	4.03(7)( <sup>+34</sup> <sub>-14</sub> )	0.543(20)( <sup>+104</sup> <sub>-24</sub> )	4.68(35)( <sup>+22</sup> <sub>-22</sub> )	3.65(8)( <sup>+16</sup> <sub>-16</sub> )	2.80(5)( <sup>+10</sup> <sub>-3</sub> )	0.867(66)( <sup>+65</sup> <sub>-6</sub> )
20-30	320	3.98(10)( <sup>+21</sup> <sub>-9</sub> )	0.565(34)( <sup>+14</sup> <sub>-18</sub> )	4.13(16)( <sup>+23</sup> <sub>-18</sub> )	3.42(12)( <sup>+15</sup> <sub>-9</sub> )	2.58(7)( <sup>+4</sup> <sub>-5</sub> )	0.868(40)( <sup>+60</sup> <sub>-23</sub> )
20-30	370	3.57(18)( <sup>+73</sup> <sub>-9</sub> )	0.480(50)( <sup>+180</sup> <sub>-12</sub> )	3.74(31)( <sup>+38</sup> <sub>-18</sub> )	3.03(15)( <sup>+7</sup> <sub>-0</sub> )	2.41(10)( <sup>+3</sup> <sub>-8</sub> )	0.932(82)( <sup>+9</sup> <sub>-6</sub> )
30-40	43	5.02(23)( <sup>+26</sup> <sub>-9</sub> )	0.711(89)( <sup>+42</sup> <sub>-14</sub> )	3.74(45)( <sup>+17</sup> <sub>-12</sub> )	5.18(23)( <sup>+12</sup> <sub>-0</sub> )	4.96(58)( <sup>+44</sup> <sub>-9</sub> )	0.721(86)( <sup>+42</sup> <sub>-10</sub> )
30-40	81	5.10(5)( <sup>+26</sup> <sub>-0</sub> )	0.707(16)( <sup>+36</sup> <sub>-0</sub> )	5.22(8)( <sup>+18</sup> <sub>-3</sub> )	4.85(7)( <sup>+12</sup> <sub>-3</sub> )	4.98(7)( <sup>+24</sup> <sub>-0</sub> )	0.784(19)( <sup>+20</sup> <sub>-3</sub> )
30-40	125	4.89(3)( <sup>+24</sup> <sub>-0</sub> )	0.691(12)( <sup>+41</sup> <sub>-0</sub> )	5.26(6)( <sup>+19</sup> <sub>-3</sub> )	4.53(5)( <sup>+9</sup> <sub>-0</sub> )	4.34(4)( <sup>+15</sup> <sub>-0</sub> )	0.811(14)( <sup>+30</sup> <sub>-0</sub> )
30-40	172	4.52(4)( <sup>+27</sup> <sub>-6</sub> )	0.664(13)( <sup>+73</sup> <sub>-10</sub> )	5.10(7)( <sup>+19</sup> <sub>-3</sub> )	4.11(5)( <sup>+19</sup> <sub>-2</sub> )	3.64(4)( <sup>+17</sup> <sub>-2</sub> )	0.849(16)( <sup>+44</sup> <sub>-4</sub> )
30-40	221	4.20(5)( <sup>+21</sup> <sub>-2</sub> )	0.648(17)( <sup>+81</sup> <sub>-18</sub> )	4.64(10)( <sup>+13</sup> <sub>-13</sub> )	3.72(6)( <sup>+16</sup> <sub>-16</sub> )	3.07(4)( <sup>+6</sup> <sub>-6</sub> )	0.872(23)( <sup>+17</sup> <sub>-3</sub> )
30-40	270	3.81(8)( <sup>+37</sup> <sub>-18</sub> )	0.562(25)( <sup>+129</sup> <sub>-26</sub> )	4.24(28)( <sup>+41</sup> <sub>-41</sub> )	3.24(9)( <sup>+15</sup> <sub>-4</sub> )	2.66(6)( <sup>+11</sup> <sub>-2</sub> )	0.851(58)( <sup>+75</sup> <sub>-11</sub> )
30-40	320	3.38(13)( <sup>+61</sup> <sub>-8</sub> )	0.480(36)( <sup>+155</sup> <sub>-11</sub> )	4.03(19)( <sup>+30</sup> <sub>-18</sub> )	2.86(12)( <sup>+38</sup> <sub>-8</sub> )	2.37(8)( <sup>+11</sup> <sub>-12</sub> )	0.855(47)( <sup>+39</sup> <sub>-23</sub> )

## D. Data summary tables

**Table D.2:** The same as table D.1, but for  $\pi^+\pi^+$  pairs.

centrality %	$\bar{k}_t$ MeV/c	$R_{\text{inv}}$ fm	$\lambda_{\text{inv}}$	$R_{\text{out}}$ fm	$R_{\text{side}}$ fm	$R_{\text{long}}$ fm	$\lambda_{\text{osl}}$
0-10	92	4.81(16)( <sup>+39</sup> <sub>-0</sub> )	0.870(65)( <sup>+80</sup> <sub>-81</sub> )	5.67(40)( <sup>+51</sup> <sub>-4</sub> )	5.45(24)( <sup>+22</sup> <sub>-4</sub> )	4.04(17)( <sup>+26</sup> <sub>-2</sub> )	0.973(71)( <sup>+23</sup> <sub>-40</sub> )
0-10	130	4.70(4)( <sup>+39</sup> <sub>-5</sub> )	0.697(14)( <sup>+81</sup> <sub>-7</sub> )	5.32(7)( <sup>+40</sup> <sub>-1</sub> )	5.05(7)( <sup>+20</sup> <sub>-1</sub> )	3.87(4)( <sup>+22</sup> <sub>-1</sub> )	0.876(17)( <sup>+40</sup> <sub>-1</sub> )
0-10	175	4.54(3)( <sup>+31</sup> <sub>-10</sub> )	0.614(10)( <sup>+89</sup> <sub>-23</sub> )	5.23(7)( <sup>+36</sup> <sub>-17</sub> )	4.79(6)( <sup>+16</sup> <sub>-4</sub> )	3.39(3)( <sup>+20</sup> <sub>-12</sub> )	0.830(14)( <sup>+60</sup> <sub>-12</sub> )
0-10	223	4.37(4)( <sup>+36</sup> <sub>-17</sub> )	0.556(11)( <sup>+104</sup> <sub>-23</sub> )	4.86(9)( <sup>+26</sup> <sub>-11</sub> )	4.62(6)( <sup>+14</sup> <sub>-9</sub> )	3.13(3)( <sup>+13</sup> <sub>-6</sub> )	0.815(19)( <sup>+43</sup> <sub>-17</sub> )
0-10	272	4.17(5)( <sup>+34</sup> <sub>-19</sub> )	0.525(15)( <sup>+101</sup> <sub>-25</sub> )	4.44(9)( <sup>+40</sup> <sub>-30</sub> )	4.28(8)( <sup>+15</sup> <sub>-7</sub> )	2.82(4)( <sup>+14</sup> <sub>-4</sub> )	0.809(22)( <sup>+65</sup> <sub>-15</sub> )
0-10	321	3.86(7)( <sup>+35</sup> <sub>-17</sub> )	0.489(19)( <sup>+101</sup> <sub>-23</sub> )	4.16(12)( <sup>+30</sup> <sub>-17</sub> )	4.06(9)( <sup>+10</sup> <sub>-4</sub> )	2.55(5)( <sup>+8</sup> <sub>-2</sub> )	0.835(28)( <sup>+21</sup> <sub>-21</sub> )
0-10	371	3.57(10)( <sup>+35</sup> <sub>-12</sub> )	0.440(26)( <sup>+14</sup> <sub>-14</sub> )	3.71(17)( <sup>+65</sup> <sub>-27</sub> )	3.78(12)( <sup>+22</sup> <sub>-17</sub> )	2.23(6)( <sup>+11</sup> <sub>-6</sub> )	0.817(37)( <sup>+14</sup> <sub>-25</sub> )
0-10	421	3.46(17)( <sup>+26</sup> <sub>-9</sub> )	0.376(37)( <sup>+54</sup> <sub>-9</sub> )	3.28(22)( <sup>+48</sup> <sub>-24</sub> )	3.55(19)( <sup>+10</sup> <sub>-12</sub> )	2.12(9)( <sup>+4</sup> <sub>-14</sub> )	0.723(48)( <sup>+17</sup> <sub>-0</sub> )
10-20	92	4.86(18)( <sup>-3</sup> )	0.851(70)( <sup>+25</sup> <sub>-6</sub> )	5.47(46)( <sup>+11</sup> <sub>-6</sub> )	5.07(21)( <sup>+2</sup> <sub>-15</sub> )	4.48(24)( <sup>+15</sup> <sub>-5</sub> )	0.963(83)( <sup>+28</sup> <sub>-10</sub> )
10-20	129	4.63(5)( <sup>+33</sup> <sub>-26</sub> )	0.678(16)( <sup>+77</sup> <sub>-6</sub> )	5.32(8)( <sup>+24</sup> <sub>-24</sub> )	4.52(7)( <sup>+11</sup> <sub>-14</sub> )	3.88(5)( <sup>+22</sup> <sub>-15</sub> )	0.836(19)( <sup>+42</sup> <sub>-50</sub> )
10-20	174	4.53(4)( <sup>+10</sup> <sub>-10</sub> )	0.635(13)( <sup>+14</sup> <sub>-14</sub> )	5.08(7)( <sup>+20</sup> <sub>-5</sub> )	4.42(6)( <sup>+4</sup> <sub>-14</sub> )	3.54(4)( <sup>+15</sup> <sub>-3</sub> )	0.833(16)( <sup>+50</sup> <sub>-9</sub> )
10-20	222	4.31(5)( <sup>+27</sup> <sub>-15</sub> )	0.587(15)( <sup>+84</sup> <sub>-20</sub> )	4.78(10)( <sup>+21</sup> <sub>-6</sub> )	4.04(6)( <sup>+16</sup> <sub>-4</sub> )	3.14(4)( <sup>+10</sup> <sub>-3</sub> )	0.828(21)( <sup>+43</sup> <sub>-9</sub> )
10-20	271	4.05(6)( <sup>+15</sup> <sub>-15</sub> )	0.549(19)( <sup>+76</sup> <sub>-76</sub> )	4.38(11)( <sup>+28</sup> <sub>-8</sub> )	3.87(8)( <sup>+10</sup> <sub>-6</sub> )	2.80(5)( <sup>+10</sup> <sub>-4</sub> )	0.837(26)( <sup>+42</sup> <sub>-15</sub> )
10-20	321	3.71(10)( <sup>+43</sup> <sub>-8</sub> )	0.477(27)( <sup>+111</sup> <sub>-11</sub> )	4.05(14)( <sup>+16</sup> <sub>-16</sub> )	3.49(11)( <sup>+9</sup> <sub>-4</sub> )	2.40(6)( <sup>+3</sup> <sub>-2</sub> )	0.796(33)( <sup>+25</sup> <sub>-10</sub> )
10-20	371	3.80(16)( <sup>+25</sup> <sub>-28</sub> )	0.474(44)( <sup>+41</sup> <sub>-35</sub> )	4.51(33)( <sup>+34</sup> <sub>-73</sub> )	3.38(16)( <sup>+0</sup> <sub>-14</sub> )	2.35(9)( <sup>+16</sup> <sub>-6</sub> )	0.951(63)( <sup>+121</sup> <sub>-34</sub> )
20-30	92	4.29(19)( <sup>+45</sup> <sub>-1</sub> )	0.721(67)( <sup>+91</sup> <sub>-1</sub> )	4.71(54)( <sup>+23</sup> <sub>-1</sub> )	4.34(21)( <sup>+15</sup> <sub>-1</sub> )	4.01(25)( <sup>+19</sup> <sub>-1</sub> )	0.774(76)( <sup>+34</sup> <sub>-0</sub> )
20-30	129	4.36(6)( <sup>+39</sup> <sub>-39</sub> )	0.653(18)( <sup>+88</sup> <sub>-88</sub> )	5.10(9)( <sup>+24</sup> <sub>-24</sub> )	4.11(7)( <sup>+7</sup> <sub>-0</sub> )	3.85(6)( <sup>+18</sup> <sub>-0</sub> )	0.825(21)( <sup>+30</sup> <sub>-30</sub> )
20-30	174	4.23(5)( <sup>+30</sup> <sub>-30</sub> )	0.623(15)( <sup>+79</sup> <sub>-12</sub> )	4.92(8)( <sup>+24</sup> <sub>-5</sub> )	3.86(6)( <sup>+17</sup> <sub>-3</sub> )	3.37(4)( <sup>+13</sup> <sub>-3</sub> )	0.828(18)( <sup>+50</sup> <sub>-7</sub> )
20-30	222	4.02(6)( <sup>+33</sup> <sub>-15</sub> )	0.571(18)( <sup>+94</sup> <sub>-21</sub> )	4.70(11)( <sup>+21</sup> <sub>-9</sub> )	3.68(7)( <sup>+20</sup> <sub>-6</sub> )	3.01(4)( <sup>+8</sup> <sub>-4</sub> )	0.843(25)( <sup>+41</sup> <sub>-14</sub> )
20-30	271	3.98(9)( <sup>+37</sup> <sub>-7</sub> )	0.570(27)( <sup>+130</sup> <sub>-52</sub> )	4.40(13)( <sup>+26</sup> <sub>-12</sub> )	3.36(9)( <sup>+26</sup> <sub>-6</sub> )	2.72(6)( <sup>+13</sup> <sub>-5</sub> )	0.879(33)( <sup>+71</sup> <sub>-5</sub> )
20-30	321	3.50(12)( <sup>+34</sup> <sub>-7</sub> )	0.497(34)( <sup>+94</sup> <sub>-52</sub> )	4.26(19)( <sup>+12</sup> <sub>-24</sub> )	3.14(12)( <sup>+10</sup> <sub>-10</sub> )	2.48(8)( <sup>+5</sup> <sub>-12</sub> )	0.920(48)( <sup>+30</sup> <sub>-30</sub> )
20-30	370	3.15(19)( <sup>+50</sup> <sub>-3</sub> )	0.416(47)( <sup>+122</sup> <sub>-2</sub> )	4.27(38)( <sup>+22</sup> <sub>-86</sub> )	2.69(16)( <sup>+9</sup> <sub>-18</sub> )	2.24(11)( <sup>+9</sup> <sub>-18</sub> )	0.985(77)( <sup>+47</sup> <sub>-75</sub> )
30-40	92	4.16(23)( <sup>+46</sup> <sub>-16</sub> )	0.767(86)( <sup>+132</sup> <sub>-7</sub> )	5.33(67)( <sup>+39</sup> <sub>-7</sub> )	3.84(21)( <sup>+12</sup> <sub>-6</sub> )	4.46(29)( <sup>+21</sup> <sub>-6</sub> )	0.936(106)( <sup>+32</sup> <sub>-11</sub> )
30-40	128	4.09(6)( <sup>+33</sup> <sub>-33</sub> )	0.659(21)( <sup>+73</sup> <sub>-5</sub> )	4.68(10)( <sup>+25</sup> <sub>-1</sub> )	3.75(7)( <sup>+4</sup> <sub>-0</sub> )	3.73(7)( <sup>+24</sup> <sub>-0</sub> )	0.816(25)( <sup>+32</sup> <sub>-32</sub> )
30-40	173	3.95(6)( <sup>+44</sup> <sub>-10</sub> )	0.621(18)( <sup>+13</sup> <sub>-5</sub> )	4.52(8)( <sup>+17</sup> <sub>-1</sub> )	3.50(6)( <sup>+15</sup> <sub>-0</sub> )	3.22(5)( <sup>+18</sup> <sub>-0</sub> )	0.820(21)( <sup>+30</sup> <sub>-30</sub> )
30-40	222	3.86(7)( <sup>+31</sup> <sub>-14</sub> )	0.592(23)( <sup>+20</sup> <sub>-5</sub> )	4.59(12)( <sup>+5</sup> <sub>-5</sub> )	3.26(7)( <sup>+9</sup> <sub>-3</sub> )	2.79(5)( <sup>+6</sup> <sub>-2</sub> )	0.858(29)( <sup>+13</sup> <sub>-7</sub> )
30-40	271	3.54(11)( <sup>+35</sup> <sub>-11</sub> )	0.505(31)( <sup>+129</sup> <sub>-58</sub> )	4.17(15)( <sup>+32</sup> <sub>-8</sub> )	3.07(11)( <sup>+37</sup> <sub>-8</sub> )	2.46(7)( <sup>+9</sup> <sub>-2</sub> )	0.808(38)( <sup>+73</sup> <sub>-19</sub> )
30-40	321	3.44(15)( <sup>+20</sup> <sub>-9</sub> )	0.517(47)( <sup>+111</sup> <sub>-13</sub> )	3.76(22)( <sup>+22</sup> <sub>-13</sub> )	2.94(15)( <sup>+10</sup> <sub>-42</sub> )	2.34(10)( <sup>+10</sup> <sub>-16</sub> )	0.867(59)( <sup>+19</sup> <sub>-40</sub> )

## D.1 Azimuthally integrated

**Table D.3:** The same as table D.1, but for constructed fiducial  $\tilde{\pi}^0\tilde{\pi}^0$  pairs without systematic uncertainties and replacing the columns of the  $\lambda$  parameters by the effective potentials  $V_{\text{eff}}$ .

centrality %	$\bar{k}_t$ MeV/c	$R_{\text{inv}}$ fm	$V_{\text{inv}}^{\text{eff}}$ MeV	$R_{\text{out}}$ fm	$R_{\text{side}}$ fm	$R_{\text{long}}$ fm	$V_{\text{out}}^{\text{eff}}$ MeV	$V_{\text{side}}^{\text{eff}}$ MeV	$V_{\text{long}}^{\text{eff}}$ MeV
0-10	87	5.70(4)	7.0(5)	6.30(27)	6.32(18)	4.81(12)	3.1(14)	5.5(6)	5.3(11)
0-10	127	5.30(3)	9.7(3)	5.78(6)	5.67(9)	4.35(5)	5.5(6)	9.1(5)	7.3(4)
0-10	174	4.97(3)	10.9(4)	5.41(6)	5.29(8)	3.80(4)	3.8(9)	11.7(6)	13.0(4)
0-10	222	4.70(4)	11.0(7)	5.01(10)	4.94(9)	3.38(4)	2.8(21)	11.0(10)	11.6(7)
0-10	271	4.38(6)	9.0(13)	4.57(26)	4.55(11)	2.97(5)	-0.1(61)	12.8(16)	10.4(13)
0-10	321	4.06(8)	13.1(24)	4.21(11)	4.19(13)	2.68(7)	2.1(69)	9.2(27)	12.4(24)
0-10	371	3.75(13)	16.9(47)	3.77(23)	3.87(18)	2.37(9)	5.0(92)	10.3(49)	17.6(48)
0-10	421	3.55(21)	26.5(87)	3.24(20)	3.55(26)	2.15(14)	-3.2(155)	1.4(91)	27.6(93)
10-20	87	5.54(4)	5.0(6)	5.92(31)	5.63(16)	5.07(16)	0.7(18)	3.7(7)	2.3(13)
10-20	127	5.19(3)	8.5(4)	5.63(7)	5.15(8)	4.40(6)	4.4(7)	9.5(5)	7.7(4)
10-20	173	4.88(4)	9.2(5)	5.33(7)	4.76(8)	3.85(5)	5.0(10)	9.0(6)	9.3(5)
10-20	221	4.55(5)	9.5(9)	4.92(10)	4.36(9)	3.38(5)	5.4(22)	12.8(10)	12.2(9)
10-20	271	4.19(8)	7.4(17)	4.50(25)	4.03(11)	2.92(6)	-0.6(63)	8.5(19)	8.0(17)
10-20	321	3.88(13)	12.0(35)	4.08(14)	3.56(14)	2.57(9)	5.3(77)	7.5(34)	21.5(35)
10-20	370	3.66(21)	-13.1(71)	3.98(30)	3.33(22)	2.39(13)	-11.5(121)	-4.0(66)	17.9(69)
20-30	86	5.02(5)	6.2(7)	5.25(35)	4.93(15)	4.71(17)	2.6(23)	5.0(7)	4.7(17)
20-30	127	4.83(4)	8.0(4)	5.32(7)	4.60(8)	4.24(7)	3.5(8)	8.4(5)	6.1(5)
20-30	173	4.56(5)	9.3(6)	5.15(7)	4.21(7)	3.64(5)	6.1(11)	10.6(7)	8.7(6)
20-30	221	4.24(7)	9.5(11)	4.77(10)	3.95(9)	3.17(6)	0.8(24)	12.3(12)	7.4(11)
20-30	271	4.01(9)	1.4(23)	4.54(27)	3.50(12)	2.76(7)	0.8(67)	9.0(22)	1.0(23)
20-30	320	3.75(15)	18.9(43)	4.19(18)	3.28(16)	2.53(11)	-3.4(93)	13.3(42)	2.2(46)
20-30	370	3.37(25)	21.7(96)	4.01(35)	2.86(22)	2.33(14)	-8.8(142)	22.1(76)	22.5(79)
30-40	86	4.65(6)	4.5(10)	5.37(47)	4.35(15)	4.76(21)	2.3(33)	4.7(8)	0.3(27)
30-40	126	4.51(5)	7.3(5)	4.98(8)	4.15(8)	4.04(8)	5.3(10)	7.4(5)	5.1(7)
30-40	173	4.24(6)	8.9(8)	4.81(8)	3.81(8)	3.43(6)	6.5(14)	10.1(8)	7.0(8)
30-40	221	4.03(8)	7.7(15)	4.61(11)	3.49(9)	2.94(7)	1.8(28)	12.0(13)	7.2(15)
30-40	271	3.68(12)	8.8(31)	4.21(22)	3.15(14)	2.56(9)	-6.7(71)	6.3(27)	4.7(29)
30-40	321	3.41(23)	-2.7(61)	3.90(21)	2.90(19)	2.36(13)	10.4(109)	-6.2(52)	11.9(61)

## D.2 Azimuthally dependent

**Table D.4:** Source extensions in the  $xyz$ -coordinate system of the emission ellipsoid and the corresponding tilt angels  $\theta_s$  resulting from fits with Equation (4.44) for  $\pi^-\pi^-$  pairs in dependence on centrality and average transverse momentum  $\bar{k}_t$ . Values in the 1st (2nd) brackets represent the corresponding statistical (systematic) errors in units of the last digit of the respective quantity.

Centrality (%)	$\bar{k}_t$ (MeV/c)	$\sigma_x^2$ (fm $^2$ )	$\sigma_y^2$ (fm $^2$ )	$\sigma_z^2$ (fm $^2$ )	$\sigma_t^2$ (fm $^2/c^2$ )	$\theta_s$ (deg)
0-10	82	48.1(14)( $^{+6}_{-6}$ )	55.4(16)( $^{+15}_{-6}$ )	23.9(8)( $^{+3}_{-3}$ )	-11.2(35)( $^{+14}_{-22}$ )	-27(2)( $^{+0}_{-0}$ )
0-10	126	38.1(9)( $^{+18}_{-9}$ )	43.8(9)( $^{+22}_{-9}$ )	21.0(4)( $^{+4}_{-4}$ )	-1.8(12)( $^{+4}_{-6}$ )	-20(1)( $^{+0}_{-1}$ )
0-10	173	31.5(8)( $^{+21}_{-12}$ )	38.8(8)( $^{+25}_{-14}$ )	17.0(2)( $^{+10}_{-6}$ )	-3.2(8)( $^{+1}_{-3}$ )	-12(1)( $^{+0}_{-0}$ )
0-10	222	26.2(9)( $^{+17}_{-12}$ )	33.2(9)( $^{+23}_{-15}$ )	12.5(2)( $^{+7}_{-5}$ )	-3.2(7)( $^{+1}_{-1}$ )	-8(1)( $^{+0}_{-0}$ )
0-10	271	22.0(10)( $^{+14}_{-13}$ )	29.5(11)( $^{+20}_{-16}$ )	9.0(1)( $^{+5}_{-5}$ )	-9.2(7)( $^{+3}_{-3}$ )	-5(1)( $^{+0}_{-0}$ )
10-20	82	41.8(7)( $^{+10}_{-7}$ )	43.7(9)( $^{+10}_{-7}$ )	18.9(7)( $^{+4}_{-4}$ )	11.1(30)( $^{+13}_{-19}$ )	-46(1)( $^{+0}_{-0}$ )
10-20	125	29.7(5)( $^{+15}_{-7}$ )	39.5(7)( $^{+19}_{-7}$ )	18.0(4)( $^{+9}_{-3}$ )	7.0(12)( $^{+3}_{-4}$ )	-40(2)( $^{+0}_{-0}$ )
10-20	173	23.0(5)( $^{+13}_{-7}$ )	33.4(6)( $^{+16}_{-9}$ )	15.4(3)( $^{+8}_{-4}$ )	7.6(9)( $^{+6}_{-4}$ )	-27(2)( $^{+0}_{-0}$ )
10-20	221	18.7(6)( $^{+10}_{-9}$ )	30.0(7)( $^{+15}_{-12}$ )	11.4(2)( $^{+6}_{-5}$ )	2.5(8)( $^{+4}_{-3}$ )	-14(2)( $^{+0}_{-0}$ )
20-30	82	33.5(6)( $^{+7}_{-5}$ )	37.3(8)( $^{+14}_{-6}$ )	14.7(7)( $^{+2}_{-5}$ )	14.6(28)( $^{+20}_{-27}$ )	-58(1)( $^{+0}_{-0}$ )
20-30	125	22.1(3)( $^{+11}_{-5}$ )	35.0(6)( $^{+15}_{-8}$ )	13.6(5)( $^{+6}_{-3}$ )	11.9(11)( $^{+8}_{-8}$ )	-60(2)( $^{+0}_{-0}$ )
20-30	172	15.2(4)( $^{+10}_{-6}$ )	30.0(6)( $^{+13}_{-9}$ )	12.9(3)( $^{+7}_{-5}$ )	10.3(8)( $^{+11}_{-8}$ )	-42(6)( $^{+1}_{-4}$ )
20-30	221	13.8(6)( $^{+7}_{-7}$ )	26.7(7)( $^{+13}_{-12}$ )	9.8(2)( $^{+5}_{-4}$ )	3.5(8)( $^{+7}_{-3}$ )	-7(3)( $^{+0}_{-1}$ )
25-35	82	29.1(6)( $^{+8}_{-7}$ )	34.4(8)( $^{+10}_{-5}$ )	12.8(7)( $^{+4}_{-3}$ )	17.4(28)( $^{+28}_{-13}$ )	-63(1)( $^{+0}_{-0}$ )
25-35	125	19.4(3)( $^{+11}_{-5}$ )	31.0(6)( $^{+17}_{-9}$ )	12.1(5)( $^{+6}_{-3}$ )	15.2(11)( $^{+13}_{-13}$ )	-66(2)( $^{+0}_{-0}$ )
25-35	172	12.7(2)( $^{+9}_{-5}$ )	27.5(5)( $^{+15}_{-9}$ )	11.1(5)( $^{+8}_{-5}$ )	11.1(8)( $^{+13}_{-8}$ )	-75(7)( $^{+2}_{-2}$ )
25-35	221	10.5(2)( $^{+3}_{-5}$ )	22.8(7)( $^{+8}_{-7}$ )	12.0(6)( $^{+4}_{-4}$ )	6.6(9)( $^{+9}_{-8}$ )	-94(7)( $^{+3}_{-0}$ )
30-45	82	27.0(6)( $^{+11}_{-11}$ )	32.6(8)( $^{+6}_{-8}$ )	11.2(8)( $^{+0}_{-5}$ )	20.2(29)( $^{+30}_{-43}$ )	-69(2)( $^{+0}_{-1}$ )
30-45	125	16.3(3)( $^{+10}_{-3}$ )	26.9(5)( $^{+15}_{-5}$ )	10.6(5)( $^{+6}_{-4}$ )	15.5(11)( $^{+13}_{-11}$ )	-75(2)( $^{+0}_{-1}$ )
30-45	172	11.1(2)( $^{+7}_{-4}$ )	25.5(5)( $^{+15}_{-8}$ )	8.8(5)( $^{+6}_{-4}$ )	10.4(8)( $^{+12}_{-6}$ )	-94(4)( $^{+1}_{-1}$ )

## D.2 Azimuthally dependent

**Table D.5:** The same as table D.4, but for  $\pi^+\pi^+$  pairs.

Centrality (%)	$\bar{k}_t$ (MeV/c)	$\sigma_x^2$ (fm $^2$ )	$\sigma_y^2$ (fm $^2$ )	$\sigma_z^2$ (fm $^2$ )	$\sigma_t^2$ (fm $^2/c^2$ )	$\theta_s$ (deg)
0-10	132	24.3(11)( $^{+1}_{-5}$ )	30.5(12)( $^{+35}_{-7}$ )	12.9(4)( $^{+2}_{-4}$ )	2.9(15)( $^{+5}_{-22}$ )	-18(2)( $^{+0}_{-4}$ )
0-10	175	22.2(8)( $^{+20}_{-14}$ )	26.8(9)( $^{+23}_{-13}$ )	10.9(2)( $^{+9}_{-6}$ )	4.5(9)( $^{+7}_{-8}$ )	-12(1)( $^{+0}_{-1}$ )
0-10	223	22.7(8)( $^{+18}_{-14}$ )	21.9(8)( $^{+18}_{-13}$ )	8.8(1)( $^{+8}_{-6}$ )	0.3(7)( $^{+5}_{-4}$ )	-6(1)( $^{+0}_{-6}$ )
0-10	272	17.1(9)( $^{+10}_{-9}$ )	21.6(9)( $^{+17}_{-10}$ )	7.4(2)( $^{+6}_{-4}$ )	-2.8(7)( $^{+5}_{-3}$ )	-6(1)( $^{+0}_{-1}$ )
10-20	131	22.2(7)( $^{+14}_{-9}$ )	27.3(9)( $^{+16}_{-10}$ )	11.9(5)( $^{+6}_{-6}$ )	9.5(16)( $^{+9}_{-10}$ )	-34(2)( $^{+1}_{-0}$ )
10-20	175	17.8(6)( $^{+12}_{-5}$ )	25.0(7)( $^{+14}_{-6}$ )	10.2(3)( $^{+7}_{-3}$ )	8.1(10)( $^{+7}_{-3}$ )	-24(2)( $^{+0}_{-1}$ )
10-20	223	14.1(6)( $^{+7}_{-4}$ )	25.0(7)( $^{+11}_{-6}$ )	8.9(2)( $^{+4}_{-2}$ )	3.1(8)( $^{+7}_{-2}$ )	-15(2)( $^{+0}_{-0}$ )
20-30	131	18.2(7)( $^{+10}_{-2}$ )	25.1(9)( $^{+17}_{-7}$ )	10.0(7)( $^{+5}_{-8}$ )	12.5(20)( $^{+18}_{-24}$ )	-50(3)( $^{+1}_{-2}$ )
20-30	175	14.0(5)( $^{+7}_{-4}$ )	22.6(6)( $^{+9}_{-5}$ )	9.7(4)( $^{+4}_{-3}$ )	9.4(10)( $^{+11}_{-8}$ )	-32(4)( $^{+1}_{-1}$ )
20-30	238	11.3(5)( $^{+3}_{-4}$ )	19.7(6)( $^{+7}_{-7}$ )	8.5(2)( $^{+2}_{-3}$ )	7.5(8)( $^{+8}_{-5}$ )	-13(4)( $^{+1}_{-1}$ )
25-35	131	18.6(7)( $^{+13}_{-5}$ )	22.8(9)( $^{+11}_{-4}$ )	9.7(9)( $^{+4}_{-5}$ )	13.7(23)( $^{+33}_{-21}$ )	-61(3)( $^{+3}_{-1}$ )
25-35	175	13.7(4)( $^{+8}_{-10}$ )	22.8(7)( $^{+11}_{-11}$ )	11.1(6)( $^{+5}_{-7}$ )	9.5(11)( $^{+14}_{-16}$ )	-56(7)( $^{+3}_{-3}$ )
25-35	193	10.2(3)( $^{+4}_{-3}$ )	21.1(5)( $^{+9}_{-4}$ )	8.6(3)( $^{+2}_{-3}$ )	8.9(7)( $^{+11}_{-7}$ )	-41(8)( $^{+1}_{-4}$ )
30-45	158	12.7(3)( $^{+3}_{-7}$ )	21.6(5)( $^{+4}_{-8}$ )	7.3(4)( $^{+1}_{-4}$ )	12.4(9)( $^{+13}_{-14}$ )	-69(2)( $^{+0}_{-0}$ )
30-45	193	10.7(2)( $^{+5}_{-8}$ )	22.1(6)( $^{+9}_{-11}$ )	8.0(5)( $^{+3}_{-4}$ )	11.5(9)( $^{+11}_{-12}$ )	-79(4)( $^{+0}_{-0}$ )

D. Data summary tables

---

# List of Figures

1.1	Scheme of the evolution of a relativistic heavy-ion collision at SIS energies generated with the transport model SMASH [1] ( <a href="https://smash-transport.github.io/">https://smash-transport.github.io/</a> ). . . . .	3
1.2	Illustration of a heavy-ion collision at SIS energies with long spectator passing times and the typical squeeze-out. Figure taken from [2]. . . . .	5
1.3	The source sizes measured by intensity interferometry are influenced by momentum-space correlations leading to reduced lengths of homogeneity. Figure taken from [3]. . . . .	6
1.4	Illustration of the so-called $m_t$ -scaling: The source radius $R_{\text{inv}}$ inversely scales with the transverse mass of different testing particles. Figure taken from [27]. . . . .	8
2.1	Illustration of measuring two identical particles emitted from locations in a source. When the particles arrive at the detectors $x'_{1,2}$ it is not possible to decide whether they took the paths a) or the paths b), and a superposition of both possibilities must be considered. . . . .	11
2.2	Illustration of the correlation signal at small relative momenta $q$ . For an ideal chaotic bosonic source (red), the probability of registering the pair increases up to two at vanishing $q$ . For a partially coherent source (blue), the correlation signal is reduced. For an ideal coherent source the correlations signal vanishes just as for distinguishable particles. An ideal fermionic source (lower black curve) can be described with coherence parameter $\lambda = -1$ and vanishing probability at $q = 0$ . . . . .	16
2.3	Illustration of the osl coordinate system: 'long' points along the beam axis, 'out' is parallel to the transverse pair momentum $k_t$ of the two particles with momentum $p_1$ and $p_2$ , and 'side' points perpendicularly to the other two components, completing a right-handed orthonormal coordinate system. .	21

## LIST OF FIGURES

---

2.4	Illustration of a relativistic heavy-ion collision creating a particle emitting source (red, in the centre). The impact parameter $b$ points perpendicular to the beam direction $z$ . Both directions span the reaction plane of the collision. A finite value of $b$ causes the source to be more extended in $y$ than in $x$ direction. Figure taken from [57]. . . . .	22
2.5	Scheme of two collision settings: Landau scenario (left) with total stopping of the participants and expanding fireball and Bjorken scenario (right) with partly transparent nuclei and longitudinally extended fireball region. . . . .	25
3.1	Left: Photograph of the HADES setup in operation mode from downstream ( <i>Jan Michael Hosan/HA Hessen Agentur GmbH</i> ). Right: Transverse cross section of the spectrometer with all sub-detectors. Following the beam the components are (i) the target surrounded by the Start and Veto detector, (ii) the Ring Imaging CHerenkov (RICH) detector, (iii) the Mini Drift Chambers (MDC) with the superconducting magnet in between, (iv) the Time-Of-Flight (TOF) wall, RPC and Pre-shower detectors, combined in the Multiplicity Electron Triggering Area (META), and (v) the forward wall. . . . .	27
3.2	Photograph of the segmented Au-target. It consists of 15 gold foils glued on Kapton bands for reducing the effect of small-angle scattering. . . . .	29
3.3	Scheme of the RICH detector. The passing electron (red down-pointing arrow) generates a light cone (blue) inside the radiator gas, which is mirrored onto a panel of photon detectors and appears as a ring. Figure taken from [67]. . . . .	29
3.4	Left: Layout of the magnet spectrometer part of HADES consisting of a superconducting magnet with six coils generating a toroidal magnetic field, two mini drift chambers before (MDC I, MDC II) and two behind (MDC III, MDC IV) the magnet. Right: Section of the hexagonal arrangement of the magnetic coils and the mini drift chambers, including the origin where they were produced. The MDC I chambers were first build at GSI, but later exchanged by chambers built at Forschungszentrum Rossendorf (FZR) due to their high radiation exposure. MDC III chambers, also built in FZR, are in operation from the very beginning. Figures are taken from [63, 67]. . . . .	30

---

LIST OF FIGURES

3.5	Technical illustration of the magnet ILSE (iron less superconducting electromagnet) in direction of the beam (right) and perpendicular from the side (left). Visible are the six coils and on top the supply slots for power supply and liquid helium cooling. Figure taken from [63]. . . . .	31
3.6	Left: Depiction of the transverse section of a smallest drift cell, containing one sense wire in the center (cyan dot), two field wires (red dots) and several cathode wires (dark-green dots). Red curves illustrate the electric field inside the cell. A traversing ionising particle (yellow curve) induces free charges in form of electrons (small green points), which drift in direction of the sense wire (yellow struggled curves) and were amplified in the grey area leading to a measurable signal. Right: Scheme of the six-stacked layers of mini drift chambers within one trapezoidal module with stereo angles of $0^\circ$ , $\pm 20^\circ$ and $\pm 40^\circ$ between the detector-system fixed $x$ axis and the parallel arranged sense wires. Figures are taken from [63, 65]. . . . .	32
3.7	Scheme of the time-of-flight wall TOF with hexagonal symmetry and eight modules per sector, covering the polar angle range from $44^\circ$ to $88^\circ$ . Figure taken from [67]. . . . .	33
3.8	Top: Picture of the layer alignment of the RPCs of one sector. Bottom: Photographs of one RPC cell consisting of three stacked aluminum plates separated by two glass plates. On top the read-out electronics is installed. Figures taken from [64, 69]. . . . .	34
3.9	Cross section of one of the 1024 pads of one module of the hadron-blind Pre-Shower detector. Electrons and positrons generate an electromagnetic shower when passing the lead converters, measured with three drift chambers. Figure taken from [64]. . . . .	35
3.10	Photograph of the Start (left) and the Veto (right) detectors within their supports and a depiction of their orientation in front and behind the gold target. Figure taken from [63]. . .	36
3.11	The forward hodoscope with the arrangement of scintillator cells surrounding the beam axis. Dimensions of the blocks are $4 \times 4 \text{ cm}^2$ (red), $8 \times 8 \text{ cm}^2$ (green) and $16 \times 16 \text{ cm}^2$ (blue). Figure taken from [64]. . . . .	37
3.12	Scheme of the complete HADES DAQ network consisting of several network nodes (violet), read-out moduls (green) and additional front-end modules (grey). All modules are connected via a dedicated network protocol (TrbNet). Data transfer to several servers is streamed via the Gigabit Ethernet. Figure taken from [69]. . . . .	38

## LIST OF FIGURES

---

4.1	Reconstructed event vertices in $x$ and $z$ direction in units of mm. The 15 separated gold segments of the target are clearly visible. . . . .	40
4.2	Mean number of charged pions per event (symbols, averaged per file) compared to the mean value (solid lines) for one day, individually for each sector (different colors in the legend). Dashed lines delineate a $\pm 5\%$ range around the corresponding means, symbols with error bars are outside this range. Figure taken from [75]. . . . .	41
4.3	Distributions of the modelled nuclei A and B, with 197 nucleons each, in the Glauber approach with an impact parameter $b = 6$ fm. The color of the nucleons correspond to the number of inelastic collisions they will experience. Figure taken from [76]. . . . .	43
4.4	Cross section as a function of $N_{\text{hits}}^{\text{TOF+RPC}}$ . Minimum bias (blue) and PT3 (green) data compared to the Glauber MC model (red histogram). Figure taken from [76]. . . . .	44
4.5	Left: Anti-correlation between charged particle multiplicity $N_{\text{hits}}^{\text{TOF+RPC}}$ and impact parameter $b$ delivered by Glauber MC simulations. Right: Distributions of the impact parameter. Colored distributions belong to defined centrality classes (blue: 0 – 10 %, red: 10 – 20 %, green: 20 – 30 %, yellow: 30 – 40 %). Figures taken from [76]. . . . .	45
4.6	Illustration of the event plane reconstruction. The projectile spectators hit the forward wall and the sum of all hits relative to the beam center define the event plane vector $\vec{Q}_{\text{EP}}$ . Figure taken from [2]. . . . .	46
4.7	Distribution of the event plane angle for one day. . . . .	47
4.8	Distribution of the difference between the event plane angles of two sub-events A and B for different centrality classes. . . . .	48
4.9	Flow chart of track reconstruction. Figure taken from [65]. . . . .	51
4.10	Left: Illustration of the vertex finder. Right: Illustration of the use of the drift time for reducing the projected volume and increasing the spatial resolution of the vertex finder procedure. Figure taken from [64]. . . . .	52
4.11	Left: Illustration of the segment finding process. Right: Projection of fired wires in the projection plane with a clear local maximum. Figure taken from [64]. . . . .	53

---

LIST OF FIGURES

4.12 Illustration of the momentum reconstruction. The deflection of the particle in the magnetic field is first approximated by a single kick of the momentum calculated with Equation (4.11). A spline method is used afterwards for solving the equation of motion at some points between the inner and outer segment. This solution is used as input for an iterative Runge-Kutta procedure solving the equation of motion numerically. Figure taken from [64]. . . . .	55
4.13 Scatter plot of particle velocities $\beta$ in dependence of the rigidity $p/Z$ . Black curves show the theoretical loci of several particle species calculated with Equation (4.17). Figure taken from [64]. . . . .	57
4.14 Slice in rigidity $p/Z$ of Figure 4.13. The $\pi^-$ distribution is fitted by a Gaussian distribution. Its mean value follows with high precision the calculated value from Equation (4.17). Figure taken from [64]. . . . .	58
4.15 Possibilities for track candidates sharing same detector hits. One found inner segment can be matched to two different outer segments with two different META hits (A) or even the same META hit (B). The combination of one inner and one outer segment can have two different META hits (C) or, the other way around, two inner segments matched to separately two outer segments share the same META hit (D). Figure taken from [82]. . . . .	59
4.16 Phase-space distribution in reduced transverse mass $m_t - m_0$ and rapidity $y$ relative to mid-rapidity, $y_{\text{cm}} = 0.74$ , of negative (upper panel) and positive (lower panel) pions measured with HADES and summed over all selected events. Dashed black curves are the corresponding polar angles in the laboratory system, gray dashed curves represent the total momentum of the pions. Figure taken from [83]. . . . .	60
4.17 Upper panel: true distribution (black) and mixed distribution (red) of negatively charged pion pairs as function of the invariant relative momentum $q_{\text{inv}}$ for centrality 0-5%. The gray shaded region indicates the range used for normalisation. Lower panel: Corresponding invariant correlation function, Equation (4.20), without further corrections. . . . .	62
4.18 $\pi^+\pi^+$ pair distribution from UrQMD as a function of $q_{\text{out}}$ and $q_{\text{long}}$ for small values of $q_{\text{side}} < 10 \text{ MeV}/c$ , ignoring the permutability of particles 1 and 2. The red dashed line depicts the edge of the hemisphere with most of the entries. Data shown for exemplary chosen pair transverse momentum range of 200 to 300 $\text{MeV}/c$ and events within the centrality class 0-10 %. . . . .	65

## LIST OF FIGURES

---

4.19	Top: Same as Figure 4.17, but for another data sample. Middle: Corresponding invariant correlation function (4.20) for experimental data (blue) and UrQMD+HGEANT simulation data (red). Bottom: Experimental correlation function divided by the simulated correlation function, yielding the so-called double-ratio correlation function. The physical correlations not included in the simulations remain at low values of $q_{\text{inv}}$ . . . . .	68
4.20	Correlation function equivalent to Equations (4.19) and (4.20), but as function of the angle differences $\Delta\phi$ and $\Delta\cos(\theta)$ for UrQMD+HGeant simulation data. . . . .	69
4.21	Examples for opening angle distributions of the correlation function from CERES [92] (top panels) and PHENIX [93] (bottom panels). For details see the text. . . . .	70
4.22	Illustration of the considered pair topologies following [92]. Left: tracks which possibly tend to cross each other are referred as cowboys (CB). Right: tracks with increasing distance over flight time and no crossing are referred as sailors (SA). . . . .	71
4.23	True pair distribution $\frac{dN}{d\Delta\phi d\Delta\cos\theta}$ (left) and correlation function equivalent to Equations (4.19) and (4.20) (right) as a function of the opening angle differences $\Delta\phi$ and $\Delta\cos(\theta)$ for data from UrQMD+HGeant. Top panels represent pairs with cowboy (CB) topology, and bottom panels represent pairs with saylor (SA) topology following Equation (4.25). . . . .	72
4.24	True (left) and mixed (right) pair distribution $\frac{dN}{dN_{\text{wires}}^{\text{shared}} dq_{\text{inv}}}$ in dependence of $q_{\text{inv}}$ and number of shared wires $N_{\text{wires}}^{\text{shared}}$ , cf. the text. . . . .	74
4.25	Correlation function (4.20) for several conditions on the number of shared wires $N_{\text{wires}}^{\text{shared}}$ : no restriction (black), at most two (violet) or one (blue) and without shared wires (red). . . . .	75
4.26	Left: Illustration of acceptable layers (marked by 'ok'), where both tracks of the pair have a registered hit (black circles), contributing to $N_{\text{layers}}^{\text{both}}$ as described in the text. Right: True pair distribution over the $q_{\text{inv}}\text{-}N_{\text{layers}}^{\text{both}}$ plane for the selection $N_{\text{wires}}^{\text{shared}} = 0$ . . . . .	76
4.27	Correlation function (4.20) for several conditions on the number of layers with hits from both tracks $N_{\text{layers}}^{\text{both}}$ for $N_{\text{wires}}^{\text{shared}} = 0$ : no further condition (violet), at least 22 (blue) and 24 (red) counted layers. Black symbols show the initial case without restrictions on $N_{\text{wires}}^{\text{shared}}$ . . . . .	77

4.28 Top: Illustration of the sliding wire window (SWW) with width of three (left) and five (right) wires. A registered hit of track one (red circle) in one of the parallel aligned wires of one MDC layer restricts track two not to have a fired wire in a symmetric window around this wire (marked with crosses). Bottom: Invariant correlation function (4.20) for different selections: no restriction (black),  $N_{\text{wires}}^{\text{shared}} = 0$  (blue) and in addition SWW of size three (red, left panel) or SWW of size five (red, right panel), respectively. . . . . 78

4.29 A zoom of the correlation function as a function of  $q_{\text{inv}}$ , at higher values of  $q_{\text{inv}}$ , for  $p_{t,12} \in [500, 600] \text{ MeV}/c$ . The Bose-Einstein signal is visible up to  $100 \text{ MeV}/c$ . Top: no condition on primary vertex in transverse direction; for larger relative momenta a linear trend with non-zero positive slope is observed. Bottom: primary vertex differences in  $x$  and  $y$  direction of mixed pairs required to be less than  $0.2 \text{ mm}$ ; no slope at high relative momenta visible. The black dashed-dotted curves are parametrisations for guiding the eyes. . . . . 80

4.30 Top: true (black) and mixed (red) yields of pion pairs for  $p_{t,12} \in [200, 300] \text{ MeV}/c$  as a function of  $q_{\text{inv}}$ . The shaded region marked by 'N' depicts the region used for the normalisation. Bottom: corresponding correlation function, Equation (4.20), (red circles) fitted with Equation (4.26) (red line). The green dashed curve represents the separable final-state interaction Coulomb part. The black squares correspond to the Coulomb-corrected correlation function. The black dotted curve shows the fit function, Equation (4.26), after the Coulomb correction. The blue long-dashed curve gives the pure Bose-Einstein part, Equation (4.27), of the correlation function. . . . . 81

4.31 Scheme of the procedure used for determining the relative momentum resolution. Pion pairs are generated with the Pluto event generator being distributed in phase space comparable to the experimental distributions. The pairs are then tracked through HGevent to simulate acceptance, resolution, and efficiency of the detector. . . . . 84

4.32 PLUTO phase space distribution of one of the pions for one million pion pairs. The value of the fireball temperature  $T$  is set to  $200 \text{ MeV}$ , the polar angle is restricted to  $[16^\circ, 88^\circ]$ , the transverse momentum to values larger than  $50 \text{ MeV}/c$  and the total momentum to values smaller than  $1 \text{ GeV}/c$ . The invariant relative momentum of all pairs is  $30 \text{ MeV}/c$  . . . . . 84

## LIST OF FIGURES

---

4.33	Relative momentum distributions as a function of $q_{\text{inv}}$ (top row), $q_{\text{out}}$ (second row), $q_{\text{side}}$ (third row) and $q_{\text{long}}$ (bottom row) for pion pairs generated with PLUTO with initial relative momentum of $q_{\text{inv}} = 30 \text{ MeV}/c$ after tracking through HGeant. The distributions are plotted for different intervals of $p_{t,12}$ (increasing from left to right) and fitted with Gaussians (red curves). . . . .	85
4.34	Relative momentum resolution in dependence of $q_{\text{inv}}$ (top row), $q_{\text{out}}$ (second row), $q_{\text{side}}$ (third row) and $q_{\text{long}}$ (bottom row) for different intervals of $p_{t,12}$ (increasing from left to right) for $\pi^-\pi^-$ . Red curves are parametrisations with a polynomial of second order. . . . .	86
4.35	Source function $S(r)$ constructed using the invariant correlation function and the imaging code <i>HBTprogs</i> from [98–100]. Results are for 5 % most central events and different intervals of pair transverse momentum. Blue curves represent Gaussian fits using the range of $r \in [0, 15] \text{ fm}$ , red curves are Gaussian distributions using the parameters from fits with Equation (4.26) applied directly to the invariant correlation function Equation (4.20). . . . .	90
4.36	Illustration of the dependence of $R_{\text{side}}$ and $R_{\text{out}}$ on the azimuthal angle of the pair relative to the event plane $\Phi =  \phi - \phi_{\text{RP}} $ (from left to right $0^\circ$ , $45^\circ$ and $90^\circ$ ), following from the initial elliptic overlap region perpendicular to the beam direction (yellow shaded) of the Au+Au collision at finite impact parameter. For $\Phi = 0^\circ$ , $R_{\text{side}}$ ( $R_{\text{out}}$ ) has a maximum (minimum) and decreases (increases) until $\Phi = 90^\circ$ , where it has a minimum (maximum) and the other way around for larger angles. . . . .	91
4.37	Illustration of the finite bin width effect acting on an oscillating function. The harmonic oscillation $\cos(2x)$ (red solid curve) is sampled by four (eight) equal sized intervals in the upper (lower) panel within a total range of $2\pi$ . The centers of the intervals (black dots) are used for reconstructing the oscillation (red dashed curves), which leads to a reduction of the amplitudes, taken into account by Equation (4.40). . . . .	93
4.38	Event plane resolution $F_n$ of 1 <sup>st</sup> (red) and 2 <sup>nd</sup> (blue) order calculated using Equations (4.7) and (4.8). . . . .	94
4.39	Left: Illustration of the finite tilt angle $\theta_s$ of the ellipsoid within the reaction plane, defined between the $z$ axis of the ellipsoid and the beam axis (long). Right: As consequence of the finite tilt angle, the smaller semi-axis tends to be measured too large and the larger semi-axis tends to be measured too small. . . . .	95

---

LIST OF FIGURES

5.1	The correlation function $C(q_{\text{inv}})$ , Equation (4.20), for $\pi^-\pi^-$ (left panels) and $\pi^+\pi^+$ (right panels) and transverse pair momenta $p_{t,12}$ from 100 to 500 MeV/c (increasing from top to bottom) in the 0 – 10 % centrality class. Black circles are experimental data, the red solid curve is a fit with Equation (4.26) containing the BE part (dotted black curve) and the Coulomb part (dashed green curve). . . . .	98
5.2	Same as Figure 5.1, but for $p_{t,12}$ from 500 to 900 MeV/c (increasing from top to bottom). . . . .	99
5.3	One-dimensional projections of the Coulomb-corrected three-dimensional correlation function $C(q_{\text{out}}, q_{\text{side}}, q_{\text{long}})$ for $\pi^-\pi^-$ and $p_{t,12}$ from 0 to 400 MeV/c in the 0 – 10 % centrality class. The two other components of $\vec{q}$ are integrated over the interval 0 to 12 MeV/c. The red curves depict Gaussian fits. . . . .	100
5.4	Same as Figure 5.3, but for $p_{t,12}$ from 400 to 800 MeV/c . . .	101
5.5	Same as Figure 5.3, but for $\pi^+\pi^+$ and $p_{t,12}$ from 100 to 800 MeV/c . . . . .	102
5.6	Two-dimensional projections of the three-dimensional correlation function $C(q_{\text{out}}, q_{\text{side}}, q_{\text{long}})$ for $\pi^-\pi^-$ and $p_{t,12}$ from 0 to 400 MeV/c for 0 – 10 % centrality (left: $q_{\text{out}}\text{-}q_{\text{side}}$ plane, middle: $q_{\text{out}}\text{-}q_{\text{long}}$ plane, right: $q_{\text{side}}\text{-}q_{\text{long}}$ plane). The third component of $\vec{q}$ is integrated from 0 to 12 MeV/c. . . . .	103
5.7	Same as Figure 5.6, but for $p_{t,12}$ from 400 to 800 MeV/c . . .	104
5.8	Same as Figure 5.6, but for $\pi^+\pi^+$ and $p_{t,12}$ from 100 to 400 MeV/c. . . . .	105
5.9	Same as Figure 5.8, but for $p_{t,12}$ from 400 to 800 MeV/c . . .	106
5.10	Two dimensional projections of the three-dimensional correlation function $C(q_{\text{out}}, q_{\text{side}}, q_{\text{long}})$ for $\pi^-\pi^-$ and $p_{t,12}$ integrated from 200 to 500 MeV/c for 0 – 10 % centrality for mean azimuthal angles $\Phi = \{0^\circ, 45^\circ, 90^\circ, 135^\circ\}$ (from top to bottom) relative to the event plane. The third component of $\vec{q}$ is integrated over 0 to 12 MeV/c. . . . .	107
5.11	Same as Figure 5.10, but for mean azimuthal angles $\Phi = \{180^\circ, 225^\circ, 270^\circ, 315^\circ\}$ (from top to bottom) relative to the event plane. . . . .	108
5.12	$R_{\text{inv}}$ (top left), $R_{\text{out}}$ (top right), $R_{\text{side}}$ (bottom left) and $R_{\text{long}}$ (bottom right) for $\pi^-\pi^-$ and centrality classes 0 – 10 % (blue circles), 10 – 20 % (green up-pointing triangles), 20 – 30 % (violet down-pointing triangles), 30 – 40 % (brown boxes) in dependence on $m_t = (k_t^2 + m_\pi^2)^{1/2}$ . Error bars contain only statistical uncertainties. . . . .	109
5.13	Same as Fig. 5.12, but for $\pi^+\pi^+$ . . . . .	110

## LIST OF FIGURES

---

5.14  $\lambda$  parameters from fits of Equation (4.26) to  $C(q_{\text{inv}})$  (left) and Equation (4.28) to  $C(q_{\text{out}}, q_{\text{side}}, q_{\text{long}})$  (right) as a function of  $p_{t,12}$  for  $\pi^-\pi^-$  (black boxes) and  $\pi^+\pi^+$  (red circles) for 0 – 10 % centrality. . . . . 111

5.15  $R_{\text{inv}}$  (black circles),  $R_{\text{out}}$  (red up-pointing triangles),  $R_{\text{side}}$  (green down-pointing triangles) and  $R_{\text{long}}$  (blue boxes) for  $\pi^-\pi^-$  (left panel) and  $\pi^+\pi^+$  (right panel) for  $p_{t,12}$  from 200 to 300 MeV/c (upper panels), 300 to 400 MeV/c (middle panels), 400 to 500 MeV/c (lower panels), as a function of the cubic root of the number of participants,  $A_{\text{part}}^{1/3}$ . Dashed lines are linear regressions to the data. Error bars contain only statistical uncertainties. . . . . 112

5.16 Cross-term  $R_{\text{out long}}^2$  from Equation (4.31) as a function of pair transverse momentum for 0 – 10 % centrality for  $\pi^-\pi^-$  (filled symbols) and  $\pi^+\pi^+$  (open symbols). Black circles represent the rapidity window  $y_{12} \in [0.39, 1.09]$ , grey up-pointing triangles  $y_{12} \in [0.29, 0.69]$  and brown down-pointing triangles  $y_{12} \in [0.79, 1.19]$ , respectively. . . . . 113

5.17 Correlation coefficient  $\rho_{\text{ol}}$ , defined in Equation (2.44), and the mean value of the chosen rapidity window (right scale) for  $\pi^-\pi^-$  (left panel) and  $\pi^+\pi^+$  (right panel) as a function of pair transverse momentum for 0 – 10 % centrality. Red squares represent fits without the cross-term  $R_{\text{out long}}^2$ ; other symbols and colors as in Figure 5.16. The blue curves belong to the rapidity intervals  $y_{12} \in [0.29, 0.69]$  (dashed),  $y_{12} \in [0.39, 1.09]$  (solid) and  $y_{12} \in [0.79, 1.19]$  (dashed-dotted). . . . . 114

5.18 Systematic variations of the HBT radius parameters of the azimuthally integrated analysis in dependence of  $p_{t,12}$  for  $\pi^-\pi^-$  and 0 – 10 % centrality. In addition to the standard configuration (red filled boxes) the following settings are chosen: fit range of  $q_{\text{inv}}$  in units of MeV/c changed to [10,60] (open boxes), [10,100] (filled circles), [6,60] (open circles), [6,100] (filled up-pointing triangles), [6,32] (open up-pointing triangles), [10,32] (filled down-pointing triangles), where for the latter two ones an explicit condition is set on the second normalisation constant  $C = 1$ , see also Table 5.1. Open down-pointing triangles (open diamonds) denote a changed pair rapidity interval of [0.39,0.74] ([0.74,1.09]). Filled green diamonds belong to an increased sliding wire window (SWW) of size 5, see Section 4.3.4. . . . . 116

5.19 Same as Figure 5.18, but for  $\pi^+\pi^+$ . . . . . 117

5.20 Same as Figure 5.18, but for the parameters  $\lambda_{\text{inv}}$  (left panels) and  $\lambda_{\text{osl}}$  (right panels).  $\pi^-\pi^-$  ( $\pi^+\pi^+$ ) data is plotted in the top (bottom) row. . . . . 118

5.21 Source radii  $R_{\text{inv}}$  (top left),  $R_{\text{out}}$  (top right),  $R_{\text{side}}$  (center left),  $R_{\text{long}}$  (center right), as well as parameters  $\lambda_{\text{inv}}$  (bottom left) and  $\lambda_{\text{osl}}$  (bottom right) as function of  $m_t$  for  $\pi^-\pi^-$  (black boxes) and  $\pi^+\pi^+$  (red circles) in 0 – 10 % centrality. Error bars contain statistical errors, hatched bands denote systematic uncertainties. Blue dashed curves represent radii of constructed fiducial  $\tilde{\pi}^0\tilde{\pi}^0$ . . . . . 120

5.22 Source radii  $R_{\text{inv}}$  (top left),  $R_{\text{out}}$  (top right),  $R_{\text{side}}$  (bottom left) and  $R_{\text{long}}$  (bottom right) for centrality classes 0 – 10 % (red circles), 10 – 20 % (violet boxes), 20 – 30 % (blue up-pointing triangles), 30 – 40 % (green down-pointing triangles) in dependence on  $m_t = \sqrt{k_t^2 + m_\pi^2}$  for constructed fiducial  $\tilde{\pi}^0\tilde{\pi}^0$ . Dashed curves represent parametrisations with Equation (5.3). . . . . 121

5.23 Fit parameters  $R_{i,0}$  (left panel) and  $\alpha_i$  (right panel) from Equation (5.3) applied to the data in Figure 5.22 in dependence on  $A_{\text{part}}^{1/3}$ ,  $i = \{\text{inv} \text{ (black circles)}, \text{out} \text{ (red up-pointing triangles)}, \text{side} \text{ (green down-pointing triangles)}, \text{long} \text{ (blue boxes)}\}$ . The dashed lines are straight-line fits to the data points. . . . . 122

5.24 Illustration of the interplay of thermal motion and collective flow. Figure taken from [107]. See text for details. . . . . 123

5.25 Acceptance- and efficiency-corrected transverse mass spectra of  $\pi^-$  (left) and  $\pi^+$  (right) at mid-rapidity. Blue curves represent a double-slope Boltzmann fit, red (green) lines denote the fraction of this fit function with larger (smaller) slope parameter. Figure taken from [83]. . . . . 124

5.26 Illustration of the impact of a finite pion mean free path  $\lambda_{\text{mfp}}$  on the measurement of the source size. Only pions emitted from the sickle-like red area are detected, decreasing mainly the measured width in 'out' direction and increasing obviously the Gaussian width in 'side' direction. . . . . 125

## LIST OF FIGURES

---

5.27 Excitation function of the HBT radius parameters $R_{\text{out}}$ (upper panel), $R_{\text{side}}$ (central panel), and $R_{\text{long}}$ (lower panel) for $\pi^-\pi^-$ and $\pi^+\pi^+$ with $m_t = 300$ MeV in central collisions of Au + Au, Pb + Au or Pb + Pb. Squares represent data by ALICE ( $\pi^+\pi^+$ ) [18], full triangles STAR ( $\pi^-\pi^-+\pi^+\pi^+$ ) [17], diamonds are for CERES ( $\pi^-\pi^-+\pi^+\pi^+$ ) [15], open triangles are for NA49 ( $\pi^-\pi^-$ ) [16], open circles are $\pi^-\pi^-$ data by E895 [13], and open (full) crosses involve $\pi^-\pi^-$ ( $\pi^+\pi^+$ ) data of E866 [14], respectively. HADES data for $\pi^-\pi^-$ ( $\pi^+\pi^+$ ) are given as open (full) stars. . . . .	127
5.28 Same as Figure 5.27, but for the approximate freeze-out volume $V_{\text{fo}}$ according to Equation (5.6). . . . .	128
5.29 Same as Figure 5.27, but for the quantity $R_{\text{out}}^2 - R_{\text{side}}^2$ . . . . .	129
5.30 HBT radius parameters $R_{\text{out}}^2$ (top left), $R_{\text{side}}^2$ (middle left), $R_{\text{long}}^2$ (bottom left), $R_{\text{out side}}^2$ (top right), $R_{\text{out long}}^2$ (middle right) and $R_{\text{side long}}^2$ (bottom right) resulting from the fit of Equations (4.28) and (4.31) to the three-dimensional correlation functions for $\pi^-\pi^-$ for different values of $k_t$ and centrality 10 – 30 % as a function of $\Phi$ . Error bars include only statistical uncertainties. Full curves represent global fits with Equation (4.38). . . . .	131
5.31 Same as Figure 5.30, but for $\pi^+\pi^+$ . . . . .	132
5.32 The ten independent fit parameter $S_{\mu\nu}$ from Equation (4.38) as a function of pair transverse momentum $p_{t,12}$ for 10 – 30 % centrality for $\pi^-\pi^-$ . Temporal components are on the left column, diagonal (non-diagonal) pure spatial components on the middle (right) column. Open circles are the direct outcome from the fits, full circles are EP-resolution corrected according to Equation (4.40). . . . .	133
5.33 Same as Figure 5.32, but for $\pi^+\pi^+$ . . . . .	134
5.34 The spatial semi-axes (left panels), the tilt angle w.r.t. the beam axis in the reaction plane (Eq. (4.44), top right), the $xy$ -eccentricity (full, Eq. (4.46)) and the $zy$ -eccentricity (empty, Eq. (4.47), middle right) and the emission duration $\sigma_t$ (bottom right) of the Gaussian emission ellipsoid of $\pi^-\pi^-$ (boxes) and $\pi^+\pi^+$ (circles) as function of transverse momentum for 10 – 30 % centrality. Error bars include only statistical uncertainties. The dotted line (to be compared to $\varepsilon_{xy}$ ) represents the initial nucleonic eccentricity derived from Glauber simulations. . . . .	136

5.35 The spatial principal axes (left column), the tilt angle w.r.t. the beam axis in the reaction plane (see Equation (4.44), top right), the  $xy$ -eccentricity (empty) and the  $zy$ -eccentricity (filled symbols, Equations (4.46) and (4.47), right middle) and the emission duration  $\sigma_t$  (bottom right) of the Gaussian emission ellipsoid for  $\pi^-\pi^-$  as function of  $\sqrt{s_{\text{NN}}}$  for semi-peripheral Au + Au collisions. Circles represent data of E895 at AGS [19] for 7.4 – 30 % centrality at average  $k_t$  of 110 MeV/c, HADES data interpolated to this value of  $k_t$  using the data of Figure 5.34 is given by stars. Boxes represent HADES interpolated data at  $k_t = 150$  MeV/c. Error bars include only statistical uncertainties. . . . . 138

5.36 Excitation function of the approximate  $\pi^-\pi^-$  freeze-out eccentricity for semi-peripheral Au + Au, Pb + Au, or Pb + Pb collisions. Stars are HADES  $\pi^-\pi^-$  data for three different transverse momentum regions with average values of  $\bar{k}_t = 110$ , 230, and 260 MeV/c. Filled (open) symbols represent  $\varepsilon_{zy}$  ( $\varepsilon_{xy}$ ); for details see the text. The circles, diamonds, triangles, and squares are corresponding data by E895 at AGS [19], CERES at SPS [20], STAR at RHIC [17], and ALICE at LHC [21], respectively. The arrow on the ordinate denotes the approximate (not constant) value of  $\varepsilon_{\text{ini}}$ , the dashed curves are for guiding the eyes without physical motivation. Error bars include only statistical uncertainties. . . . . 140

5.37 Excitation function of the squared emission duration, either directly taken from the corresponding fit parameter of the spatial correlation tensor,  $\sigma_t^2 = S_{00}$  (cf. Equation (4.38)), or derived from the difference of the 'out' and 'side' radii,  $(\Delta\tau)^2 = (R_{\text{out}}^2 - R_{\text{side}}^2)/(\beta_t^2)$ , for semi-peripheral (10 – 30 %) Au + Au, Pb + Au, or Pb + Pb collisions. Stars are HADES  $\pi^-\pi^-$  data of  $\sigma_t^2$  for three different transverse momentum regions with average values of  $\bar{k}_t = 110$ , 230, and 310 MeV/c. The circles are corresponding  $\sigma_t^2$  data by E895 at AGS [19]. The diamond, triangles and square represent data of  $(\Delta\tau)^2$  by CERES at SPS [20], STAR at RHIC [17], and ALICE at LHC [21], respectively. Error bars include only statistical uncertainties. . . . . 141

5.38 Available published and preliminary data for the tilt angle  $\theta_s$  in dependence on  $p_{t,12}$  for semi-peripheral collisions of Au+Au. Error bars include only statistical uncertainties. . . . . 142

5.39 Excitation function of the volume of homogeneity  $V'_{\text{fo}}$  according to Equation (5.8) as a function of  $\sqrt{s_{\text{NN}}}$ . Symbols and colors are the same as in Figure 5.37. Error bars include only statistical uncertainties. . . . . 143

## LIST OF FIGURES

---

5.40 Excitation function of the semi-axes  $\sigma_x$  (upper panel),  $\sigma_y$  (middle panel) and  $\sigma_z$  (lower panel) as a function of  $\sqrt{s_{\text{NN}}}$ . Symbols and colors are the same as in Figure 5.37. Values are taken from Figure 5.35 (Equation (4.51)) for  $\sqrt{s_{\text{NN}}}$  lower (higher) than 5 GeV. Dashed guiding-eye curves represent trends if possible tilt angles  $\theta_s$  are taken into account. Error bars include only statistical uncertainties. . . . . 144

5.41 The spatial semi-axes (left columns), the tilt angle w.r.t. the beam axis in the reaction plane (Equation (4.44), top right), the  $xy$ -eccentricity (Equation (4.46), right middle) and the  $zy$ -eccentricity (Equation (4.47), bottom right) of the Gaussian emission ellipsoid of  $\pi^-\pi^-$  as function of transverse momentum for 0 – 10 % (circles), 10 – 20 % (boxes), 20 – 30 % (up-pointing triangles), 25 – 35 % (diamonds), and 30 – 45 % (down-pointing triangles), respectively. Error bars include only statistical uncertainties. Dotted lines represent the initial nucleonic eccentricities for the corresponding centrality classes derived from Glauber simulations. . . . . 147

5.42 Same as Figure 5.41, but for  $\pi^+\pi^+$ . . . . . 148

5.43 Final eccentricity  $\varepsilon_{\text{final}}$  ( $xy$ -eccentricity) plotted against initial nucleonic eccentricity  $\varepsilon_{\text{ini}}$  derived from Glauber simulations for different values of pair transverse momenta of negatively charged pion pairs. The dashed line depicts  $\varepsilon_{\text{final}} = \varepsilon_{\text{ini}}$ . Error bars include only statistical uncertainties. . . . . 149

5.44 Tilt angle  $\theta_s$  in dependence on the impact parameter  $b$  derived from Glauber simulations for different values of pair transverse momenta. Filled (open) crosses denote  $\pi^-\pi^-$  ( $\pi^+\pi^+$ ) pairs; for better visibility data points are shifted slightly to the right (left). . . . . 150

5.45 Comparison of the freeze-out volumes  $V_{\text{fo}}$  calculated with Equation (5.8) (full symbols) and using the azimuthally integrated approximation given by Equation (5.6) (empty symbols) for different centralities (top left: 0 – 10 %, top right: 10 – 20 %, bottom left: 20 – 30 %, bottom right: 30 – 40 %) for  $\pi^-\pi^-$  (black boxes) and  $\pi^+\pi^+$  (red circles) in dependence on pair transverse momentum. . . . . 152

5.46 Temporal ( $S_{00}$ , respectively  $\sigma_t^2$ ) and spatio-temporal components ( $S_{01}$ ,  $S_{02}$ ,  $S_{03}$ ) of fits with Equation (4.38) to the six freeze-out variances  $R_{ij,i\neq j}^2$  ( $i, j = \text{'out', 'side', 'long'}$ ) for  $\pi^-\pi^-$  in dependence on pair transverse momentum for centralities of 0 – 10 % (circles), 10 – 20 % (boxes), 20 – 30 % (up-pointing triangles), 25 – 35 % (diamonds) and 30 – 45 % (down-pointing triangles). Error bars include only statistical uncertainties. . . . . 153

---

LIST OF FIGURES

5.47 Same as Figure 5.46, but for $\pi^+\pi^+$ . . . . .	154
B.1 HBT radius parameters and $\lambda_{\text{osl}}$ of the azimuthally integrated analysis in dependence on $p_{t,12}$ for $\pi^-\pi^-$ and 0 – 10 % centrality and different intervals of pair rapidity: [0.29,0.69] (grey up-pointing rectangles), [0.39,1.09] (black circles), [0.79,1.19] (brown down-pointing rectangles). Red boxes show results at mid-rapidity setting explicitly $R_{\text{out long}}^2 = 0$ . Error bars contain only statistical uncertainties. . . . .	169
B.2 Same as Figure B.1, but for $\pi^+\pi^+$ . . . . .	170
B.3 HBT radius parameters and $\lambda$ parameters of the azimuthally integrated analysis in dependence on $p_{t,12}$ for $\pi^-\pi^-$ (black boxes) and $\pi^+\pi^+$ (red circles) and 0 – 10 % centrality. Open symbols represent reversed-field data (magnetic field with the same strength, but opposite direction), filled symbols display data for normal magnetic field configuration. Error bars contain only statistical uncertainties. . . . .	171
B.4 Effective Coulomb potentials extracted with Eq. (5.2) using $R_{\text{inv}}$ (black circles), $R_{\text{out}}$ (red boxes), $R_{\text{side}}$ (green up-pointing triangles) and $R_{\text{long}}$ (blue down-pointing triangles) for centralities of 0 – 10 % (top right), 10 – 20 % (top left), 20 – 30 % (bottom left) and 30 – 40 % (bottom right), respectively. Error bars contain only statistical uncertainties. . . . .	172
B.5 Applying Equation (5.2) to the calculated curves of $R_{\text{side}}$ from [50] (top and bottom left). Red circles correspond to a mean radial-flow velocity $\langle\beta\rangle = 0.32$ , green crosses to $\langle\beta\rangle = 0.5$ , and blue boxes represent the case without radial flow. Data points were extracted with <i>WebPlotDigitizer</i> ( <a href="https://apps.automeris.io/wpd/">https://apps.automeris.io/wpd/</a> ). The initial Gaussian radius is $R_0 = 4.47$ fm, and the corresponding initial Coulomb potential is 26.4 MeV. The extracted effective Coulomb potentials $V_{\text{eff}}$ are exhibited in the bottom right. . . . .	173
B.6 Comparing calculations of $R_{\text{side}}$ from [50] to experimental data of Figure 5.21. Calculated values of [50] (blue curves) are scaled with $R_0 = 4.47$ fm ( $R_0 = 5.5$ fm) in the left (right) panel. . . . .	174

## LIST OF FIGURES

---

B.7 The spatial principal axes (left column), the tilt angle w.r.t. the beam axis in the reaction plane (Equation (4.44), top right), the $xy$ eccentricity (Equation (4.46), middle right) and the $yz$ eccentricity (Equation (4.46), bottom right) of the Gaussian emission ellipsoid of $\pi^-\pi^-$ as function of pair transverse momentum for 24 – 34 % centrality. Data of standard intervals of $p_{t,12}$ (black boxes) and that shifted by 50 MeV/c (red circles) is separated. Error bars include statistical uncertainties only. The dotted line depicts the initial nucleon eccentricity from Glauber simulations. . . . .	176
B.8 Same as Figure B.7, but for 26 – 36 % centrality. . . . .	177
B.9 Same as Figure B.7, but for 26 – 36 % centrality and the alternative scenario described in the text. . . . .	178
B.10 Tilt angle $\theta_s$ in dependence of the impact parameter $b$ , the latter one derived from Glauber simulations, for $\pi^-\pi^-$ pairs and different values of pair transverse momenta. Left panel represents the standard scenario, while in the right panel the arrangement of the data follows an alternative scenario with details are given in the text. Error bars include only statistical uncertainties. . . . .	179
B.11 Final eccentricity $\varepsilon_{\text{final}}$ ( $xy$ eccentricity) plotted against initial nucleon eccentricity $\varepsilon_{\text{ini}}$ derived from Glauber simulations for different values of pair transverse momenta of negatively charged pion pairs. Left panel represents the standard scenario, while in the right panel the arrangement of the data follows an alternative scenario with details are given in the text. The dashed line denotes $\varepsilon_{\text{final}} = \varepsilon_{\text{ini}}$ . Error bars include only statistical uncertainties. . . . .	179
B.12 Constructed charge-sign corrected temporal and spatial variances according to Equation (B.1) for different centralities in dependence on $p_{t,12}$ : $\sigma_t^2$ (top left), $\sigma_x$ (top right), $\sigma_y$ (bottom left) and $\sigma_z$ (bottom right). Error bars include only statistical uncertainties. . . . .	180
B.13 Final eccentricity $\varepsilon_{xy}$ in dependence on $p_{t,12}$ for $\pi^-\pi^-$ for 10 – 30 % centrality. Filled (open) brown circles represent $\varepsilon_{xy}$ ( $\varepsilon_{zy}$ ) calculated with Equation (4.46) (Equation (4.47)). Green (blue) boxes are for the values calculated with Equation (4.52) (Eq. (4.53)). The black dashed line gives the initial eccentricity $\varepsilon_{\text{ini}}$ determined from GlauberMC simulations. . .	181
B.14 $\sigma_x$ ( $\sigma_z$ ) of $\pi^-\pi^-$ pairs as a function of $\sqrt{s_{\text{NN}}}$ for $\bar{k}_t = 310$ MeV/c and 10 – 30 % centrality. Red dashed-dotted curves indicate the correct trends when determining $\theta_s$ and performing a major-axis transformation. Blue dashed curves show the trends obtained when ignoring a finite tilt angle. . . . .	182

# List of Tables

4.1	Centrality classes used in the azimuthally integrated analysis, corresponding boundary values of the charged particle multiplicity, correlated mean value of the impact parameter, and mean number of participating nucleons in Au+Au collisions at $1.23A$ GeV. . . . .	49
4.2	Centrality classes used in the azimuthally dependent analysis, mean number of the impact parameter, the number of participants, and the event plane resolutions for the first and second order Fourier coefficients. . . . .	49
5.1	Fit range variations in Equations (4.26) and (4.28) and possible constraints as well for generating Figures 5.18 to 5.20, used for systematic error investigations. In the three-dimensional case, $q_{\text{inv}}$ is determined by Equation (4.29). . . . .	115
D.1	Source parameters resulting from fits with Equations (4.26) and (4.28) for $\pi^-\pi^-$ pairs in dependence on centrality and average transverse momentum $\bar{k}_t$ . Values in the 1st (2nd) brackets represent the corresponding statistical (systematic) errors in units of the last digit of the respective quantity. . .	189
D.2	The same as table D.1, but for $\pi^+\pi^+$ pairs. . . . .	190
D.3	The same as table D.1, but for constructed fiducial $\tilde{\pi}^0\tilde{\pi}^0$ pairs without systematic uncertainties and replacing the columns of the $\lambda$ parameters by the effective potentials $V_{\text{eff}}$ . . . . .	191
D.4	Source extensions in the $xyz$ -coordinate system of the emission ellipsoid and the corresponding tilt angles $\theta_s$ resulting from fits with Equation (4.44) for $\pi^-\pi^-$ pairs in dependence on centrality and average transverse momentum $\bar{k}_t$ . Values in the 1st (2nd) brackets represent the corresponding statistical (systematic) errors in units of the last digit of the respective quantity. . . . .	192
D.5	The same as table D.4, but for $\pi^+\pi^+$ pairs. . . . .	193



# Bibliography

- [1] J. Weil et al. “Particle production and equilibrium properties within a new hadron transport approach for heavy-ion collisions”, *Phys. Rev. C* 94 (2016), 054905.
- [2] B. Kardan. “Collective flow and correlations measurements in Gold-Gold collisions at 1.23 AGeV with HADES”. To be published (2021). PhD thesis. Goethe-Universität, Frankfurt (Main).
- [3] M. A. Lisa et al. “Femtoscopy in relativistic heavy ion collisions”, *Ann. Rev. Nucl. Part. Sci.* 55 (2005), 357–402.
- [4] R. Hanbury Brown and R. Q. Twiss. “A test of a new type of stellar interferometer on Sirius”, *Nature* 178 (1956), 1046–1048.
- [5] G. Goldhaber et al. “Pion-pion correlations in antiproton annihilation events”, *Phys. Rev. Lett.* 3 (1959), 181–183.
- [6] G. Goldhaber et al. “Influence of Bose-Einstein statistics on the anti-proton proton annihilation process”, *Phys. Rev.* 120 (1960), 300–312.
- [7] G. I. Kopylov and M. I. Podgoretsky. “Correlations of identical particles emitted by highly excited nuclei”, *Sov. J. Nucl. Phys.* 15 (1972), 219–223. [*Yad. Fiz.* 15 (1972), 392].
- [8] G. I. Kopylov and M. I. Podgoretsky. “Multiple production and interference of particles emitted by moving sources”, *Sov. J. Nucl. Phys.* 18 (1974), 336–341. [*Yad. Fiz.* 18, 656 (1973)].
- [9] G. I. Kopylov. “Like particle correlations as a tool to study the multiple production mechanism”, *Phys. Lett. B* 50 (1974), 472–474.
- [10] R. Lednicky and V. L. Lyuboshits. “Final State Interaction Effect on Pairing Correlations Between Particles with Small Relative Momenta”, *Sov. J. Nucl. Phys.* 35 (1982), 770. [*Yad. Fiz.* 35, 1316 (1981)].
- [11] R. Lednicky. “Correlation femtoscopy”, *Nucl. Phys. A* 774 (2006), 189–198.
- [12] M. G. Bowler. “Extended Sources, Final State Interactions and Bose-Einstein Correlations”, *Z. Phys. C* 39 (1988), 81.

- [13] M. A. Lisa et al. “Bombarding energy dependence of pi-minus interferometry at the Brookhaven AGS”, *Phys. Rev. Lett.* 84 (2000), 2798–2802.
- [14] R. A. Soltz, M. Baker, and J. H. Lee. “Systematic investigation of two-pion correlations at the AGS”, *Nucl. Phys. A* 661 (1999), 439–443.
- [15] D. Adamová et al. “Beam energy and centrality dependence of two pion Bose-Einstein correlations at SPS energies”, *Nucl. Phys. A* 714 (2003), 124–144.
- [16] C. Alt et al. “Bose-Einstein correlations of pi-pi- pairs in central Pb+Pb collisions at A-20, A-30, A-40, A-80, and A-158 GeV”, *Phys. Rev. C* 77 (2008), 064908.
- [17] L. Adamczyk et al. “Beam-energy-dependent two-pion interferometry and the freeze-out eccentricity of pions measured in heavy ion collisions at the STAR detector”, *Phys. Rev. C* 92 (2015), 014904.
- [18] K. Aamodt et al. “Two-pion Bose-Einstein correlations in central Pb-Pb collisions at  $\sqrt{s_{NN}} = 2.76$  TeV”, *Phys. Lett. B* 696 (2011), 328–337.
- [19] M. A. Lisa et al. “Azimuthal dependence of pion interferometry at the AGS”, *Phys. Lett. B* 496 (2000), 1–8.
- [20] D. Adamová et al. “Azimuthal dependence of pion source radii in Pb+Au collisions at 158-A-GeV”, *Phys. Rev. C* 78 (2008), 064901.
- [21] D. Adamová et al. “Azimuthally differential pion femtoscopy in Pb-Pb collisions at  $\sqrt{s_{NN}} = 2.76$  TeV”, *Phys. Rev. Lett.* 118 (2017), 222301.
- [22] W. B. Christie et al. “Pion correlations in 1.8A GeV Ar on KCl and La and 1.2A GeV Xe on La”, *Phys. Rev. C* 45 (1992), 2836–2853.
- [23] W. B. Christie et al. “Pion correlations for 1.2A GeV Lanthanum on Lanthanum”, *Phys. Rev. C* 47 (1993), 779–787.
- [24] W. A. Zajc et al. “Two pion correlations in heavy ion collisions”, *Phys. Rev. C* 29 (1984), 2173–2187.
- [25] D. Miskowiec. “Pion pion correlations in Au + Au collisions at AGS energy”, *Nucl. Phys. A* 590 (1995), 473C–476C.
- [26] I. G. Bearden et al. “Two particle correlations from NA44”, *Proceedings, 2nd Catania Relativistic Ion Studies, Acicastello, Italy, June 8-12. 1998*, 114–123.
- [27] J. Adam et al. “One-dimensional pion, kaon, and proton femtoscopy in Pb-Pb collisions at  $\sqrt{s_{NN}} = 2.76$  TeV”, *Phys. Rev. C* 92 (2015), 054908.

- [28] L. Adamczyk et al. “Freeze-out dynamics via charged kaon femtoscopy in  $\sqrt{s_{NN}} = 200$  GeV central Au + Au collisions”, *Phys. Rev. C* 88 (2013), 034906.
- [29] L. Adamczyk et al. “ $\Lambda\Lambda$  Correlation Function in Au+Au collisions at  $\sqrt{s_{NN}} = 200$  GeV”, *Phys. Rev. Lett.* 114 (2015), 022301.
- [30] L. Adamczyk et al. “Measurement of Interaction between Antiprotons”, *Nature* 527 (2015), 345–348.
- [31] S. Acharya et al. “p-p, p- $\Lambda$  and  $\Lambda$ - $\Lambda$  correlations studied via femtoscopy in pp reactions at  $\sqrt{s} = 7$  TeV”, *Phys. Rev. C* 99 (2019), 024001.
- [32] S. Acharya et al. “Study of the  $\Lambda$ - $\Lambda$  interaction with femtoscopy correlations in pp and p-Pb collisions at the LHC”, *Phys. Lett. B* 797 (2019), 134822.
- [33] S. Acharya et al. “Investigation of the p- $\Sigma^0$  interaction via femtoscopy in pp collisions”, *Phys. Lett. B* 805 (2020), 135419.
- [34] J. Lidrych. “Femtoscopy with Unlike-sign Kaons at STAR in 200 GeV Au+Au Collisions”, *Acta Phys. Polon. Supp.* 9 (2016), 263.
- [35] D. Antonczyk and D. Miskowiec. “Pion-pion and pion-proton correlations: New results from CERES”, *Braz. J. Phys.* 37 (2007), 979–985.
- [36] M. Zawisza. “Pion-proton correlations and asymmetry measurement in Au+Au collisions at  $\sqrt{s_{NN}} = 200$  GeV data”, *Phys. Part. Nucl. Lett.* 8 (2011), 924–927.
- [37] J. Adam et al. “The Proton- $\Omega$  correlation function in Au+Au collisions at  $\sqrt{s_{NN}}=200$  GeV”, *Phys. Lett. B* 790 (2019), 490–497.
- [38] Yu. Sinyukov et al. “Coulomb corrections for interferometry analysis of expanding hadron systems”, *Phys. Lett. B* 432 (1998), 248–257.
- [39] G. Paic and P. K. Skowronski. “Effect of hard processes on momentum correlations in pp and p anti-p collisions”, *J. Phys. G* 31 (2005), 1045–1054.
- [40] U. A. Wiedemann and U. W. Heinz. “Particle interferometry for relativistic heavy ion collisions”, *Phys. Rept.* 319 (1999), 145–230.
- [41] G. Goebel. “Untersuchung der Bose-Einstein Korrelationen geladener Pionen in relativistischen Schwerionenkollisionen der Systeme Au+Au und Ni+Ni im Energiebereich von 1A GeV bis 2A GeV”. PhD thesis. Ruprecht-Karls-Universität, Heidelberg, 1995.
- [42] S. Chapman and U. W. Heinz. “HBT correlators: Current formalism versus Wigner function formulation”, *Phys. Lett. B* 340 (1994), 250–253.

- [43] S. Chapman, P. Scotto, and U. W. Heinz. “Model independent features of the two particle correlation function”, *Acta Phys. Hung. A* 1 (1995), 1–31.
- [44] C. DeWitt, A. Blandin, and C. Cohen-Tannoudji. *Lecture notes in Quantum Optics and Electronics*. Universite de Grenoble. Ecole d’ete de physique theorique. 1965.
- [45] M. Gyulassy, S. K. Kauffmann, and L. W. Wilson. “Pion Interferometry of Nuclear Collisions. 1. Theory”, *Phys. Rev. C* 20 (1979), 2267–2292.
- [46] D. Kincses, M. I. Nagy, and M. Csanad. “Coulomb and strong interactions in the final state of HBT correlations for Levy type source functions”, (2019). arXiv: 1912.01381 [hep-ph].
- [47] G. Baym and P. Braun-Munzinger. “Physics of Coulomb corrections in Hanbury-Brown-Twiss interferometry in ultrarelativistic heavy ion collisions”, *Nucl. Phys. A* 610 (1996), 286C–296C.
- [48] G. Baym. “The Physics of Hanbury Brown-Twiss intensity interferometry: From stars to nuclear collisions”, *Acta Phys. Polon. B* 29 (1998), 1839–1884.
- [49] H. W. Barz. “Effects of nuclear Coulomb field on two meson correlations”, *Phys. Rev. C* 53 (1996), 2536–2538.
- [50] H. W. Barz. “Combined effects of nuclear Coulomb field, radial flow, and opaqueness on two pion correlations”, *Phys. Rev. C* 59 (1999), 2214–2220.
- [51] S. Chapman, J. R. Nix, and U. W. Heinz. “Extracting source parameters from Gaussian fits to two particle correlations”, *Phys. Rev. C* 52 (1995), 2694–2703.
- [52] G. F. Bertsch. “Pion Interferometry as a Probe of the Plasma”, *Nucl. Phys. A* 498 (1989), 173C–180C.
- [53] S. Pratt. “Pion Interferometry of Quark-Gluon Plasma”, *Phys. Rev. D* 33 (1986), 1314–1327.
- [54] M. I. Podgoretsky. “On the Comparison of Identical Pion Correlations in Different Reference Frames”, *Sov. J. Nucl. Phys.* 37 (1983), 272. [Yad. Fiz. 37, 455 (1983)].
- [55] F. B. Yano and S. E. Koonin. “Determining Pion Source Parameters in Relativistic Heavy Ion Collisions”, *Phys. Lett. B* 78 (1978), 556–559.
- [56] W. A. Zajc. “Interferometry: New ideas and new directions”, *Nucl. Phys. A* 525 (1991), 315C–326C.
- [57] A. K. Chaudhuri. “Viscous Hydrodynamic Model for Relativistic Heavy Ion Collisions”, *Adv. High Energy Phys.* 2013 (2013), 693180.

- [58] M. Herrmann and G. F. Bertsch. “Source dimensions in ultrarelativistic heavy ion collisions”, *Phys. Rev. C* 51 (1995), 328–338.
- [59] B. R. Schlei, D. Strottman, and N. Xu. “The Linear correlation coefficient versus the cross term in Bose-Einstein correlations”, *Phys. Lett. B* 420 (1998), 1–7.
- [60] U. A. Wiedemann. “Two particle interferometry for noncentral heavy ion collisions”, *Phys. Rev. C* 57 (1998), 266–279.
- [61] J. D. Bjorken. “Highly Relativistic Nucleus-Nucleus Collisions: The Central Rapidity Region”, *Phys. Rev. D* 27 (1983), 140–151.
- [62] U. A. Wiedemann, P. Scotto, and U. W. Heinz. “Transverse momentum dependence of Hanbury-Brown-Twiss correlation radii”, *Phys. Rev. C* 53 (1996), 918–931.
- [63] G. Agakishiev et al. “The High-Acceptance Dielectron Spectrometer HADES”, *Eur. Phys. J. A* 41 (2009), 243–277.
- [64] H. Schuldes. “Charged kaon and  $\phi$  reconstruction in Au+Au collisions at 1.23 AGeV”. PhD thesis. Goethe-Universität, Frankfurt (Main), 2016.
- [65] T. Scheib. “ $\Lambda$  and  $K_s^0$  production in Au+Au collisions at 1.23A GeV”. PhD thesis. Goethe-Universität, Frankfurt (Main), 2017.
- [66] B. Kindlern et al. “Targets for the electron-positron pair spectrometer HADES”, *Nucl. Instrum. Meth. A* 655 (2009), 95–99.
- [67] J. Markert. “Untersuchung zum Ansprechverhalten der Vieldraht-Driftkammern niedriger Massenbelegung des HADES-Experimentes”. PhD thesis. Goethe-Universität, Frankfurt (Main), 2005.
- [68] M. Tanabashi et al. (PDG). “Review of Particle Physics”, *Phys. Rev. D* 98 (2018), 030001.
- [69] J. Michel. “Development and Implementation of a New Trigger and Data Acquisition System for the HADES Detector”. PhD thesis. Goethe-Universität, Frankfurt (Main), 2012.
- [70] G. Kornakov. “New Advances and Developments on the RPC TOF Wall of the HADES Experiment at GSI”. PhD thesis. Universdad de Santiago de Compostela, 2012.
- [71] D. Belver et al. “The HADES RPC inner TOF wall”, *Nucl. Instrum. Meth. A* 602 (2009), 687–690.
- [72] J. Pietraszko et al. “Radiation damage in single crystal CVD diamond material investigated with a high current relativistic  $^{197}Au$  beam”, *Nucl. Instrum. Meth. A* 763 (2014), 1–5.
- [73] S. A. Bass et al. “Microscopic models for ultrarelativistic heavy ion collisions”, *Prog. Part. Nucl. Phys.* 41 (1998), 255–369.

- [74] R. Brun et al. “Geant: Simulation Program for Particle Physics Experiments. User Guide and Reference Manual”, (1978).
- [75] P. Sellheim. “Reconstruction of the low-mass dielectron signal in  $1.23A$  GeV Au+Au collisions”. PhD thesis. Goethe-Universität, Frankfurt (Main), 2017.
- [76] J. Adamczewski-Musch et al. “Centrality determination of Au + Au collisions at  $1.23A$  GeV with HADES”, *Eur. Phys. J. A* 54 (2018), 85.
- [77] A. Bialas, M. Bleszynski, and W. Czyz. “Multiplicity Distributions in Nucleus-Nucleus Collisions at High-Energies”, *Nucl. Phys. B* 111 (1976), 461–476.
- [78] R. J. Glauber. “Cross-sections in deuterium at high-energies”, *Phys. Rev.* 100 (1955), 242–248.
- [79] M. L. Miller et al. “Glauber modeling in high energy nuclear collisions”, *Ann. Rev. Nucl. Part. Sci.* 57 (2007), 205–243.
- [80] H. Liu et al. “Sideward flow in Au + Au collisions between  $2A$  GeV and  $8A$  GeV”, *Phys. Rev. Lett.* 84 (2000), 5488–5492.
- [81] J.-Y. Ollitrault. “On the measurement of azimuthal anisotropies in nucleus-nucleus collisions”, (1997). arXiv: 9711003 [nucl-ex].
- [82] A. Schmah. “Produktion von Seltsamkeit in Ar+KCl Reaktionen bei  $1.756$  AGeV mit HADES”. PhD thesis. Technische Universität Darmstadt, 2008.
- [83] J. Adamczewski-Musch et al. “Charged-pion production in **Au + Au** collisions at  $\sqrt{s_{NN}} = 2.4$  GeV: HADES Collaboration”, *Eur. Phys. J. A* 56.10 (2020), 259.
- [84] A. Wagner. “Systematische Untersuchung symmetrischer Schwerionenreaktionen: Pionen als Sonden der Reaktionsdynamik.” PhD thesis. Technische Universität Darmstadt, 1996.
- [85] B. J. VerWest and R. A. Arndt. “NN single pion production cross-section below 1500 MeV”, *Phys. Rev. C* 25 (1982), 1979.
- [86] C. Hartnack et al. “What pions can tell us about the neutron skin of nuclei”, *CERN Proc. 1* (2019), 211–218.
- [87] S. Acharya et al. “Measurement of strange baryon–antibaryon interactions with femtoscopic correlations”, *Phys. Lett. B* 802 (2020), 135223.
- [88] D. Miskowiec and S. Voloshin. “On the normalization of the HBT correlation function”, *Acta Phys. Hung. A* 9 (1999), 283–287.
- [89] O. Arnold. “Study of the hyperon-nucleon interaction via femtoscopy in elementary systems with HADES and ALICE”. PhD thesis. Technische Universität München, 2017.

[90] Z. Chajecki and M. A. Lisa. “Global Conservation Laws and Femtoscopy of Small Systems”, *Phys. Rev. C* 78 (2008), 064903.

[91] A. M. Sirunyan et al. “Bose-Einstein correlations in  $pp$ ,  $p\text{Pb}$ , and  $\text{PbPb}$  collisions at  $\sqrt{s_{NN}} = 0.9 - 7$  TeV”, *Phys. Rev. C* 97 (2018), 064912.

[92] S. Schuchmann. “Bose-Einstein-Korrelationen in Pb-Au Stößen bei einer Strahlenergie von 80 GeV pro Nukleon”. Diploma thesis. Goethe-Universität, Frankfurt (Main), 2008.

[93] A. Mwai. “Beam Energy and System-size Dependence of the Space-time Extent of the Pion Emission Source Produced in Heavy-Ion Collisions”. PhD thesis. Stony Brook U., 2014.

[94] M. Lopez-Noriega. “Pion Interferometry in AuAu Collisions at a Center of Mass Energy per Nucleon of 200 GeV”. PhD thesis. Ohio State University, 2004.

[95] A. Kisiel. “Non-identical Particle Correlation Analysis in the Presence of Non-femtoscopic Correlations”, *Acta Phys. Polon. B* 48 (2017), 717.

[96] A. Adare et al. “Lévy-stable two-pion Bose-Einstein correlations in  $\sqrt{s_{NN}} = 200$  GeV Au+Au collisions”, *Phys. Rev. C* 97 (2018), 064911.

[97] I. Fröhlich et al. “Design of the Pluto Event Generator”, *J. Phys. Conf. Ser.* 219 (2010), 032039.

[98] D. A. Brown and P. Danielewicz. “Imaging of sources in heavy ion reactions”, *Phys. Lett. B* 398 (1997), 252–258.

[99] D. A. Brown and P. Danielewicz. “Optimized discretization of sources imaged in heavy ion reactions”, *Phys. Rev. C* 57 (1998), 2474–2483.

[100] D. A. Brown and P. Danielewicz. “Observing nongaussian sources in heavy ion reactions”, *Phys. Rev. C* 64 (2001), 014902.

[101] D. A. Brown et al. “Imaging three dimensional two-particle correlations for heavy-ion reaction studies”, *Phys. Rev. C* 72 (2005), 054902.

[102] R. Metzler, E. Barkai, and J. Klafter. “Anomalous Diffusion and Relaxation Close to Thermal Equilibrium: A Fractional Fokker-Planck Equation Approach”, *Phys. Rev. Lett.* 82 (1999), 3563–3567.

[103] D. Kincses. “Shape analysis of HBT correlations at STAR”, *Phys. Part. Nucl.* 51 (2020), 267–269.

[104] U. W. Heinz et al. “Symmetry constraints for the emission angle dependence of HBT radii”, *Phys. Rev. C* 66 (2002), 044903.

[105] A. Enokizono. “Space-time evolution of hot and dense matter probed by Bose-Einstein correlation in  $Au + Au$  collisions at  $\sqrt{s_{NN}} = 200$  GeV”. PhD thesis. Hiroshima University, 2004.

- [106] L. Q. Shan et al. “Effect of collective phase transition in the AMPT model on two-pion HBT radii”, *J. Phys. G* 36 (2009), 115102.
- [107] J. Gramling. “Azimuthally Sensitive Hanbury Brown–Twiss Interferometry measured with the ALICE Experiment”. Diploma thesis. Ruprecht-Karls-Universität, Heidelberg, 2012.
- [108] F. Retiere and M. A. Lisa. “Observable implications of geometrical and dynamical aspects of freeze out in heavy ion collisions”, *Phys. Rev. C* 70 (2004), 044907.
- [109] L. Adamczyk et al. “Bulk Properties of the Medium Produced in Relativistic Heavy-Ion Collisions from the Beam Energy Scan Program”, *Phys. Rev. C* 96 (2017), 044904.
- [110] G. E. Brown, J. Stachel, and G. M. Welke. “Pions from resonance decay in Brookhaven relativistic heavy ion collisions”, *Phys. Lett. B* 253 (1991), 19–22.
- [111] U. A. Wiedemann and U. W. Heinz. “Resonance contributions to HBT correlation radii”, *Phys. Rev. C* 56 (1997), 3265–3286.
- [112] A. Wagner et al. “The Emission pattern of high-energy pions: A New probe for the early phase of heavy ion collisions”, *Phys. Rev. Lett.* 85 (2000), 18–21.
- [113] H. Heiselberg and A. P. Vischer. “Bose-Einstein correlations from opaque sources”, *Eur. Phys. J. C* 1 (1998), 593–597.
- [114] B. Tomasik and U. W. Heinz. “Fine tuning two particle interferometry. 2. Opacity effects”, (1998). arXiv: 9805016 [nucl-th].
- [115] J. Adamczewski-Musch et al. “Identical pion intensity interferometry in central Au+Au collisions at 1.23A GeV”, *Phys. Lett. B* 795 (2019), 446–451.
- [116] J. Adamczewski-Musch et al. “Identical pion intensity interferometry at  $\sqrt{s_{\text{NN}}}=2.4$  GeV”, *Eur. Phys. J. A* 56 (2020), 140.
- [117] E. Khyzhniak. “Azimuthally-Differential Pion Femtoscopy in Cu + Au and Au + Au Collisions at  $\sqrt{s_{\text{NN}}} = 200$  GeV in the STAR Experiment”, *Phys. Part. Nucl.* 51 (2020), 270–273.
- [118] M. A. Lisa. “Timescales in heavy ion collisions”, *Acta Phys. Polon. B* 47 (2016), 1847.
- [119] M. A. Lisa et al. “Shape analysis of strongly-interacting systems: The Heavy ion case”, *New J. Phys.* 13 (2011), 065006.
- [120] Y. Kawamura. “Azimuthal-angle dependence of pion femtoscopy relative to the first-order event plane in  $\sqrt{s_{\text{NN}}} = 200$  GeV Au+Au and Cu+Au collisions at STAR”. Presentation given at WWND 2019, Beaver Creek.

- [121] L. Adamczyk et al. “Inclusive charged hadron elliptic flow in Au + Au collisions at  $\sqrt{s_{NN}} = 7.7 - 39$  GeV”, *Phys. Rev. C* 86 (2012), 054908.
- [122] L. Ahle et al. “System, centrality, and transverse mass dependence of two pion correlation radii in heavy ion collisions at 11.6A GeV and 14.6A GeV”, *Phys. Rev. C* 66 (2002), 054906.
- [123] D. Cebra et al. “Coulomb effect in Au+Au and Pb+Pb collisions as a function of collision energy”, (2014). arXiv: 1408.1369 [nucl-ex].
- [124] A. Wagner et al. “Evidence for different freezeout radii of high-energy and low-energy pions emitted in Au + Au collisions at 1A GeV”, *Phys. Lett. B* 420 (1998), 20–24.



# Danksagung

Zuerst möchte ich Professor Burkhard Kämpfer danken, der mich bereits als Masterand in seine Gruppe aufgenommen hat und mir die Möglichkeit eröffnet hat, diesem spannenden Thema meine Promotion zu widmen. Zudem möchte ich ihm für die vielen Bemerkungen danken, die mich immer wieder über meinen Tellerrand hinaus schauen ließen.

Professor Thomas Cowan möchte ich danken, mich am Institut für Strahlenphysik aufgenommen zu haben und mir damit die Arbeit im Umfeld vieler exzellenter Wissenschaftler zu ermöglichen.

Ich bedanke mich bei Professor Christoph Blume für die vielen kritischen Begutachtungen meiner Resultate und Zwischenergebnisse und Wegweisungen für weitere Analysen.

Ganz besonders bedanken möchte ich mich bei Roland Kotte, der mir der beste Betreuer war den ich mir vorstellen können. Ich danke dir für die theoretische und praktische Einführung in die Thematik dieser Arbeit und dass ich von deiner enormen Erfahrung und Expertise profitieren konnte, aber auch dafür, dass ich immer die nötige Freiheit hatte, mich meinen eigenen Ideen zu widmen. Ich bin sehr froh, in diesem kollegialen und gefühltschwanglosen Miteinander gearbeitet zu haben.

Paul Petring und Daniela Scheibler danke ich für die Bereitstellung der IT und die kompetente Lösung der damit angefallenen Probleme.

Bedanken möchte ich mich auch bei meinen Arbeitskollegen in der Abteilung Kernphysik für die sehr angenehme Arbeitsatmosphäre. Besonderer Dank gilt dabei meinem Gruppenleiter Andreas Wagner für sein Vertrauen in meine Arbeit und seinem Erfahrungsschatz, den er mit mir geteilt hat. Ein besonderes Dankeschön möchte ich auch Lothar Naumann für die vielen interessanten Gespräche und Erläuterungen, insbesondere was die Hardware-Seite unserer Experimente betraf, aussprechen. Sie haben meinen Horizont ein ganzes Stück erweitert. Xingming Fan danke ich für die vielen kleinen

Hilfen, die man sich als Bürokollegen und -nachbarn gegeben hat, aber nicht zuletzt auch für die kulturelle Erweiterung meines Horizontes.

Besonders möchte ich nochmal meinem “Leidensgenossen” Uwe Hernandez Acosta danken, für die vielen technischen Hilfen, die kritischen Fragen eines Theoretikers und so manchem spitzfindigen Kommentar zu meinen Abbildungen. Bei unseren vielen gemeinsamen Kaffeepausen ging uns nie der Diskussionsstoff aus und sie trugen sehr zum Wohlgefühl bei der Arbeit bei.

Vielen Dank sende ich an die gesamte HADES Kollaboration, ohne eure Vorarbeit wäre diese Arbeit nicht möglich gewesen. Ich bedanke mich für eure Ideen, Diskussionen, Erklärungen und Ratschläge, aber auch für die tolle gemeinsame Zeit bei Konferenzen und Strahlzeiten. Es hat jedes Mal Spaß mit euch gemacht und ihr wart wie eine große Familie. Besonders im Zuge dieser Arbeit möchte ich mich nochmal bei Jochen Markert für die vielen technischen Hilfen bedanken. Behruz Kardan und Małgorzata Gumberidze danke ich für ihre Zuarbeit und die vielen E-Mail-Diskussionen, die mir bei ausgewählten Thematiken sehr geholfen haben und hoffentlich beiderseitig zum besseren Verständnis beigetragen haben. Bardzo dziękuję!

Ich danke meinen Freunden, meinen Eltern und meiner Familie für all ihre Unterstützung. Nicht zuletzt danke ich insbesondere meiner Lebenspartnerin Nadine für ihre uneingeschränkte Hilfe. Du hast mir immer den Rücken freigehalten.

## Erklärung

Hiermit versichere ich, dass ich die vorliegende Arbeit ohne unzulässige Hilfe Dritter und ohne Benutzung anderer als der angegebenen Hilfsmittel angefertigt habe. Die aus fremden Quellen direkt oder indirekt übernommenen Gedanken sind als solche kenntlich gemacht. Die Arbeit wurde bisher weder im Inland noch im Ausland in gleicher oder ähnlicher Form einer anderen Prüfungsbehörde vorgelegt.

Diese Dissertation wurde am Helmholtz-Zentrum Dresden-Rossendorf e.V., Institut für Strahlenphysik (Leiter: Prof. Dr. T. E. Cowan und Prof. Dr. U. Schramm) unter der direkten wissenschaftlichen Betreuung durch Dr. R. Kotte und dem zuständigen Hochschullehrer Herrn Prof. Dr. Burkhard Kämpfer angefertigt. Ich habe bisher an keiner Institution, weder im Inland noch im Ausland, einen Antrag auf die Eröffnung eines Promotionsverfahrens gestellt. Ich erkläre ferner, dass ich die Promotionsordnung der Fakultät Mathematik und Naturwissenschaften der Technischen Universität Dresden vom 23. Februar 2011 anerkenne.

Robert André Heinrich Greifenhagen  
Dresden, 26.06.2020